Kinematic and Anatomical Measurement for Biomechanical Finger Models

Oliver Warlow

In fulfilment of the requirements for the degree of Doctor of Philosophy

Newcastle University

Newcastle upon Tyne, U.K.

April 2012

For NorNor and Max

Biomechanical models of the fingers are used to gain a greater understanding of their internal loading which will help guide clinicians treat injuries and pathologies. These models require accurate measurement of body kinematics, external reaction forces and anthropometry. The aim of this PhD was to gain a greater understanding of the predicted internal loading using biomechanical finger models and propose improvements in the kinematic and anatomical measurements required as their inputs.

Through sensitivity analysis, correlations between uncertainty in the anthropometry and kinematics with predicted internal loading were found. This showed that the predicted internal loading was most sensitive to changes in the moment arm of the flexor digitorum profundus tendon.

A new method of motion capture of the fingers using functionally defined joint centres was assessed. This method required the subject to complete a set of calibration movements. Subjects with an injury or pathology may have significantly reduced mobility, therefore an analysis was carried out to quantify the effect of reducing the available movement to that of a subject with pathological mobility. This resulted in errors of less than 5% in the predicted internal loading. It was important to note however, that in the extreme cases of deformity and lack of mobility this functional technique would not be suitable.

Finally, a combined method of ultrasound and stereo-photogrammetry to measure the in-vivo moment arm of the flexor digitorum profundus was developed, enabling non-invasive subject specific measurements. Measurement made using this technique found moment arms within the range of previous studies but they were found to alter the predicted internal loading by up to 84%. This demonstrated the importance of subject specific measurement. Although this was only a pilot study with a single subject it showed how this technique could be applied not just to the fingers but to other parts of the body where subject specific measurements of moments arms are important.

I would like to thank my supervisors, Sian Lawson for convincing me to start my PhD and to John Hedley and Garth Johnson for getting me to the end; My parents and family for constant encouragement and vital proof reading; Jo for being there through it all; Everyone who has climbed with me over the last three years for giving me the escape; Dave Green, Andreas Kontaxis and Brook Galna who's technical help and ideas were invaluable; Brian Stoker for making my ideas possible; James Humphrey for caffeinated distraction; Alessandro Sala for passing through; Pier, Milad, Pauline, James, Cate, Martin, Sophia and especially Richard for putting up with me.

Table of contents

List of abbreviations and acronyms

Abbreviation	Stands for
2D	Two Dimensional
3D	Three Dimensional
ACS	Anatomical coordinate System
AoR	Axis of Rotation
ATT	Axis Transformation Technique
CET	Central Band of the Extensor Tendon
CoP	Centre of Pressure
CoR	Centre of Rotation
CP	Control Points
CT	Computed Tomography
CTF	Cluster Technical Frame
CTT	Centre Transformation Technique
CSA	Cross Sectional Area
DIR	Dorsal Interosseous
DoF	Degree of Freedom
DIP	Distal Interphalangeal
EDC	Extensor Digitorum Communis

EIT	Extensor Indicis
EMG	Electromyography
FDP	Flexor Digitorum Profundus
FDS	Flexor Digitorum Superficialis
IAoR	Instantaneous Axis of Rotation
ICoR	Instantaneous Centre of Rotation
ISB	International Society of Biomechanics
JRF	Joint Reaction Force
JW	Joint Wrapping
LED	Light Emitting Diode
LUR	Lumbrical
MCP	Metacarpo-phalangeal
MRI	Magnetic Resonance Imaging
nJRF	Normalised Joint Reaction Force
PIP	Proximal Interphalangeal
PIU	Palmar Interosseous
PFT	Phalanx Fitting Technique
PTT	Phalanx Transformation Technique
RCL	Radial collateral ligament
RLB	Radial Band of the Extensor Tendon
RoM	Range of Motion
SVD	Singular Value Decomposition
TET	Terminal Band of the Extensor Tendon
UCL	Ulnar collateral ligament
ULB	Ulnar Band of the Extensor Tendon
UTE	Ultra-short Echo Time

Chapter 1. Introduction

1.1 Motivation

The ability to understand the internal loading on the human body can be of great assistance to clinicians, engineers and any other person involved in the prevention and treatment of musculoskeletal disorders. Kinematic analysis and musculoskeletal modelling of the fingers is substantially less developed than analysis of the lower limb. Although techniques and models have been proposed, there is still plenty of room for critical analysis of these studies and improvements to be made. The main thing that struck me through my initial research was the potential for great variation in predicted internal loading depending on the model used and accuracy of experimental measurement. This led to my research not only being focused on improving the accuracy of experimental measurement as input to musculoskeletal models, but also on the ability to quantify the errors and express them in terms relevant to real clinical applications.

1.2 Biomechanical models and their inputs

The first attempts at directly measuring joint forces were in the 1960’s using an instrumented hip joint prosthesis (Stokes, 1981). The original wired systems have since been superseded by more modern wireless systems (Westerhoff et al., 2009). The direct measurement of muscle and tendon loading is difficult due to the invasive nature of the procedures (Erdemir et al., 2007). Previous studies have used buckle transducers (Komi et al., 1987) and the less invasive optical fibre methods (Finni et al., 1998) to measure *in-vivo* loading for the Achilles tendon. Force transducers have also been applied to the flexor tendons of hand (Schuind et al., 1992). The disadvantage of these invasive techniques is that there was compromise in the range of positions that the subject could adopt and movement may have been affected by the local anaesthetic.

Addressing these problems of direct measurement, the field of musculo-skeletal modelling has emerged. This is the science of calculating internal forces from non-invasive external measurements. The idea of simplifying the human form to something more easily understood using scientific and mathematical techniques is not new and was first explored by Giovanni Borelli (1608-1679). His studies aimed to explain the mechanics of human and animal movement through comparison with machines. This principle of translating complex biological systems into simplified models is still maintained today.

When applied to the musculoskeletal system, models can be classified as two techniques. The first referred to as 'Forward Dynamic', calculates the kinematics and external forces applied to a body, from known muscle forces. The second referred to as 'Inverse Dynamic' uses measured kinematics and external reaction forces to calculate resultant joint moments, contact forces and soft tissue loading. This second technique and the accurate measurement of its inputs is the main focus of this thesis.

There are three primary inputs to an inverse dynamic model. The first is the body kinematics, these are the body segment positions, orientations and accelerations relative to a known datum point. The second is the external forces, also referred to as ground reaction forces applied to the body segments. By modelling the body as a chain of linked segments these forces are used along with the kinematics to calculate the moments and forces acting on each joint as a result of external forces. The third input is the soft tissue architecture data i.e. the size and position of all the muscles, tendons and ligaments relative to the joints as well as information about the joint and bone geometry.

The solution of the equations to find the required muscles activations are indeterminate due to the load sharing between muscles and the antagonistic muscle action (Erdemir et al., 2007). This normally means a criterion has to be defined that represents the neurological control of the muscles. This takes the form of a cost function that will minimise a given function of muscle stress.

The accurate measurement of any one of these inputs is important in gaining an accurate estimation of the internal loading.

1.3 Aims and objectives

The first objective of this study was to gain an understanding of the errors in predicted muscle, tendon and joint forces from existing musculoskeletal models of the finger. This was done by comparison of existing models and also a sensitivity analysis of the model to variations in experimental input. This could be variation in kinematics, external reaction force and anthropometric measurement.

The second objective was to use these findings to develop and assess new methods of experimental measurement for both kinematics and subject specific anatomy. The kinematic analysis was to provide as accurate a measurement as possible whilst minimising any restriction on the subjects' movements. In the measurement of subject specific anatomy it was of great importance to be able to measure non-invasively and preferably with the subject able to maintain movement of the fingers. This should enable the subject to maintain movement and force be applied to their finger whilst undergoing measurement.

1.4 Thesis Outline

Chapter 2 introduces and summarises the relevant anatomy of the hand, the concept of biomechanical models, their inputs and the use of inverse dynamics.

Chapter 3 is a study of influential model factors and the model sensitivity to changes in experimental input. The results from this chapter are used to assess the techniques of kinematic and anatomical measurement used in Chapters 5, 6 and 8.

Chapter 4 introduces the general principles and methods of motion capture. A review of available methods of motion analysis is made including specific application to the hand and fingers.

Chapter 5 introduces a new method of motion capture of the fingers using small hemispherical markers. A comparison is made between two methods of functional joint axis definition.

Chapter 6 uses the methods developed in Chapter 5 and assesses the influence of the calibration range of motion on the accuracy.

Chapter 7 reviews the methods of measuring tendon and muscle moment arms. A comparison of published moment arms for the flexor digitorum profundus tendon is made.

Chapter 8 proposes a new method of measuring finger tendon moment arms using combined ultrasound and stereo-photogrammetry. This includes a description of the full calibration procedure for spatial synchronisation of an ultrasound image in the photogrammetric reference frame.

Chapter 9 concludes the thesis with a summary of the findings with suggestions and potential for future work discussed.

Chapter 2. Anatomy and biomechanical modelling of the finger

The hand is the most important human organ for carrying out dextrous tasks. Without it we would not be able to grasp and manipulate tools, a crucial part in the evolution process that separates humans from the rest of the animal kingdom. The hand consists of bones, ligaments, muscles and tendons, resulting in a complex multi-articular body. The kinematics of the thumb and fingers are a function of muscle and tendon forces and joint geometry. Biomechanical models are a way of representing the hand anatomy in such a way as to provide quantitative assessment of movement and internal loading. Before any model can be constructed, first the underlying anatomy must be understood.

2.1 Anatomy of the hand

The bones and joints of the wrist and hand are visualised in Figure 2.1. Starting from the wrist, there are the proximal carpal bones that articulate on the distal surface of the radius bone of the forearm. The scaphoid and the lunate are the two carpal bones that directly articulate with the radius. The triquetrum and pisiform are the other two proximal carpal bones providing support. The distal carpal bones consist of the trapezium, trapezoid, capitate and hamate. These provide the articular surfaces for the metacarpal bones.

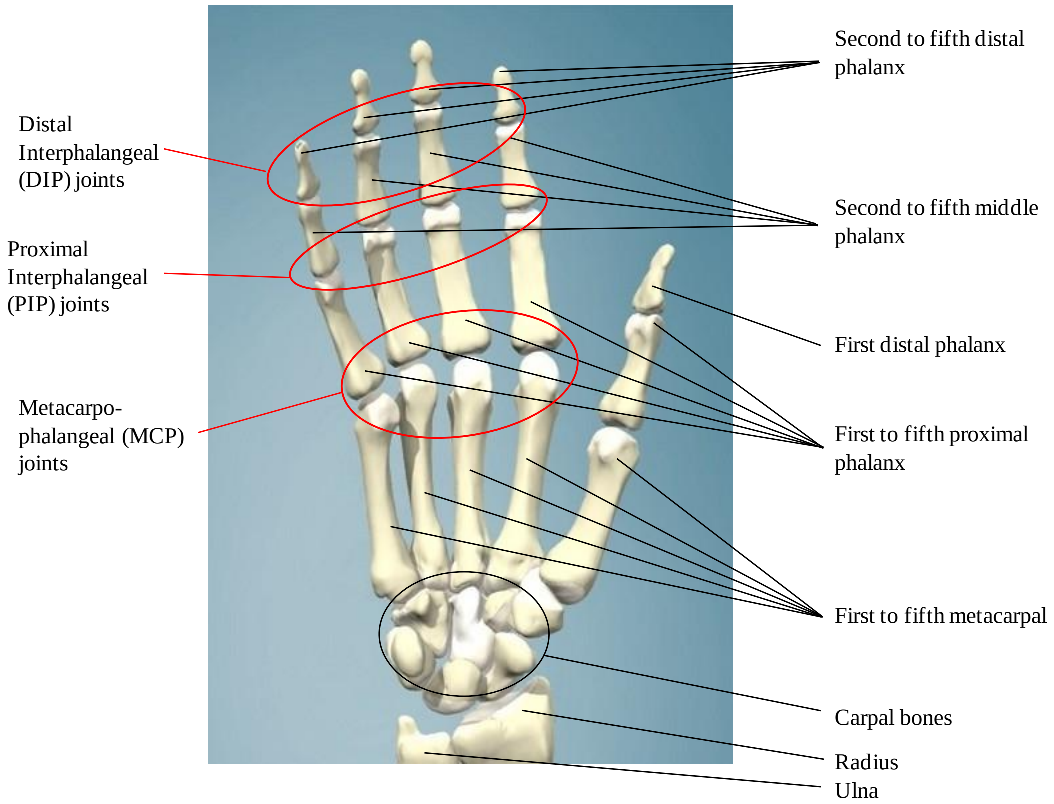

Figure 2.1: *Bones and joints of the hand. Figure adapted from www.anatomytv.com.*

The metacarpals are numbered one to five starting from the radial side. Therefore the number one refers to the thumb, two to the index finger, three to the middle finger, four to the ring finger and five to the little finger. The orientation of the first metacarpal gives it unique articulation relative to the others, providing us with our opposable thumbs. Metacarpals two to five provide the support and shape to the palm region of the hand.

At the distal end of each metacarpal lie the proximal phalanges one to five linked by the metacarpo-phalangeal (MCP) joints. For the thumb, the distal phalanx joins to the proximal phalanges via an interphalangeal joint. For the other fingers the middle phalanx joins to the proximal phalanx via proximal interphalangeal (PIP) joint. On these fingers the distal phalanx joins to the middle phalanx via the distal interphalangeal (DIP) joint.

All of the interphalangeal joints and the MCP joint are classed as synovial. The MCP joints are additionally classed as condyloid joints, meaning they are biaxial allowing two degrees of freedom (DoF), one about the flexion/extension and the other about the abduction/adduction axis. The supporting muscle, tendon and ligament structures do not allow this joint to rotate about the supination/pronation axis. The PIP and DIP joints are classed as hinges. This means they are uniaxial allowing only one degree of freedom about the flexion/extension axis. Although predominantly restricted by the bone geometry this single degree of freedom is also maintained by the collateral ligaments.

There is no significant muscle mass on the phalanges themselves, with no muscle insertions more distal than the proximal phalanx. This both keeps the mass of the fingers to a minimum and ensures there is no significant change in thickness with muscle contraction, maximising the fingers' and dexterity. The muscles providing control to the fingers are located in the forearm, these are connected to the fingers via long tendons.

The modelling undertaken in this study was predominantly focused on the index finger, so only the muscle and tendon structure for this finger is described fully (Figure 2.2 and Figure 2.3).

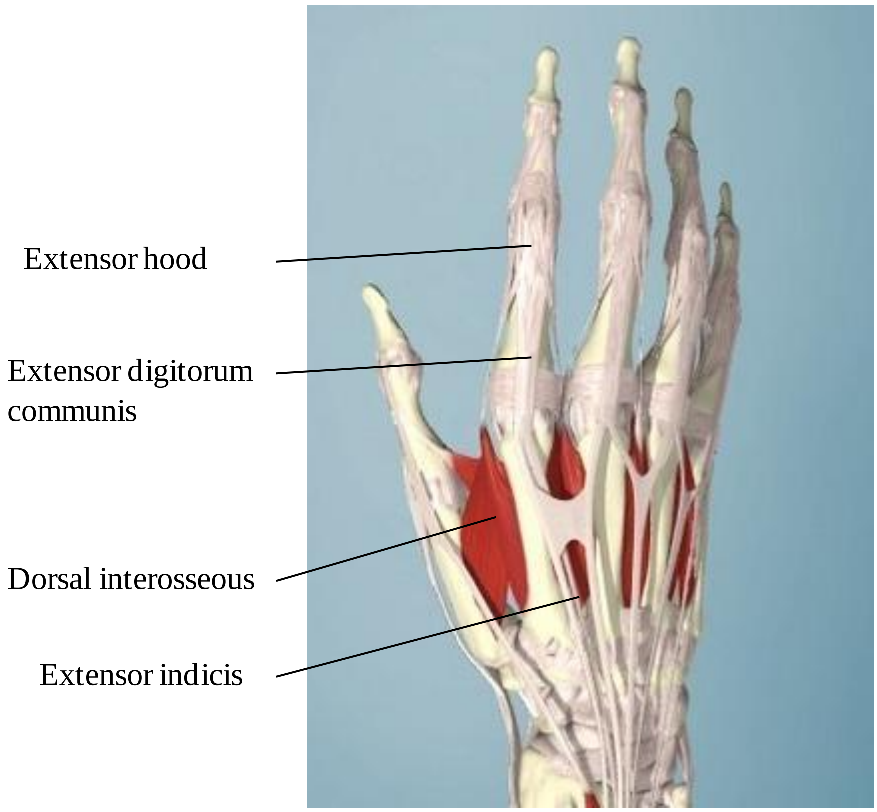

Figure 2.2: *Dorsal view of the right hand showing muscles and tendons. Figure adapted from www.anatomytv.com.*

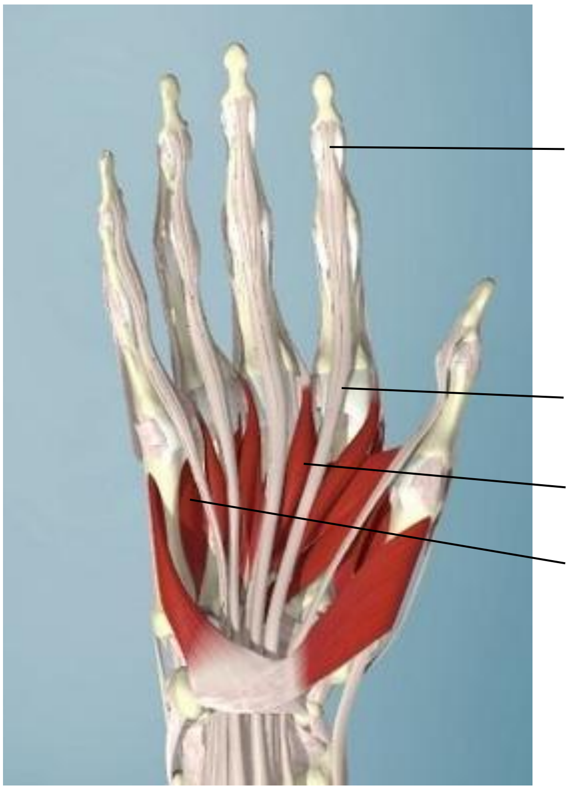

Figure 2.3: *Palmer view of the right hand showing muscles and tendons. Figure adapted from www.anatomytv.com.*

Three muscles act across the MCP joint; the dorsal interosseous (DIR), palmar interosseous (PIU) and the lumbrical (LUR). The DIR has its origin on the metacarpal shaft and insertion on the extensor hood distal to the MCP joint. It also has an insertion at the base of the proximal phalanx. It provides an abduction and flexion moment across the MCP joint. Due to its insertion in the extensor hood it also extends the two interphalangeal joints. The LUR and PIU origins are on the metacarpal shaft and insertion on the proximal phalanx, they also has an insertion on the ulnar and radial aspect of the extensor hood respectively. This means as it flexes the MCP joint is also extends the interphalangeal joints as well as adducting the MCP joint. The LUR origin is on the flexor digitorum profundus (FDP, described later) and insertion on the extensor hood. It flexes the MCP joint while extending the interphalangeal joints.

There are two flexor muscles located in the forearm, the flexor digitorum profundus (FDP) and flexor digitorum superficialis (FDS). Both of these divide into four tendons of the same name. These pass through the carpal tunnel and provide flexion of fingers two to four. The FDP inserts on the distal phalanx of the finger and flexes the two interphalangeal joints, the MCP joint and the wrist. The FDS inserts on the middle phalanx of the finger and flexes the PIP, MCP and wrist joints.

For the index finger there are two extensor muscles in the forearm, the extensor digitorum communis (EDC) and the extensor indicis (EIT), the second is only present for this finger. The EDC splits into three tendons that make up the tendon extensor hood acting across the interphalangeal joints. Acting across the PIP joint are the radial, ulnar and central bands (RLB, ULB and CET). These apply an extension moment at this joint and provide stability. The radial and ulnar bands re-join to form the terminal band of the extensor tendon (TET). This crosses the DIP joint and it has an insertion on the dorsal side of the distal phalanx, providing an extension moment across this joint. The EIT inserts into the proximal end of the extensor hood. A summary of all the muscle/tendon units and the joints which they cross is given in Table 2.1.

Functional unit	Abreviation	Acting across
Flexor Digitorum Profundus	FDP	DIP,PIP&MCP
Flexor Digitorum Superficialis	FDS	PIP&MCP
Central Band of the Extensor Tendon	CET	PIP
Radial Band of the Extensor Tendon	RLB	PIP
Ulnar Band of the Extensor Tendon	ULB	PIP
Terminal Band of the Extensor Tendon	TET	DIP
Extensor Indicis	EIT	MCP
Dorsal Interosseous	DIR	MCP
Extensor Digitorum Communis	EDC	MCP
Palmar Interosseous	PIU	MCP
Lumbrical	LUR	MCP

Table 2.1: *List of muscle and tendon units with their abbreviations and the joints that they cross.*

The kinematics of finger flexion are characterised by the presence of the pulleys that constrain the movement of the flexor tendons (Figure 2.4). By examining a simple two dimensional linkage model the role of these pulleys can be understood (Figure 2.5). The four segments shown are each connected by pin joints with segment 1 fixed. In Position A all the segments are aligned. A flexible string of length l_o connects segment four with the fixed wall. The length of the string is now shorted so the linkage is held in Position B. If there are no additional constraints on the string it will have a new length l_D i.e. the required shortening of the string is:

$$l_s = l_o - l_D. \quad \textbf{(2.1)}$$

We can now consider the case where the string is constrained at each pin joint. This constraint means that the distance between the string and joint perpendicular to the segment long axis is fixed. In this case the new length l_P is equal to the sum of l_1, l_2, l_3 and l_4. The required shortening of the string is:

$$l_s = l_o - l_P. \quad \textbf{(2.2)}$$

From the figure it is clear that $l_P > l_D$, therefore the required shortening of the string will be less when the constraint is applied.

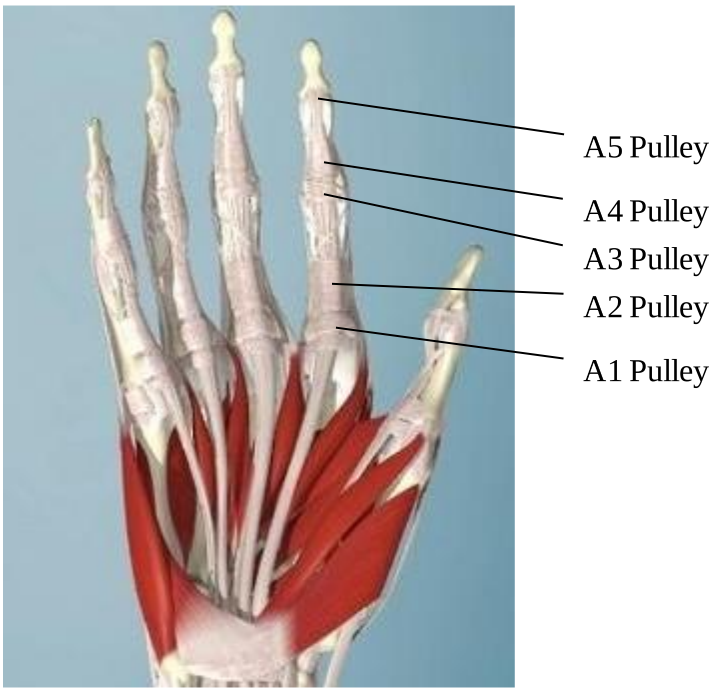

Figure 2.4: *Annular pulleys of the index finger of the right hand shown in the palmar view. Figure adapted from www.anatomytv.com.*

The pulleys of the fingers constrain the flexor tendons to follow a path similar to that shown by the solid line in Position B. It will not be identical as the pulley mechanism of the finger is more complex than that shown. In reality many of the pulleys act in pairs either side of joint rather than the simplified case shown. The pulleys give the hand its functional abilities in several ways. They don't allow the tendons to 'bow-string' across the palm, if this was the case then we would have no ability to grasp objects. As the tendons act as described above, less tendon excursion is needed to flex the finger joints. This results in a shorter muscle body allowing it to be positioned more proximal on the forearm. Minimal weight in the distal part of the upper limb gives optimal functional ability.

The presence of pulleys means higher forces are needed to apply or resist an external load. This is because the effective moment arm of the tendon across each joint is kept low, rather than allowed to increase as the joint is flexed. This means stronger (thicker) muscle bodies are required to flex the fingers. This suits the musculature of the body with shorter thicker muscles positioned proximally on the forearm.

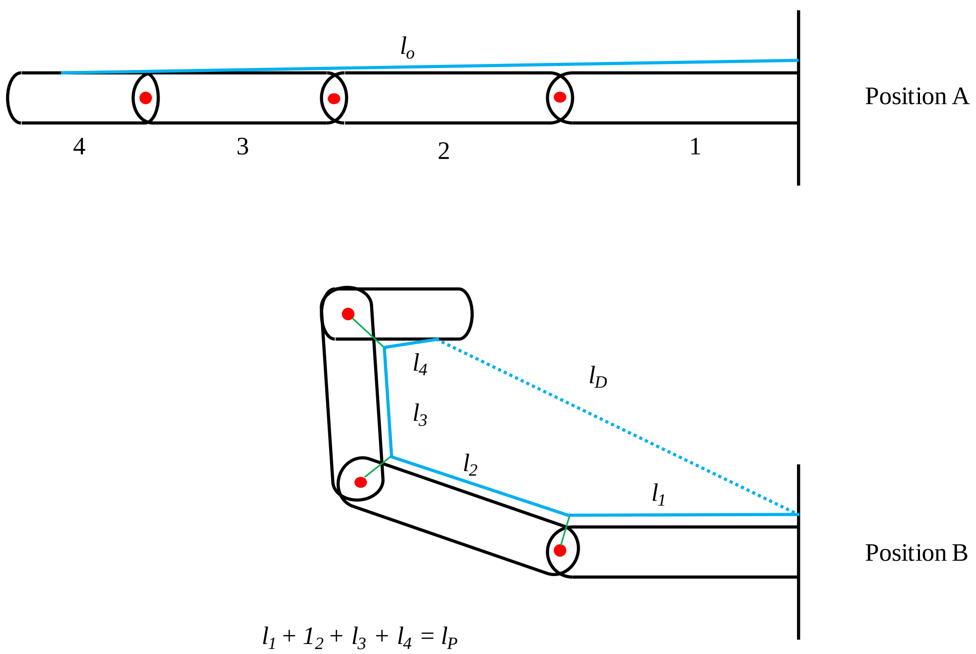

Figure 2.5: *Demonstrating the function of the pulley system. String starts with length l_o in Position A. If no constraints were present the string would shorten to length l_D to achieve Position B. With the inclusion of the constraints the string need only shorten to length l_P where $l_P > l_D$.*

2.2 Biomechanical models

Biomechanical models of the hand are used as a way of predicting the internal loading. The anatomy described needs to be represented in such a way that this can be done in a quantitative way. Due to the nature of activities carried out by the hand, a three-dimensional (3D) modelling approach is normally required. All models simplify the anatomy of the hand to a linked chain of segments that can articulate relative to each other (Figure 2.6). Each articulation is controlled by a joint of set kinematic properties (hinge, ball etc) and there will be a number of actuators acting across it. These actuators represent the muscles, tendons and ligaments acting across a given joint and they are represented by their line of action and moment arm. From these, the moment they apply across the joint as a function of tension in the actuator can be calculated.

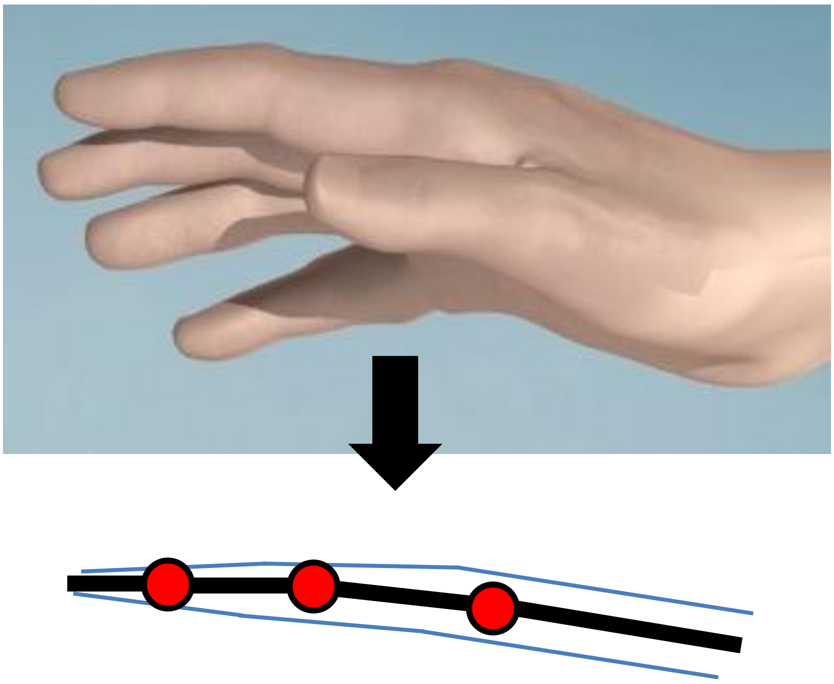

Figure 2.6: *All models represent the hand as a linked chain of segments. The muscles, tendons and ligaments are simplified to their line of action and moment arm acting across the joints.*

The first established hand models were those proposed by Landsmeer (Landsmeer, 1961) considering the hand in the simplified two dimensional (2D) case. 3D models of the hand have been developed for a variety of applications in the past (Qin et al., 2010; Wu et al., 2008; Vigouroux et al., 2007; Vigouroux et al., 2006; Sancho-Bru Joaquin et al., 2003; Sancho-Bru et al., 2001; Fowler and Nicol, 2000; Biggs and Horch, 1999; Valero-Cuevas et al., 1998; Esteki and Mansour, 1997; Brook et al., 1995; An et al., 1979). The model proposed by An et al (1979) was the first to use 3D moment arms for each muscle/tendon unit. An et al (1979) defined their model properties on the average measurements taken from cadaveric hands. This work has provided a basis for many models proposed subsequently. Some of these studies (Wu et al., 2008; Esteki and Mansour, 1997; Brook et al., 1995) were in the development of simulation models; these were in principle inverse dynamic models that either simulated a movement input or a force input to the finger. The resultant muscle/tendon tensions were then calculated. Wu et al (2008) used commercial modelling software (AnyBody) to model low impact tapping to improve treatment of repetitive strain injury. Estiki and Mansour (1997) used a whole hand model to simulate grip types and subsequently evaluate surgical outcomes for patients with tetraplegia. Brook et al (1995) developed a model of the index finger based the previous study of An et al (1979), and as with Wu et al (2008) this was compared with electromyography (EMG) data from the literature.

Other studies required a subject to carry out either a set of tasks or exercises. By taking measurements of the kinematics and external reaction forces, using the principle of inverse dynamics, the kinetics could be calculated. Vigouroux et al (2006 and 2007), studied high loading cases encountered in rock climbing. Climbers are known to suffer acute injuries to both the tendons and pulley mechanism of the fingers. The model used was based heavily on the previous work of An et al (1979) and Brook et al (1995). In these cases the hand was in a static pose, although the physical reality would require dynamic loading. Sancho-Bru et al (2001 and 2003) also used static measurements to represent a dynamic situation both for a free flexion and a high loading case. Valero-Cuevas et al (1998) used a phantom robot to track the movement and loading on the thumb dynamically. Fowler and Nicol (2000) used photogrammetric techniques similar to those used in gait analysis using clusters of retro-reflective markers to track hand movement. Combined with a load cell mounted into objects simulating simple tasks, accurate finger position and finger tip loading could be used as input to their model.

Their model differed significantly from most others due to the inclusion of three DoF at the PIP joint (instead of one DoF about the flexion/extension axis only).

Biomechanical models are used to predict internal loading of the hand as this is either very difficult or not practical to measure directly. Studies have been made on cadaveric hands to calculate both the failure strength and predicted load using certain grip types (Schöffl et al., 2009). Every model includes a cost function that represents muscle coordination and neurological control, making it not possible to use cadavers to validate models. It has been possible to use direct invasive techniques (Schuind et al., 1992), however as discussed in Chapter 1, there was compromise in the range of positions and movement of the subject. EMG measurements have been used to validate models (Valero-Cuevas et al., 1998) and can also be used as an input to constrain them (Vigouroux et al., 2007). Accurate EMG measurement requires the insertion of fine-wire probes into one or more of the extrinsic muscles. This is both painful for the subject and the calculation of muscle activation from EMG response is subject to error. The combination of these factors means that most models have been validated through comparison with other studies in which the subject carried out a similar set of activities.

2.3 Model inputs

As mentioned in Chapter 1, the measurement of any of the three model inputs is important in achieving an accurate calculation of the internal loading. These are the body kinematics, anthropometric measures and the external reaction force. This section briefly describes these three inputs and their measurement. Body kinematics and anthropometric measurement are covered with more detail in Chapters 4 and 7.

2.3.1 Body kinematics

Body kinematics are the spatial position and orientation of body segments in terms of displacement, velocity and acceleration. In the case of the hand models considered in this thesis the relevant body segments are the phalanges and metacarpals of the hand.

The body kinematics are combined with the external reaction forces to determine the body kinetics. This procedure to calculate the forces and moments between the body segments is known as inverse dynamics (as described in Section 2.4).

To calculate the body kinematics some form of motion capture must be carried out. In general these can be classed as video or inertial based. Photographic methods of measuring body segment position cannot strictly be classed at kinematic measurements as they only give a static position. They have however been used for the hand by several authors assuming static equilibrium to calculate the required moments and moments between the body segments (Vigouroux et al., 2006; Vergara et al., 2003).

Inertial based systems rely on accelerometers and gyroscopes to determine the accelerations and orientation of sensors attached to the subject. These can be transformed into velocities and displacements by integrating the acceleration signals. This method of motion capture is becoming more popular especially for gait analysis applications because of its cost relative to photogrammetric techniques and the lack of restriction on the subject to stay within a laboratory environment (Kavanagh and Menz, 2008). The size of the sensors means that this type of technique has yet to be used to track small body segments such as the fingers of the hand.

Video based systems use a camera or set of cameras to measure the position of the body segments either directly or using special markers. Marker based photogrammetric systems are the most common form of motion analysis to determine human kinematics (Andriacchi and Alexander, 2000). Either active or passive markers are tracked by an array of specialised cameras and their positions reconstructed in a 3D workspace. This method is well established in the field of biomechanics and has been used in application to the hand in numerous studies (Metcalf et al., 2008; Carpinella et al., 2006; Cerveri et al., 2005; Degeorges et al., 2005; Su et al., 2005; Miyata et al., 2004; Zhang et al., 2003; Fowler and Nicol, 1999b; Rash et al., 1999; Chiu et al., 1998).

2.3.2 Anthropometric data

The anthropometric data are used to define the mechanical properties of the articulated linkage that the finger is modelled as. This includes information about the bone geometry such as the size of each bone, the location of the axes of rotation and the position and size of any soft tissues relative to bones. The soft tissues of relevance are the muscles, tendons and ligaments.

For use in biomechanics models it is ultimately the calculation of the unit-force moment applied by each of these tissues across a given joint that is important. To calculate this it is necessary to measure or otherwise predict the moment arm and the line of action of each muscle or tendon. The moment arm can be thought of as the leverage across the joint and is equal to the perpendicular distance from the line of action of the muscle/tendon to the joint centre. The line of action is the direction of pull of this muscle/tendon. There is potential for confusion between the ‘unit-force moment’ and the ‘moment arm’ as some authors may not make a distinction between the two. In this thesis the terms will only be referred to as they are described above.

Using simple 2D mechanics the moment about a pin joint produced by a force applied, equals the product of the force applied and the distance to the pin joint perpendicular to this force. Using the properties of the cross (vector) product this can be generalised in 3D for the moment (***M***) applied by any force of magnitude (*T*) and direction (***e***) applied a distance (***r***) from a point of rotation. The moment applied by the force is calculated as:

$$\boldsymbol{M} = T \underbrace{(\boldsymbol{r} \times \boldsymbol{e})}_{\substack{unit-force\\ moment}} . \qquad \textbf{(2.3)}$$

In this case ***r*** is the moment arm of the tendon and ***e*** is the line of action. This is shown with relevance to a finger joint in Figure 2.7.

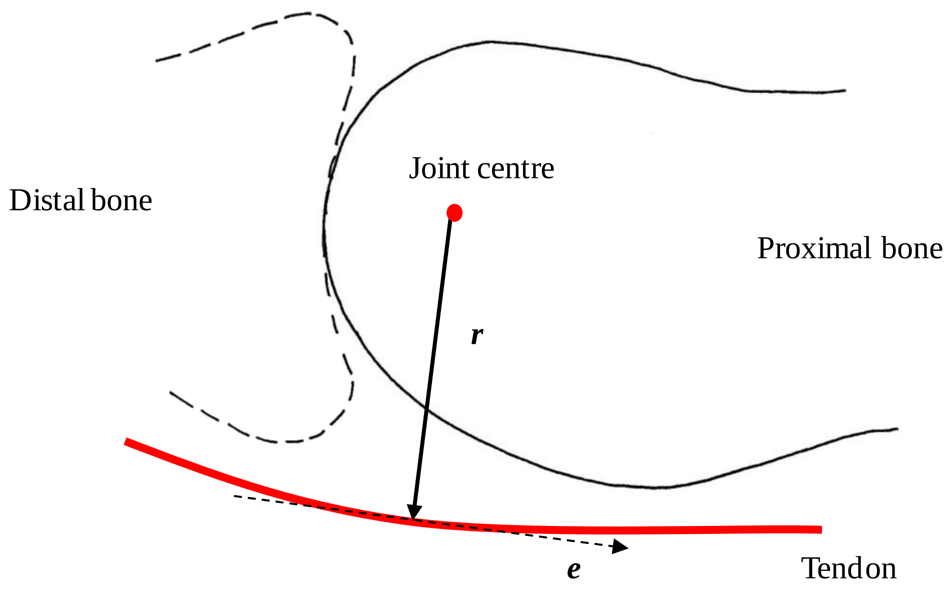

Figure 2.7: *Showing the moment arm (**r**) and line of action (**e**) of a tendon crossing a joint.*

Location of the bone features and axes of rotation relative to known landmarks is important in a number of ways. Depending on the method of motion analysis, the locations of the axes of rotation are used to define the kinematics of each body segment. Additionally these locations are also required for calculating the force path used in the inverse dynamic analysis (see section 2.4).

The unit-force moment of each muscle, tendon or ligament unit is used to solve the equilibrium equations described in section 2.4. This unit-force moment is calculated either from the moment arm or from both the moment arm and line of action. The moment arm can be thought of as the leverage across a joint, and the line of action, the direction of the force applied.

All anthropometric data ultimately rely on some form of anatomical measurement. These methods of anatomical measurement can be divided into two categories, invasive and non-invasive. In the case of live humans it is not possible to carry out invasive measurement, so this is carried out only on cadaver specimens. Non-invasive techniques normally require some form of medical imaging such as X-ray, computed tomography (CT), magnetic resonance imaging (MRI) or ultrasound. Such imaging can be carried out both on live subjects and cadavers.

A full description of measurement and calculation of these parameters is presented in Section 7.1.

2.3.3 External reaction forces

The third input to a biomechanical model is the external reaction force. This is used in the inverse dynamic analysis to calculate the body kinetics.

The conventional way of determining these forces is to use a force transducer. This can either be rigidly mounted in the laboratory, such as a force plate designed to measure the foot contact forces as a subject walks, or as a smaller transducer mounted in an object that the subject can pick up or otherwise interact with.

A force transducer can be capable of measuring between one and six forces and moments. If it is classed as mono-axial (Figure 2.8 (a)) it will measure force in only one direction, normally perpendicular to the transducer surface. A tri-axis transducer (Figure 2.8 (b)) is able to measure the force in three orthogonal directions i.e. the force perpendicular to the surface and the two shear forces. A six axis transducer (Figure 2.8 (c)) will measure these three forces and the moments about each of the three axes.

Mono-Axial force transducers have been used in several studies related to the hand (Vigouroux et al., 2008; Schweizer, 2001; Valero-Cuevas et al., 1998). A low-friction thimble placed over the finger was used by Valero-Cuevas et al (1998) to ensure only a perpendicular force was applied to the surface of a mono-axial force transducer. This experiment was not intended to represent a real situation but instead to eliminate shear forces (that would normally be present) to provide accurate input to a biomechanical model. Power grips used in the sport of rock climbing have been of interest to researchers due to the high loads present in the fingers. Schweizer (2001) used a mono-axial transducer to measure maximal force in these grip types. Because mono-axial transducers are smaller than tri-axial and six axis transducers they can be placed in an arrangement so as to create as true to life loading situation at possible. This was utilised by Vigouroux et al (2008) to examine load sharing across fingers with four transducers mounted in close proximity. To measure the force with a tri-axial force sensor the same authors were only able to measure the loading at a single finger (Vigouroux et al., 2006).

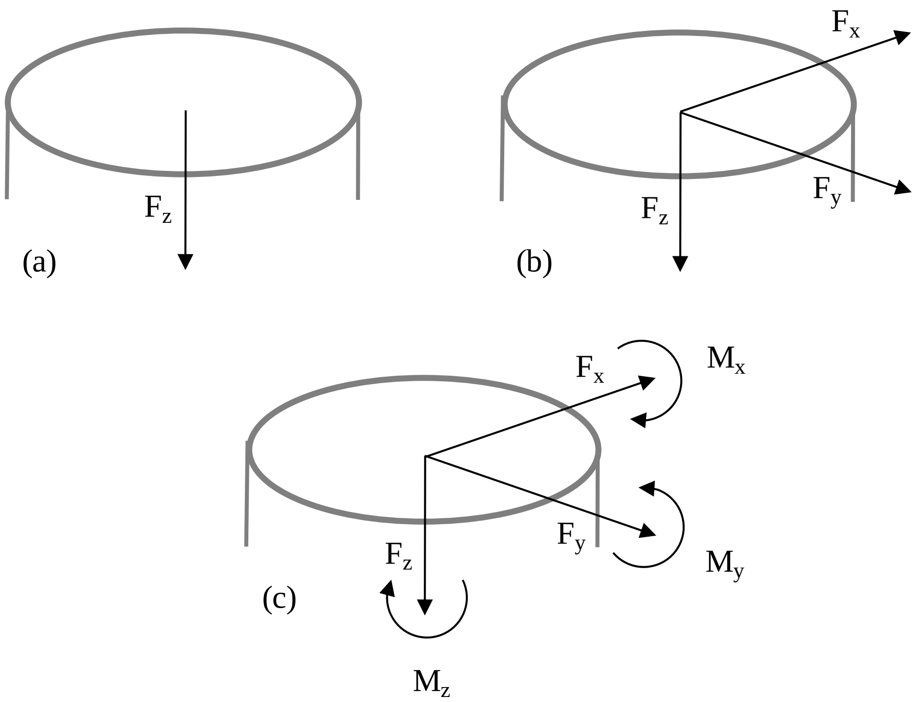

Figure 2.8: *A mono-axial force transducer (a) with only the force perpendicular to the surface measured. A tri-axial transducer (b) measuring the perpendicular force and the two shear forces. A six axis transducer (c) measuring the three forces and the moments about each of these axes.*

To get the most accurate measurement of the external reaction force a six axis force transducer needs to be used. The additional information gained from measuring the moments about each axis allows the exact position of the point of application of the force to be calculated.

Six axis force transducers can be bought ‘off the shelf’ or bespoke made to suit specific applications (Fowler and Nicol, 1999a). It is possible to mount transducers in a way so as to simulate every-day tasks such as opening a jar, twisting a tap, holding a kettle or turning a key (Figure 2.9). The ability to produce smaller and smaller six axis force transducers has allowed some researchers to mount multiple transducers into an object small and light enough to be picked up (Gislason et al., 2009). This allowed accurate force measurements to be taken from all three fingers and the thumb simultaneously. The rig was still bulky however and required compromise on how the subject could handle it.

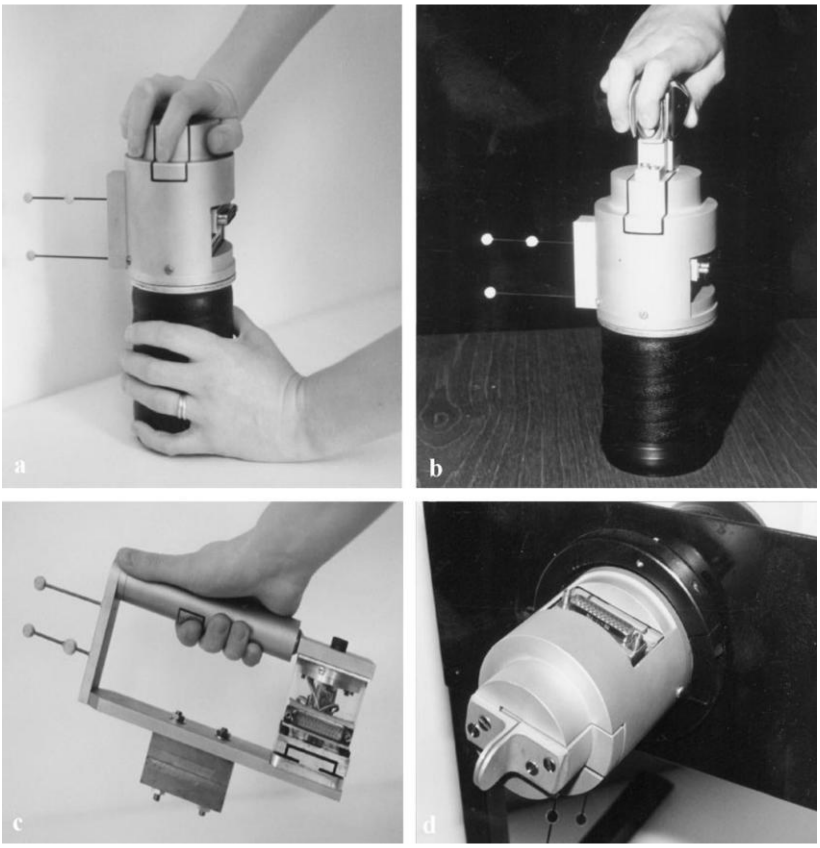

Figure 2.9: *A six axis force transducer mounted to simulate opening a jar (a), twisting a tap (b), holding a kettle (c) or turning a key (d). Adapted from Fowler and Nicol (1999a).*

2.4 Inverse dynamic modelling

In this thesis the application of inverse dynamic models is of significant interest. Inverse dynamics relies on the principle that the finger is modelled as a linked chain of rigid segments. Firstly the magnitude and direction of the external loads applied to the finger are measured along with the position and orientation of each individual segment. By setting up a series of Newton-Euler equilibrium equations for each segment the moments and forces at each joint can be calculated.

Subsequently, the force and moment equilibrium equations for each joint can be written in the generalised form (Chao et al., 1989):

$$\sum_{i=1}^{n} T_{\boldsymbol{i}}\,\boldsymbol{e}_i + \sum_{j=1}^{m} A_{\boldsymbol{j}}\,\boldsymbol{k}_j - \boldsymbol{F} = 0, \qquad \textbf{(2.4)}$$

$$\sum_{i=1}^{n} T_i(\boldsymbol{r}_i \times \boldsymbol{e}_i) + \sum_{j=1}^{m} A_j\left(\boldsymbol{S}_j \times \boldsymbol{k}_j\right) + \boldsymbol{M} = 0, \qquad \textbf{(2.5)}$$

where

T_i = magnitude of the force applied by tendon/muscle *i* (N).

$\boldsymbol{e}_i$ = unit vector of the direction of T_i.

A_j = magnitude of the external reaction force *j* (N).

$\boldsymbol{k}_j$ = unit vector of the direction of A_j.

$\boldsymbol{F}$ = the joint reaction force vector (N).

$\boldsymbol{r}_i$ = moment arm of the tendon/muscle *i* (mm).

$\boldsymbol{S}_j$ = position of the external reaction force *j* (mm).

$\boldsymbol{M}$ = passive moments applied across the joint (Nmm).

There are a total of *n* tendon forces crossing the joint with a total of *m* external reaction forces.

The parameters $\boldsymbol{e}_i$ and $\boldsymbol{r}_i$ are known from the body anthropometric data as detailed in Chapter 7. The parameters A_j, $\boldsymbol{k}_j$ and $\boldsymbol{S}_j$ are found using the kinematic analysis and the external reaction measurement. The passive moments across the joint $\boldsymbol{M}$ are a result of friction and ligament forces that are not dependent on any muscle activation. The moment equilibrium equation (2.5) is solved to find T_i, this can then be used to solve the force equilibrium equation (2.4) to find joint reaction forces.

There will be equilibrium equations for each joint included in the model with the tendon tensions T_i common between them, meaning they must all be solved simultaneously. Additionally, all models include constraints on how the values of T_i relate to each other based on the subject anatomy.

The tension in the TET (T_{TET}) is constrained to the tensions in the RLB and ULB by:

$$T_{TET} = \propto_{RLB} T_{RLB} + \propto_{ULB} T_{ULB}. \quad \textbf{(2.6)}$$

An example of how this is represented in a model can be seen in Figure 3.2. Some models such as those proposed by Fowler and Nicol (2000) and Chao et al (1989) take the value of the alpha coefficients as $\alpha_{RLB} = \alpha_{ULB} = 1$, whereas others such as Brook et al (1993) describe these coefficients as cosine terms depending on the angle of convergence of RLB and ULB.

To describe how tension is transferred to and shared between bands of the extensor hood (RLB, ULB and CET) another three constraint equations are defined. Chao et al (1989) described these relationships with fixed coefficient values shown by:

$$T_{RLB} = 0.167T_{EDC} + 0.667T_{LUR},$$

$$T_{ULB} = 0.167T_{EDC} + 0.333T_{PIU}, \quad \textbf{(2.7)}$$

$$T_{CET} = 0.333T_{PIU} + 0.333T_{LUR} + 0.167T_{EDC} + 0.333T_{DIR}.$$

These are based on available anatomical knowledge. Brook et al (1995) proposed a method subsequently in which variable alpha coefficients were used. This was subsequently used by Vigouroux et al (2006) in their model:

$$T_{RLB} = \propto_{EDC} T_{EDC} + \propto_{LUR} T_{LUR},$$

$$T_{ULB} = \propto_{EDC} T_{EDC} + \propto_{PIU} T_{PIU}, \quad \textbf{(2.8)}$$

$$T_{CET} = (1 - \propto_{PIU})T_{PIU} + (1 - \propto_{LUR})T_{LUR} + (1 - 2 \propto_{EDC})T_{EDC}.$$

These coefficients were constrained to take a value between 0 and 1. The optimal value was determined simultaneously to solving the constraint equations for T_i.

The total number of unknowns (V) will depend on the model and will be the sum of the unknown tendon/muscle tensions and any unknown alpha coefficients. The number of constraint equations (U) will depend on the model used. In every model $V > U$, i.e. the system is indeterminate. This means there is more than one solution of T that will meet the constraints. Methods have been described using reduction of variables (Chao et al., 1989), however it is more common to use optimisation methods. An additional constraint is applied to the solution of T in the form of a cost function (2.9). This cost function represents the neurological control applied to the muscles and it is optimised to find its minimum value.

$$c = f(T_i, \dots, T_n). \quad \textbf{(2.9)}$$

It is normally a function of the stress, calculated as the tendon/muscle force divided by its cross sectional area (CSA). It can be expressed in terms of either a minimal overall stress:

$$c = \sum_{i=1}^{n} \left(\frac{T_i}{CSA_i}\right)^2, \quad \textbf{(2.10)}$$

or by minimising the maximum stress σ, so that:

$$\frac{T_i}{CSA_i} \leq \sigma, \ \ i = 1,\dots,n. \quad \textbf{(2.11)}$$

The choice of which cost function to use is important and authors have proposed that the optimisation schemes vary depending on the activity being carried out. Sancho-Bru et al (2001) states that minimising the overall stress, represented minimal muscle fatigue. However this scheme was also used by Vigouourx et al (2006), for a maximal loading case. Brook et al (1993) also used this scheme, although no justification was made. Fowler and Nicol (2000) proposed that for static loading cases the minimal maximum stress would provide the best model. This shows that the argument for what cost function for a given application is best remains unresolved. An investigation on the effect of cost function on model outcome forms a part of this thesis in Chapter 3.

Chapter 3. Influential model factors and sensitivity analysis

The work presented in this chapter has been accepted for publication in 'The Proceedings of the Institution of Mechanical Engineers, Part H: Journal of Engineering in Medicine' with the title "*Sensitivity of a biomechanical model of the finger to errors in experimental input"* (Warlow and Johnson, 2012).

As was introduced in Chapter 2 a number of models of the hand and fingers have been proposed and the challenges facing their validation summarised. In this chapter an analysis was carried out to determine the significance of using different models for predicting internal loading, and the sensitivity of these models to changes in experimental input.

The study was split into two parts. For the first, the results from two different models of the index finger of the right hand were compared using identical sets of experimental data (body kinematics and external reaction force). Identical sets of data were used to ensure any significant differences in results were from the models alone. This comparison was done to show how and why results (i.e. resultant tendon tension and internal loading) can be quite different between models. The range of validity for each model was determined with regard to joint angle. From these analyses the most appropriate model for further use in this thesis was chosen and modifications proposed to improve its range of validity.

For the second part of the study, the appropriately chosen model was used and a sensitivity analysis to changes in input was carried out. The relationship between model outputs and errors in body kinematic and anthropometric measurement was established. These correlations are used later in Chapters 5 and 6 to assess the performance of the proposed method of kinematic analysis and in Chapter 8 to assess the effect of using subject specific muscle/tendon moment arms in the model.

3.1 Model selection

All models are a simplification of reality, including only what the researcher deems to be necessary components. To provide contrast between those that included different levels of complexity, two different models were used. The first, proposed by Fowler and Nicol (Fowler and Nicol, 2000) will be referred to as 'Model A'. The second, referred to as 'Model B', as proposed by Vigouroux et al (Vigouroux et al., 2006) was based on the normative model developed by An et al (1979).

Each model represented the phalanges and metacarpal as a linked chain of rigid segments. To ensure valid comparison between models a consistent definition of anatomical coordinate systems (ACSs) needed to be established. The positions and orientations of these axes were in accordance with the International Society of Biomechanics (ISB) recommendations (Wu et al., 2005) and are shown in Figure 3.1. For each segment the *y-axis* was directed proximally defining the long axis. The *x-axis* was directed palmarly and with the *y-axis* defined the sagittal plane of the segment. The *z-axis* was perpendicular to this plane and directed radially (it was coincident with the flexion axis of rotation at the interphalangeal joints).

The location of the segment origins was chosen to match those proposed Fowler et al (2001). The origin of each phalanx segment was coincident with the joint centre located proximally to the segment. The origin of the metacarpal segment was coincident with the joint centre located distally to the segment. This convention was chosen to suit the requirements of this study. If required it would be straightforward to express this origin in the position midway between the head and base of each segment (as proposed in the ISB recommendations (Wu et al., 2005)).

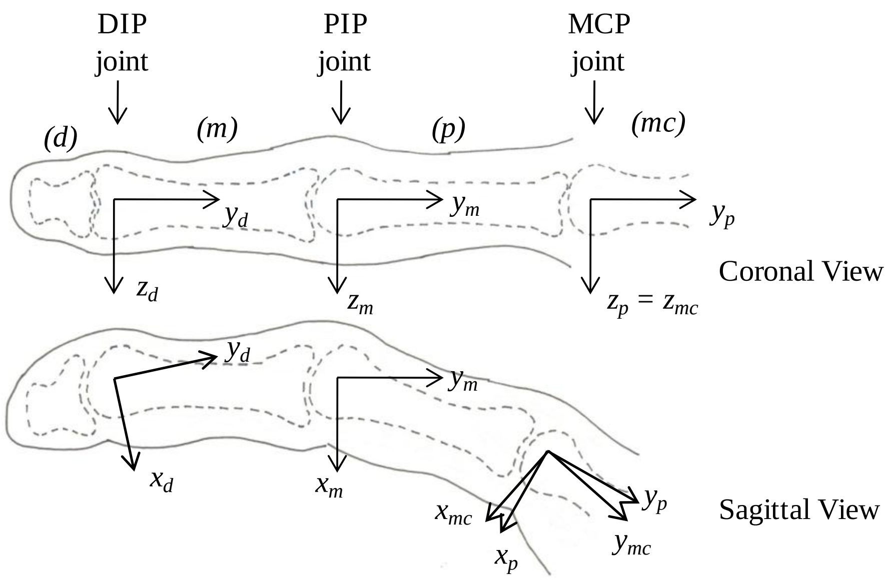

Figure 3.1: *Position and orientation of the ACSs of the phalanges and metacarpal of the right hand. For the each phalanx (d = distal, m = middle, p = proximal) the origin of each ACS was positioned at the joint centre at the proximal end of the segment. The metacarpal (mc) origin was coincident with the joint centre located distally to the segment. The x-axis was directed palmarly, the y-axis directed proximally and the z-axis directed radially for each segment.*

Model A included three segments representing the distal, middle and proximal phalanges, as shown in Figure 3.2. Joining these were the distal interphalangeal (DIP) and proximal interphalangeal (PIP) joints. The DIP joint was defined as a one degree of freedom (DoF) hinge about the flexion/extension (z) axis. The PIP joint modelled with three DoF about the flexion/extension (z) axis, the abduction/adduction (x) axis and the pronation/supination (y) axis. Acting across these joints were actuators representing six muscle/tendon functional units. These are described as functional units as they cannot be regarded as independent muscles and tendons. This is of particular relevance in the extensor hood where the extensor tendon is considered as a set of functional units bound by inter-dependent physical constraints. The flexor tendons were the flexor digitorum profundus (FDP) and the flexor digitorum superficialis (FDP). The extensor tendon was separated into four functional units, the central band (CET), the radial band (RLB), the ulnar band (ULB) and the terminal band (TET). Only the FDP and TET acted across the DIP joint. The remaining four actuators acted across the PIP joint in addition to the FDP that crossed both joints. At the PIP joint radial and ulnar collateral ligaments (RCL and UCL) were included to provide joint stability.

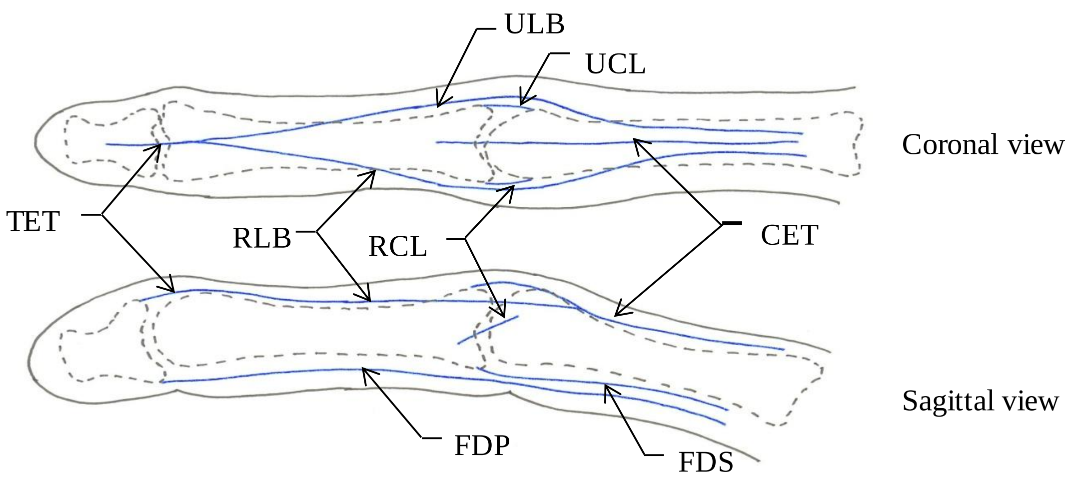

Figure 3.2: *Model A. Functional tendon/muscle units crossing the DIP and PIP joints.*

The force in the TET was defined by the equation:

$$F_{TET} = F_{ULB} + F_{RLB}. \tag{3.1}$$

This comes from equation (2.6), where F_{TET} is the force in the terminal extensor tendon and F_{ULB} and F_{RLB} are the forces in the ulnar and radial bands respectively. In this case the alpha coefficients of equation (2.6) have the value of one ($\alpha_{RLB} = \alpha_{ULB} = 1$).

The moment arms and lines of action for each functional unit were measured by magnetic resonance imaging (MRI) (Fowler et al., 2001). The measurements were made from a single 29 year old female subject with the hand in five positions. By normalising to the middle phalanx length these measurements could be scaled to our test subject (the reasons for using this as a scaling factor are discussed in Section 7.2). To transform these properties to suit joint angles not identical to those imaged, the actuator properties were either interpolated or extrapolated as a function of flexion angle. Interpolation was used when the required joint angle lay between those that were previously measured and extrapolation was used when the joint angle lay out with the range of those previously measured. The cost function used to find the muscle activation minimised the overall maximum tendon stress (An et al., 1984). This is equivalent to equation (2.11).

In addition to the segments used in Model A, Model B included the metacarpal and the metacarpo-phalangeal (MCP) joint (Figure 3.3). The DIP joint was defined identically to Model A. The PIP joint howevdr, was modelled with only one DoF about the flexion/extension (z) axis. The MCP joint was modelled as a two DoF universal joint able to rotate about the flexion/extension (z) and abduction/adduction (x) axes. The same six functional units as used in Model A crossed the DIP and PIP joints. The FDP and FDS crossed the MCP joint as well as an additional four functional units. These were: the dorsal interosseous (DIR), which attached to the radial side of the proximal phalanx, and the extensor digitorum communis (EDC), palmer interosseous (PIU) and lumbrical (LUR). The model properties for both Models A and B are summarised in Table 3.1and Table 3.2.

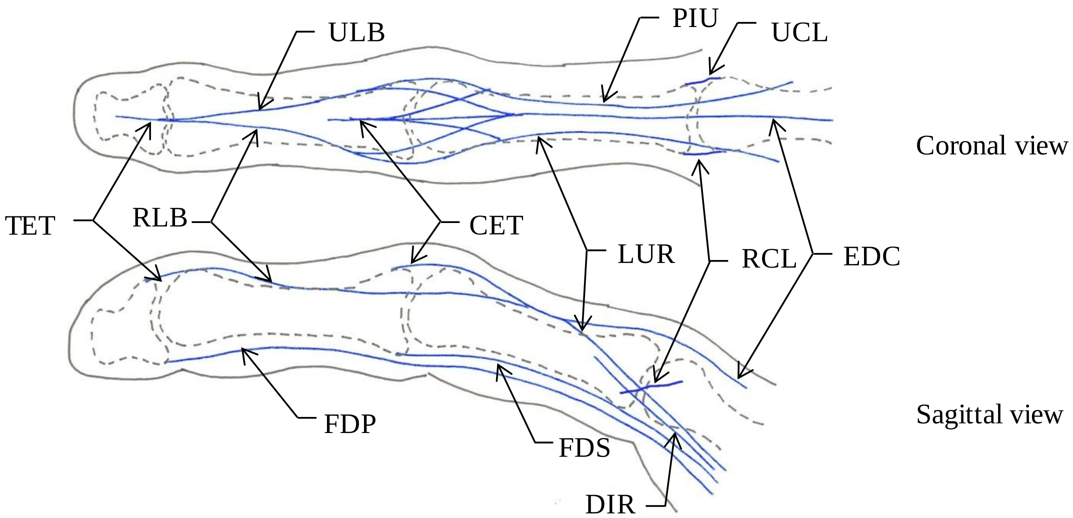

Figure 3.3: *Model B: Functional tendon/muscle units crossing the DIP, PIP and MCP joints.*

Model	Joint	Degee of freedom about axes		
		abduction/aduction (X axis)	**pronation/supination (Y axis)**	**flexion/extension (Z axis)**
A	DIP	0	0	1
	PIP	1	1	1
	MCP	0	0	0
B	DIP	0	0	1
	PIP	0	0	1
	MCP	1	0	1

Table 3.1: *Joints included in each model and the degrees of freedom given to them. A value of one was given if the degree of freedom at the given joint was included and zero if not.*

Functional unit	Abbreviation	Acting across	Included in model
flexor digitorum profundus	FDP	DIP, PIP & MCP	A & B
flexor digitorum superficialis	FDS	PIP & MCP	A & B
central band of the extensor tendon	CET	PIP	A & B
radial lateral band of the extensor tendon	RLB	PIP	A & B
ulnar lateral band of the extensor tendon	ULB	PIP	A & B
terminal extensor tendon	TET	DIP	A & B
dorsal interosseous	DIR	MCP	B
extensor digitorum communis	EDC	MCP	B
palmar interosseus	PIU	MCP	B
lumbrical	LUR	MCP	B

Table 3.2: *Tendon/muscle functional units included in each model and the joints across which they act.*

As was mentioned in Chapter 2, the force balance throughout the extensor mechanism for Model B was governed by equation (3.2), developed from the original equations proposed by Chao et al (1989).

$$T_{RLB} = \propto_{EDC} T_{EDC} + \propto_{LUR} T_{LUR}$$

$$T_{ULB} = \propto_{EDC} T_{EDC} + \propto_{PIU} T_{PIU} \qquad \textbf{(3.2)}$$

$$T_{CET} = (1 - \propto_{PIU}) T_{PIU} + (1 - \propto_{LUR}) T_{LUR} + (1 - 2 \propto_{EDC}) T_{EDC}.$$

Where T_{RLB}, T_{ULB}, T_{EDC}, T_{PIU}, T_{LUR} and T_{CET} were the tensions in each relevant functional unit. The coefficients α_{EDC}, α_{PIU} and α_{LUR} defined the balance of tension in the extensor hood. Each α coefficient could take any value between 0 and 1. These values were optimised simultaneously with the actuator tensions. In addition to the muscle/tendon functional units detailed in Table 3.2 the radial and ulnar collateral ligaments (RCL and UCL) of the MCP were included to provide stability at this joint.

The moment arms and lines of action were taken from the cadaveric study carried out by An et al (1979). These measurements were taken with the hand in a neutral position. To obtain the moment arms and lines of action for the hand in any given pose, appropriate coordinate transformations were carried out. The cost function used in this model minimised the total muscle stress, equivalent to equation (2.10).

3.2 Methods

The aim of this study was to establish the influential model factors both through comparison of models and sensitivity analysis. The experimental procedure described in Section 3.2.1 was used to carry out the comparison described in Section 3.2.2 and the sensitivity analysis described in Section 3.2.3. I programmed both models using MATLAB (The MathWorks), based on the published models described in Section 3.1.

3.2.1 Experimental Procedure

Two sets of experimental data were collected. Both used a six axis force transducer (AMTI Inc, U.S.A) to measure the external reaction force at the finger tip. This was mounted in a rig to measure the force at the tip of a single finger (Figure 3.4). A plate was rigidly attached to the load surface of the transducer with a 15x20mm pad for the finger to press against. The transducer was fixed to a base plate to which a rigid rest was attached. This rest allowed the other fingers of the hand to lie next to the measured finger without applying any load to the transducer. This meant the subject did not have to unnaturally hold their other fingers flexed or extended to keep them away from the transducer. The rest was wide enough that any finger could be measured with the others laying on the rest. Attached to the base plate were three 10mm retro-reflective spheres. These defined a cluster technical frame (CTF) fixed in space relative to the transducer. The transducer position and orientation were calibrated relative to the CTF using four hemispherical markers placed on the pad and rest. These markers were placed at known fixed locations relative to the transducer, therefore providing the calibration. During the experiment these four additional markers were removed leaving only three defining the CTF to locate the position and orientation of the transducer. This meant the whole rig could be moved in the photogrammetric frame without the need for re-calibration. The base plate could be adjusted vertically relative to an elbow rest fixed to the base of the rig (Figure 3.5). This set up allowed basic grip types to be tested. As it was a comparison between models and their sensitivity to inputs being carried out, it was not considered of great importance to simulate a range of day-to-day hand grip situations. It was more important to have a repeatable accurate measure and this set-up was deemed suitable.

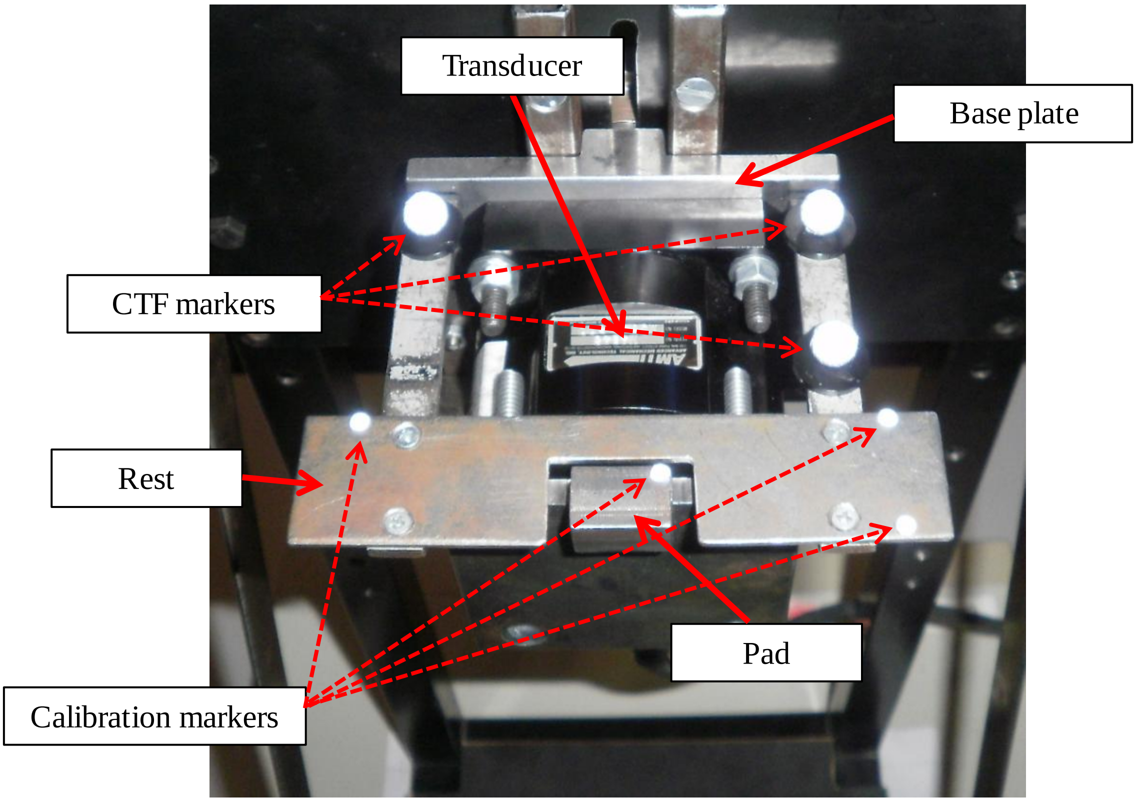

Figure 3.4: *Force transducer rig.*

Figure 3.5: *Force transducer rig showing the elbow rest and the height adjustable transducer.*

For the model comparison a set of data was collected by experiment 1. One subject was tested; a right handed male aged 24 years. The finger kinematics were measured using a stereo-photogrammetric system (Vicon U.K. Ltd) with a sampling frequency of 100Hz. Eight 4mm diameter retro-reflective markers were attached directly to the skin in accordance with a previous study (Su et al., 2005). The method of joint angle definition followed that specified by this author. For this part of the study two hand positions were tested with three repetitions of each: the first with the fingers in an 'open handed' position, as show in Figure 3.6(a), the second, shown in Figure 3.6(b) with the fingers in a 'closed' position such that the PIP joint was highly-flexed and the DIP joint hyper-extended. This second position was tested by Vigouroux et al (2006), and is representative of a high loading case. The subject was required to apply a force vertically downward on the pad with their index finger. The forearm was vertical and the elbow flexed at ninety degrees and supported by an elbow rest. The subject was asked to apply a force that was comfortable for them to maintain for up to five seconds. Three repetitions of each grip type were made and a period of approximately two seconds of constant force from each trial was used for analysis.

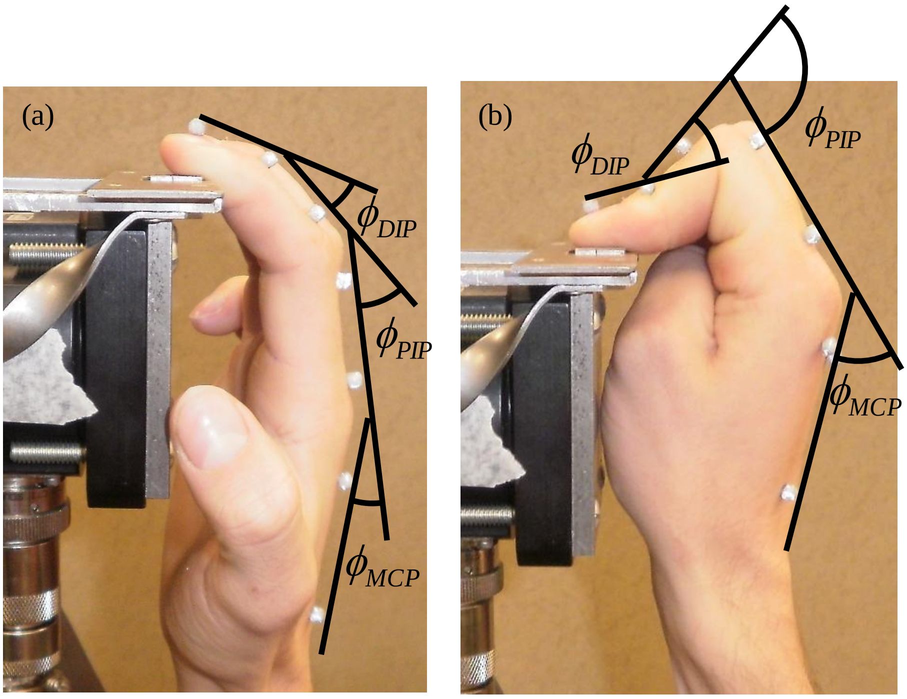

Figure 3.6: *The two hand positions tested in experiment 1. Open hand psotiion shown on the left with typical joint angles of ϕ_{DIP} = 30° to 40°, ϕ_{PIP} = 30° to 40° and ϕ_{MCP} = -10° to 10°. Closed position shown in the right with typical joint angles of ϕ_{DIP} = -15° to -25°, ϕ_{PIP} = 100° to 120° and ϕ_{MCP} = -15° to 15°.*

A second set of data was collected by experiment 2. These data were used to carry out a sensitivity analysis only on Model B, the reasons for this are discussed in Section 3.4. One subject was tested; a right handed male aged 26 years. The finger kinematics were measured using a stereo-photogrammetric system (Vicon U.K. Ltd). For this experiment a set of 12x4mm hemispherical markers were attached to the index finger of the right hand. This was in accordance with the procedure described in Chapter 5 for definition of the ACSs using the phalanx transformation technique (PTT). The accuracy afforded by this technique allowed a valid sensitivity analysis to be carried out. For this experiment only the open hand grip type was tested (Figure 3.6(a)) with the subject required to apply a range of finger tip forces with a total of twenty repetitions.

3.2.2 Model comparison

Identical sets experimental data (kinematics and external reaction forces) were used as input to each model. The metrics for the initial comparison were the tensions in the muscle/tendon functional units common to both models. These were the FDP, FDS, CET, RLB, ULB and TET. Any significant difference between models was determined statistically using a two sample t-test. Significant difference was determined within a 95% confidence interval.

Additional configurations of the models were run to identify the effect of the cost function and anthropometric measurements on the results. As described in Section 2.4 it is common to use a cost function that either minimises overall stress (mean stress) or the single largest stress (min max). For Model A the cost function was adjusted from a 'min max' to 'mean stress' and for Model B cost function was adjusted from 'mean stress' to 'min max'. Any significant effect of the cost function was determined using a two sample t-test.

The anthropometric data used differed between each model, with Model A using data measured from the MRI of a single subject (Fowler et al., 2001) and Model B using a set of data measured from cadaveric specimens (An et al., 1979). To gauge the influence of these different ways of measuring the subject anatomy Model A was run using the cadaveric data and Model B run using the MRI data. Whether this change had a significant effect on the models was determined using a two sample t-test.

3.2.3 Sensitivity analysis

As is detailed in Chapter 2, there are three primary inputs to biomechanics models; body kinematics, anthropometric measures and the external reaction force.

Small changes in the magnitude of external reaction force will have little effect on results as all internal forces are normalised to the vertical component of this external force. The error of concern in this study therefore, is in the location of the centre of pressure (CoP). This relies on accurate measurement of not only the forces, but also the moments applied to the transducer. Although the transducer was calibrated to measure moments to within 1N (<1% load), this accuracy cannot be relied upon. However, in the experiments carried out in my work, the error in location of this CoP relative to the finger can be considered part of the error in the measurement of body kinematics. For this reason sensitivity analysis was carried out only to body kinematics and to anthropometric measurement.

The body kinematics analysis required the artificial displacement of the joint centres. The anthropometric analysis involved the adjustment of the moment arms of each functional unit. The unit-force moment used in the inverse dynamic modelling described in Section 2.3.2 directly correlates to the moment arm.

A new set of experimental data was collected for the sensitivity analyses to utilise the more accurate methods of kinematic analysis developed in Chapter 5. Using the PTT meant full definition of the ACS of each phalanx and metacarpal of the index of the finger of the right hand could be defined as per Figure 3.1.

For the body kinematics sensitivity analysis the assumed location of each joint centre (DIP, PIP and MCP) was displaced to simulate errors in their measurement. These displacements were applied systematically in the palmar/dorsal, proximal/distal and radial/ulnar directions at the three joints. Each displacement was made independently of the others, therefore interaction effects were not calculated. This was not deemed necessary at this stage as only the primary effects were of interest within the scope of this thesis. To provide results that could be generalised and compared with other subjects in the future, the displacements were defined in terms of percentage of middle phalanx length, chosen as a scaling factor because it has been used for this purpose in previous studies (Wu et al., 2010; Fowler et al., 2001). The middle phalanx length was the length of the middle phalanx of the index finger, defined as the distance between the functionally defined DIP and PIP joints.

The maximum displacement for each joint in each direction was 20% of middle phalanx length and the displacement step size was 1% of middle phalanx length. The step size was the amount that each joint centre was displaced between each trial in the sensitivity analysis. These percentages were chosen to achieve approximately a 5mm maximum displacement. This ensured that even the most extreme errors in ACS position were taken into account (as calculated in Chapter 5 and 6).

For the anthropometric data sensitivity analysis, the moment arms of a total of thirteen functional units acting across the three joints were adjusted. There were a total of thirteen (rather than the ten detailed in Table 3.2) as the FDP crosses all three joints (DIP, PIP and MCP) and the FDS crossed two joints (PIP and MCP). As with the body kinematics analysis, the components of the moment arms were adjusted in the palmar/dorsal, proximal/distal and radial/ulnar directions at the three joints. Again all adjustments were made independently, and expressed as a percentage of middle phalanx length. A maximum percentage of 20% was chosen to ensure the likely maximum errors in the functional unit with the largest moment arm were covered. This percentage was applied to every functional unit in every direction. It was decided to be systematic in the application of the adjustments despite this resulting in some unrealistically large changes for some functional units.

In addition to the tensions in each functional unit, the joint reaction force (JRF) was also calculated. This force was calculated be re-arranging equation (2.4) to:

$$\boldsymbol{F} = \sum_{i=1}^{n} T_i\, \boldsymbol{e}_i + \sum_{j=1}^{m} A_j\, \boldsymbol{k}_j, \tag{3.3}$$

where,

T_i = the magnitude of the force applied by tendon/muscle i (N),

$\boldsymbol{e}_i$ = unit vector of the direction of T_i,

A_j = the magnitude of the external reaction force j (N),

$\boldsymbol{k}_j$ = unit vector of the direction of A_j,

$\boldsymbol{F}$ = the JRF vector (N).

Equation (3.3) gives the JRF vector for each individual joint.

3.3 Results

3.3.1 Model comparison

Both models only found valid solutions (all tensions < 1kN) for the 'open handed' grip type. These results averaged across the grip time are shown in Figure 3.7 with the error bars indicating ± standard deviation. The mean total flexor tension (sum of the FDP and FDS) differed between models by 31-44N (29-32%) and the mean total extensor tension (sum of the CET, RLB, ULB and TET) differed by 102-149N (74-79%). These differences were found to be significantly different ($p < 0.05$) for all tendon units across all trials.

No valid solutions were found using either model with the 'closed handed' grip type. This is discussed further in Section 3.4. This meant that direct comparison between models could only be done for the 'open handed' grip type.

The results of altering the cost function in each model are shown in Figure 3.8. For Model A it was found that the cost function had a significant effect on the tension in all the functional units except the FDP and RLB. For model B the cost function was found to have a significant effect on all tensions.

When altering the anthropometric data used in each model is was impossible to run Model A using the data from the cadaveric study (measured by An et al (1979)) and produce valid results. This was because of the increased complexity of Model A (see Section 3.4). For this reason it was only possible to apply the alternative anthropometric data (i.e. that measured using MRI by Fowler et al (2001)) to Model B shown in Figure 3.9. This change was found to have a significant effect on all tensions apart from in the CET.

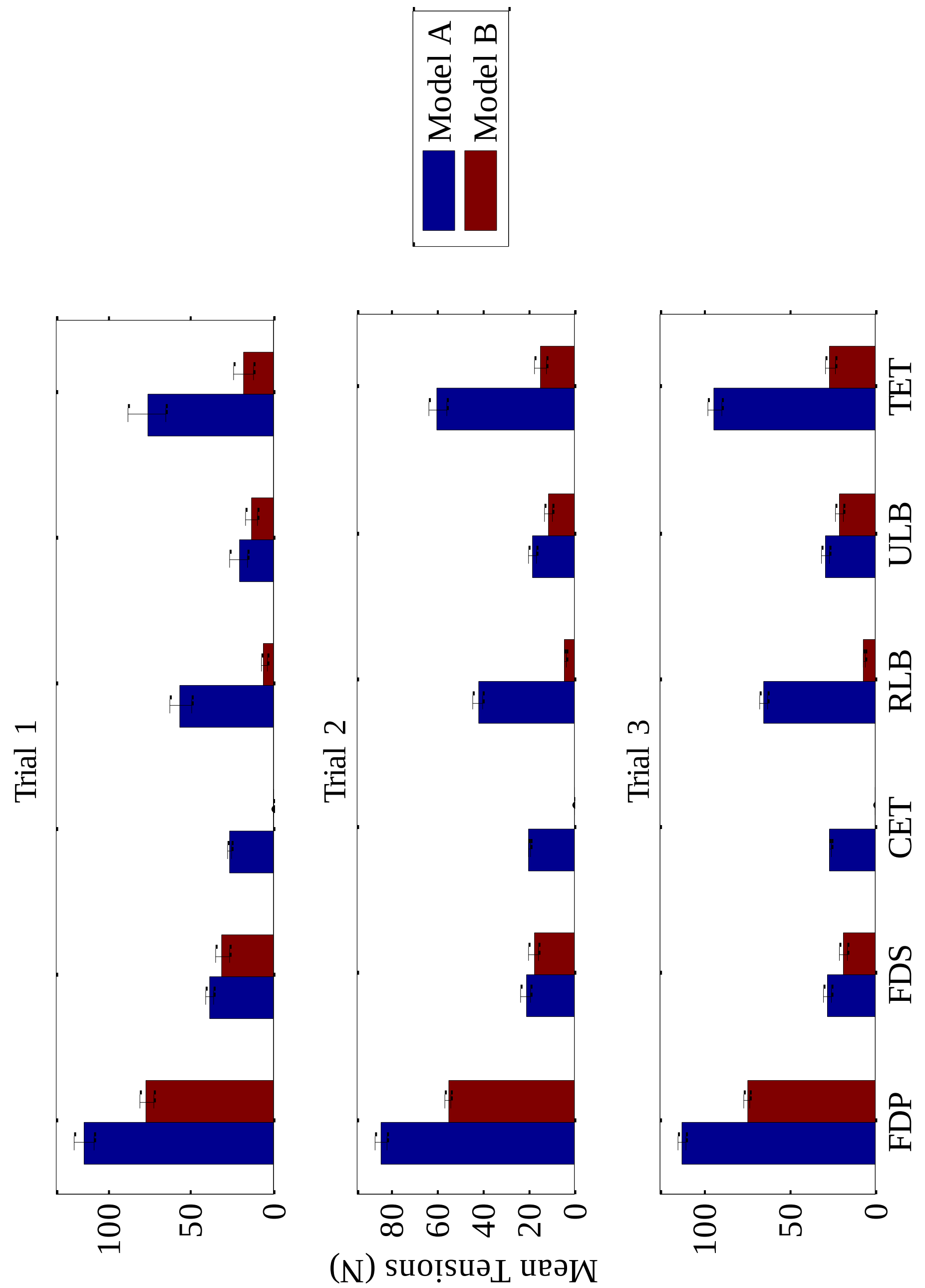

Figure 3.7: *Mean calculated tensions for three trials of the 'open handed' grip type. Error bars represent ±1 Standard Deviation. Functional units: flexor digitorum profundus (FDP), flexor digitorum superficialis (FDS), central band of the extensor tendon (CET), radial lateral band of the extensor tendon (RLB), ulnar lateral band of the extensor tendon (ULB), terminal extensor tendon (TET).*

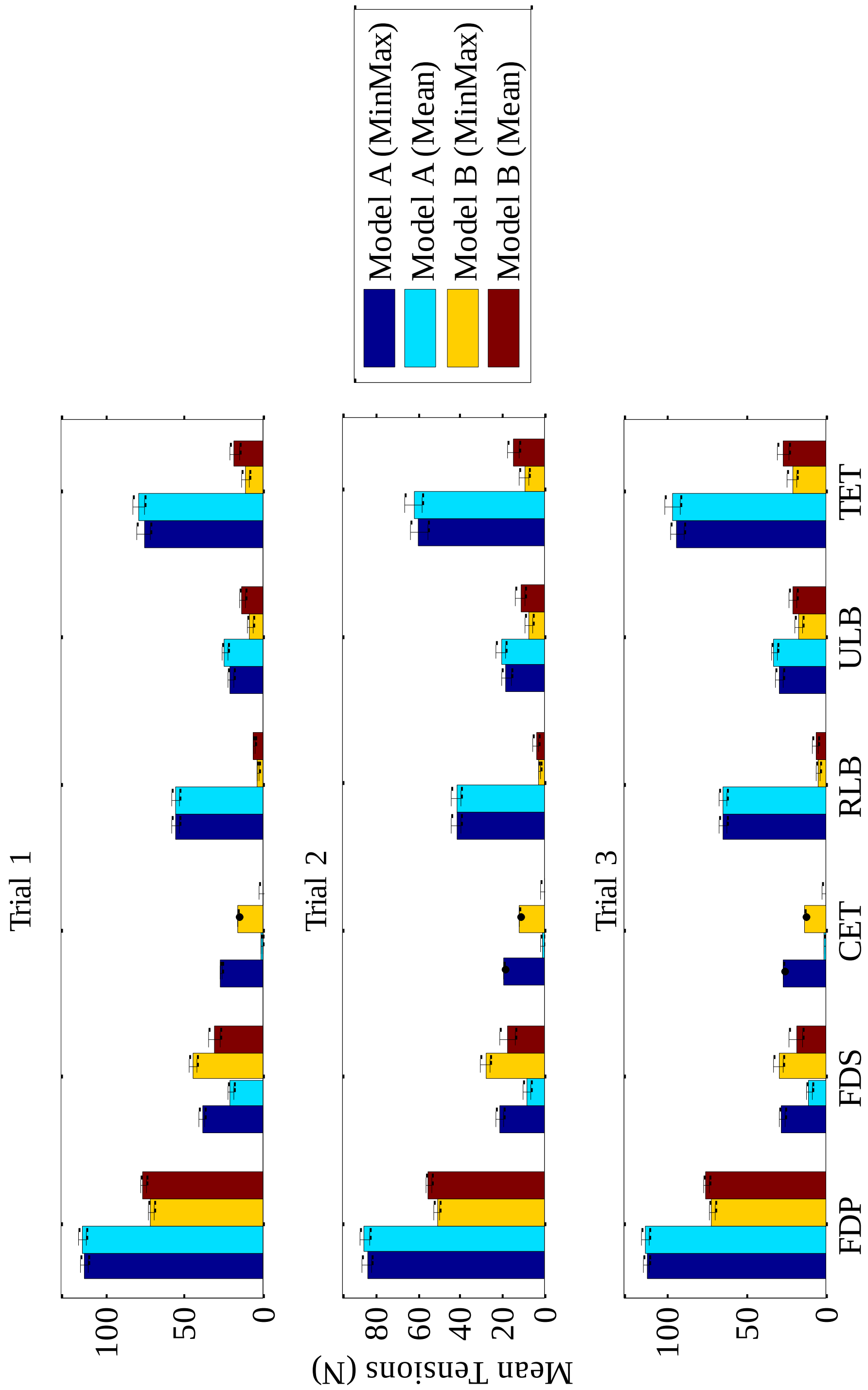

Figure 3.8: *Effect of the cost function on calculated tensions. The two cost functions were minimising the maximum tension (MinMax) and minimising the overall tension (Mean). Functional units: flexor digitorum profundus (FDP), flexor digitorum superficialis (FDS), central band of the extensor tendon (CET), radial lateral band of the extensor tendon (RLB), ulnar lateral band of the extensor tendon (ULB), terminal extensor tendon (TET).*

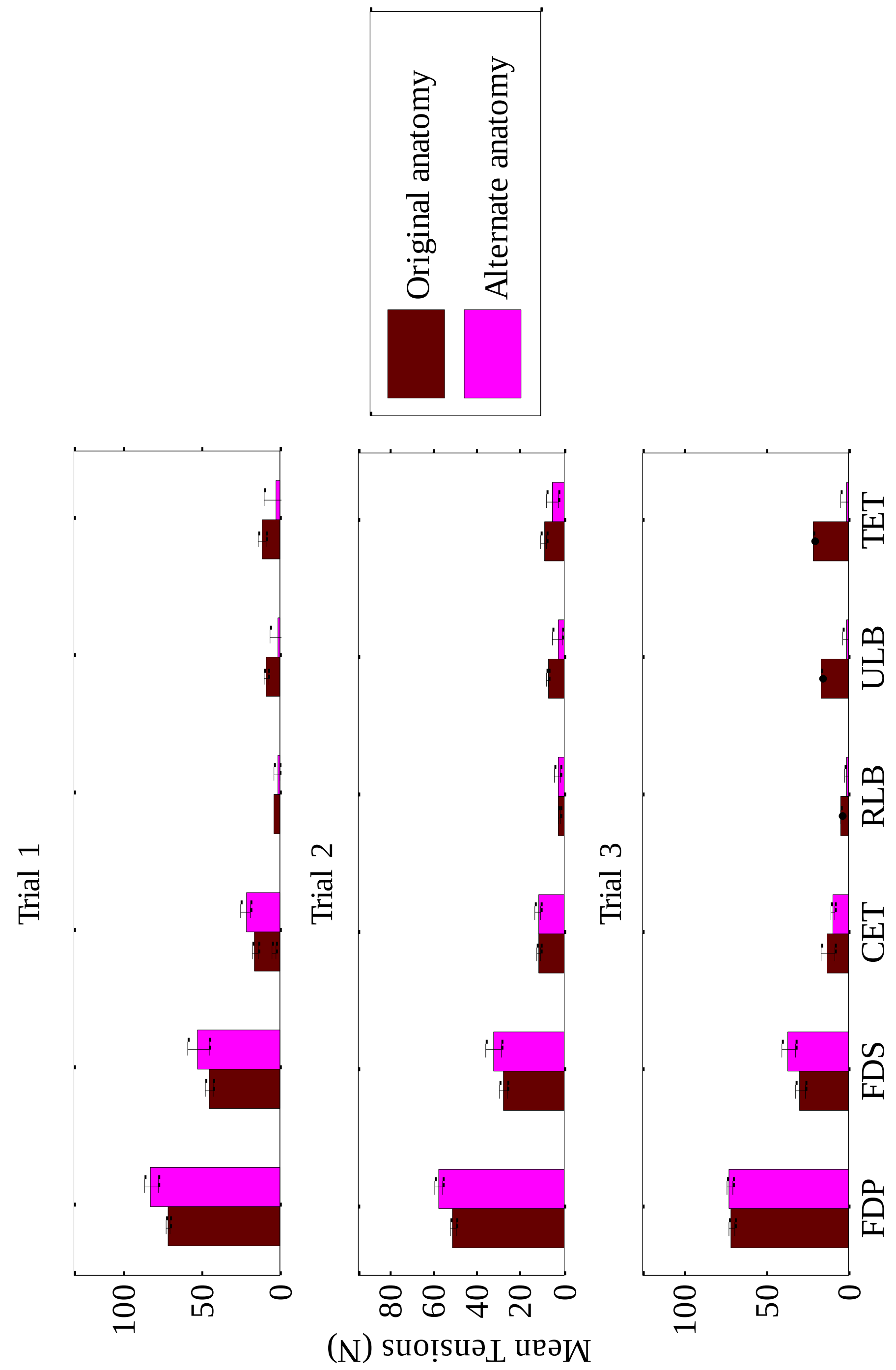

Figure 3.9: *Effect of altering the anatomy on the calculated tensions from Model B. The original anatomy was that measured by An et al (1979) and the alternate was that measured by Fowler et al (2001). Functional units: flexor digitorum profundus (FDP), flexor digitorum superficialis (FDS), central band of the extensor tendon (CET), radial lateral band of the extensor tendon (RLB), ulnar lateral band of the extensor tendon (ULB), terminal extensor tendon (TET).*

3.3.2 Sensitivity analysis

To enable the model output results to be averaged across the twenty trials recorded, the tensions in the functional units and the JRF were normalised to the vertical component of the external reaction force (i.e. the largest force) to give nJRF. The magnitude of these tensions is shown in Figure 3.10 and is referred to as the baseline output. The normalised mean JRF was 4.6 with a standard deviation of 0.5.

The results of the sensitivity to joint centre location are shown in Figure 3.11 and Figure 3.12. The horizontal axis of the plots are split into three divisions representing a specific joint. These are split into three further subdivisions representing displacement in palmar/dorsal (+/- *x*), proximal/distal (+/- *y*) and radial/ulnar (+/- *z*) directions of the ACS. The vertical axes show the change in the mean JRF from the baseline output. To improve clarity the outputs have been divided into flexors and extensors (shown in the top and bottom plots of Figure 3.11). Figure 3.12 shows the change in nJRF for each of the individual joints (DIP, PIP and MCP) from the baseline output. Additionally the mean nJRF is presented in the bottom plot. It can be observed that the profile and magnitude for each joint is very similar, closely following the mean nJRF profile and therefore only this mean force is considered further.

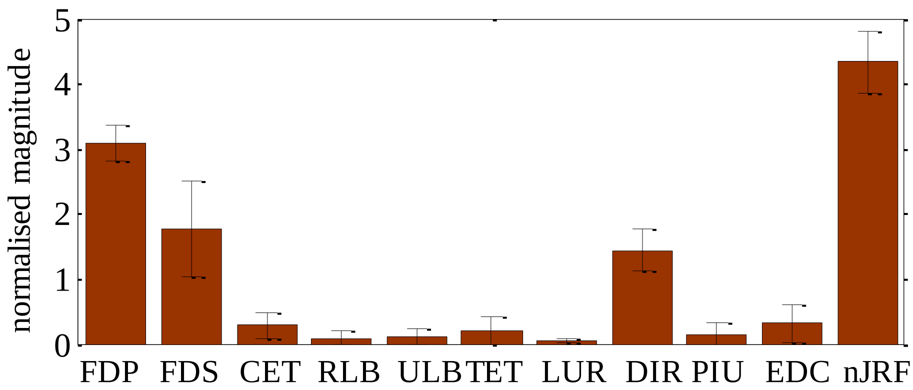

Figure 3.10: *Baseline magnitude of the normalised tension in each tendon functional unit and the mean nJRF. Error bars represent ± 1 standard deviation. Functional units: flexor digitorum profundus (FDP), flexor digitorum superficialis (FDS), central band of the extensor tendon (CET), radial lateral band of the extensor tendon (RLB), ulnar lateral band of the extensor tendon (ULB), terminal extensor tendon (TET), lumbrical (LUR), dorsal interosseous (DIR), palmer interosseous (PIU), extensor digitorum communis (EDC).*

At the DIP joint the outputs were predominantly sensitive to changes in the proximal/distal direction. All the outputs generally follow a linear correlation with this change. FDP and CET had a positive correlation whilst the RLB, ULB, TET and EDC had a negative correlation. The mean nJRF followed a more complex relationship with a negative correlation in the distal ($-y$) direction and a less pronounced positive correlation in the proximal ($+y$) direction.

At the PIP joint the outputs were sensitive to changes in the palmar/dorsal and proximal/distal directions only. The CET had a positive correlation, whilst the FDP, RLB, ULB, TET and EDC had a negative correlation with changes in the palmar ($+x$) direction. The other outputs had little sensitivity to changes in this direction. The FDP, FDS, RLB, ULB, TET and EDC had a positive correlation whilst the PIU and CET had a negative correlation with changes in the proximal ($+y$) direction. The mean nJRF followed a negative correlation to changes the palmar ($+x$) direction and a positive correlation to changes in the proximal ($+y$) direction.

At the MCP joint the outputs were sensitive to the changes in all three directions. The FDP, RLB, ULB, TET and EDC had a positive correlation whilst the FDS had a negative correlation with changes in the palmar ($+x$) direction. The FDS and CET had a positive correlation whilst the FDP, RLB, ULB, TET and EDC had a negative correlation with changes in the proximal ($+y$) direction. The FDS had a positive correlation whilst the FDP, DIR, RLB, ULB, TET and EDC had a negative correlation with changes in the radial ($+z$) direction. The mean nJRF had a positive correlation with changes in the palmar ($+x$) direction and a negative correlation with changes in the proximal ($+y$) and radial ($+z$) directions.

The results of the sensitivity analysis to the anthropometric data are shown in Figure 3.13. The figure is split into three plots, showing the sensitivity to adjustments of the moment arms at the three joints. The horizontal axes of each plot are spit into sections representing each functional unit crossing the joint, these are again split into sections representing the adjustment in the three axial directions (as in Figure 3.11 and Figure 3.12). From this plot it was evident that the model outputs are most sensitive to any changes in the moment arm of the FDP. There was also sensitivity to changes in the moment arm of the FDS, DIR and EDC although these were less pronounced. Adjustments in all other functional units had little effect on the outputs.

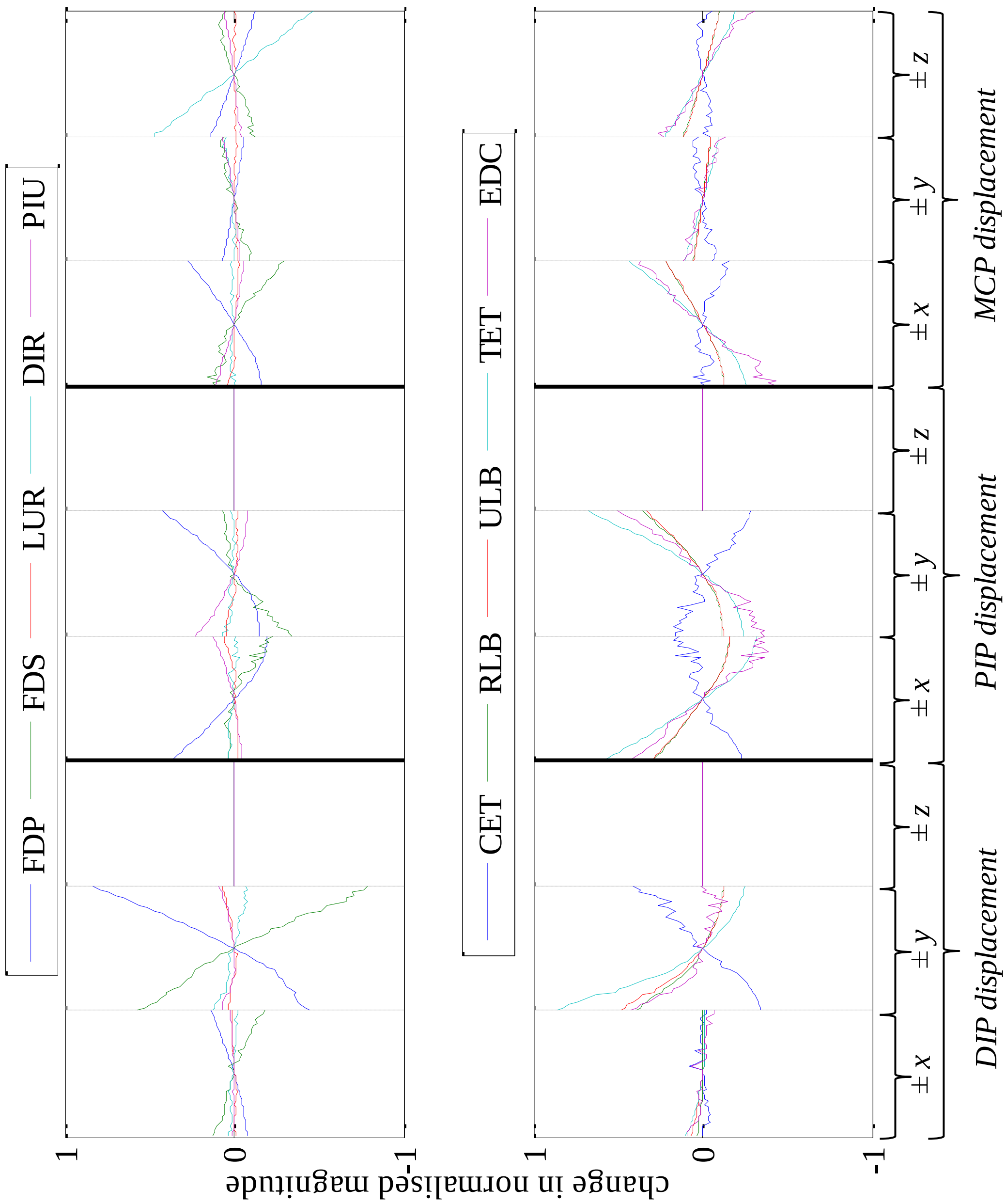

Figure 3.11: *Sensitivity of the normalised magnitude of the tension in the tendon functional units to displacement of the joint centres. Displacement = 20% of the middle phalanx length in palmar/dorsal (+/- x), proximal/distal (+/- y) and radial/ulnar (+/- z) directions. The top graph shows sensitivity of the flexor tendon units and the bottom graph the extensor tendon units.*

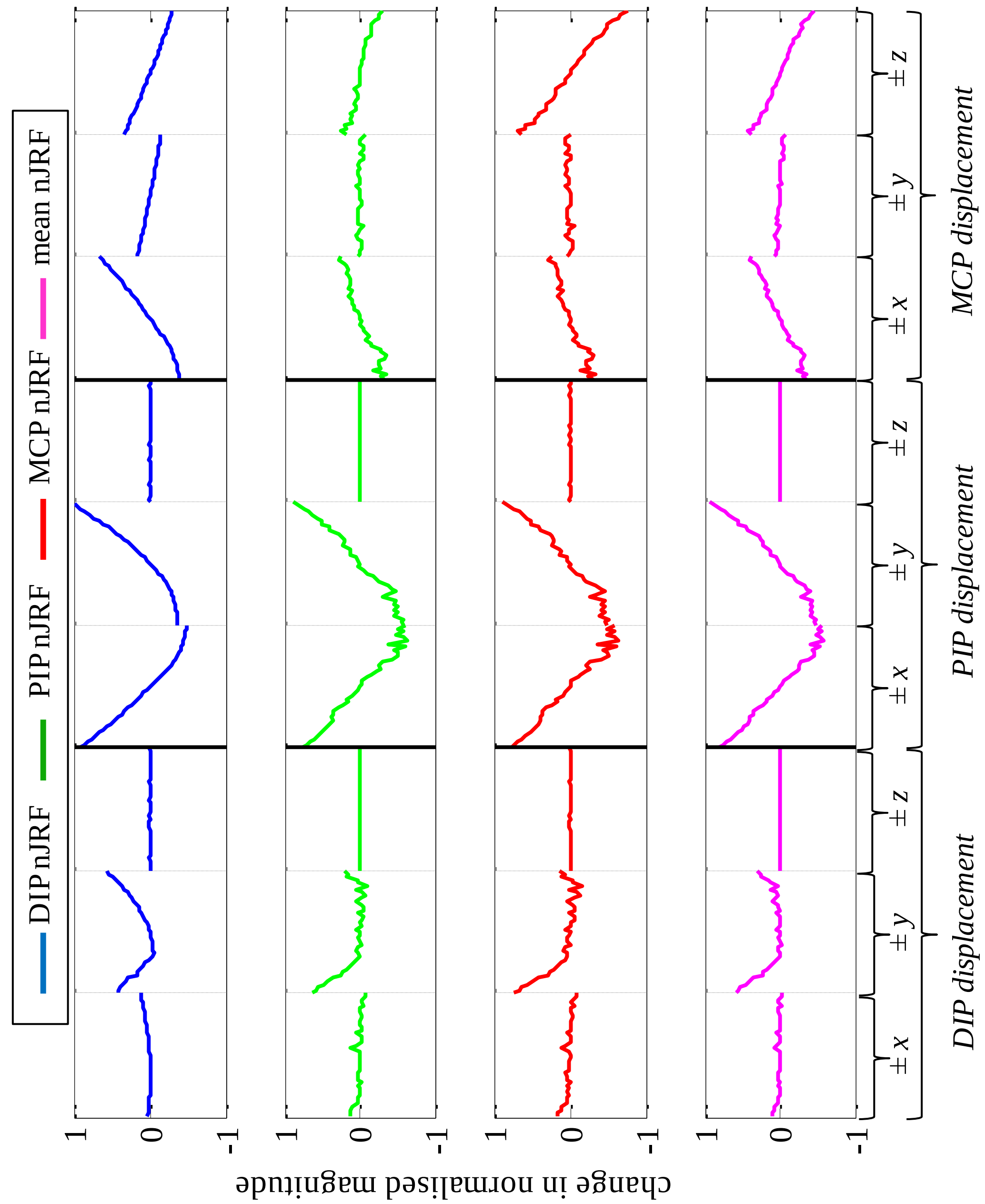

Figure 3.12: *Sensitivity of the nJRF of each individual joint and the mean nJRF to displacement of the joint centres. Displacement = 20% of the middle phalanx length in palmar/dorsal (+/- x), proximal/distal (+/- y) and radial/ulnar (+/- z) directions.*

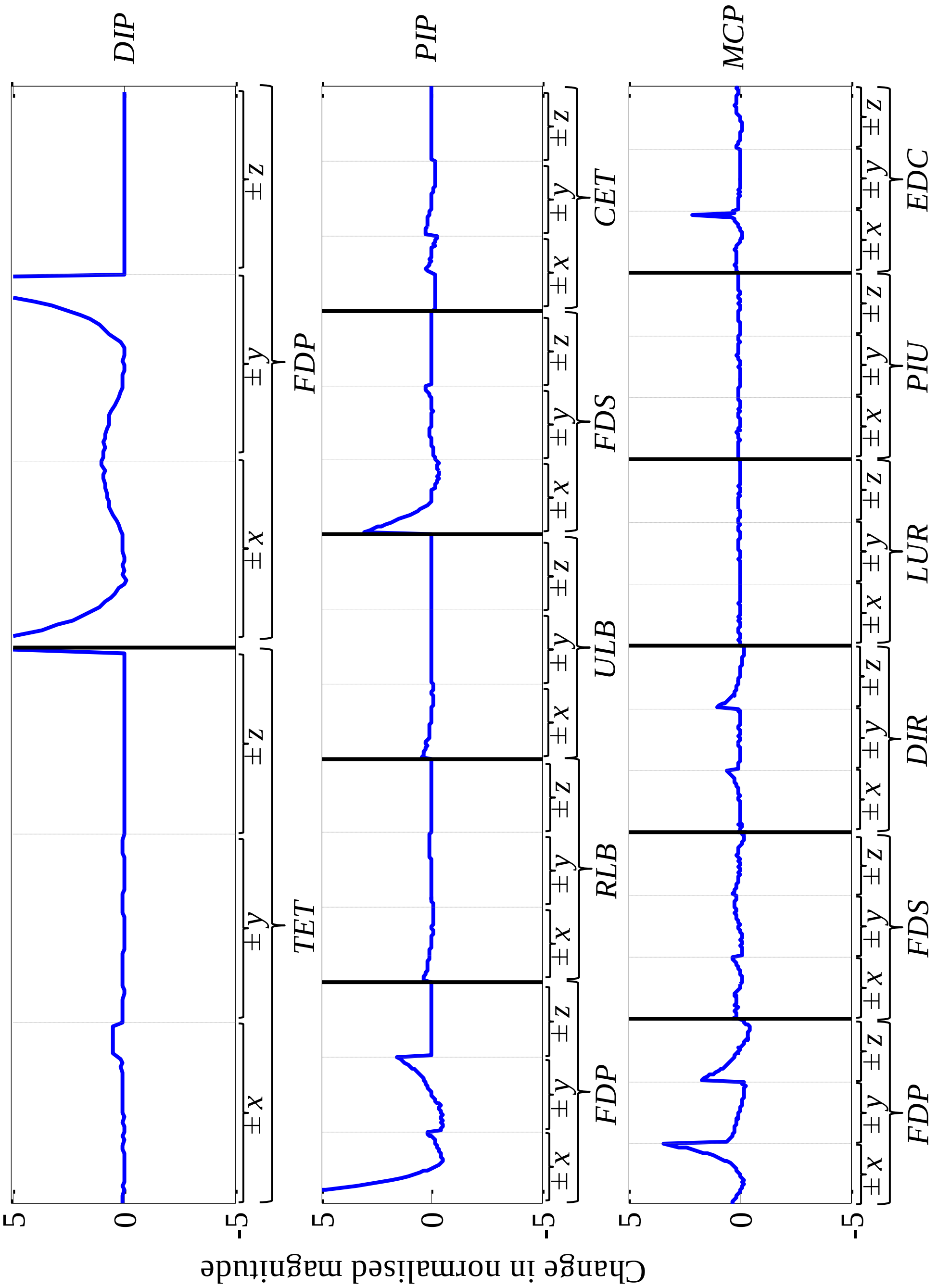

Figure 3.13: *Sensitivity of the mean nJRF to change in the moment arms of each functional unit at each joint. The top graph represents sensitivity to changes at the DIP joint, the middle graph to changes at the PIP joint and the bottom graph to changes at the MCP joint. Displacement = 20% of the middle phalanx length in palmar/dorsal (+/- x), proximal/distal (+/- y) and radial/ulnar (+/- z) directions.*

3.4 Discussion

The first part of this chapter was concerned with examining the difference in outputs calculated using two different phalangeal models. A single set of experimental inputs were used to ensure no inter-subject or experimental error would affect the results. If more subjects were available additional comparison could have been made between the models, however the conclusions reached in this chapter are independent of any subject specific factors.

With both models, no valid solutions were found when the hand was in the ‘closed grip’ position. Both models relied on some form of anatomical measure, either from cadaveric specimens or MRI. The cadaveric data were presented in a neutral position, therefore transformations had to be applied to find the appropriate moment arms and lines of action for the hand position measured by the experiment. The MRI data exist only at discrete hand positions, therefore interpolations and extrapolations needed to be made to fit the hand position measured by the experiment. Using either of these methods can result in inaccurate calculation of the moment arms and lines of action when any of the finger joints are highly flexed or extended. This is shown in Figure 3.14 for the cadaver study carried out by An et al (1979). The unit-force moments about the z (flexion/extension) axis are shown for each functional unit crossing the PIP joint. When the angle of flexion goes beyond 100° the unit-force moment flips from flexion to extension or vice-versa which is not representative of reality. Similar effects were observed for the MRI data measured by Fowler et al (2001) at the DIP joint. For the ‘closed grip’ type the DIP was hyper-extended from -15° to -25° and the PIP highly flexed from 100° to 120°. This meant the moment arms were outside the valid range as demonstrated in Figure 3.14 resulting in unrealistically high tensions being calculated.

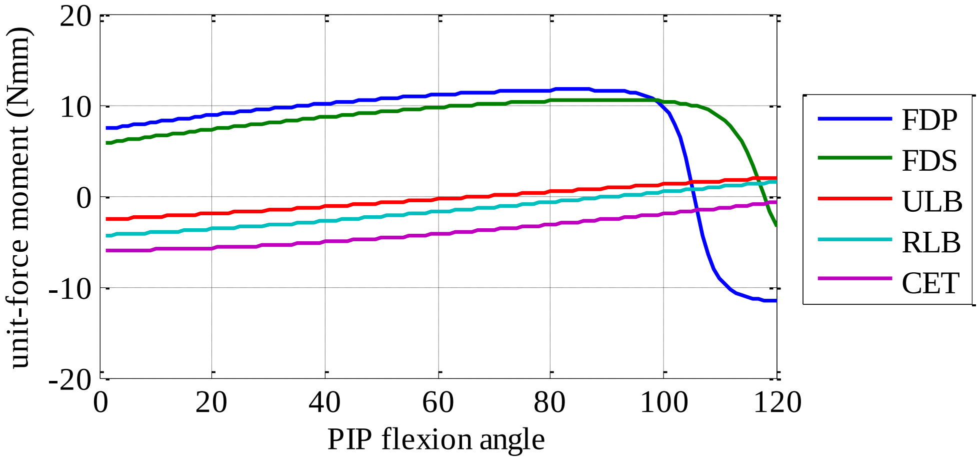

Figure 3.14: *Unit-force moment about the flexion/extension axis of the PIP joint for the five function units crossing calculated from the cadaver dataset of An et al (1979).*

A way of increasing these models' range of validity without additional experimental measurement would be to apply corrections to these invalid moment arms. A method has been proposed (Landsmeer, 1961) using two-dimensional models to represent the muscles and tendons. The extensors were modelled as wrapping around the articular surface of the joint. The flexors were modelled as running through a tendon sheath. For the PIP joint, the moment arms calculated using these models were smaller than those found by An et al (1979) , however they continued to be valid even when the joint had gone beyond 100° of flexion. A way of increasing the range validity of the cadaveric measurement would be to use the cadaveric data as measured to the point that the flexion or extension is out of the range of validity. At this point the models proposed by Landsmeer (1961) can be used with coefficients matched to produce a smooth transition between methods.

As only the results of the 'open grip' type were valid, just this grip was used for model comparison and sensitivity analysis. The cost function used to calculate tendon tensions was found to have a significant effect on most outputs. When the minimal maximum stress constraint was applied, there was a greater contribution from the CET providing joint stabilisation, but there was little effect on the magnitude of the other tensions. The type of activity being carried out will influence the neurological control of the balance between muscle forces, therefore it was difficult to determine which cost function was best. As it was a static test, it would be more likely that the minimum overall maximum tendon stress used by Model A would be more applicable. What is clear from the results was that although cost function is important there are other model factors that had a greater effect on the results.

A comparison was made using alternate sets of anthropometric data as input to each model. Originally model A used the data from the MRI study (Fowler et al., 2001) and Model B used those from the cadaver study (An et al., 1979). No feasible solutions were found when running Model A using the data from the cadaveric study. The authors of Model A produced a more complex model by including more anatomical structures and DoF at the PIP joint. The additional complexities given to this joint in Model A meant any inaccuracy in subject anatomy or external measurement was likely to result in no feasible solution being found. Solutions were found for Model B using alternate anatomy and this change in anatomy was found to have a significant effect. Despite the significant effect of the anatomy there were still greater differences between the models from other factors.

It is my opinion that the difference between models was predominantly due to the way the PIP joint was modelled. The increased DoF and additional ligament structures at the PIP joint used in Model A require a measurement of kinematics and anatomy beyond what was possible in my experiment. It resulted in very large antagonistic muscle forces that in my opinion were un-realistic. Therefore it was decided the results of this model are unlikely to be as viable as those from Model B. It was this Model B that was taken forward and used for the sensitivity analysis.

As discussed in Section 3.2.3 it was decided to carry out sensitivity analysis to changes in the position of the joint centres and to changes in the moment arms of each functional unit. This would give an indication of what inputs were the most important to accurately predict the internal loading of the finger. From Figure 3.9 it has already been observed that changes in the anatomy had a significant effect. The sensitivity analysis aimed to quantify this fully, as well as the effect of displacements in locations of the joint centres.

For the joint position sensitivity analysis it was found that at the DIP joint the outputs were sensitive to changes in the proximal/distal directions and less sensitive to changes in the palmar/dorsal directions of the distal phalanx ACS. Figure 3.15 shows the orientation of the distal phalanx ACS relative to the external reaction force was such that this force acted almost entirely in the dorsal (-*x*) direction. This meant that any change in the location of the joint centre in the palmar/dorsal direction had very little effect on the joint moment and subsequently tendon tension.

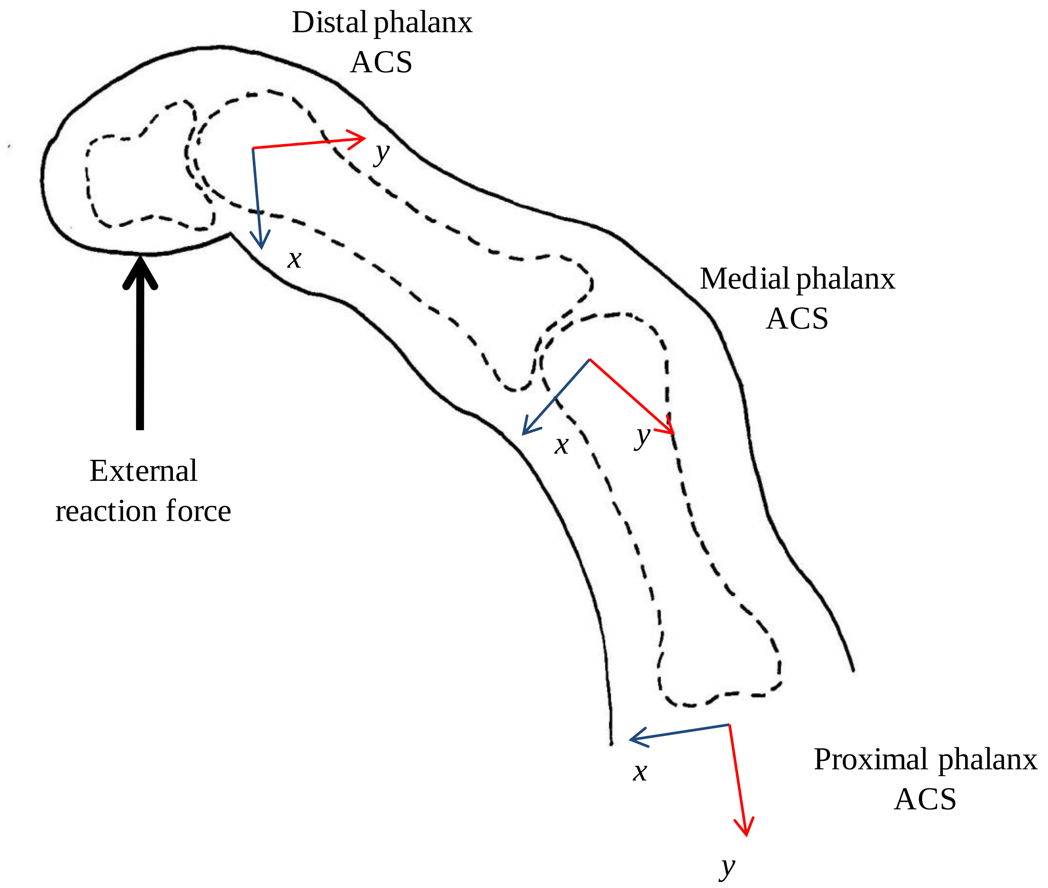

Figure 3.15: *Showing the position and orientation of each phalanx ACS relative to the external reaction force. The x-axis is represented by a blue line and the y-axis is represented by the red.*

The model only included a DoF about the *z-axis* (flexion/extension) for the DIP joint, therefore any change in the radial/ulnar direction would not affect the model outputs despite altering the moment about the *x* (abduction/adduction) and *y-axes* (pronation/supination). This left only displacement in the proximal/distal direction having any large effect. The tension in the FDP had a positive correlation with the displacement. From Figure 3.15 it is evident that decreasing or increasing the distance between the distal phalanx ACS origin and the external reaction force in the *y* direction would directly correlate with an increase and decrease in the moment at this joint. As the only flexor crossing this joint was the FDP, the tension in this changed to ensure the moment equilibrium across the DIP joint was maintained. As the moment across the PIP joint was unaffected by changes in the location of the DIP joint any change in the

FDP tension had to be counterbalanced by a change in the FDS to maintain equilibrium. This change in the flexor tendons had a knock on effect on the extensors to maintain stability across all three joints. The RLB, ULB, TET and EDC followed very similar trends as they are constrained by equations (3.1) and (3.2). The correlation of these tensions with displacement in the proximal/distal direction was not entirely linear. Displacement in a proximal (+*y*) direction had less effect than displacement in the negative direction. This could be caused by an increase in FDP tension and reduction in FDS tension resulting in less stabilising force being required at the MCP joint compared to a decrease in FDP and increase in FDS.

The mean nJRF had a negative correlation with the displacement in the *y* direction, but only for a negative displacement. This correlation occurred because the increase in magnitude of force in the TET was greater than the decrease in the FDP (the only two functional units that cross the DIP joint). For a positive displacement in the *y* direction the correlation became more positive as the change in magnitude of extensors was less marked, as discussed above.

At the PIP joint the orientation of the middle phalanx meant there was a sensitivity to displacement in both the palmar/dorsal and proximal/distal directions of the middle phalanx ACS. Like the DIP joint there was no change with displacement in the direction of the *z-axis* (flexion/extension) due to there only being one DoF at this joint. The orientation of the middle phalanx (Figure 3.15) meant that a displacement of the joint centre in a dorsal (-*x*) direction or in a proximal (+*y*) direction would result in an increased moment at the joint. This was reflected in a corresponding increase in tension in the flexor tendons and change in the extensor tension to maintain joint stability. As the majority of the functional units followed the same pattern of correlation the mean nJRF followed this also.

At the MCP joint there was sensitivity to displacements in the direction of all three axes of the proximal ACS. The orientation of the proximal phalanx (Figure 3.15) meant that as for the PIP joint, a displacement of the joint centre along the *x-axis* (abduction/adduction) in a negative direction resulted in an increase in joint moment. Unlike the PIP joint however this moment is kept in equilibrium by an increase in the FDS and DIR rather than the FDP (which in fact decreased). This decrease in the FDP subsequently resulted in a decrease in the TET and therefore the EDC. In total this amounted to a net decrease in the mean nJRF which is an opposite effect to that observed at the PIP. As the external reaction force was almost aligned with the *y-axis* (proximal/distal) of the proximal phalanx ACS, displacement in this direction had little effect on tensions or external reaction force. In this orientation of the hand, displacement of the MCP joint in the radial (+*z*) direction resulted in the moment about the *x-axis* (abduction/adduction) decreasing i.e. the required abduction moment decreased. This correlated with the change in the DIR which has a far greater abduction moment than a flexion moment across the MCP joint. This functional unit had the most significant sensitivity to changes in the radial/ulnar direction and correspondingly the mean nJRF followed a similar trend to the DIR.

These correlations can be used to generate coefficients between errors in the location of the joint centre and error in the internal loading. It has been shown in this study that these coefficients will be a result of the specific orientation of the joint segments relative to the external reaction force. Therefore if any other grip types were to be tested additional sensitivity analysis would need to be carried out.

The sensitivity of mean nJRF to changes in the anatomy showed that for this grip type the moment arm of the FDP was the most significant. In general, for this functional unit, decreases in the moment arm in the palmar (+*x*) direction and increases in the proximal (+*y*) direction of each ACS will decrease the unit-force moment. This meant a larger tension would be required and therefore the mean nJRF increased. It was observed that the four most highly loaded functional units (FDP, FDS, DIR and EDC) in Figure 3.10 had the most sensitivity to the moment arm displacement (Figure 3.13). Therefore it can be concluded that sensitivity to displacement of the moment arm correlates with the baseline output. Because some functional units had a low magnitude of tension such as the LUR a change in tension of as little as 1N would result in a very large percentage change. For this reason errors were only considered in absolute terms rather than percentage.

3.5 Conclusions

This chapter was split into two parts, the first to compare models and assess their validity and the second to carry out a sensitivity analysis. Two sets of experimental data were collected, one for each part. It was found that the models chosen were not suitable for analysis of grip types where the joints were either highly-flexed or extended. This was due to limitations in the anthropometric data available. This would need to be collected over a wider range of joint angles to produce a valid model. The most significant difference between models was deemed to be the way the PIP joint was modelled with Model A using a much more complex joint. This was likely to result in unrealistically high forces in the extensor mechanism to stabilise this joint. It was therefore decided to only use Model B in further analyses.

The body kinematics sensitivity analysis showed strong correlations between tension in each functional unit and the displacement in the three joint locations. This can be used to assess the viability of any method of kinematic analysis where the error in location of the joint centres can be quantified.

The anthropometric data sensitivity analysis showed that the largest sensitivity resulted from changes in the most highly loaded functional units. This meant that for this grip type accurate measurement of the FDP, FDS, DIR and EDC moment arms was critical.

Chapter 4. Principles of motion capture and its application to the hand and fingers

"Human movement analysis aims at gathering quantitative information about the mechanics of the musculo-skeletal system during the execution of a motor task"

(Cappozzo et al., 2005)

This statement summarises the principless of motion capture experiments. Qualitative assessment of a subject's movement would be what an observer might do in recognising somebody with a limp or struggling to lift a bag. This kind of assessment has and continues to be useful for clinicians, physiotherapists, sports coaches and more. They can use their knowledge and expertise to assess a subject's ability without any need for additional metrics. The aim of modern motion analysis is to provide a way of quantitative assessment. A quantitative analysis gives a means of standardising assessment, eliminating the variation that would exist between human observers. It also can provide more information than can be measured or judged by eye. This can be used in conjunction with the observers' experience and knowledge to provide a more thorough analysis.

The earliest known instance of applying scientific principles to an animal locomotion problem was the set of photographs taken by Eadward Muybridge (1830-1904) of a galloping horse in 1877. Since then the field of motion capture has come a long way with many sophisticated methods of defining human body kinematics using advanced computing power and instrumentation (Andriacchi and Alexander, 2000).

Body kinematics are the spatial position and orientation of body segments in terms of displacement, velocity and acceleration. As described in Chapter 2 we can use the known body kinematics in combination with known external reaction forces and body anthropometric data to predict internal loading using biomechanical models.

4.1 Notation Glossary

The following defines the notation used for describing rotation and translations between coordinate systems in this thesis.

A letter contained within curly brackets represents a coordinate system such as $\{A\}$ and $\{B\}$.

A single capital letter in bold font represents a square matrix, either a 3x3 or a 4x4. A 3x3 matrix will either define a set of rotations between two coordinate systems or define a set of orthogonal axes. In a set of axes, an x, y or z subscript represents a vector defining a single axis of the set. A 4x4 matrix represents a full transformation (rotation and translation) between two coordinate systems. Preceding superscripts and subscripts are used to define which coordinate systems a transformation matrix refers to. For example, the orientation matrix ${}^{B}_{A}\boldsymbol{R}$ defines the rotation from coordinate system $\{A\}$ to system $\{B\}$.

A bold font lower case letter represents a three dimensional (3D) positional coordinate or a 3D vector. As with the matrices, a preceding superscript defines what coordinate system this quantity is defined in. For example, ${}^{A}\boldsymbol{c}$ defines the position $\boldsymbol{c}$ in the coordinate system $\{A\}$.

A lower case letter not in bold font with an x, y or z subscript represents the individual components of a vector or 3D position coordinate. For example c_x, c_y, and c_z represent the x, y, and z components of the position $\boldsymbol{c}$.

A trailing superscript gives additional information about an axis undergoing basic rotations. Trailing superscripts of ' or " represent the axes of a coordinate system after the first and second rotations respectively.

To keep equations simple and un-cluttered some subscripts and superscripts may be (although not always) excluded if they are the same for each matrix, vector or position in that equation.

4.2 Defining position and orientation of body segments

In some cases an observer may only be interested in a single angle between body segments. Assuming planar motion this can be achieved using two dimensional (2D) motion capture to determine the long axis of each segment of interest. In current human motion analysis however, knowledge of the 3D kinematics of the body segments is considered standard.

3D kinematic analysis relies on a set of reference frames being defined and the rotations and translations between them known. These rotations and translations can either be defined relative to a fixed global reference frame or local technical frames (Cappozzo et al., 2005). This allows the motion of one segment to be considered with reference to those adjacent to it, or it may be considered with reference to a fixed reference frame. A global fixed reference frame would be used if the subject was walking across a force plate or otherwise interacting with an object fixed in the lab environment. It is also possible to have a local fixed reference frame, for example in upper arm motion it is normal to define motion relative to the thorax technical frame which is fixed if the subject is assumed to be stationary (Masjedi, 2009).

4.2.1 Definition of anatomical coordinate systems

Given the assumption that body segments are 'rigid' i.e. that the underlying bone is a rigid structure, it can be assumed that all distances and relative positions of points on a single segment will remain invariant (Woltring, 1991). With this assumption a set of Cartesian axes fixed to the underlying bone can be defined. This creates an anatomical coordinate system (ACS) for each body segment. With each segment given its own ACS the relative position and rotation of each segment is known with regard either to other body segments (used in inertial analysis) or to a global reference frame (used in photogrammetric analysis).

One of the major advantages of defining ACSs is that inter and intra subject repeatability is improved (Cappozzo et al., 2005). If the ACSs between two different studies are the same or at least well defined then work carried out between different institutions and research groups can be easily compared and assessed. To this end it has been attempted to recommend a standard definition of body segment ACSs as international standards (Wu et al., 2005; Wu et al., 2002). The ACSs recommended in these standards are defined relative to anatomical landmarks.

Research carried out prior to the publication of these recommendations may not adhere to the standards. This may be simply because there were no recommendations in place, or the definition chosen suited the research being carried out at the time. This is of particular relevance to the hand and fingers as the ACS used by An et al (1979) differs from the recommendations, both in orientation of the axes and location of the segment origin. As this work is key in the field, later research has often taken the definition of these ACSs as standard, whilst others have opted to take a convention more in-line with those recommended by Wu et al (2005). Although this does make comparison between studies more problematic, as long as their conventions are defined clearly by the author, transformations can be made to a common convention. The conventions used in this thesis are defined in Section 3.1. They have been chosen with thought both to the current recommendation but also to the requirements of my research.

4.2.2 Vector transformation

A coordinate or vector in any Cartesian coordinate system can be referred to in another system by the application of a set of rotations and translations. This process is known as coordinate or vector transformation. A position ${}^{A}\boldsymbol{p}$ defined in coordinate system $\{A\}$ can be expressed in the coordinate system $\{B\}$ by applying the transformation:

$$ {}^{B}\boldsymbol{p} = {}^{B}_{A}\boldsymbol{R}\,{}^{A}\boldsymbol{p} + {}^{B}\boldsymbol{o}. \tag{4.1} $$

This is shown in Figure 4.1.

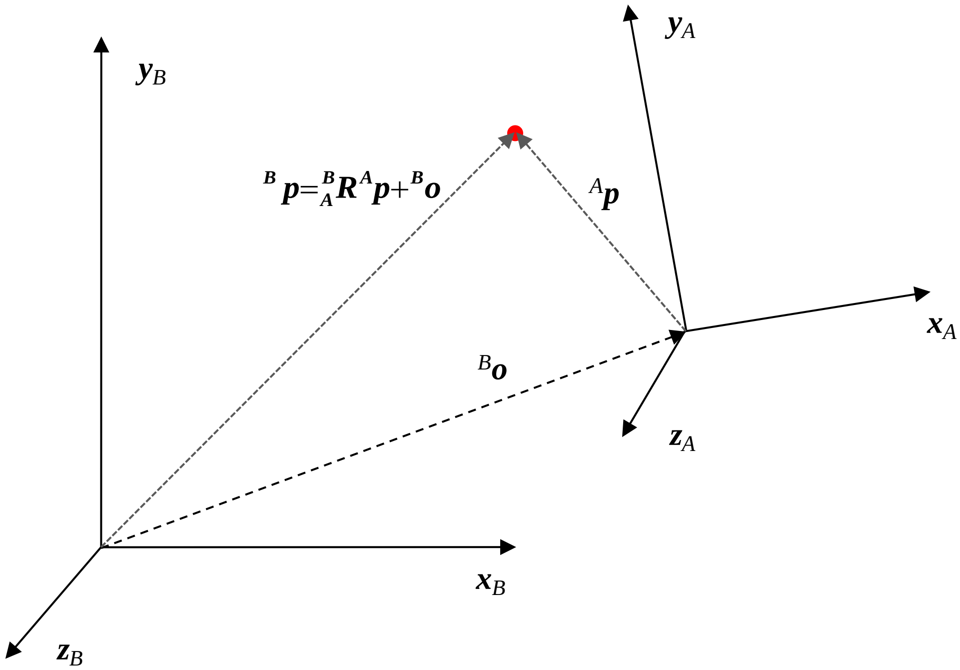

Figure 4.1: *Position* $\boldsymbol{p}$ *expressed in two coordinate systems* $\{A\}$ *and* $\{B\}$*, and the transformation between them.*

The rotation between coordinate frames is given by the orientation matrix:

$$ {}^{B}_{A}\boldsymbol{R} = \begin{bmatrix} cos\theta_{x_B x_A} & cos\theta_{x_B y_A} & cos\theta_{x_B z_A} \\ cos\theta_{y_B x_A} & cos\theta_{y_B y_A} & cos\theta_{y_B z_A} \\ cos\theta_{z_B x_A} & cos\theta_{z_B y_A} & cos\theta_{z_B z_A} \end{bmatrix}, \qquad \textbf{(4.2)} $$

and the translation vector:

$$ {}^{B}\boldsymbol{o} = \begin{bmatrix} {}^{B}o_x \\ {}^{B}o_y \\ {}^{B}o_z \end{bmatrix}. \qquad \textbf{(4.3)} $$

Each element of this rotation matrix is the cosine of the angle between the two axes specified in the subscript of θ. From this it can be deduced that if each axis of both coordinate systems align then this matrix will become the identity matrix. In a practical sense for its calculation, the columns of this matrix consist of the normalised direction vectors of the axes of coordinate system $\{A\}$ expressed in coordinate system $\{B\}$.

Multiplication of ${}^{A}\boldsymbol{p}$ by this matrix rotates its reference frame to the coordinate system $\{B\}$, however it is still expressed relative to the origin of system $\{B\}$. To transform it fully the translation ${}^{B}\boldsymbol{o}$ must be applied. This translation is the origin of coordinate system $\{A\}$ expressed in system $\{B\}$.

In practice it is more common to express equation (4.1) in terms of a single transformation instead of separate calculations for rotations and translations. In this case the equation becomes:

$$ {}^{B}\boldsymbol{p} = {}^{B}_{A}\boldsymbol{T}\,{}^{A}\boldsymbol{p}. \tag{4.4}$$

The construction of these matrices is shown in:

$$\begin{bmatrix} {}^{B}p_x \\ {}^{B}p_y \\ {}^{B}p_z \\ 1 \end{bmatrix} = \begin{bmatrix} & {}^{B}_{A}\boldsymbol{R} & & {}^{B}\boldsymbol{o} \\ 0 & 0 & 0 & 1 \end{bmatrix} \begin{bmatrix} {}^{A}p_x \\ {}^{A}p_y \\ {}^{A}p_z \\ 1 \end{bmatrix}. \tag{4.5}$$

The position vectors each have an additional element of value 1. This is included for this calculation only and is ignored when using the positions in any other calculation.

4.2.3 Euler and Cardan angles

Through the procedure described above the rotations and translations between any two body segments can be fully defined. For 3D kinematic analysis of the human body where each segment is constrained by those adjacent to it, these movements are best described by a series of basic rotations. This allows rotations to be described in a language consistent with human anatomy. These three basic rotations occur about the *x*, *y* and *z-axes* of magnitude α, β and γ respectively shown in Figure 4.2. The three basic rotation matrices are:

$$\boldsymbol{R}_x = \begin{bmatrix} 1 & 0 & 0 \\ 0 & \cos\alpha & -\sin\alpha \\ 0 & \sin\alpha & \cos\alpha \end{bmatrix},$$

$$\boldsymbol{R}_y = \begin{bmatrix} \cos\beta & 0 & \sin\beta \\ 0 & 1 & 0 \\ -\sin\beta & 0 & \cos\beta \end{bmatrix}, \tag{4.6}$$

$$\boldsymbol{R}_z = \begin{bmatrix} \cos\gamma & -\sin\gamma & 0 \\ \sin\gamma & \cos\gamma & 0 \\ 0 & 0 & 1 \end{bmatrix}.$$

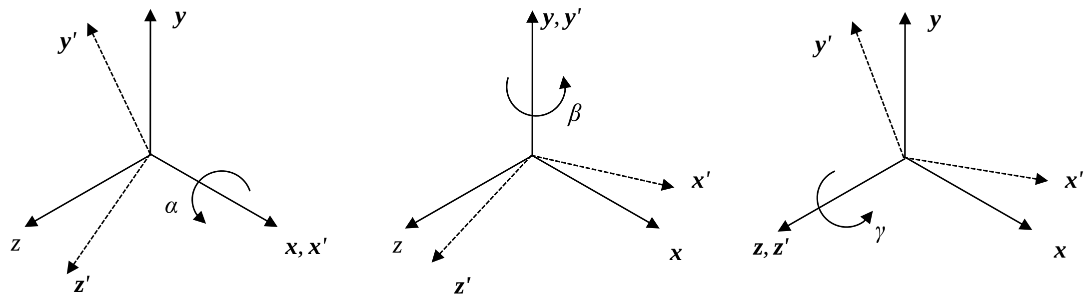

Figure 4.2: *Basic rotations about the x-axis, y-axis and z-axis.*

These rotations are applied sequentially and assume that the two bodies are initially aligned (i.e. the orientation matrix is equal to the identity matrix ***I***) and all rotations occur about axes fixed to the articulating (normally distal) segment. Because these axes are fixed to the articulating segment the second and third rotations will occur about intermediate local reference frames denoted by the notation (′) and (″) respectively. An example of a sequence of rotations (***xy′z″***) between systems $\{B\}$ and $\{A\}$ is shown in Figure 4.3. Because matrix multiplication is non-commutative the result is entirely dependent on the sequence of rotations. The final orientation matrix is defined by post multiplying the initial identity matrix by each basic rotation matrix in turn. For the rotation sequence ***xy′z″*** the orientation matrix will be:

$$
{}_{B}^{A}\boldsymbol{R} = \left\{\left[(\boldsymbol{R}_{\alpha}\boldsymbol{I})\boldsymbol{R}_{\beta}\right]\boldsymbol{R}_{\gamma}\right\} = \begin{bmatrix} r_{11} & r_{12} & r_{13} \\ r_{21} & r_{22} & r_{23} \\ r_{31} & r_{32} & r_{33} \end{bmatrix} = \tag{4.7}
$$

$$
\begin{bmatrix} \cos\beta\cos\gamma & -\cos\beta\sin\gamma & \sin\beta \\ \sin\alpha\sin\beta\cos\gamma + \cos\alpha\sin\gamma & -\sin\alpha\sin\beta\sin\gamma + \cos\alpha\cos\gamma & -\sin\alpha\cos\beta \\ -\cos\alpha\sin\beta\cos\gamma + \sin\alpha\sin\gamma & \cos\alpha\sin\beta + \sin\alpha\cos\gamma & \cos\alpha\cos\beta \end{bmatrix}
$$

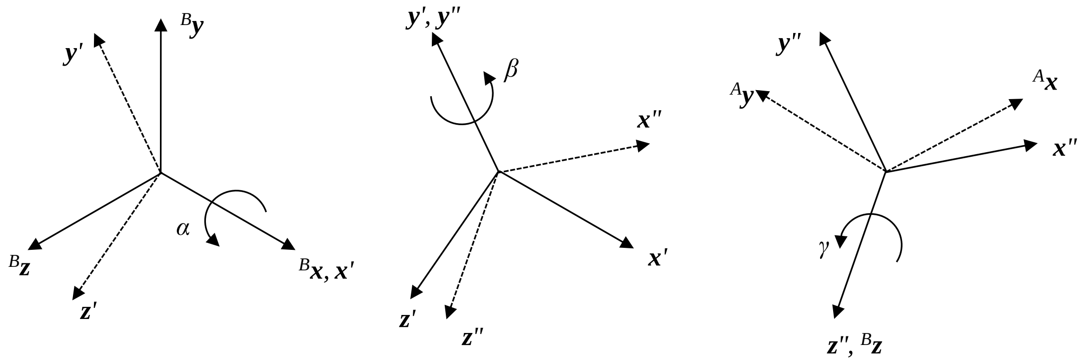

Figure 4.3: *Sequence of rotations. Firstly about* $^B\mathbf{x}$*, secondly about* $\mathbf{y}'$ *and thirdly about* $\mathbf{z}''$*.*

This process works in both directions such that an orientation matrix can be decomposed to give the individual rotations. Using the rotation sequence shown in equation (4.7) the decomposition would yield:

$$\alpha = \sin^{-1}\left(\frac{-r_{23}}{\cos\beta}\right)$$

$$\beta = \sin^{-1}(r_{13}) \qquad \textbf{(4.8)}$$

$$\gamma = \sin^{-1}\left(\frac{-r_{12}}{\cos\beta}\right)$$

Because matrix multiplication is non commutative, without knowing the order of the rotations it is impossible to decompose the orientation matrix to its basic angles. Additionally it has been shown that the sequence of rotation will have a significant effect on the resultant angles (Cappozzo et al., 2005). It is therefore important to consider the sequence and convention with regard to the joint being examined.

The convention is that rotation sequences can be defined with the terminal rotation about the same axis as the first rotation (Euler sequence) or with each rotation about individual axes (Cardan sequence). There are six possible Euler sequences (***xy'x''***, ***xz'x''***, ***yx'y''***, ***yz'y''***, ***zx'z''*** and ***zy'z''***) and six possible Cardan sequences (***xy'z''***, ***xz'y''***, ***yz'x''***, ***yx'z''***, ***zx'y''*** and ***zy'x''***). The rotation sequence is chosen to best suit the application to which it is to be applied, both to accurately represent how a body might be rotating and to avoid gimbal lock.

Gimbal lock occurs when the second rotation is of a magnitude close to 90°. As is demonstrated in Figure 4.4, when the rotation about $\boldsymbol{y}'$ (β) approaches this value, the axis $\boldsymbol{z}''$ aligns with the original ${}^{B}\boldsymbol{x}$. This means rotations about $\boldsymbol{z}''$ are not unique and can result in unrealistically large magnitudes of α and γ. This is also demonstrated in equation (4.7) as the value of $\cos\beta$ will approach zero, producing a singularity condition.

To ensure avoidance of gimbal lock and for the best description of specific joint kinematics, the most suitable rotation sequence is chosen for the description of specific joints.

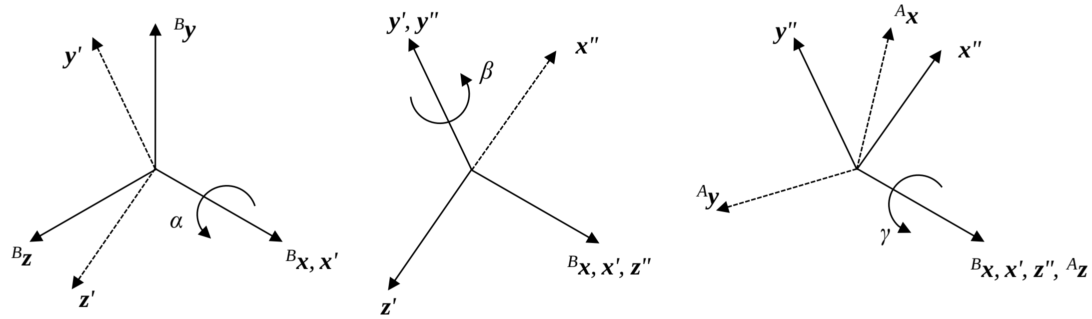

Figure 4.4: *Gimbal lock occurs when the second rotation is of a magnitude close to 90°. In this case the third axis of rotation (*$\boldsymbol{z}''$*) aligns with the first (*${}^{B}\boldsymbol{x}$*). This can result in large rotations α and γ which are not representative of reality.*

4.3 Available methods of kinematic analysis

Methods of kinematic analysis can be generally classed as photographic/video based or inertial based. This section gives a brief overview of these two methods and the reasons for the selection of stereo-photogrammetry for the experimental work done in this thesis.

4.3.1 Photographic and video methods

Photographic/video based methods use cameras to locate the spatial position and orientation of markers or body segments within a known reference frame. These can be divided into marker based and markerless systems. A marker based system detects highly reflective or light emitting markers attached to a subject. The position and orientation of the body segments can be inferred from the location of these markers. A markerless system tracks the body segments directly from photographic or video images. This allows data to be collected using non-specialised equipment (Addis and Lawson, 2010). Although it does have its advantages in cost and flexibility, markerless tracking systems are not currently accurate enough for most biomechanical modelling applications. Both marker based and markerless systems can provide pseudo-static (photographic) or dynamic (video) data. For biomechanical applications video based systems are considered the standard. The science of using two or more cameras to determine the 3D position of a body is known as stereo-photogrammetry and is the most common form of kinematic analysis for biomechanical applications (Mundermann et al., 2006). Various commercial hardware and software products are available (Vicon, U.K.; Qualisys, Sweden and Motion Analysis, USA) for these applications.

4.3.2 Inertial methods

Inertial based systems use devices containing a number of sensors including accelerometers, gyroscopes and magnetometers mounted together to measure the orientations and accelerations of individual body segments. These systems are all dynamic systems and often do not require the subject to be in a laboratory environment. However to calculate the velocity and displacement of body segments integrations must be performed on the acceleration data. There are commercial enterprises providing these kinds of sensors (Xsens, Netherlands; METAmotion, USA and Animazoo, U.K.).

4.3.3 Method selection

The experimentation required in my work could all be carried out in a laboratory environment with accuracy being paramount. Additionally the ACS could be defined with the attachment of small (4mm diameter) lightweight markers compared to more bulky inertial sensing units. These factors combined meant that stereo-photogrammetry was deemed the most suitable for the biomechanical analysis done in this thesis.

4.4 Stereo-photogrammetric motion capture

By definition stereo-photogrammetry is the determination of the position of an object in 3D space by its location in two or more photographic images. In practice in a biomechanical context it is common to use an array of infra-red cameras to track retro-reflective markers fixed to an object or subject. This is the most widely available and accurate way of measuring the position and orientation of body segments. Therefore within this thesis the term stereo-photogrammetry will refer to the use of this type of camera and marker. As well as in a biomechanics context these techniques are also used in the films, gaming and arts sectors as a way of tracking human movement.

4.4.1 Reference frames

In a basic sense the location of markers attached to a body can directly give a measurement of the position of the body. For example, if a joint angle were required, markers could be placed on a joint centre and on those two adjacent to it. The joint angle could then be calculated as the angle between these three markers. This method however has several draw-backs. The markers must be accurately located on the joint centre consistently. There is also likely to be significant skin movement artefact (the movement of soft tissue relative to the skeleton) around the joint centres (Cappozzo et al., 1996). Finally, with this method it is only possible to calculate a joint angle about a single degree of freedom as nothing is known about the orientation of the body segments. This makes performing further analyses such as inverse dynamics likely to incur large errors. It is therefore normal to try and fully define the ACS of each segment to ensure the most accurate measurement of the subject kinematics. This is done by defining every object, body segment and force with its own unique reference frame. Each of these reference frames can be expressed relative to each other using the transformation techniques described in Section 4.2.2.

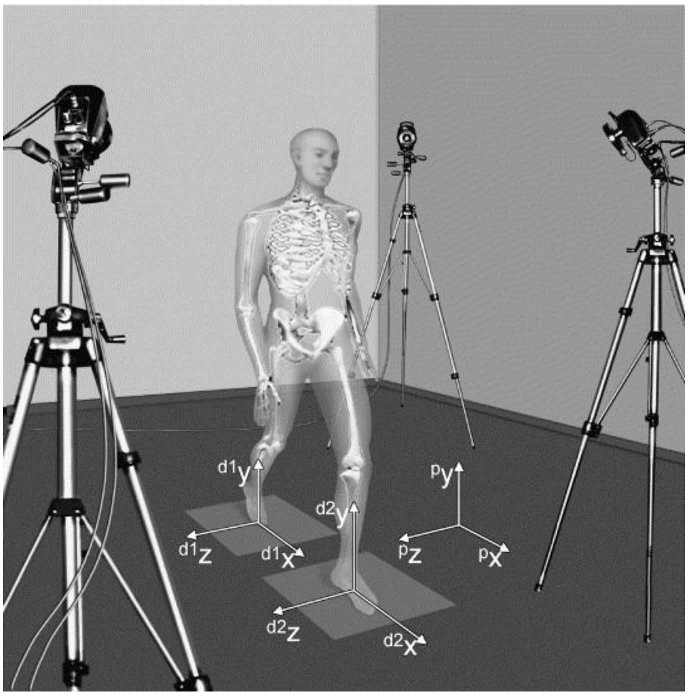

Figure 4.5: *A motion analysis laboratory with fixed global frames. Examples of these are the photogrammetric frame fixed using a calibration object and dynamometer frames fixed to force plates. Adapted from Cappozzo et al (2005).*

There are a number of common global reference frames. In stereo-photogrammetry the photogrammetric global frame is defined relative to a calibration object. Dynamometer frames can be defined and are fixed to a force measurement device such as a force plate or transducer. A motor task frame is relevant to how the subject moves or interacts with their surrounding environment. The axes of a motor task frame will most often align with direction of travel and/or gravity. All global frames are normally fixed relative to each other (Figure 4.5). Local technical frames can be fixed to subjects or objects and can move relative both to the global reference frames and also to each other. In stereo-photogrammetry these local frames are fixed to a group of markers known as a cluster technical frame (CTF) shown in Figure 4.6. A CTF usually has to have at least three markers to define it. They can consist of less than three if some other information about the object/segment orientation is known or assumed. Often more than three markers are used either to provide a redundancy in case of marker loss or occlusion. Additional markers can also be used to give a more accurate measure of and to compensate for skin movement artefact (Taylor et al., 2005).

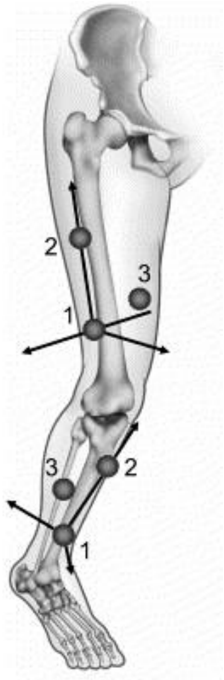

Figure 4.6: *Using sets of three non-collinear markers to define local technical frames fixed to body segments. Adapted from Cappozzo et al (2005).*

The procedure for defining a CTF relative to a cluster of three markers is as follows. The three markers must be non-collinear i.e. it is not possible to draw a straight line through all three markers. The angle between markers *ABC* (Figure 4.7) should be as close to 90° as possible. This reduces the sensitivity of the CTF orientation to deformation of the marker cluster. One of the markers is chosen as the origin marker; in this case marker *B*. A second marker is chosen to define the primary axis (*x*); in this case marker *A*. This axis is equal to the normalised vector ($\hat{\boldsymbol{v}}_1$) between these two markers. A second normalised vector ($\hat{\boldsymbol{v}}_2$) is then defined as that from marker *B* to *C*. The *z-axis* is the normal to the plane on which vectors $\hat{\boldsymbol{v}}_1$ and $\hat{\boldsymbol{v}}_2$ lie. This *z-axis* is calculated as the normalised vector $\boldsymbol{v}_3$ which is the cross product of vectors $\hat{\boldsymbol{v}}_1$ and $\hat{\boldsymbol{v}}_2$. Finally the *y-axis* is equal to $\hat{\boldsymbol{v}}_4$ calculated by taking the cross product of $\hat{\boldsymbol{v}}_3$ and $\hat{\boldsymbol{v}}_1$.

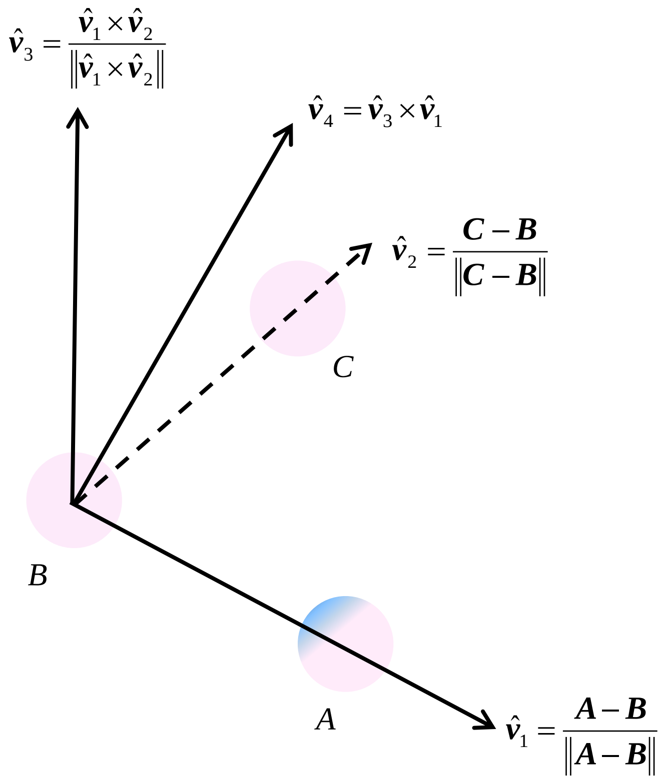

Figure 4.7: *Calculation of a CTF from three non-collinear markers.*

4.4.2 Defining anatomical frames relative to the CTFs

Once each CTF has been constructed, their relation to the underlying ACSs must be determined. If the markers are placed over known landmarks, the position of the underlying anatomy can be inferred directly from these. This can be either a direct relationship with a single marker, or by construction of a virtual marker derived from the relative position of two or more markers (Cappozzo et al., 2005). These methods are susceptible to a number of errors. It relies on the assessor to place the markers both accurately and in a repeatable way on the anatomical landmarks. These positions can be highly susceptible to skin movement artefact (Cappozzo et al., 1996) as well as not necessarily being optimal to reduce marker occlusion and restriction on the subject. In order to address some of these issues it is common to position the markers in such a way to minimise both occlusion and skin movement artefact. This means that the position and orientation of the underlying ACS needs to be determined using a separate calibration procedure. This can be done using anatomical pointing, functional definition or a combination of the two. Problems with repeatability are reduced as this calibration procedure removes any direct relationship between location of an individual marker and the anatomy.

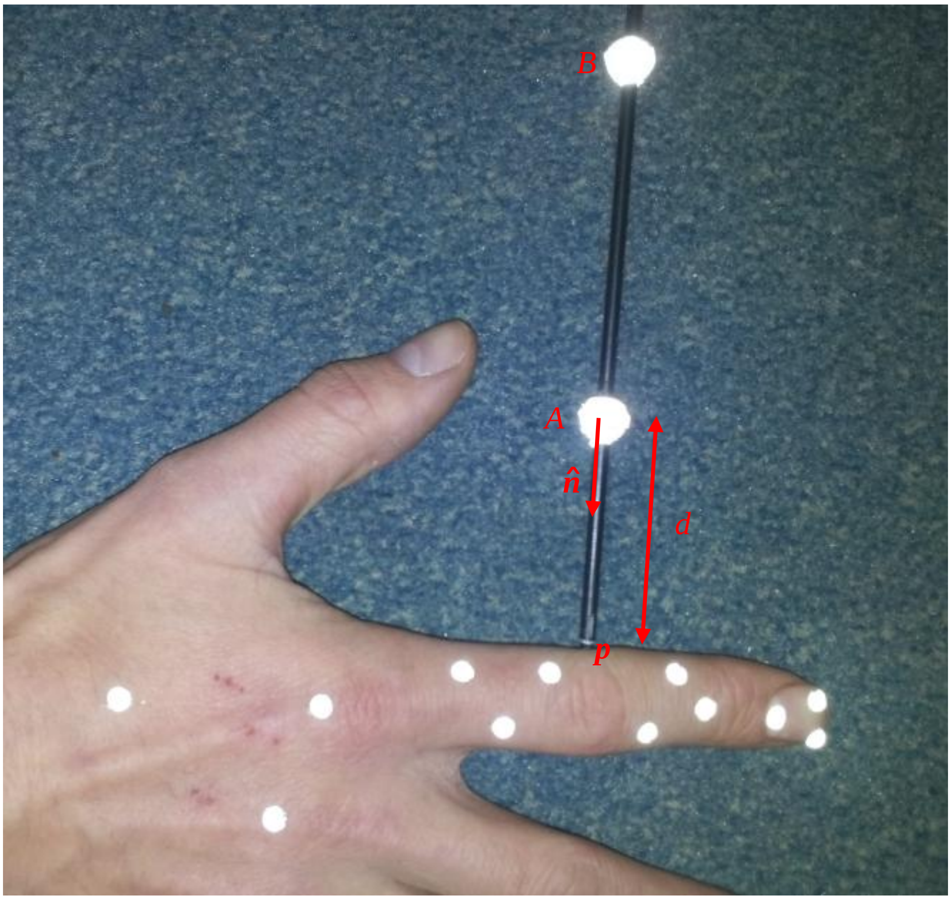

Figure 4.8: *Anatomical pointing using a calibrated pointer to define positions relative to the CTFs.*

Anatomical pointing involves the use of a calibrated pointer with at least two markers (A and B) fixed to it (Figure 4.8). In this case the distance to the point (d) from marker A is known. The unit vector ($\hat{\boldsymbol{n}}$) between markers A and B is calculated as:

$$\hat{\boldsymbol{n}} = \frac{(A - B)}{\|A - B\|}. \tag{4.9}$$

The position of the point ($\boldsymbol{p}$) is therefore known in the photogrammetric frame according to the equation:

$$\boldsymbol{p} = A + \hat{\boldsymbol{n}}d. \tag{4.10}$$

This pointer can then be used to point at known anatomical positions, defining them in the relevant CTF. These positions are then used to construct the ACS relative to the CTF. Although this makes the ACS independent of marker placement inaccuracy, it is still susceptible to other factors. The assessor must be able to locate the landmarks in a repeatable and accurate way. Even then, there are a number of assumptions about how the underlying anatomy relates to these external landmarks. This results in a lack of repeatability and precision in location of the ACS (Della Croce et al., 2005). This is of particular relevance to joint centres and axes of rotation. The location of rotation centres for various joints can be defined relative to other bony landmarks using cadaver dissection and medical imaging such as computed tomography (CT) and magnetic resonance imaging (MRI). This approach, known as the predictive approach uses empirical relations between the externally located landmarks and the relevant joint centres (Ehrig et al., 2006). Assuming that these axes of rotation can be accurately located relative to externally palpable landmarks for a cadaver or imaged subject, there are still difficulties in transforming these axes to the general subject. Assumptions are made about anatomical similarity between subjects and anthropometric scaling is used to determine the position of the axes for each joint relative to external landmarks for a specific subject. These assumptions are not always valid particularly when the subject has some kind of injury or deformity that results in abnormal anatomy (Della Croce et al., 2005). Additionally most of these datasets are based on adult studies so may not be applicable to studies of children (Harrington et al., 2007). Therefore the only way of getting a true measure of the axes of rotation for the joints of a specific subject non-invasively would be obtain relevant imaging (such as MRI). This is often not practical, for reasons of expense, time and resource.

Alternative methods of determining the joint axes have been proposed known as ‘functional methods’. Instead of relying on the relation between joint axes and palpable landmarks, they use the relative motion of joint segments to define them.

Functional methods for defining the axes of rotation of machines were first described for 2D kinematics in the 19th century (Reuleaux, 1876). Assuming one body remains fixed, a perpendicular to the line joining two positions of a point located on the rotating body is defined. Multiple perpendiculars are found in this way and the apex of these perpendiculars defines the centroid. This method has been applied in a biomechanics context with regard to the ankle joint (Maganaris et al., 1998) shown in Figure 4.9. This method only works in 2D and requires a manual definition of the perpendiculars, therefore more complex methods have been developed making use of the data available with 3D motion analysis. These modern techniques can be classed into either fitting or transformation methods.

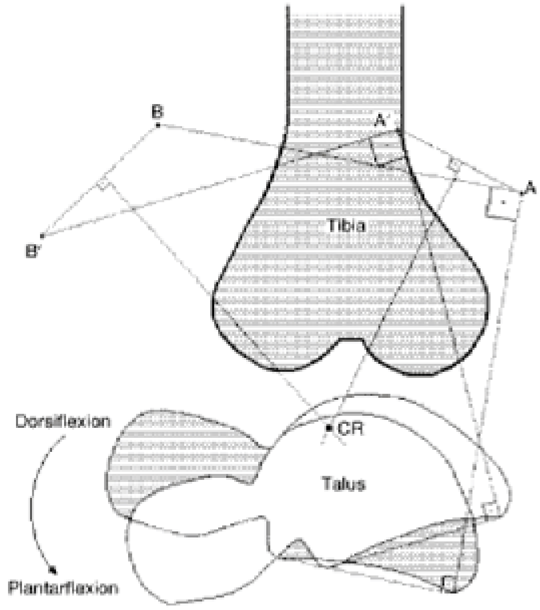

Figure 4.9: *Showing the method of (Maganaris et al., 1998). Two reference points were marked in relation to the Talus. The intersections of the perpendicular bisectors to the lines connecting the points A and A' and points B and B' defined the centre of rotation.*

Fitting methods depend on transforming a marker or group of markers attached to a given segment into the CTF of an adjacent segment. The trajectories of these markers are then fitted onto the surface of concentric spheres (for spherical joints) or cylinders (for one degree of freedom hinge joints) as shown in Figure 4.10. The properties of these spheres or cylinders are optimised to find the best fit to the marker trajectories. Variations of this technique have been proposed by several authors (Halvorsen, 2003; Zhang et al., 2003; Gamage and Lasenby, 2002; Piazza et al., 2001; Halvorsen et al., 1999; Leardini et al., 1999; Shea et al., 1997).

Transformation methods rely on two rigid CTFs being fully defined on adjacent segments. They then assume there will be a common axis that remains invariant in both CTFs throughout the movement of the joint (Figure 4.11). Like the fitting methods there have been many variations of these techniques proposed (Ehrig et al., 2007; Ehrig et al., 2006; Schwartz and Rozumalski, 2005; Marin et al., 2003; Woltring et al., 1985).

The selection of the technique appropriate for calculation of hand and finger kinematics is covered fully in Chapter 5.

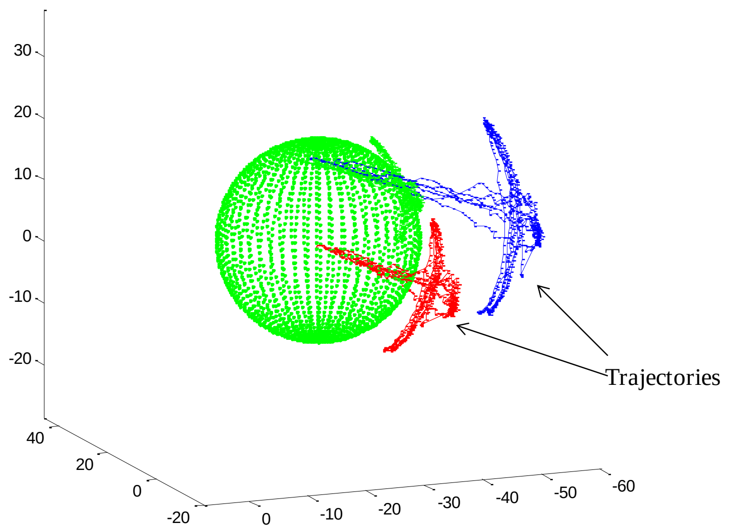

Figure 4.10: *Fitting technique. For a spherical joint as shown, a set of concentric spheres is fitted to a set of marker trajectories. For a hinge joint the trajectories would be fitted to a cylinder.*

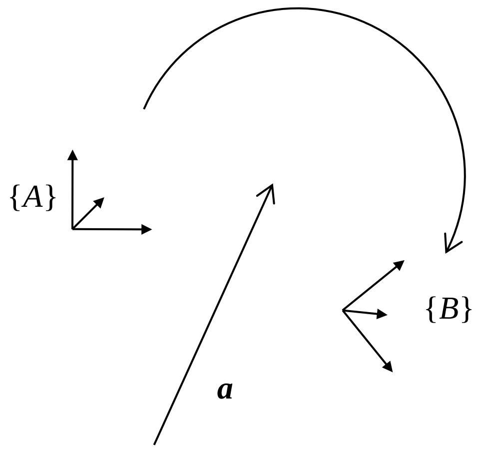

Figure 4.11: *Transformation methods assume a fixed axis (**a**) or a centre of rotation between two coordinate systems* $\{A\}$ *and* $\{B\}$*.*

4.4.3 Advantages and disadvantages of stereo-photogrammetric motion capture

As mentioned previously stereo-photogrammetric motion capture is considered the gold standard method of human kinematic analysis. As it has become established over the last few decades, a huge pool of expertise and knowledge has been acquired globally. The hardware and software developed by the established commercial companies allows it to be used by almost anyone (within financial reason) with only a few hours training. This availability has meant a huge amount of research has been done not only using the systems but on improving the techniques of how they are used. There a number of both commercial (Anybody, Denmark) and freeware tools (OpenSIMM, USA) available for post processing the data.

Spatial accuracy achieved is always improving with the reconstruction of marker positions being well within the required precision for biomechanical analysis (error <0.1mm). Additionally it is possible to reconstruct markers as small as 3mm in diameter (Metcalf et al., 2008). This allows the placement of more than one marker on small segments such as individual phalanges of the fingers (Buczek et al., 2011; Cerveri et al., 2005). A major problem with this (and other) types of motion capture is the presence of skin movement artefact. This is something which affects all data collected using skin mounted markers (or sensors) as the soft tissue deforms over the underlying skeletal structure. It has been shown that location of the markers is of vital importance in reducing this artefact (Cappozzo et al., 1996). Despite the knowledge acquired about skin deformation at different parts of the body it will always inherently be part of the data collected using stereo-photogrammetry and must therefore be accounted for.

Stereo-photogrammetry captures spatial information only, therefore if the velocities and accelerations of markers or body segments are also needed, differentiation of the data must be carried out. This can incur large errors due to noise in the data. It is therefore important that appropriate filtering is applied. For inertial systems it is the opposite with only the accelerations of body segments recorded requiring integration of the data to acquire velocities and displacements. The errors incurred, occur from the estimate of the constants of integration calculated from assumed orientations and positions of segments at given reference points (Veltink et al., 2003). Depending on what data are required the user must assess what outputs they require from the kinematic analysis and therefore which technique would be most appropriate.

Stereo-photogrammetric capture requires the subject to be within a designated capture volume. This is traditionally in a motion capture laboratory, although it is possible to set up the systems in any suitable location using tri-pods or other ways of rigidly mounting the cameras. For reconstruction, a marker must be visible to at least two cameras (although accuracy is increased with three or more), therefore occlusion can be a serious problem if there are any obstructions in the capture volume such as other subjects or objects that the subject is interacting with. This means the location of the cameras must be chosen carefully and can restrict the type of movement that can be captured.

Another major drawback of these systems is the cost. A basic system can cost a laboratory $300,000 (Simon, 2004), which will rise significantly for additional cameras and peripherals such as force plates. This restricts its use to well financed institutions such as universities, research hospitals and large production companies (for the gaming and film industry).

In conclusion stereo-photogrammetry is still considered the best option for capturing the movement of small body segments (such as hands and fingers). For the applications in my work, accurate spatial location of the body segments is of great importance and only stereo-photogrammetry can achieve this. The system available (Vicon T-Series and MX-14 Series) allows the capture of small markers placed on the phalanges, making it the best experimental method to use in my work.

4.5 Methods of hand and finger motion capture

Techniques using photographic measurements in both two (Vigouroux et al., 2006) and three dimensions (Vergara et al., 2003) have been proposed to measure the required inputs for biomechanical models (Figure 4.12). Their principal disadvantage is that they rely on photographs rather than video data, restricting them to pseudo-static applications. However, there have been a number of methods developed for tracking finger and hand motion using stereo-photogrammetry. Some of these use only one or two markers attached to each phalanx. Those techniques using less than three markers, have limitations in that they are more susceptible to skin movement artefact and repeatability problems due to marker placement error. It is common in these cases to place the markers directly on anatomical landmarks, which can have a significant effect on the skin movement artefact (Cappozzo et al., 1996).

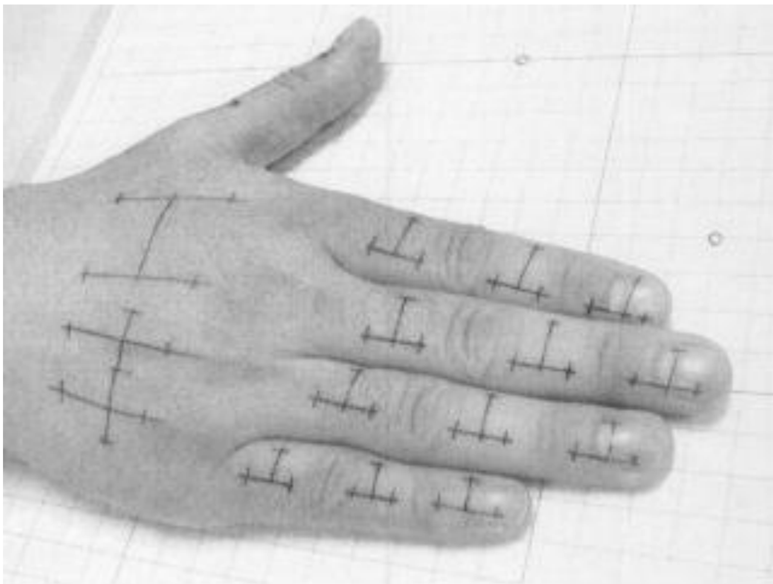

Figure 4.12: *Markers drawn onto the dorsal surface of the hand and captured using still photography as used by Vegara et al (2003).*

Marker placement error and its effect on repeatability is a particular concern when the joint angles are calculated directly from the marker positions (Carpinella et al., 2006; Rash et al., 1999). As a way of reducing this and skin movement artefact, some authors defined anatomical axes based on the relative position of markers (Metcalf et al., 2008; Su et al., 2005; Miyata et al., 2004; Zhang et al., 2003; Chiu et al., 1998). Authors such as Metcalf et al (2008) took advantage of improvements in the motion capture technology and used markers as small as 3mm in diameter (Figure 4.13). These relied on there being a degree of flexion/extension of the joints to provide a valid definition of the ACS. This meant that with the hand in a neutral pose (with close to zero flexion at each joint) this definition could become inaccurate.

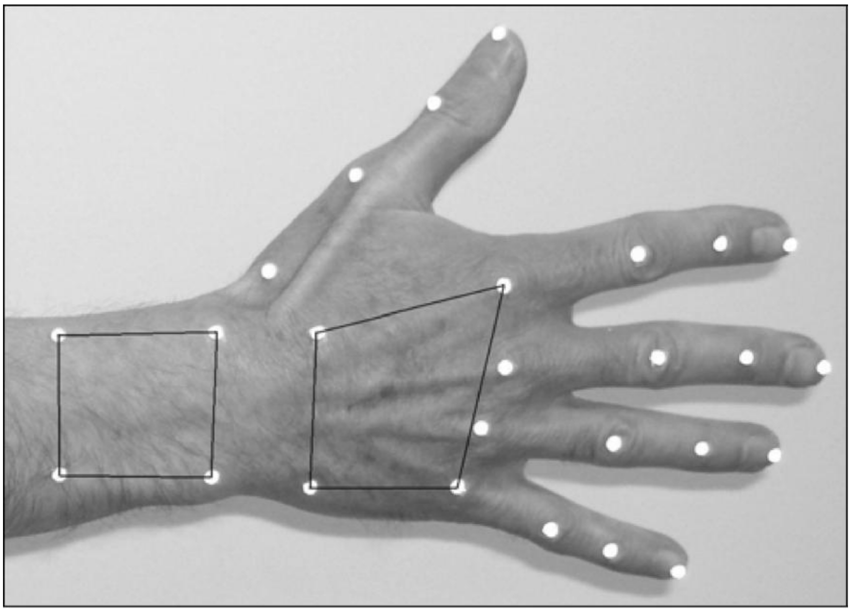

Figure 4.13: *Advances in motion capture technology has allowed the use of small hemispherical markers with diameters as small as 3mm as used by Metcalf et al (2008).*

Other authors reduced errors by using clusters of three non-collinear markers attached to each phalanx and the dorsal surface of the hand to create CTFs rigidly attached to each segment (Figure 4.14) (Degeorges et al., 2005; Fowler and Nicol, 1999b). These techniques restricted the movement of the subject due to the markers standing proud of the surface of the hand. To address this, sets of non-collinear markers have also been attached directly to the skin without using clusters (Figure 4.15) (Buczek et al., 2011; Cerveri et al., 2005). Using these methods the underlying anatomy was defined using either purely anatomical landmarks (Buczek et al., 2011; Degeorges et al., 2005) or a combination of anatomical landmarks and functional definition (Cerveri et al., 2005; Fowler and Nicol, 1999b). The concept of using a functional approach has been applied to other parts of the body such as the lower limb (Andriacchi and Alexander, 2000). The use of CTFs rigidly attached to each segment reduced the susceptibility to marker placement repeatability errors, allowing the observer to attach markers to positions least likely to be affected by skin movement artefact.

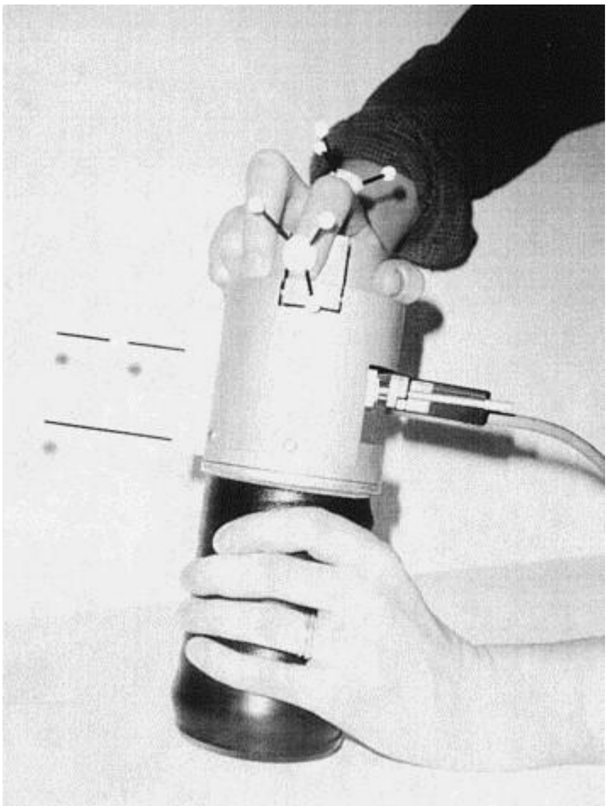

Figure 4.14: *Tri-pods have been used to mount sets of three non-collinear markers to each phalanx as used by Fowler and Nicol (1999b).*

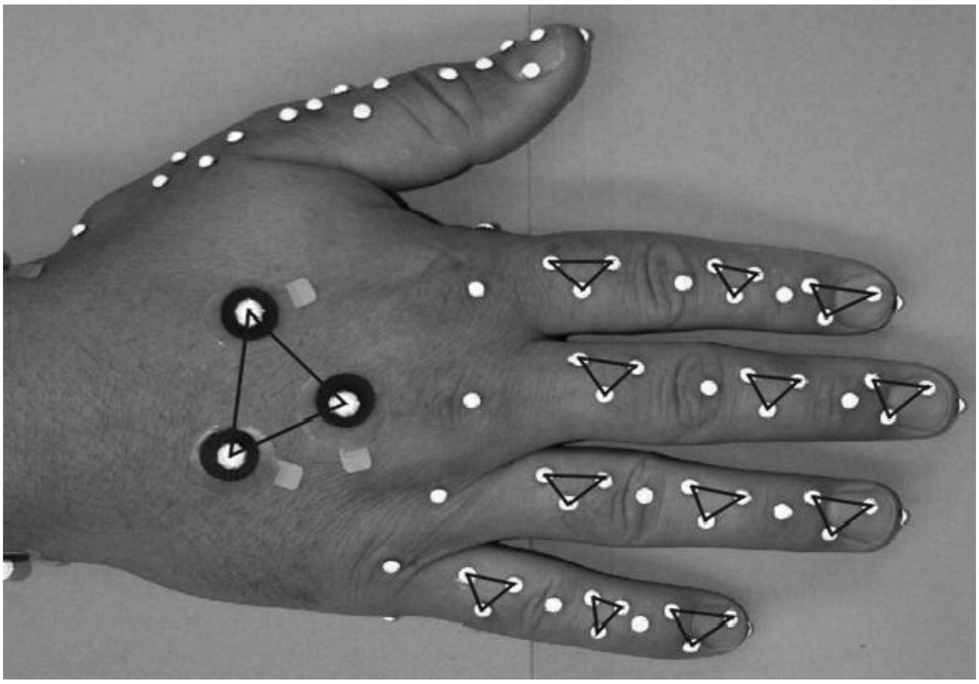

Figure 4.15: *Utilising small markers, Buczek et al (2011) defined technical frames fixed to each phalanx without the need for tri-pods.*

The previous studies that used functional methods for finding the axes of rotation of the fingers used both fitting and transformation techniques. For finding the axes of rotation of the interphalangeal joints, Cerveri et al (2005) used a fitting technique referred to as cylinder axis fit and for the centre of rotation of the metacarpo-phalangeal (MCP) joint an algebraic sphere fit method. Fowler and Nicol (1999), used an established axis transformation technique (Woltring et al., 1985) for calculation of both the interphalangeal joints and the MCP joint.

The next two chapters describe and assess a new method of kinematic analysis of the fingers. This new method combines techniques used previously both for the fingers and other limbs using functional methods of axis definition.

Chapter 5. Accuracy of a new method of finger motion capture using functional joint centres

The work presented in this chapter and the next has been accepted for publication in 'The Proceedings of the Institution of Mechanical Engineers, Part H: Journal of Engineering in Medicine' with the title "*A technique for motion capture of the finger using functional joint centres and the effect of calibration range of motion on its accuracy"* (Warlow and Lawson, 2012).

A key aim of this thesis is to both establish a reliable method of kinematic analysis of the fingers and to be able to assess its accuracy. Additionally, it was desirable to keep the restriction on the subject to a minimum. The ability to put a level of confidence on any measurement was of great importance when considering the sensitivity of the biomechanical models to errors in input as discussed in Chapter 3.

This and the following chapter introduce and assess both a new marker set suitable for stereo-photogrammetric motion capture of the hand and two techniques for defining the anatomical coordinate systems (ACSs) functionally. These techniques draw from the literature adapting what has been developed for both the upper and lower limbs, combining them using state of the art motion capture technology. The marker set used allowed the definition of a cluster technical frame (CTF) on each relevant body segment whilst minimising any impairment on its movement by keeping the mass and protrusion from the skin surface to a minimum.

The first technique for defining the joint axes functionally, referred to as the phalanx transformation technique (PTT), applied the theories of the axis transformation technique (ATT) (Ehrig et al., 2007) and centre transformation technique (CTT) (Ehrig et al., 2006), originally developed for the knee and hip.

The second technique, referred to as the phalanx fitting technique (PFT), was based on the geometric axis fit technique (Shakarji, 1998).

By assessing the practicality of the marker set proposed and the accuracy achievable using both the PTT and PFT it was possible to determine whether a transformation or fitting technique was most appropriate for functional definition of the phalanx ACSs. The accuracy in the definition of each joint axis was measured in terms of displacement error. To provide clinical relevance, it was important to show how these errors would impact on the output from a biomechanical model. The results found in Chapter 3, correlating joint displacement error with error in joint reaction force (JRF) were used to do this.

5.1 Methods

5.1.1 Experimental procedure

Thirteen subjects (seven male and six female) were recruited to take part in the experiment (age: 24 ± 3 years; height: 1.77 ± 0.08 m; mean ± SD). A six camera Vicon T20 motion capture system (Vicon, U.K.) was used with a sampling rate of 100Hz.

A total 12 hemispherical markers, 4mm in diameter were attached in groups of three to each phalanx of the index finger and the dorsal surface of the right hand (Figure 5.1). For this study only the index finger was examined as it was the accuracy achieved using the specified marker set and the difference between the two mathematical techniques that was of interest rather than differences between fingers. The markers were attached using water soluble adhesive and the total mass of the 12 markers was 0.3g. The markers were attached in groups of three, in a non-collinear arrangement to define a CTF fixed to each phalanx and the dorsal surface of the hand.

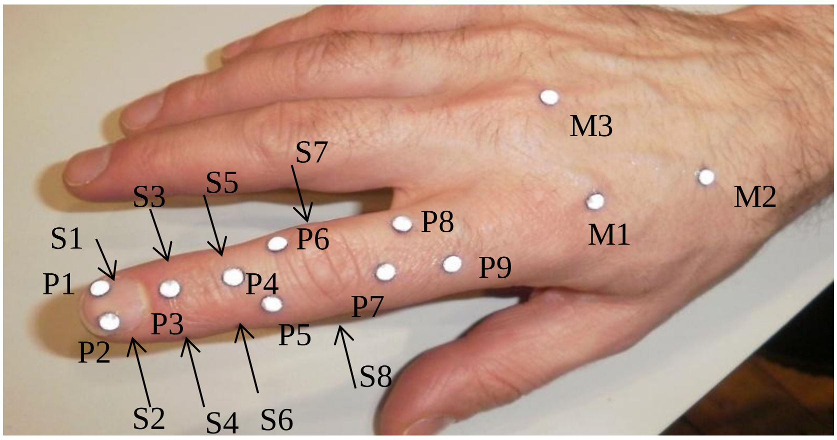

Figure 5.1: *Position of markers P1-9 attached to the three phalanges of the right index finger and markers M1-3 attached to the dorsal surface of the hand. Positions S1-S8 were pointed using a calibrated pointer. The proximally directed axis of the distal phalanx was defined on the radial and ulnar side by the positions S1-S6. The approximate centres of the distal and proximal interphalangeal (DIP and PIP) joints were defined as the average of S5S6 and S7S8 respectively.*

For calculation of the axis of rotation (AoR) at the interphalangeal joints and the centre of rotation (CoR) at the metacarpo-phalangeal joint each subject was required to perform five repetitions of a set of calibration movements. These were; a full flexion/extension of the distal and proximal interphalangeal (DIP and PIP) joints, and full flexion/extension and abduction/ adduction of the metacarpo-phalangeal (MCP) joint. These movements defined the functional joint centres in each CTF relevant for the joint of interest. Along with the pointed positions S1-8, these could then be used to define the ACSs relative to each CTF.

The errors at each joint calculated when using either the PTT or PFT were then compared. The null hypothesis tested was that the errors would be the same for either technique (95% confidence interval). Additionally the absolute position of the ACS could be compared as the same experimental data were used for either technique. The null hypothesis tested was that the position of each ACS would be the same using either technique and that any difference would be within experimental error.

5.1.2 Definition of anatomical coordinate systems

The process of defining the anatomical coordinate systems was identical for both the PTT and PFT. Firstly, anatomical positions were defined in the phalanx CTFs using a calibrated pointer. This procedure is common in lower limb motion analysis (Cappozzo et al., 2005). The pointer consisted of a rod 250mm long with markers positioned 25mm and 50mm from the pointed end (Figure 5.2). The positions S1-S8 were pointed with the hand in a neutral pose (Figure 5.1). The positions S5- S8 were positioned at the apex of the flexion crease on both the radial and ulnar side of the interphalangeal joints. S5-S8 were used to find the mid-point of the finger at either joint. The positions S1 and S2 were positioned midway between the dorsal and palmar surface of the finger 5mm proximal to the finger tip. The positions S3 and S4 bisected the lines created by S1S5 and S2S6. The positions S1-S6 were then used to define the long axis of the distal phalanx.

Figure 5.2: *Calibrated pointer used to define the positions S1-S8.*

The positions and orientations of each ACS were identical to those defined in Figure 3.1. An explanation of these coordinate systems can be found in Section 3.1.

The pointed positions (S1-S8) were combined with the functional axes to define the ACS for each segment. The AoR found from the calibration movements were of infinite length, therefore it was necessary to find the point on this line closest to the centre of each phalanx to define its centre. The centres were defined by finding the point on these AoR closest to the mean of positions S5 and S6 for the DIP joint and positions S7 and S8 for the PIP joint. The MCP was defined as a CoR, therefore no anatomical pointing was needed. The AoR themselves defined the *z-axes* of the distal, middle and proximal phalanges. As described previously the *y-axis* of the distal phalanx was defined using the positions S1-S6. The *y-axes* of the middle and proximal phalanges were defined as the line linking the distal and proximal joint centres of that segment. A condition was placed on the *y-axes* in that they had to be perpendicular to the existing *z-axis*. The dorsally directed *x-axes* were taken as the cross product of the *z* and *y-axes* for each segment.

5.1.3 Phalanx transformation technique (PTT)

The DIP and PIP joints were modelled as having one degree of freedom acting as a hinge about the flexion/extension axis. The MCP joint is thought to have two degrees of freedom, one about the flexion/extension axis and one about the abduction/adduction axis. For the purposes of defining a functional joint centre however, it was modelled as a spherical joint.

The ATT (Ehrig et al., 2007) was used to find the interphalangeal joints' AoR. This method assumed there was a common AoR $\boldsymbol{a}$ between two adjacent segments. A point $\boldsymbol{c}$ laying on the axis could then be defined in one of the CTFs adjacent to the joint of interest. This same point can also be defined in the other adjacent CTF as $\tilde{\boldsymbol{c}}$. Using the known rotations $\boldsymbol{R}$ and translations $\boldsymbol{t}$ between the two CTFs the two points should adhere to the relationship:

$$\boldsymbol{c} = \boldsymbol{R}\tilde{\boldsymbol{c}} + \boldsymbol{t}, \qquad \textbf{(5.1)}$$

as shown in Figure 5.3. Using this relationship, a constraint function f_{ATT} was defined as:

$$f_{ATT}(\boldsymbol{c}, \tilde{\boldsymbol{c}}) = \sum_{i=1}^{N} \|\boldsymbol{R}_i\tilde{\boldsymbol{c}} + \boldsymbol{t}_i - \boldsymbol{c}\|^2, \qquad \textbf{(5.2)}$$

Where N was the total number of capture frames. The valid solutions of $\tilde{\boldsymbol{c}}$ and $\boldsymbol{c}$ were non-unique as they could be positioned anywhere along the axis $\boldsymbol{a}$, therefore this equation was expressed as a least squares problem and solved using singular value decomposition (SVD) (Ehrig et al., 2007), see Appendix A. This found solutions of the normal vector defining the AoR in each relevant CTF defined as $\tilde{\boldsymbol{a}}$ and $\boldsymbol{a}$. Once the axes were defined, unique solutions of $\tilde{\boldsymbol{c}}$ and $\boldsymbol{c}$ were found using the average positions of S5S6 and S7S8 for the DIP and PIP joints respectively as described in Section 5.1.2.

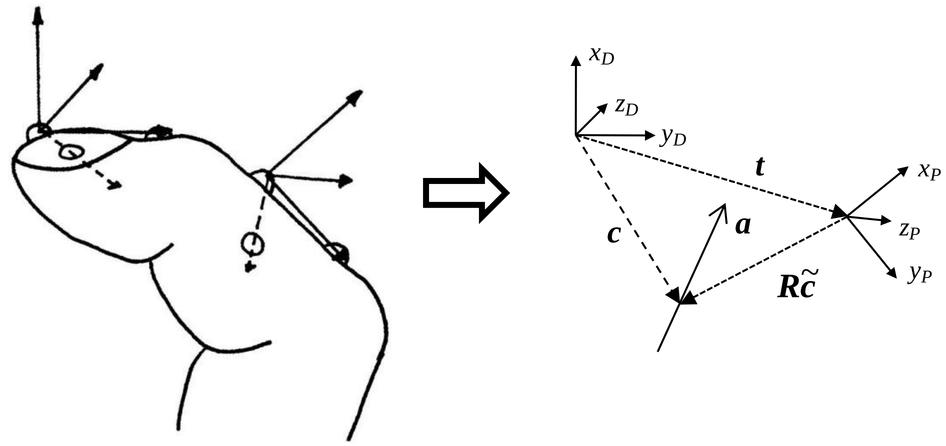

Figure 5.3: *The phalanx transformation technique. CTFs were defined on each phalanx and the transformation between them defined as rotations **R** and translations **t**. Any position **c** laying on the common AoR **a** can be expressed in the other CTF by the relationship* $\boldsymbol{c} = \boldsymbol{R}\tilde{\boldsymbol{c}} + \boldsymbol{t}$.

Each of the DIP and PIP joints' AoR were then defined in the global frame $\left(\boldsymbol{a}_D^g,\ \boldsymbol{a}_P^g,\ \boldsymbol{c}_D^g,\ \boldsymbol{c}_P^g\right)$. For each individual time frame the mean value of these axes and origins in the global (photogrammetric) coordinate system were taken as the ACS flexion/extension axis ($\boldsymbol{a}^g$) and origin ($\boldsymbol{c}^g$) (Figure 5.4). The distance from these mean origins to the two original joint centres in the adjacent CTFs is indicative of the precision of the joint definition. It is proposed however, that in the absence of more detailed anatomical study, the distance can be used to predict the error in joint position, as stated by Ehrig et al (2011). Therefore, error for any given capture frame was expressed by:

$$\boldsymbol{e} = \left(\boldsymbol{c}_D^g - \boldsymbol{c}_P^g\right)/2. \tag{5.3}$$

The error was averaged across the entire range of calibration by taking the mean of the absolute magnitude of each component, as expressed by:

$$\boldsymbol{e}_{PTT} = \frac{1}{N}\sum_{i=1}^{N}\left(\left|e_{x,i}\right|, \left|e_{y,i}\right|, \left|e_{z,i}\right|\right), \tag{5.4}$$

where N was the total number of capture frames. In this manner the errors at the two interphalangeal joints ($\boldsymbol{e}_{DIP}$ and $\boldsymbol{e}_{PIP}$) were calculated as being equal to $\boldsymbol{e}_{PTT}$.

The MCP joint was found using the CTT (Ehrig et al., 2006). In the same manner as the ATT, rigid body transformations were defined between CTFs fixed to segments adjacent to the joint (proximal segment and metacarpal segment). The constraint function defined as f_{CTT} was identical to equation (5.2). Instead of a fixed AoR used by the ATT however, a fixed CoR was assumed meaning that $\tilde{\boldsymbol{c}}$ and $\boldsymbol{c}$ had unique solutions. The equation could therefore be solved using an optimisation routine. This was carried out using an interior-point algorithm in the *optimisation toolbox* available in MATLAB (The MathWorks). As with the interphalangeal joints, these joint centres were expressed in the global frame ($\boldsymbol{c}_D^g$, $\boldsymbol{c}_P^g$) and the mean taken as the ACS origin. The error ($\boldsymbol{e}_{MCP}$) was calculated in an identical manner as the error at the interphalangeal joints. Computation for a set of calibration movements was between 2-5 seconds.

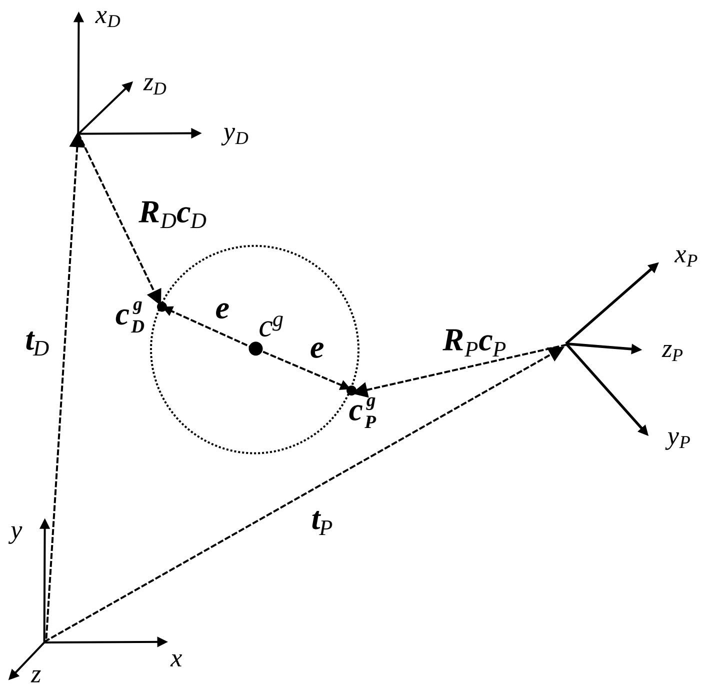

Figure 5.4: *Calculation of joint centre position. The joint centres in the global frame ($\boldsymbol{c}_D^g$ and $\boldsymbol{c}_P^g$) were calculated from their positions in each cluster technical frame. The joint centre was then taken as the mean of these two values. The precision and subsequently error* $\boldsymbol{e}$ *was then taken as half the discrepancy between the two original joint centres.*

5.1.4 Phalanx fitting technique (PFT)

The PFT used the geometric axis fit technique (Ehrig et al., 2007; Shakarji, 1998) to find the DIP and PIP AoR. As with the PTT, this method assumed there was a fixed AoR $\boldsymbol{a}$ between two adjacent segments. The markers from one segment were transformed into the CTF of the adjacent segment (Figure 5.5). A set of constraints was then defined to find the AoR based on the marker trajectories. The first constraint assumed that the marker would move in a plane, the normal to which was the AoR $\boldsymbol{a}$. A vector was defined, starting at a distance d from the centre $\boldsymbol{c}_1$ along the vector $\boldsymbol{a}$ and finishing at trajectory position $\boldsymbol{p}$. To meet the planar constraint, this was perpendicular to $\boldsymbol{a}$ (i.e. $cos90^o = 0$) and could therefore be expressed mathematically using the properties of the scalar product:

$$\boldsymbol{a}.(\boldsymbol{p}-\boldsymbol{c_1}-d\boldsymbol{a})=0. \qquad \textbf{(5.5)}$$

A second constraint was used to fix the distance r between the centre $\boldsymbol{c}_1$ and the marker trajectory $\boldsymbol{p}$. Using the properties of the cross product it can be shown that:

$$\boldsymbol{a}\times(\boldsymbol{p}-\boldsymbol{c_1})=\|\boldsymbol{a}\|\|\boldsymbol{p}-\boldsymbol{c}_1\|\boldsymbol{n}. \qquad \textbf{(5.6)}$$

This holds assuming the vector ($\boldsymbol{p}$ - $\boldsymbol{c}_1$) is approximately perpendicular to $\boldsymbol{a}$ (i.e. $sin(\sim 90^o) = 1$). $\boldsymbol{n}$ is the normal vector to the plane defined by $\boldsymbol{a}$ and ($\boldsymbol{p} - \boldsymbol{c}_1$). Because $\boldsymbol{a}$ and $\boldsymbol{n}$ are unit vectors and $\|\boldsymbol{p} - \boldsymbol{c}_1\| = r$ then the constraint becomes:

$$\|\boldsymbol{a}\times(\boldsymbol{p}-\boldsymbol{c_1})\|=r. \qquad \textbf{(5.7)}$$

This can be re-arranged and combined with (5.5) to give the constraint:

$$\{\boldsymbol{a}.(\boldsymbol{p}-\boldsymbol{c_1}-d\boldsymbol{a})\}^2+\{\|\boldsymbol{a}\times(\boldsymbol{p}-\boldsymbol{c_1})\|-r\}^2=0. \qquad \textbf{(5.8)}$$

There are a total of M markers fixed to a segment and N capture frames. Therefore the complete constraint function for all markers and frames is given by:

$$\begin{aligned} &f_{geom}(\boldsymbol{c}_1,r_1,\dots,r_M d_1,\dots,d_M,\boldsymbol{a}) \\ &=\sum_{j=1}^{M}\sum_{i=1}^{N}\left[\{\boldsymbol{a}.(\boldsymbol{p}_{ij}-\boldsymbol{c}_1-d_j\boldsymbol{a})\}^2+\{\|\boldsymbol{a}\times(\boldsymbol{p}_{ij}-\boldsymbol{c}_1)\|-r_j\}^2\right]. \end{aligned} \qquad \textbf{(5.9)}$$

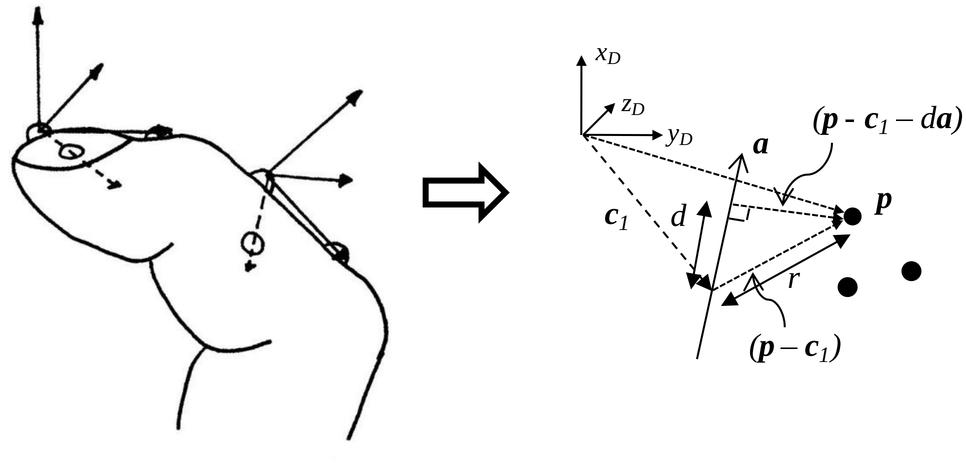

Figure 5.5: *The markers on one phalanx are all transformed into the cluster technical frame fixed to that adjacent to it, to give the trajectories* $\boldsymbol{p}$*. The markers were then assumed to rotate around a common AoR* $\boldsymbol{a}$*. A constraint equation was defined using:* $\boldsymbol{p}$ *that defines the position of any given marker,* $\boldsymbol{c}_1$ *the point defining a unique solution of* $\boldsymbol{a}$*, d the distance from* $\boldsymbol{c}_1$ *in the direction* $\boldsymbol{a}$ *that gives the point with minimal perpendicular distance to the marker, and r the radii of the marker trajectory from vector* $\boldsymbol{a}$*.*

The optimal solution of this constraint function that minimised f_{geom} was found using an interior-point algorithm within the *optimisation toolbox* available in MATLAB (The MathWorks) using a multi-start algorithm to ensure the global optimum was found. Computation for a set of calibration movements was between 5-10 seconds.

Unlike the methods described by (Shakarji, 1998) and (Ehrig et al., 2007), the AoR were calculated twice, both in the CTF distal and proximal to the joint of interest. This meant that in a similar way to the PTT two equivalent centres were calculated for each joint enabling an estimate of errors in their position.

The MCP joint position and error were found using the CTT (Ehrig et al., 2006) in an identical manner to the PTT using equation (5.2).

Using the PFT, both the interphalangeal joints and the MCP joint were all found using optimisation methods. This allowed additional constraints to be added regarding the length of the finger segments. Assuming that the phalanges are rigid, the distance between each joint will be minimal throughout the entire calibration movement. A cost function was defined as the standard deviation in both the middle and proximal phalanx lengths. This was included in the optimisation procedure.

5.1.5 Application to a biomechanical model

In Chapter 3, the relationship between errors in the position of the joint centres and errors in the output from a biomechanical model were quantified. This enabled the generation of coefficients to express errors in predicted JRF as a function of the displacement error at each joint centre ($\boldsymbol{e}_{DIP}$, $\boldsymbol{e}_{PIP}$ and $\boldsymbol{e}_{MCP}$). These errors in joint centre position were estimated using both the PTT and PFT. Combining these with the coefficients it was possible to calculate the error in terms of JRF expressed as e_{JRF}.

5.2 Results

The components and total magnitude of the joint errors using the PTT and PFT are shown in Table 5.1 and visualised in Figure 5.6. The results shown are those averaged across the 13 subjects. At the interphalangeal joints the total magnitudes of the errors ($||\boldsymbol{e}_{DIP}||$ and $||\boldsymbol{e}_{PIP}||$) were significantly different between techniques ($p < 0.05$) with the PFT errors being larger. In terms of the components there was only a significant difference in e_x and e_y. At the MCP joint there was no significant difference in $||\boldsymbol{e}_{MCP}||$ between techniques. The total magnitude of errors averaged across all three joints was 0.6mm and 1.1mm for the PTT and PFT respectively.

The errors expressed in terms of e_{JRF} were calculated resulting in an error of 2.2% for the PTT of 2.2% and 6.3% for the PFT.

	e_x		e_y		e_z		$\|\boldsymbol{e}\|$	
	PTT	PFT	PTT	PFT	PTT	PFT	PTT	PFT
$\boldsymbol{e}_{DIP}$ *(mm)*	0.1	0.4	0.1	0.6	0.3	0.4	0.3	0.9
$\boldsymbol{e}_{PIP}$ *(mm)*	0.2	0.4	0.1	1.1	0.9	1.1	0.9	1.7
$\boldsymbol{e}_{MCP}$ *(mm)*	0.3	0.4	0.2	0.3	0.5	0.3	0.7	0.7

Table 5.1: *The error at each joint ($\boldsymbol{e}_{DIP}$, $\boldsymbol{e}_{PIP}$ and $\boldsymbol{e}_{MCP}$) for the mean of thirteen subjects, expressed in component form (e_x, e_y and e_z) and total magnitude ($\|\boldsymbol{e}\|$) for all subjects. Errors shown for both the PTT and PFT.*

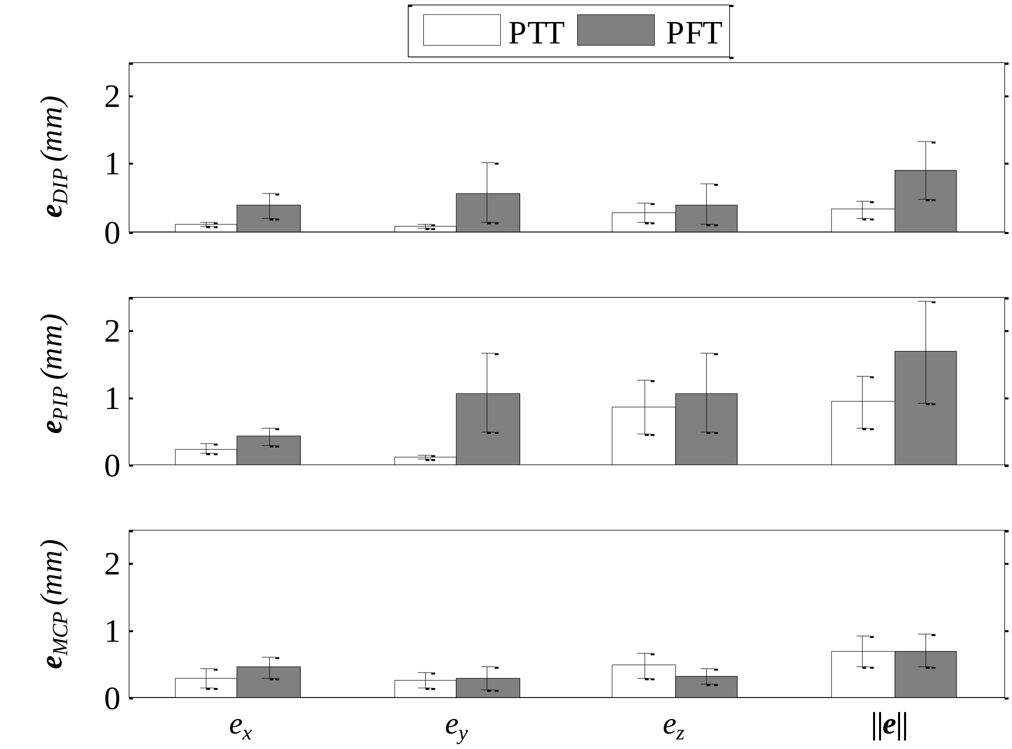

Figure 5.6: *The error at each joint ($\mathbf{e}_{DIP}$, $\mathbf{e}_{PIP}$ and $\mathbf{e}_{MCP}$) for the mean of thirteen subjects, expressed in component form (e_x, e_y and e_z) and total magnitude ($\|\mathbf{e}\|$) for all subjects. Errors shown for both the PTT and PFT, error bars represent ± standard deviation.*

The difference between each ACS origin calculated using either the PTT or PFT was tested for statistical significance. Because the position of each origin was expressed in Cartesian coordinates each component was compared meaning a total of three comparisons for each segment origin. The metacarpal origin was not included as it was coincident with the origin of the proximal phalanx. It was found there was no significant difference between the PTT and PFT in the position of any ACS origin calculated. This difference between each ACS origin was also compared with the cumulative error of the PTT and PFT. This comparison is shown in Figure 5.7 . This shows that for each component at each joint the difference in ACS origin is within the cumulative experimental error.

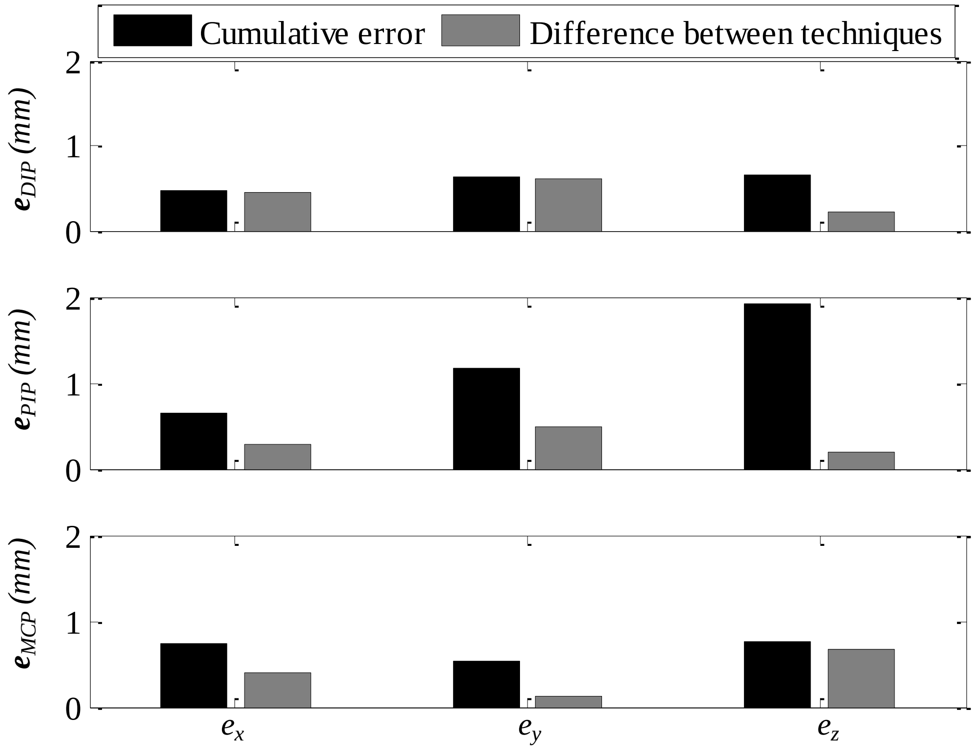

Figure 5.7: *Comparison between the cumulative error and the difference in each ACS origin calculated using with the PTT or PFT.*

5.3 Discussion

This chapter has assessed the application of a skin-mounted marker set consisting of 12x4mm hemispherical markers to define the kinematics of the index finger. Two methods of defining the ACS using functional techniques were used. Two were used so both a fitting and transformation technique could be assessed in the context of finger kinematics. The same experimental input could be used for either technique allowing a direct comparison to be made. The accurate determination of the ACSs is an important input to biomechanical models, therefore the effect of ACS accuracy on the biomechanical model was analysed.

No invasive or imaging procedures had to be used to determine the ACS accuracy. This meant the procedure could be carried out on multiple subjects within a standard motion analysis lab without the need for additional apparatus.

Previous authors have tried to assess the accuracy in their methods of motion capture using different methods. Repeatability of measured joint angles has been used (Degeorges et al., 2005), however this does not provide a measure of accuracy adequate for most biomechanical modelling applications. A mechanical linkage of known dimensions has also been used (Fowler and Nicol, 1999b). But such a linkage does not take into account skin movement artefact known to have an effect on accuracy (Taylor et al., 2010; Taylor et al., 2005; Andriacchi et al., 1998; Cappozzo et al., 1996; Peters et al.). For assessment of the functional techniques used to define the ACS numerical simulations have been used (Ehrig et al., 2007; Ehrig et al., 2006; Cerveri et al., 2005). These studies applied noise to simulate both skin movement artefact and experimental measurement uncertainty. With all simulations however, the way errors were introduced may not necessarily be an accurate representation of reality.

In this study the joint errors were assumed to be equal to half the magnitude of the discrepancy between segment origins calculated in adjacent CTFs. Discrepancy in origin was computationally identical to the residuals f_{ATT} or f_{CTT} depending on which joint was being considered. These residuals have been shown to correlate with joint error with a coefficient of 0.5 (Ehrig et al., 2011), hence confirming this assumption.

The total magnitude of the joint errors across the three joints using the PFT was almost double that of the PTT at 1.1mm compared to 0.6mm. This was predominantly due to the difference at the inter-phalangeal joints. A significant difference in error magnitude was found at these joints whereas at the MCP joint there was no significant difference. Similar results between techniques at the MCP joint were expected as the same mathematical technique (CTT) was used to find it in each case.

It is my opinion that the difference in techniques is due to the PTT using the position of all six markers on adjacent segments simultaneously, rather than one at a time as with the PFT. It would be of future interested to examine the deformation of the CTF on each phalanx as this would give further insight into the errors, this was out with the scope of my present study however.

Looking at the components of the error at the interphalangeal joints in more detail there was only a significant difference in the e_x and e_y components (dorsal and proximal directions) and not in the e_z components (radial direction). Figure 5.6 shows that for the PFT there were similar magnitudes of error in each component, however for the PTT the component e_z was larger than the other two. This meant that error magnitudes were similar between techniques for this component. The reasons for the errors of this component being larger than the others when using the PTT can be understood by considering how these joint centres were calculated. Because the AoR calculated initially was of infinite length, the average position of S5S6 and S7S8 were used to adjust the position of the joint centre to the middle of each phalanx (see Section 5.1.2). These adjustments were made along the AoR i.e. in the direction of the *z-axis*. This means the adjustment will affect the error in this direction only. Because the errors using the PTT were in general smaller, this effect was only obvious when this technique was used.

The reliance on anatomical pointing to locate the AoR correctly, meant that neither technique was purely functional. To my knowledge there is currently no way of fully defining segment ACSs without some form of input regarding anatomical positions. A direction of future research could be to be able to fully define the AoR without the need for any anatomical reference points.

The MCP joint was defined in a purely functional manner, therefore the slight increase in e_z compared to the other components was due to other factors, such as the limitation of assuming a spherical MCP joint for the kinematic model (discussed further in Chapter 6).

No patterns were seen in the components of error at the MCP joint. The difference in the error components was due to the addition of the length constraint in the PFT. This did not have a significant effect on the magnitude of the error however, and did not significantly affect the position of the joint centre.

When transformed into percentage errors in the output of a biomechanical model (e_{JRF}) the difference in techniques was more marked. Using the PFT the percentage error was almost three times larger at 6.3% compared to 2.2% for the PTT. This error in predicted JRF did not relate to the total magnitude of the joint errors (1.1mm for the PFT was less than two times larger than 0.6mm for the PTT) in a linear manner. This was because errors were dependent on the magnitudes of each individual component (e_x, e_y, e_z) at each joint.

The positions of the ACSs defined using either technique were compared to ascertain if within experimental uncertainty, each technique was finding the same joint centres. The use of identical experimental input made this comparison possible and found that all three independent segment origins, each expressed in two adjacent CTFs, were statistically the same and within experimental uncertainty when calculated using either technique.

The accuracy of these techniques compared favourably with previous functional methods of definition. For assessment of the hip joint, Leardini et al (1999) found that functional methods estimated the joint centre within 13mm of the geometric centre found using X-Ray. Using the optimal common shape technique Taylor et al (2010) were able to estimate the hip joint centre to within 3.5mm. My study modelled the MCP as a spherical joint and the errors were 0.7mm for both techniques. For a hinge joint Schwartz and Rozumalski (Schwartz and Rozumalski, 2005) estimated the joint centre to within 3.8mm. In my study the interphalangeal joints were defined as hinges with errors of 0.3-0.9mm for the PTT and 0.9-1.7mm for the PFT. It is important to note however that large skin artefacts are expected in the lower limb. Therefore the decrease in errors in my study was more due to the difference in anatomy encountered rather than a vast improvement in motion capture. Buczek et al (2011) noted that there would be greater skin artefact especially around the MCP joint when the subject gripped a cylinder. As my study did not involve the subject interacting with any objects this could not be quantified. However it would be assumed that because the ACS are all defined in two adjacent segment CTFs then skin movement artefact would be reduced as much as possible.

5.4 Conclusions

In conclusion it has been shown that the proposed marker set, calibration movements and techniques used to calculate the segment ACSs, provide a useful tool for accurate calculation of finger kinematics in comparison with previously proposed techniques. Of the two I tested, the PTT was both more accurate in measurement of joint positions and biomechanical model outputs. This improvement when using a transformation technique compared to fitting technique has been observed previously (Ehrig et al., 2007; Ehrig et al., 2006). Some subjects, including those with injuries or pathologies such as arthritis, may have a significantly reduced range of motion (RoM) of the joints (Chung et al., 2009; Jennings and Livingstone, 2008; Goodson et al., 2007; Lluch, 2006; Chung et al., 2004; Goldfarb and Stern, 2003). These pathologies can also significantly deform the joint altering the position and kinematics of the joints' rotational axes. The influence of reduced RoM on accuracy has not been covered in this chapter, however it is of great relevance to the clinical application of these techniques and will be studied in Chapter 6.

Chapter 6. Effect of calibration range of motion on the accurate definition of functional joint centres of the fingers

In the previous chapter, a marker set for finger motion capture and two techniques defining the anatomical coordinate systems (ACSs) functionally were proposed. It was found that in application to the fingers, the phalanx transformation technique (PTT) resulted in the smallest errors. As with all functional methods of joint definition, the subject was required to undertake a series of calibration movements (flexion/extension and abduction/adduction of joints) defining the axes and centres of rotation (AoR and CoR). For the most accurate joint definition, a large range of motion (RoM) was preferred as this minimised error from measurement noise and skin movement artefact. Some subjects however, like those with injuries or pathologies such as arthritis, may have a significantly reduced RoM or even fixed flexion/extension or ulnar drift at the metacarpo-phalangeal (MCP) joint (Chung et al., 2009; Jennings and Livingstone, 2008; Goodson et al., 2007; Lluch, 2006; Chung et al., 2004; Goldfarb and Stern, 2003). It is therefore important to understand the influence of reduced RoM on the accuracy of joint definition.

Most methods of functional joint definition described in the literature assume either a constant AoR or CoR, depending on which joint was being defined. This is not strictly true, as it is known that the cam profile of the metacarpal head results in a non-constant CoR at the MCP joint (Pagowski and Piekarski, 1977). At the interphalangeal joints, the AoR is also thought to change as the joint is flexed and extended (Holcomb et al., 1958). Therefore in reality functional joint centres defined assuming a constant AoR or CoR are in fact the mean positions of a set of instantaneous axes and centres of rotation (IAoR and ICoR).

The aim of this chapter is to examine the effect of the calibration RoM on the accurate definition of the joint centres of the fingers. Errors were found in terms displacement, and to provide clinical relevance they were also expressed in terms of percentage error in predicted internal loading. Analysis was carried out to define the IAoR and ICoR as a function of joint angle.

6.1 Methods

6.1.1 Experimental procedure and definition of anatomical coordinate systems

The same experimental data collected for the work carried out in Chapter 5 were used for the analyses in this chapter. The ACSs were defined in an identical manner using functional joint centres and anatomical pointing. This chapter considered only the application of the PTT to find the functional ACSs.

6.1.2 Reduced arc analysis

For calculation of the AoR and CoR each subject was required to make a set of calibration movements. These were a full flexion/extension of the two interphalangeal joints, full flexion/extension and abduction/ adduction of the MCP joint.

The methods of calculating the joint centres relied on the subject being able to carry out the calibration movements to as full an extent as possible. Potentially, subjects of future interest may have a significantly reduced RoM, therefore the calibration data were adapted to simulate a reduced RoM (Figure 6.1). New sets of calibration data were created with arcs reduced from a magnitude equal to $|\theta_f|$ to a magnitude of zero in decrements of 2°. A new type of error was defined ($\boldsymbol{e}_{ROM}$), equal to the vector between the original joint centre and those defined with the reduced arc (φ).

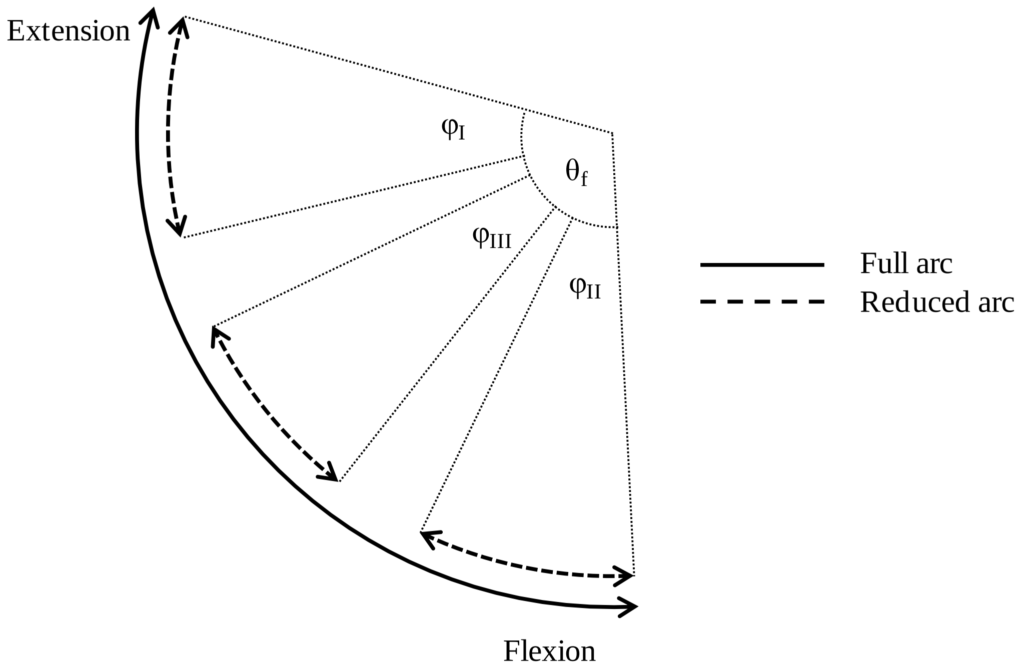

Figure 6.1: *The full arc of flexion/extension was defined as θ_f. For reduced arc analysis the magnitude was reduced by decrements of 2° to give φ. Simulations were made with the arc φ fixed about three locations. These were the point of greatest extension (φ_I), the point of greatest flexion (φ_{II}) and the centre of the original arc (φ_{III}).*

The total joint error ($\boldsymbol{e}_{total}$) was expressed as the sum of this error and the original error:

$$\boldsymbol{e}_{total} = \boldsymbol{e}_{ROM} \pm \boldsymbol{e}_{PTT}. \quad \textbf{(6.1)}$$

The worst case scenario was taken i.e. the sign of $\boldsymbol{e}_{PTT}$ was chosen to ensure the largest value of $\boldsymbol{e}_{total}$.

When reducing the RoM it was important to consider where φ was relative to the original θ_f. The subject could have a reduced RoM with the finger at an extended position, flexed position or somewhere between these two extremes. Simulations were made with three types of reduced arc: φ_I, φ_{II}, and φ_{III}, type I with the minimum magnitude at full extension, Type II with the minimum at full flexion and Type III with the minimum in the middle of θ_f.

6.1.3 Multiple arc analysis

The PTT assumed a constant AoR at the interphalangeal joints and a constant CoR at the MCP joint. Although a good approximation for finding the functional joint axes it was not strictly true. A further analysis was therefore made to calculate the change in position of the IAoR and ICoR throughout finger flexion. New arcs of calibration data where created from the original arc θ_f (Figure 6.2). Each of these arcs defined as φ_i, with $i = 1,...,Q$ had equal magnitude and were centred about different angles of flexion. Each arc centre was separated by angle ψ. Taking the magnitude of each smaller arc as $|\varphi_i|$, the magnitude of the original arc as $|\theta_f|$ and the separation angle ψ, Q was defined as:

$$Q = \frac{|\theta_f| - |\varphi_i|}{\psi} + 1. \tag{6.2}$$

Q was rounded down to the closest integer.

For each joint the IAoR or ICoR were found for every φ_i. $\boldsymbol{e}_{ROM}$ and $\boldsymbol{e}_{PTT}$ were calculated, however they had different properties than when used for the reduced arc analysis. The measurement inaccuracy was independent of joint angle so the $\boldsymbol{e}_{PTT}$ primarily gave a measure of the change in skin movement artefact with degree of flexion. The $\boldsymbol{e}_{ROM}$ gave a measure of the difference between the IAoR or ICoR from their positions calculated using the full arc. This was used to calculate coefficients (c_{ROM}) to transform from the mean AoR and CoR to the IAoR and ICoR as a function of flexion angle. These were calculated for the restricted arc θ_r. The magnitude of this arc was calculated using:

$$|\theta_r| = |\theta_f| - |\varphi|. \tag{6.3}$$

Because θ_f was fixed, the magnitude $|\theta_r|$ decreased as the magnitude $|\varphi|$ increased. A balance was established to ensure $|\varphi|$ was large enough to provide accurate measurement of the IAoR and ICoR, but not so large as to greatly reduce $|\theta_r|$.

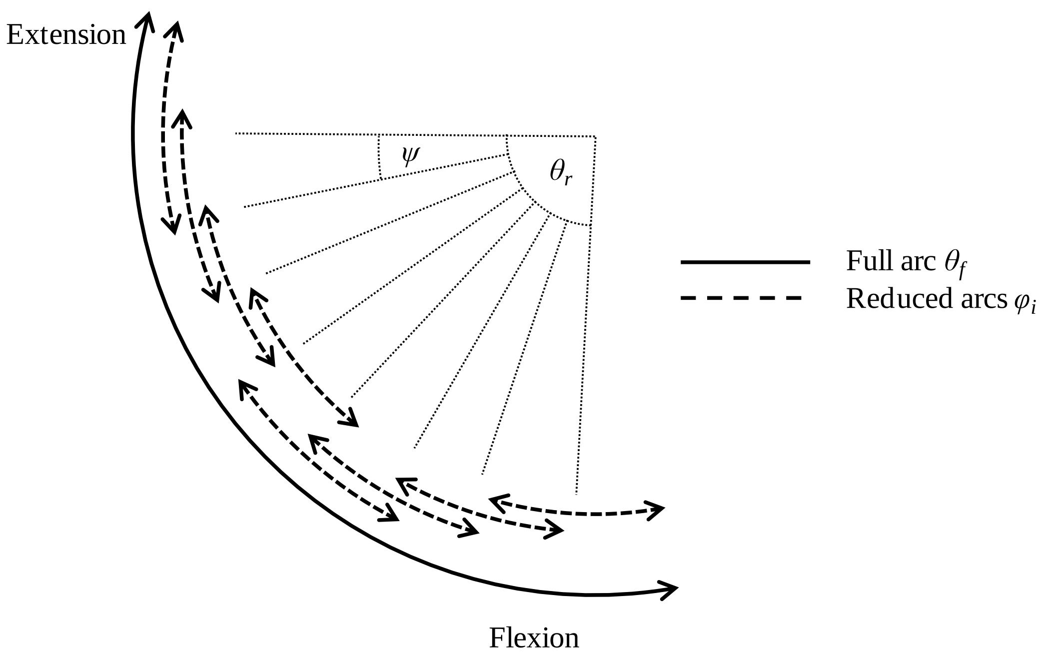

Figure 6.2: *To find the instantaneous axes and centres of rotation the full arc θ_f was divided into a number of restricted arcs φ_i. These were all of equal magnitude and their centres separated by equal division ψ.*

A criterion was used to determine if $|\varphi|$ was large enough. The mean error of $\boldsymbol{e}_{ROM}$ was calculated across the whole of θ_r as the sum of all the $\boldsymbol{e}_{ROM}$ divided by Q:

$$\overline{\boldsymbol{e}}_{ROM} = \sum_{i=1}^{Q} \frac{\boldsymbol{e}_{ROM,i}}{Q}. \tag{6.4}$$

This was then compared to the equivalent $\boldsymbol{e}_{total}$ for the given subject. This was then used to define the criterion:

$$|\varphi| \; valid \; if \;\; \overline{\boldsymbol{e}}_{ROM} < \boldsymbol{e}_{total}. \tag{6.5}$$

6.1.4 Application to a biomechanical model

As carried out in Chapter 5, all errors could be expressed in terms of the predicted joint reaction force (JRF) as e_{JRF}.

6.2 Results

6.2.1 Reduced arc analysis

For the reduced arc analyses, the magnitudes $||\boldsymbol{e}_{PTT}||$, $||\boldsymbol{e}_{ROM}||$ and $||\boldsymbol{e}_{total}||$ are shown in Figure 6.3, Figure 6.4 and Figure 6.5 respectively. For the interphalangeal joints' RoM all the errors followed similar profiles as the RoM decreased. For the MCP joints, the errors increased until the RoM reached around 10-20°, where the magnitude started to decrease.

Considering the interphalangeal joints, the largest magnitude of $||\boldsymbol{e}_{PTT}||$ was observed for the Type II reduction with smaller magnitudes observed for the Type I and III reductions. Looking at the magnitude of $||\boldsymbol{e}_{ROM}||$, Type I and II reductions had similar magnitudes with the Type III reduction yielding the smallest errors. The magnitude of $||\boldsymbol{e}_{ROM}||$ was in general larger than $||\boldsymbol{e}_{PTT}||$. $||\boldsymbol{e}_{total}||$ reflects this with the smallest errors observed for the Type III reduction and the Type II reduction was the largest.

Considering the MCP joint, the largest magnitude of $||\boldsymbol{e}_{PTT}||$ was observed for the Type I reduction with smaller magnitudes observed for the Type II and III reductions. Considering $||\boldsymbol{e}_{ROM}||$, the Type I reduction still yielded the largest errors, but there was more distinction between Type II and III with the smallest observed for Type II reduction. As with the interphalangeal joints the larger magnitude of errors was observed for $||\boldsymbol{e}_{ROM}||$. This meant a similar difference in magnitude of errors was observed for $||\boldsymbol{e}_{total}||$ as was observed for $||\boldsymbol{e}_{ROM}||$.

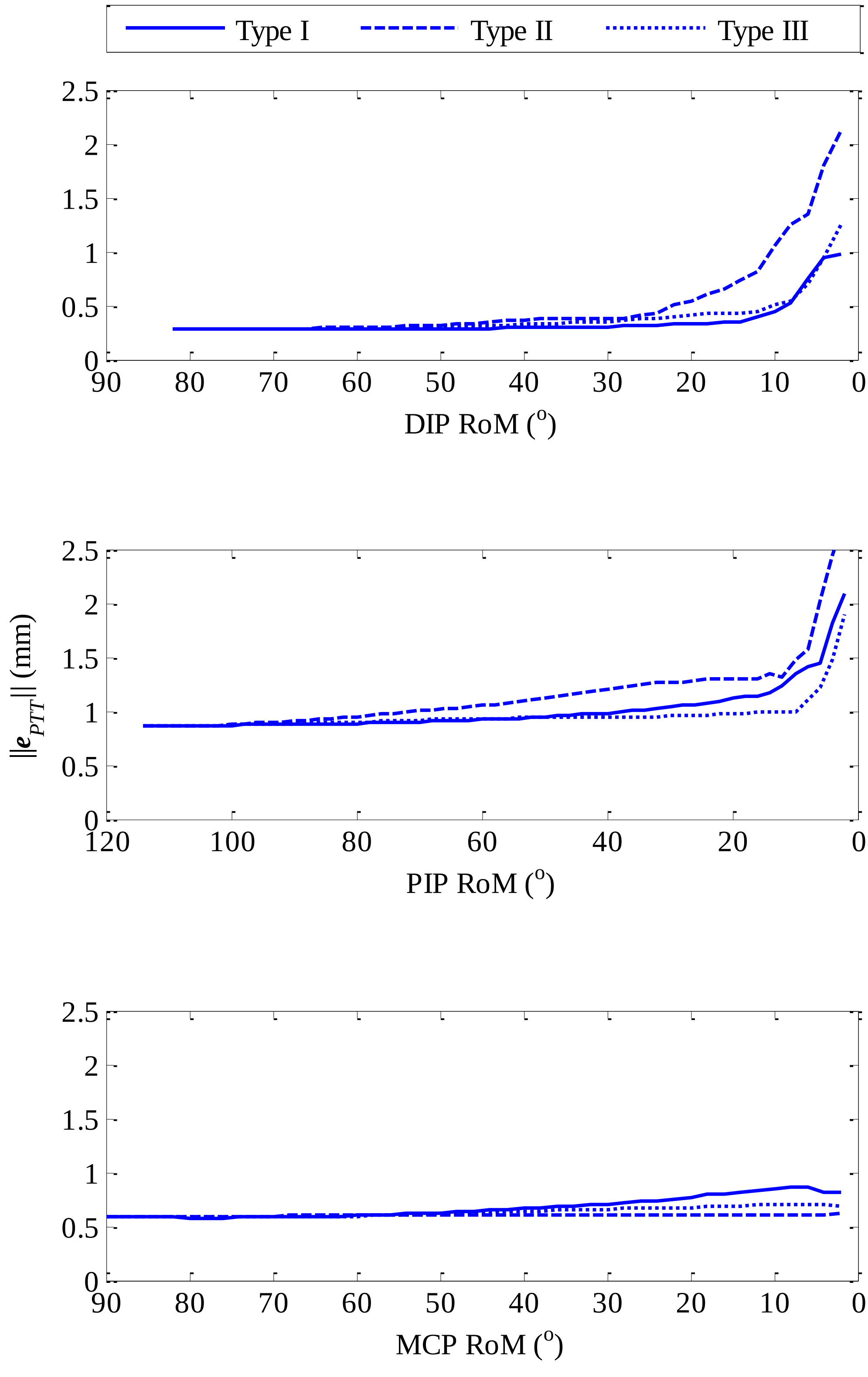

Figure 6.3: *||e_{PTT}|| for Type I, II and II reductions at the three joints.*

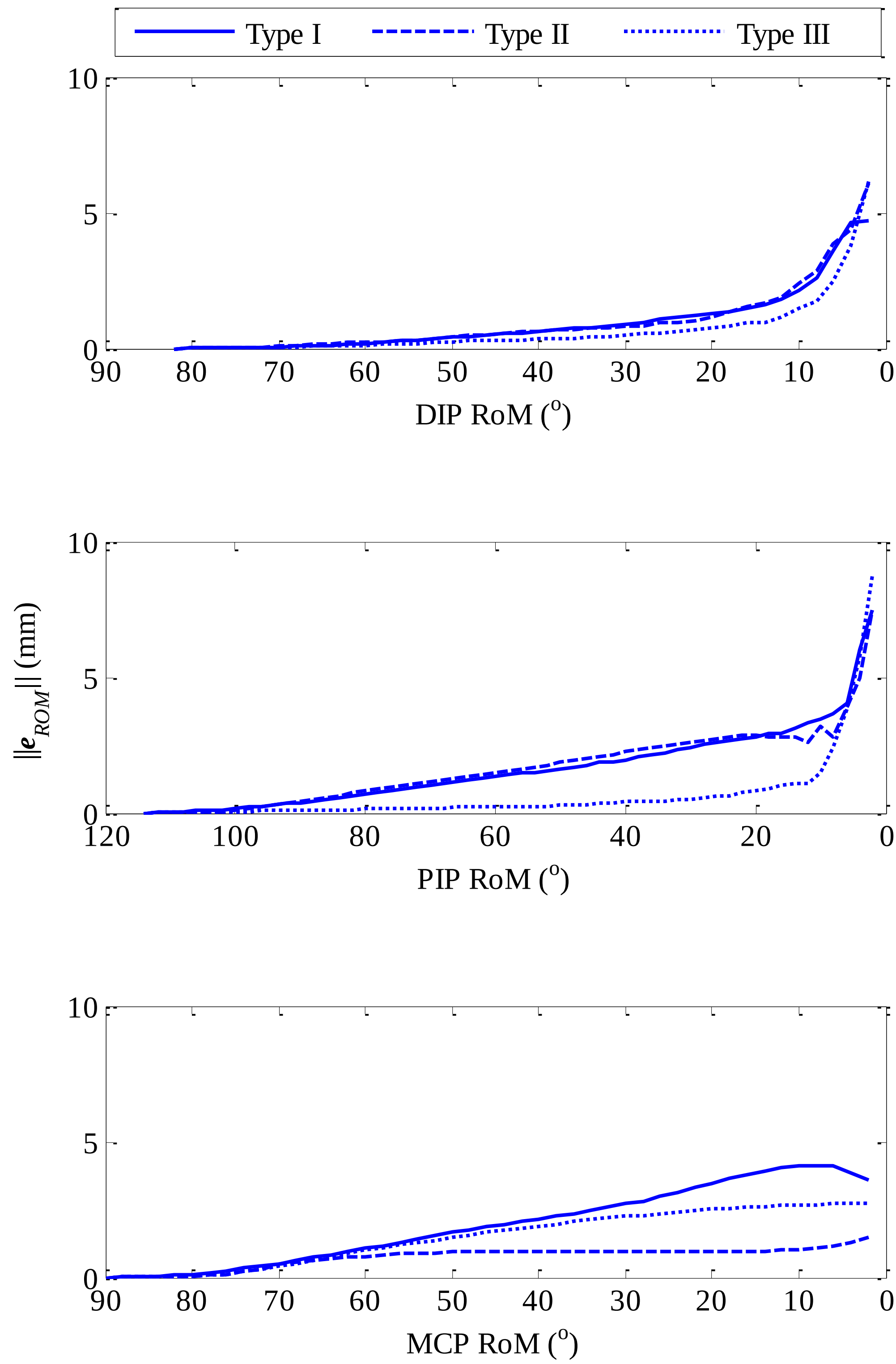

Figure 6.4: *||$\boldsymbol{e}_{ROM}$|| for Type I, II and II reductions at the three joints.*

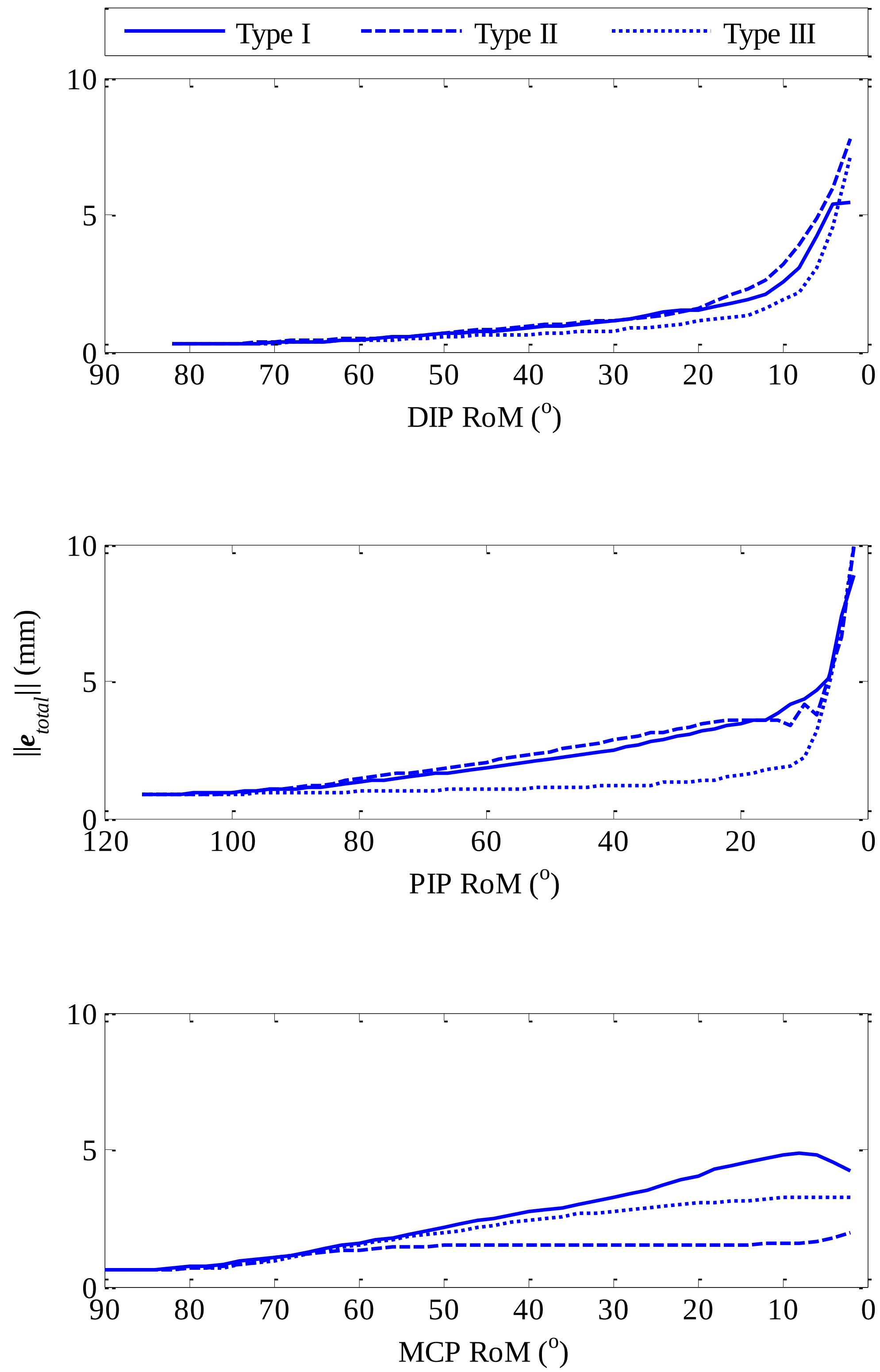

Figure 6.5: *||$\boldsymbol{e}_{total}$|| for Type I, II and II reductions at the three joints.*

In Figure 6.6, the mean of the Type I and II reductions were compared with numerical simulation studies (Ehrig et al., 2007; Ehrig et al., 2006). These numerical simulations followed an exponential profile at all joints. At the distal interphalangeal (DIP) joint the PTT had a smaller $||\boldsymbol{e}_{total}||$ than the numerical simulations. At the proximal interphalangeal (PIP) joint, $||\boldsymbol{e}_{total}||$ was similar between studies. This similarity remained until a RoM of approximately 45°. At this point errors in the numerical simulation rose rapidly. This pattern was repeated at the MCP joint with a similar magnitude observed until a RoM of 45°.

Using the mean $\boldsymbol{e}_{total}$ of the Type I and II reductions e_{JRF} was calculated as shown in Figure 6.7. This error for a reduced RoM given as an example of the restriction on a subject with rheumatoid arthritis (Goodson et al., 2007) is shown in Table 6.1. Additionally, the magnitude $||\boldsymbol{e}_{total}||$ averaged across the three joints is shown. The mean value of e_{JRF} doubled in comparison to the un-restricted case to e_{JRF} = 4.4%. The standard deviation also increased to 2.7%. From these increases it could be assumed that in general, errors in the predicted internal loading would be <7%.

	RoM restriction at joint (°)			*average $||\boldsymbol{e}_{total}||$ across all joints (mm)*		*e_{JRF} (%)*	
	DIP	*PIP*	*MCP*	*mean*	*S.D.*	*mean*	*S.D.*
un-restricted	-	-	-	*0.6*	*0.2*	*2.2*	*0.7*
restricted	*58*	*66*	*50*	*1.4*	*0.5*	*4.4*	*2.7*

Table 6.1: *Summary table of the magnitude of the errors in joint position $||\boldsymbol{e}_{total}||$ averaged across all three joints and the errors in predicted internal reaction force e_{JRF}. These were calculated as a mean and standard deviation for the 13 subjects. Shown are the results for the unrestricted calibration RoM and for a simulated RoM of a subject suffering from rheumatoid arthritis.*

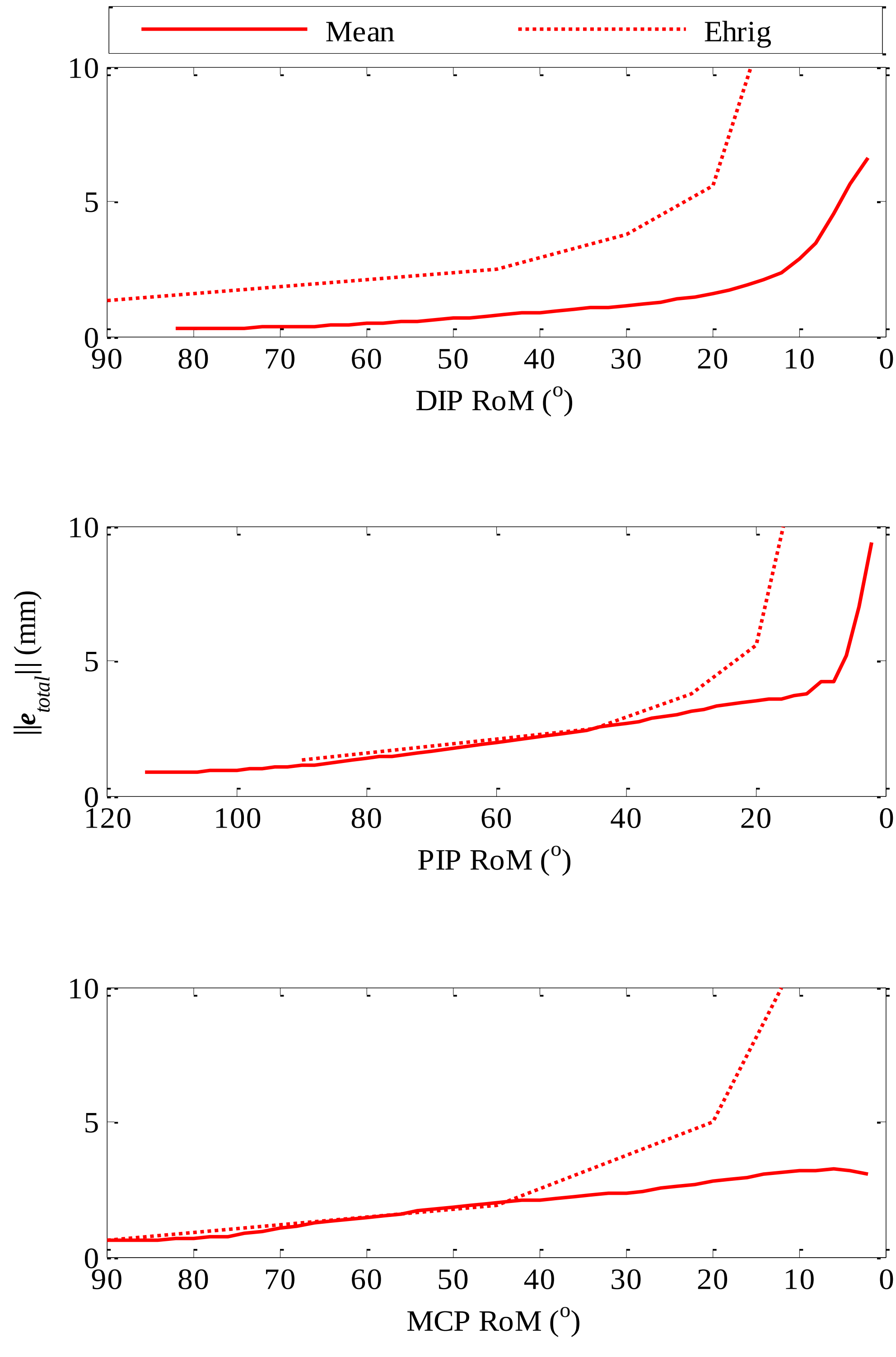

Figure 6.6: *Mean $||\boldsymbol{e}_{total}||$ Type I and II reductions compared with the numerical simulations (Ehrig et al., 2007; Ehrig et al., 2006).*

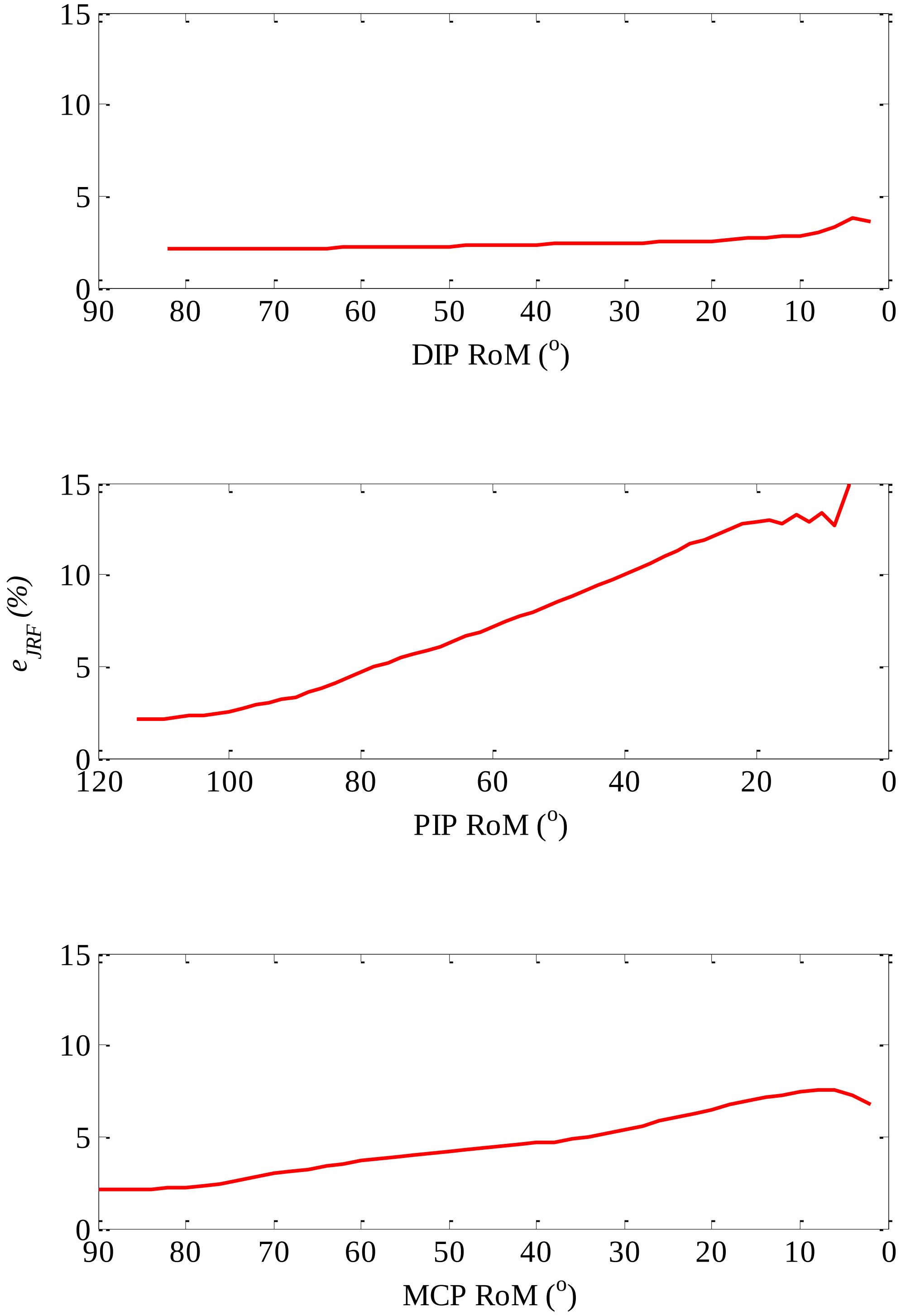

Figure 6.7: *e_{JRF} calculated from the mean $\mathbf{e}_{total}$ of the Type I and II reductions.*

6.2.2 *Multiple arc analysis*

Figure 6.8 shows the magnitude of $||\boldsymbol{e}_{PTT}||$ averaged across all subjects with the magnitude $|\varphi|$ = $30°$. The horizontal axis represents the flexion angle about which the arc φ_i was centred. For the interphalangeal joints $||\boldsymbol{e}_{PTT}||$ increased as the flexion angle increased. The PIP joint had a greater $||\boldsymbol{e}_{PTT}||$ compared to the DIP. A relatively flat profile was observed for the analysis of the MCP joint.

It was hypothesised that $\boldsymbol{e}_{ROM}$ was a product of the joint geometry, it was therefore not suitable to average these results across subjects. In this chapter only the $\boldsymbol{e}_{ROM}$ results from a single subject are presented in full (Figure 6.10). The full results from the other subjects can be found in Appendix B.

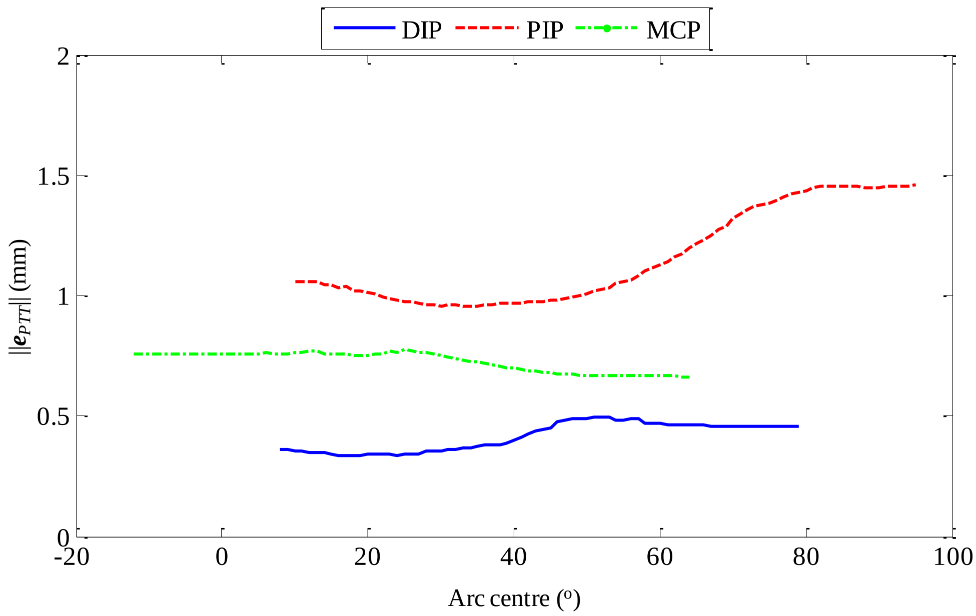

Figure 6.8: *$||\boldsymbol{e}_{PTT}||$ from multiple arc analysis averaged across all subjects. The horizontal axis represents the centre of the calibration arc. Each line represents the change in $||\boldsymbol{e}_{PTT}||$ with centre of calibration arc for a given joint.*

To assess the appropriate magnitude $|\varphi|$ required, the components of $\boldsymbol{e}_{ROM}$ for differing $|\varphi|$ at the DIP joint for the subject are shown in Figure 6.9. As $|\varphi|$ was increased from 20° to 50°, $|\theta_r|$ decreased as per equation (6.3), however the scatter in the data also decreased, resulting in an almost linear relationship between angle and $|\varphi|$. This plot in combination with the validity criterion (equation (6.5)) was used to find the most suitable magnitude of $|\varphi|$. The result of this for each subject and each joint with a magnitude of $|\varphi|$ = 30° are shown in Table 6.2. A black inequality (<) indicates that the criterion was met and a red inequality (>) indicates that it was not. For the DIP joint 10 out of 13 subjects met the criterion. For the PIP joint all subjects met the criterion. For the MCP joint only one subject met the criterion. Of all values of $|\varphi|$, 30° was deemed to be the most appropriate balance between valid data whilst maintaining a large enough $|\theta_r|$.

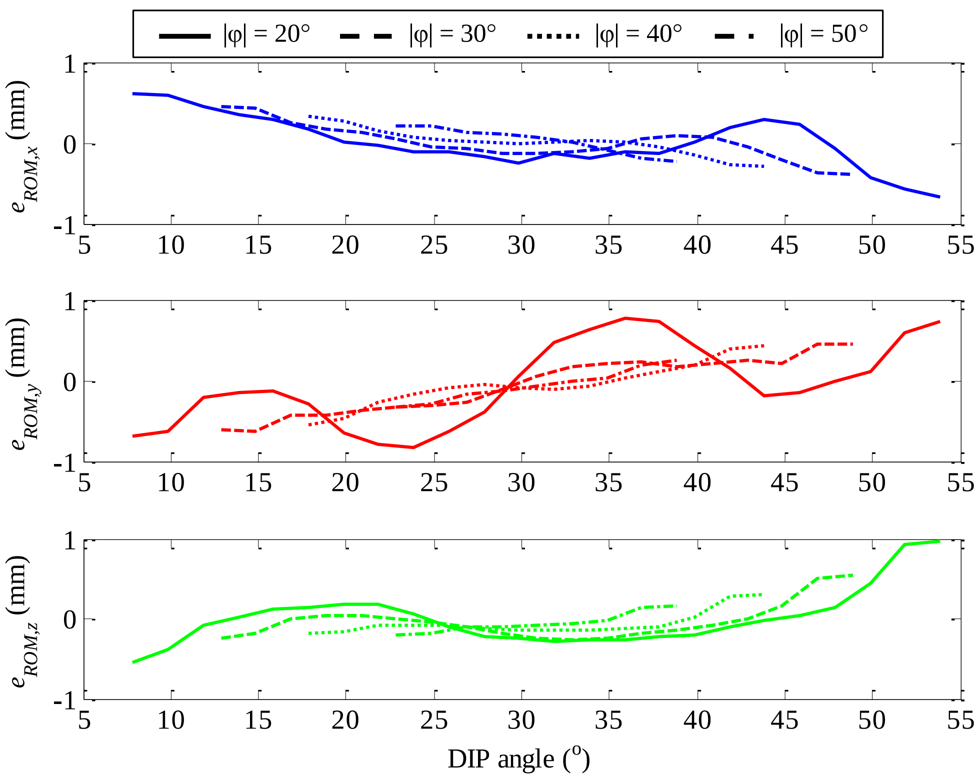

Figure 6.9: *$\boldsymbol{e}_{ROM}$ from multiple arc analysis for a single subject for the DIP joint. The magnitude $|\varphi|$ varied from 20° to 50°.*

Joint	DIP			PIP			MCP		
Subject	$\bar{e}_{ROM}$ (mm)		e_{total} (mm)	$\bar{e}_{ROM}$ (mm)		e_{total} (mm)	$\bar{e}_{ROM}$ (mm)		e_{total} (mm)
1	0.0	<	0.2	0.4	<	1.4	3.1	>	1.0
2	0.2	<	0.3	0.1	<	1.6	0.7	>	0.5
3	0.1	<	0.2	0.3	<	0.5	1.6	>	0.4
4	0.4	>	0.3	0.2	<	1.2	1.5	>	0.7
5	0.2	<	0.2	0.2	<	0.9	4.1	>	0.8
6	0.1	>	0.1	0.2	<	0.6	1.8	>	0.4
7	0.1	<	0.4	0.0	<	0.4	0.7	>	0.3
8	0.2	<	0.5	0.2	<	0.6	3.1	>	1.0
9	0.4	>	0.3	0.1	<	0.8	0.6	>	0.5
10	0.1	<	0.3	0.1	<	0.3	3.0	>	0.9
11	0.6	>	0.3	0.3	<	1.4	1.5	>	0.4
12	0.1	<	0.5	0.2	<	1.3	0.5	<	0.6
13	0.4	<	0.5	0.4	<	0.8	0.5	>	0.3

Table 6.2: *Comparison of the mean error of all arcs ($\bar{e}_{ROM}$) for a magnitude $|\varphi| = 30°$ with the total error (e_{total}) for a full RoM. Shown for all subjects.*

.

After determining a magnitude of 30° as most suitable, the components of $\boldsymbol{e}_{ROM}$ were calculated for multiple arcs at each joint (Figure 6.10). It is important to note that the criterion was not met for the MCP joint.

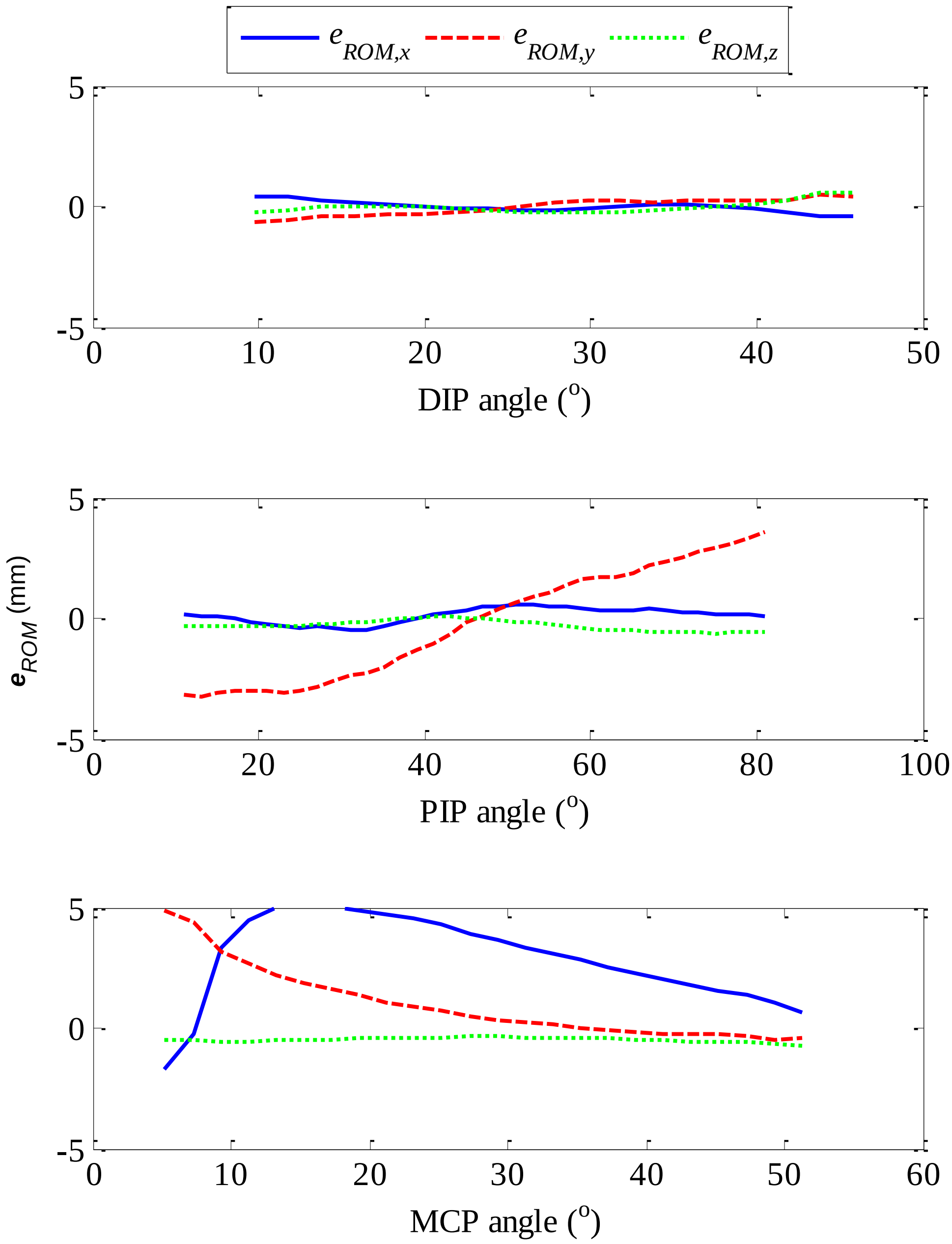

Figure 6.10: ***e***$_{ROM}$ *from multiple arc analysis for a single subject at all joints with a magnitude |φ| = 30°. Each plot represents the* ***e***$_{ROM}$ *changing with centre of calibration arc for a given joint.*

In more detailed analysis of the profiles and considering only the interphalangeal joints, similar trends were observed between each joint with the $\boldsymbol{e}_{ROM,x}$ decreasing, $\boldsymbol{e}_{ROM,y}$ increasing and $\boldsymbol{e}_{ROM,z}$ remaining relatively constant. Assuming a linear relationship, coefficients could be calculated to transform from the average AoR to the IAoR presented in Table 6.3 for all 13 subjects. These transformations were calculated in the relevant segment ACS. In general as the joint angle increased the IAoR moved along the proximally directed axis in a positive direction (increasing $e_{ROM,y}$) and along the palmerly directed axis in a negative direction (decreasing $e_{ROM,x}$) i.e. it moved proximally and dorsally with increased flexion. This is visualised in Figure 6.11.

Subject	Transformation coefficients $\boldsymbol{c}_{ROM}$ (mm/°)					
	DIP			PIP		
	$c_{ROM,x}$	$c_{ROM,y}$	$c_{ROM,z}$	$c_{ROM,x}$	$c_{ROM,y}$	$c_{ROM,z}$
1	-0.02	0.03	0.01	0.01	0.11	-0.01
2	-0.04	-0.03	0.01	0.02	0.04	0.00
3	-0.04	0.01	0.01	0.01	0.08	0.01
4	-0.05	-0.01	-0.02	0.00	0.09	0.01
5	0.00	0.04	0.00	0.01	0.07	0.00
6	-0.06	0.03	-0.01	0.02	0.06	0.01
7	0.01	0.01	-0.01	-0.04	0.06	0.00
8	0.02	0.02	-0.01	-0.01	0.08	0.00
9	-0.07	-0.01	0.00	-0.02	0.11	0.01
10	-0.01	-0.02	0.00	-0.03	0.00	0.00
11	-0.02	0.03	0.03	-0.01	0.07	0.00
12	-0.04	-0.01	-0.01	-0.02	0.03	0.01
13	0.05	0.08	-0.02	0.03	0.10	-0.03

Table 6.3: *Coefficients to transform between the average and instantaneous axis of rotation of the interphalangeal joints for each subject.*

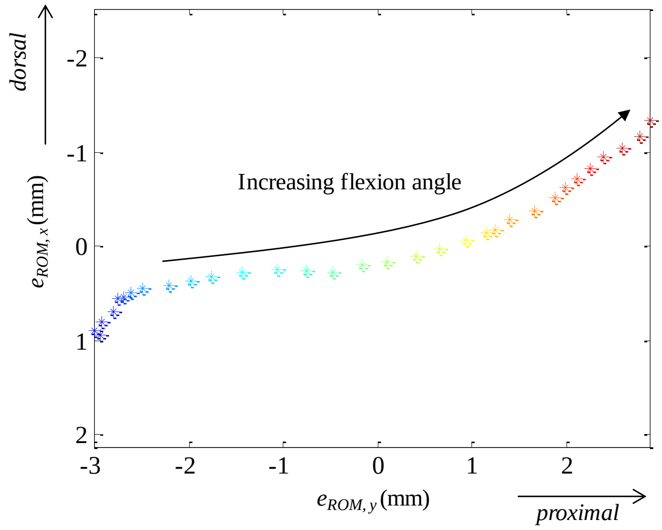

Figure 6.11: *Visualisation of the change in position of the IAoR with flexion angle in the sagittal plane.*

6.3 Discussion

The influence of calibration RoM on accurately predicting the position of each ACS was important in assessing the applicability of the proposed marker set and PTT. This is of particular relevance to those with an injury or pathology that may reduce the RoM they have in the fingers.

6.3.1 Reduced arc analysis

From the reduced arc analysis at the interphalangeal joint, all reduction types resulted in similar shaped $||\boldsymbol{e}_{PTT}||$, $||\boldsymbol{e}_{ROM}||$ and $||\boldsymbol{e}_{total}||$ profiles, although with different magnitudes.

Assuming any instrumentation errors and those resulting from joint kinematics were equal between reduction types, any difference in $||\boldsymbol{e}_{PTT}||$ would indicate a difference in skin movement artefact. Therefore, examination of the $||\boldsymbol{e}_{PTT}||$ profiles allowed a quantification of the skin movement artefact. The most skin movement artefact occurred when the joints were highly flexed, due to the skin being stretched across the dorsal side of the joint. This agreed with what was observed in Figure 6.3, with the largest $||\boldsymbol{e}_{PTT}||$ observed with Type II reduction i.e. when the joint tended towards full flexion. From examination of $||\boldsymbol{e}_{PTT}||$ for the Type I and Type III reductions it can be concluded that there was little difference in skin artefact between them.

$\boldsymbol{e}_{ROM}$ provided a measure of the displacement between the joint centre calculated using the full RoM and that calculated using the reduced arc. It can be assumed that this displacement would be largest at the extremes of the RoM because that calculated from the full RoM would lie approximately in the middle of all calculated centres. This could be observed in the magnitude of $||\boldsymbol{e}_{ROM}||$ in Figure 6.4, with the smallest error observed for the Type III restriction.

The profiles of $||\boldsymbol{e}_{total}||$ more closely followed the profiles of $||\boldsymbol{e}_{ROM}||$ rather than $||\boldsymbol{e}_{PTT}||$. This was because the magnitude of $||\boldsymbol{e}_{ROM}||$ was in general larger than $||\boldsymbol{e}_{PTT}||$.

Now considering the MCP joint, the results and conclusions were different than at the interphalangeal joints. $||\boldsymbol{e}_{PTT}||$ provided a measure of skin movement artefact as it did for the interphalangeal joints. This time however the largest magnitude was observed when applying the Type I reduction. As this joint could extend more than the interphalangeal joints there was more skin movement artefact at full extension as the skin wrinkled on the dorsal surface i.e. largest error with Type I reduction.

When considering $||\boldsymbol{e}_{ROM}||$ it would have been expected that the least error would occur with the Type III reduction. This was not the case however and the smallest magnitude was observed for the Type II reduction. As with the interphalangeal joints the greater magnitude of this type of error was reflected in the $||\boldsymbol{e}_{total}||$ profiles. With the current assumption of a CoR at this joint, these error patterns cannot be explained. The limitations of the CoR model become apparent when analysing the errors in this level of detail. This is discussed further in Section 6.3.2 when analysing the results of the multiple arc analysis.

These results showed that the specific RoM available for calibration (φ_I, φ_{II}, and φ_{III}) will have an effect on the results, not just the magnitude of RoM. These specifics must be considered, particularly if the subject is restricted to a RoM with the fingers in a flexed position.

$||\boldsymbol{e}_{ROM}||$ had the greatest effect on $||\boldsymbol{e}_{total}||$ and this error was in general largest at the two extremes of motion (at least at the interphalangeal joints). Therefore, for further analyses, the mean of $||\boldsymbol{e}_{total}||$ for the Type I and II reductions was taken.

Considering the interphalangeal joints, this mean $||\boldsymbol{e}_{total}||$ at the DIP joint was less than at the PIP joint. This can be understood by considering the marker set used. Markers P1 and P2 were attached directly to the finger nail and P3 was attached 2mm proximal to it (Figure 5.1). Due to the rigidity of the nail, these attachment locations had a small amount of skin movement artefact and subsequently a reduced $||\boldsymbol{e}_{total}||$.

In comparison with the numerical simulations (Ehrig et al., 2007; Ehrig et al., 2006), at the DIP joint $||\boldsymbol{e}_{total}||$ had a similar profile although with a reduced magnitude. As has been discussed previously, the skin artefact at the DIP joint was minimal due to the marker locations. Although the magnitude of $||\boldsymbol{e}_{total}||$ was similar to the numerical study at the PIP joint the profiles differed. As noted previously the error profile will change depending on which arc of motion was used. The numerical simulations used a Gaussian distribution for the errors from measurement inaccuracy and skin artefact, rather than one that considered the degree of flexion. This could account for the difference between this study and the numerical simulation.

$||\boldsymbol{e}_{total}||$ was calculated as a displacement, however to make this work of clinical relevance it was important to understand how these displacements would affect the outputs of biomechanical models. Therefore the effect on the mean JRF was examined.

To give an indication of this technique's applicability to an arthritic patient, the typical ranges of motion of a rheumatoid subject were applied (Goodson et al., 2007) to all the joints simultaneously. This was done as it was expected that a subject would have reduced RoM at more than one joint. Because many of the tendons cross multiple joints, e_{JRF} was influenced simultaneously by errors at more than one joint. An error at one joint could have an opposite effect on e_{JRF} than at another joint. The results indicated that e_{JRF} was typically <7%. This was compared with <4% error found when the subject had a full RoM. Considering the other errors inherent in the models (discussed in Chapter 3), this was deemed an acceptable margin of error.

6.3.2 Multiple arc analysis

Multiple arc analysis determined how the IAoR and ICoR changed with joint angle and additionally provided a further assessment of how the skin movement artefact changed with degree of flexion.

From analysis of $||\boldsymbol{e}_{PTT}||$ in Figure 6.8, similar patterns of skin movement artefact were observed as with the reduced arc analysis. This pattern was an increase in $||\boldsymbol{e}_{PTT}||$ at the interphalangeal joints with flexion angle, with a greater magnitude at the PIP joint. At the MCP joint, $||\boldsymbol{e}_{PTT}||$ was relatively constant throughout both flexion and abduction. The reduced arc analysis indicated that there would be an increase in $||\boldsymbol{e}_{PTT}||$ as the joint was extended, but this was not clear with this multiple arc analysis. As is discussed later the multiple arc analysis was not valid for the current method of determining the MCP joint functional axis. Therefore a lack of correlation between analyses was not unexpected.

Discussed in Section 6.3.1, $\boldsymbol{e}_{ROM}$ represented the displacement between the joint centre calculated using the full RoM and those centres calculated using each $|\varphi|$. Using this relationship the validity criterion was established as per equation (6.5). Using this criterion the multiple arc analysis was only valid at the interphalangeal joints and not at the MCP joint. The results of the reduced arc analysis also indicated that the errors at the MCP joint did not behave as expected. This suggested that the assumption of a functional CoR at the MCP joint was not strictly true. As it was in reality a two degree of freedom joint, modelling it with two AoR would perhaps have given more accurate results. It would certainly warrant further research to model this joint differently. These compromises only became apparent when examining the errors in this level of detail and therefore further development of this joint model was deemed outside the scope of the study.

The interphalangeal joints predominantly flexed in the saggital plane and the normal to this was the radially directed *z-axis*. The change in IAoR was expected to be principally within this saggital plane, therefore the component $\boldsymbol{e}_{ROM,z}$ was expected to be minimal as observed in Figure 6.10 and Table 6.3. Although the transformation coefficients were unique for every subject and cannot be averaged across subjects, a general trend was observed across subjects. This showed $\boldsymbol{e}_{ROM,x}$ decreasing and $\boldsymbol{e}_{ROM,y}$ increasing as the flexion angle increased. In terms of anatomical axes, this meant the position of the IAoR moved proximally and dorsally as the joints were flexed.

At either interphalangeal joint the radius of the distal phalanx joint surface is larger than the proximal surface. In addition the cam profile of the proximal articular surface means an increase in radius of the joint contact surface as the joint was flexed. The resulting rolling and sliding motion resulted in the non-constant AoR. The results of this study predict how this IAoR will change with joint flexion. It should be noted however that the magnitude of this change in IAoR is very high (>5mm for the PIP joint). Measurement inaccuracies and deformation of the CTFs could be the cause of this. It is likely that more accurate results could be obtained using rod clusters of the style described by Fowler and Nicol (1999). As explained at the start of the previous chapter, it was a requirement that there be as little restriction on the subject as possible hence the use of the surface mounted hemispherical markers in my study.

6.4 Conclusions

The standard deviation in the mean JRF was 0.5 (Section 3.3.2), therefore an acceptable level of accuracy would be if errors are kept within this boundary. It has been shown therefore, the proposed marker set and PTT will provide acceptable definition of the functional joint centres and ACSs, even when the subject has a significantly reduced RoM at one or more joints. The position of the IAoR of the interphalangeal joints as a function of flexion angle has also been predicted and shown to move proximally and dorsally with joint flexion.

The assumption of a CoR at the MCP joint was shown to be flawed when the errors were analysed in detail. This does not mean it cannot be used however, as errors were deemed to still remain within acceptable limits. It would be interesting however to conduct further analyses using different kinematic models of this joint.

Chapter 7. Measurement of tendon and muscle moments

At any articulating joint in the human body there will be tendons, ligaments or muscles that apply forces and moments across it. Ligaments can apply a passive force only i.e. they are not attached to muscles and instead apply a force proportional to strain due to their elasticity. These provide stabilising forces and constrain the kinematics of the joint. Direct reference to ligaments is often excluded from biomechanical models, instead the joint constraints and kinematics are defined in such as way as to include their influence. For this reason only the measurement of moment arms and lines of action for muscles and tendons are considered in this chapter.

The parameter ultimately used in biomechanical models is what is referred to in this thesis as the unit-force moment (see Section 2.3.2). Depending on the method of measurement it may only be the moment arm of a muscle or tendon that is measured. This is the case for excursion methods (Section 7.1.2) where it is assumed that the moment acts purely around the axis of rotation of the joint. In this case it is not possible to measure the line of action and it is assumed to be perpendicular to the joint axis.

Accurate measurement of the anatomy is important in being able to calculate the forces and moments applied by the muscles and tendons. As was demonstrated in Chapter 3, models can be sensitive to any variation in moment arm particularly in highly loaded elements. This chapter will review the current methods available for measuring these anatomical parameters. Their advantages and disadvantages will be discussed as well as suggestions for further research which leads onto the work covered in Chapter 8.

7.1 Methods of determining moment arms and lines of action

Methods of determining the moment arms and/or lines of action of muscles and tendons can be divided into four categories (Masjedi, 2009); geometric methods, excursion methods, direct load methods and origin insertion methods. All rely on some form of direct anatomical measurement, whether that is from a previously published dataset or directly in a subject specific case.

7.1.1 Geometric (measurement relative to joint centre)

Geometric methods are based on the principle of identifying the moment arm and line of action relative the joint axes. Once these two parameters are defined the unit-force moment can be calculated. This method relies on medical imaging such as X-Ray, computed tomography (CT), magnetic resonance imaging (MRI) or ultrasonography.

It is common to use MRI to measure the moment arms and lines of action as demonstrated by Rugg et al (1990) for measurement of the Achilles and tibialis anterior tendons of the lower limb. In this case the centre of rotation (CoR) of the ankle joint was determined using the two dimensional (2D) Reuleaux method (Reuleaux, 1876), where at least two scans need to be made with different degrees of ankle flexion. This method has been used for subsequent studies of the Achilles tendon moment arm (Figure 7.1) (Fath et al., 2010; Maganaris et al., 2000; Maganaris et al., 1998) and also for the tendons of the hand (Wilson et al., 1999). A problem associated with the use of MRI is the amount of time it takes to scan a subject (Blemker et al., 2007), making it difficult to image subjects under loaded or dynamic conditions. By only scanning in 2D however, fast scan times can be achieved such as the 2 second scan used by Maganaris et al (1998). This gives the potential to measure the moment arms under load which is known to have an effect on their magnitude (Maganaris et al., 2000).

Figure 7.1: *Measurement of the Achilles tendon moment arm relative to the geometric joint centre using MRI. Adapted from Maganris et al (2000).*

Magnanaris et al (2000) compared their geometric method using MRI with a tendon excursion method using ultrasonography (discussed in Section 7.1.2). They highlighted the issue of assuming a planar motion of the ankle joint. The joint CoR can be misplaced both through this assumption and also if the CoR does not align with the scan plane. A similar study was carried out by Fath et al (2010) comparing a geometric method using MRI and an excursion method using ultrasound to measure moment arms of the Achilles tendon. They found similar results to Maganaris et al (2000) with up to 25% larger moment arms when using a geometric method compared to the excursion. Although the limitations of the geometric method were recognised, most of this discrepancy was attributed to contraction of the tendon during flexion. This is known to affect the results of the excursion experiments.

There have been studies to measure the muscle and tendon moment arms of the fingers using geometric MRI methods (Fowler et al., 2001; Kier and Wells., 1999; Wilson et al., 1999).

Wilson et al (1999) compared both a 2D and three dimensional (3D) geometric method with a tendon excursion method. These all used parameters measured from MRI and only for the flexor digitorum profundus (FDP) across the third metacarpo-phalangeal (MCP) joint. For the 3D geometric method the CoR was found functionally using helical axes. The 2D geometric method used the method of Reuleaux. They found much greater variation in the moment arms when using the 2D method compared to the 3D, explained by increased variation in the definition of the CoR. The scan times necessary for the 3D geometric method were as long as 9.5 minutes. This made it difficult for the subject to maintain a completely still hand for the duration.

Fowler et al (2001) used a 3D geometric technique to measure the moment arms of all the muscles and tendons of the index finger crossing the distal interphalangeal (DIP), proximal interphalangeal (PIP) and MCP joints (Figure 7.2). 3D MRI was used, with the bones, muscles and tendons manually digitised in each image slice. In this case each joint CoR was defined geometrically using the curvature of the articulating joint surfaces. The authors made the assumption that there was sliding only at the joints (although they acknowledged that this may not actually have been the case) and the CoR will therefore lie at the centre of curvature. Measurements were taken from a single subject over a range of joint angles. The aim of this study was to show proof of concept for a technique of measuring subject specific inputs to a biomechanical model, hence measuring every muscle/tendon of the index finger. Although these data were not intended to be used as a reference set of moment arms and lines of action they do compare well with previous excursion studies by An et al (1983) and origin/insertion methods by An et al (1979). Kier et al (1999) used similar methods, but only examined the tendons in the carpal tunnel.

Although MRI has the advantage of generating 3D images non-invasively it is not without its drawbacks. There is a large cost commitment associated with imaging a subject (Wilson et al., 1999). Due to the long scan times, the subject must be able to remain motionless for the entire scan time. This can exclude subjects with tremors or other movement disorders which may prevent this. It also makes measurement under loaded conditions difficult.

Figure 7.2: *MRI used by Fowler et al (2001) to measure the position of finger tendons relative to the geometric joint centres to give moment arms and lines of action.*

Another factor that is hardly mentioned in papers using MRI is the difficulty in imaging tendon and bone. MRI measures the time it takes for water molecules to re-align after a magnetic field is applied. The proximity of larger protons will affect this relaxation time (T2 relaxation time), hence how an image is created. Conventional MRI is only able to detect a signal from protons that have a T2 relaxation time in excess of 10ms (Benjamin et al., 2008; Robson et al., 2004; Henkelman et al., 2001). This means that signals from tissues with these short relaxation times will not be detected as the signal will have decayed before the MRI system can switch to its receiving mode (Tyler et al., 2007). The type of tissues that typically has a majority of short T2 components includes tendons and bone (Gatehouse and Bydder, 2003). These tissues will have either a very low or no signal and appear as dark spaces on a scan (Tyler et al., 2007; Robson and Bydder, 2006; Gatehouse and Bydder, 2003). This can have a clinical benefit as it can provide a consistent background against which abnormalities that increase T2 relaxation time can be identified. However for the identification of bone, tendon and ligament locations useful for the construction of a biomechanical model, this inability to be able to clearly identify the tissues is a major drawback (Blemker et al., 2007).

The signal from collagen has a direction dependence on the term ($3cos^2\theta$ - 1) with θ being the orientation of the fibres in the magnetic field (Gatehouse and Bydder, 2003). Therefore a maximum value will be reached when $\theta \approx 55°$, also known as the 'magic angle'. At this angle it is possible to obtain increased signal from tendons. Although it is possible to use this procedure using standard pulse sequences its applicability is limited due to the need for orientation of the fibres to be very specific. For example in the flexed digits of the hand, it would be impossible to orientate the fibres of all tendons at this angle simultaneously.

Another method of imaging tissues with a short T2 relaxation time is by using ultra-short echo time (UTE) pulse sequences. This technique enables very short echo times to be obtained in the region of 50-250μs (Gatehouse and Bydder, 2003). This is up to 200 times shorter than conventional sequences. These techniques have successfully been used for examination of cartilage (Gold et al., 1998), Achilles tendon (Robson et al., 2004; Gatehouse and Bydder, 2003; Gold et al., 2001) and tissue attachment points (Benjamin et al., 2008). These studies have mainly been focused on the detection of abnormality in the tissues. However they have enabled a clearer view of the short T2 tissues, allowing their location to be much more clearly established compared to more conventional methods. This could potentially allow for much more reliable subject specific biomechanical models to be produced with a better knowledge of bone, tendon and ligament location.

Of the available non-invasive, non-harmful imaging techniques, B-mode ultrasonography can provide clear imaging of tendon and muscle (Fry et al., 2004). Additionally its low cost and ability to provide real-time images makes it a useful tool. For measurement of muscle and tendon moment arms it has predominantly been used in the excursion method (Fath et al., 2010; Ito et al., 2000; Maganaris et al., 2000). One study has used B-mode ultrasonogrpahy to measure the moment arms and lines of action using the geometric method for measurement of the Achilles tendon (Manal et al., 2010). Their study used a combination of ultrasound and stereo-photogrammetry to measure the tendon line of action relative to the ankle CoR (Figure 7.3). Markers placed on the medial and lateral malleoli were used to identify the CoR relative to these external landmarks. Markers were also placed on the probe head to track its position in the same reference frame. The centre line (line of action) of the tendon could them be digitised in the ultrasound image and transformed into the same coordinate system as the CoR and hence the moment arm calculated. There are areas of their study that could be improved however. Firstly, the methods of defining the ankle CoR is susceptible to error. Because the markers are placed directly on anatomical landmarks, the position of the CoR is susceptible to greater skin movement artefact, repeatability issues and assumptions about where the CoR lies relative to these external landmarks. It would be more accurate to use marker cluster technical frames and investigate the possibility of defining the CoR functionally to reduce these errors. Only two markers were used to locate the probe in the photogrammetric frame. It is not clear therefore how the orientation of the probe could be defined without making assumptions about how it was held by the investigator. Assumptions were made about how the scan plane was positioned and orientated relative to the probe body, this cannot be assumed and an additional calibration should have been carried out (Prager et al., 1998). Despite the compromises in this specific experiment, this method has the advantage of being able to measure the instantaneous moment arms as no range of joint flexion is needed. This gives the potential to measure the moment arms under dynamic and loaded conditions which are known to have an effect (Blemker et al., 2007; Tsaopoulos et al., 2006; Maganaris, 2004; Maganaris et al., 2000; Keir and Wells, 1999). The cost involved is also significantly less than using MRI techniques.

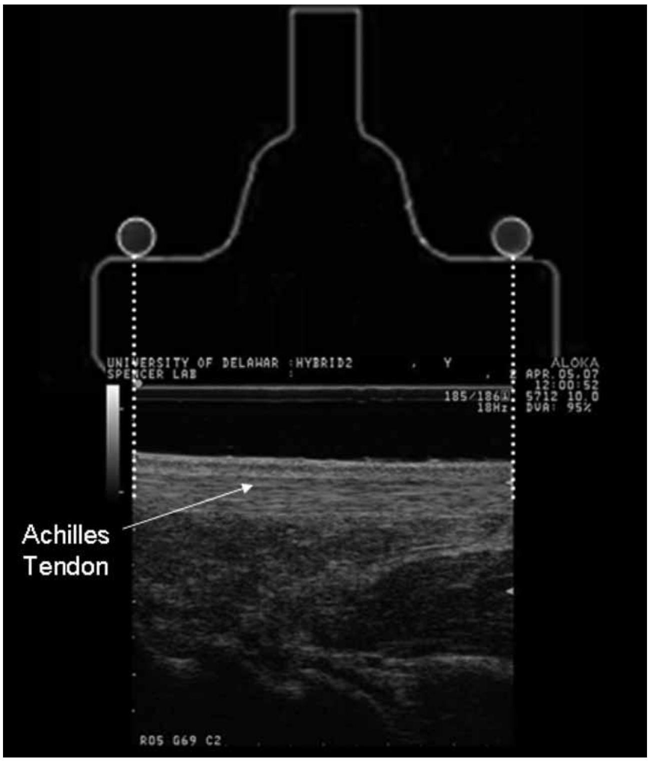

Figure 7.3: *Ultrasound image of the Achilles tendon in the sagittal plane used by Manal et al (2010). The tendon position is measured in the ultrasound image frame and combined with the joint centre measured in the stereo-photogrammetric frame to calculate the moment arm.*

7.1.2 Excursion

The excursion method is based on the principle that the moment arm can be derived from measurement of the change in joint angle with excursion (displacement) of the tendon (Landsmeer, 1961). Using the principle of virtual work the moment arm (***M***) can be expressed as:

$$\boldsymbol{M} = \frac{dx}{d\varphi} \tag{7.1}$$

where x is the tendon displacement and φ is the joint angle. Excursion methods assume that the actuator acts perpendicular to the joint, therefore the unit-force moment is identical to the moment arm.

Excursion methods have the advantage over geometric and origin insertion methods in that they do not require the position of the CoR to be known. They do require the assumption of planar motion at the joint however (Tsaopoulos et al., 2006), which can introduce errors for joints with more complex kinematics. A range of motion is required to be able to measure the moment arm in this way. There are a number of ways of measuring both the excursions and joint angles. As with the geometric methods, medical imaging such as MRI and ultrasound have been used to measure these parameters (Fath et al., 2010; Ito et al., 2000; Maganaris et al., 2000; Wilson et al., 1999). Invasive procedures on cadavers have also been used to measure the moment arms of the finger muscles and tendons (Franko et al., 2011; Buford et al., 2005; An et al., 1983) as shown in Figure 7.4.

Wilson et al (1999) measured the excursion of the FDP tendon crossing the third MCP joint using MRI. Two bony landmarks were identified on either side of the joint and the tendon length between them calculated. This was repeated with the joint at a different degree of flexion to give the excursion. It is not clear how the joint angle was measured. This method relies on accurate identification of the bony landmarks in each image as well as accurate measurement of the joint angle. Despite this, the authors found the results to be very repeatable in comparison with 2D and 3D geometric methods. Interestingly Wilson et al (1999) found the opposite to the studies of Maganaris et al (2000) and Fath et al (2010). In these cases the excursion method gave larger moment arms than the geometric methods. This was assumed to be due to the averaging of the moment arm across a range of joint angles for the excursion method.

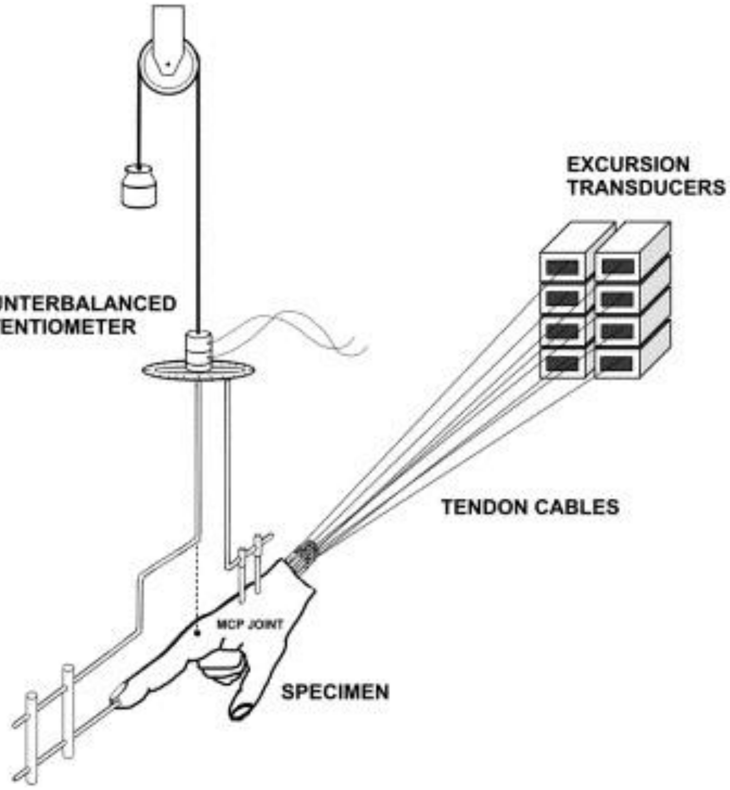

Figure 7.4: *Tendon excursion on a cadaver specimen. The tendons are connected to cables attached to a transducer capable of measuring excursion. In this way as the joints are flexed excursion is measured. Adapted from Buford et al (2005).*

Maganaris et al (2000) used ultrasound to measure the excursion of the tibialis anterior muscle/tendon and compared this with a geometric method. The excursion was not measured directly in the tendon, instead the pennation angle at the muscle/tendon boundary was measured and the excursion calculated from this. With the muscle at rest there was little difference between the geometric and excursion methods. At maximum voluntary contraction however the two methods differed. The geometric method recorded an increase in moment arm, which is what would be expected as the tendon pulls away from the joint. The excursion method produces very similar results to the ‘at rest’ case, likely due to stretching of the tendon. The excursion method is based on the principle of virtual work and therefore any stretching of the tendon will invalidate it, leading the author to conclude that it is not applicable to tendons in a loaded condition.

Ito et al (2000) also measured the moment arm of the tibialis anterior. They attempted to counter the problem produced by tendon stretch by ensuring that the subject was applying the same amount of force through the different joint angles. Their results were comparable with Maganaris et al (2000) and Fath et al (2010) with the loaded conditions yielding higher moment arms than the at rest condition.

Fath et al (2010 measured the displacement of the muscle/tendon junction directly. This was used to measure the moment arm of the Achilles tendon and compared with a geometric method. Results were similar to Maganaris et al (2000) with the geometric method yielding higher moment arms than excursion.

To date the methods of excursion for measurement of moment arms examined either pennation angle or the location of the muscle tendon junction. Recently methods have been developed to measure the excursion of the FDP at wrist level (Korstanje et al., 2010a). This used an automated speckle tracking technique that automated the process of measuring tendon excursion (Korstanje et al., 2010b). The use of an automated system can reduce repeatability error and the authors' suggested an error of only 1.3%. Also no anatomical landmarks need to be identified to measure relative displacement. As with the previous excursion studies, the results suggested larger excursions (i.e. larger moment arms) occurred when the tendon was loaded.

An et al (1983) carried out a study using seven cadaveric hands to measure moment arms of the index finger. The same principle of virtual work used was used. To measure the tendon displacement the dissected hand was placed in a rig capable of measuring the joint angles and tendon displacements using potentiometers. The ability to measure in a controlled environment made it possible to reduce experimental errors and the authors proposed a correlation between joint thickness and tendon moment arms. The study by Burford et al (2005) used similar techniques, this time looking only at the moment arms crossing the MCP joint. To achieve this, the interphalangeal joints were fixed at 0° flexion. The authors were able to measure how the moment arm changed with joint angle, unlike other excursion studies that presented only averaged data. Because the moment arm is known to change with the degree of flexion this is an important consideration. Franko et al (2011) again used cadavers to examine only the digital flexors. This was done across all joints of all five digits. Regression equations were calculated to relate moment arms to joint angle.

The use of cadaver specimens does have its drawbacks. The load on the tendon is known to have an effect on the moment arm, and this is difficult to simulate in a laboratory environment. Assumptions also have to be made about how the data can be scaled from subject to subject, which may not necessarily be valid (Bisi et al., 2011; Ito et al., 2000). This is of particular relevance to subjects that may have anatomy significantly different from any cadaver study, such as children or those with pathology and deformities.

7.1.3 Origin-insertion

The origin-insertion method is based on the principle that the muscle or tendon will take the most direct path between two specified attachments points. In the case of it being under tension this can be thought of as a taught string and the moment arms and line of action can be calculated relative to the axes of rotation. In some cases it may be more representative to use via points and wrapping surfaces to better represent the path of a particular muscle or tendon (Marsden and Swailes, 2008). These can be visualised as shown in Figure 7.5. In principle all origin-insertion methods can be classed as modelling techniques as they do not measure the moment arms directly, instead making assumptions about via points and wrapping surfaces. Some are quite simple such as that proposed for the fingers by An et al (1979). Others are more complex and use measurements of human anatomy to build models using software such as AnyBody and SIMM (Scheys et al., 2008; Blemker et al., 2007; Arnold et al., 2000). These software tools are designed to produce subject specific models. They can be used by scaling existing models based on cadaveric studies, or subject specific models can be built using medical imaging such as MRI as shown in Figure 7.6 (Blemker et al., 2007). It has been shown that using subject specific models based on MRI can result in significantly different moment arms than those based on anthropometric scaling (Scheys et al., 2008). This provides an argument for the use of subject specific modelling using MRI, but as with all the other techniques described, MRI is not without its drawbacks as discussed previously.

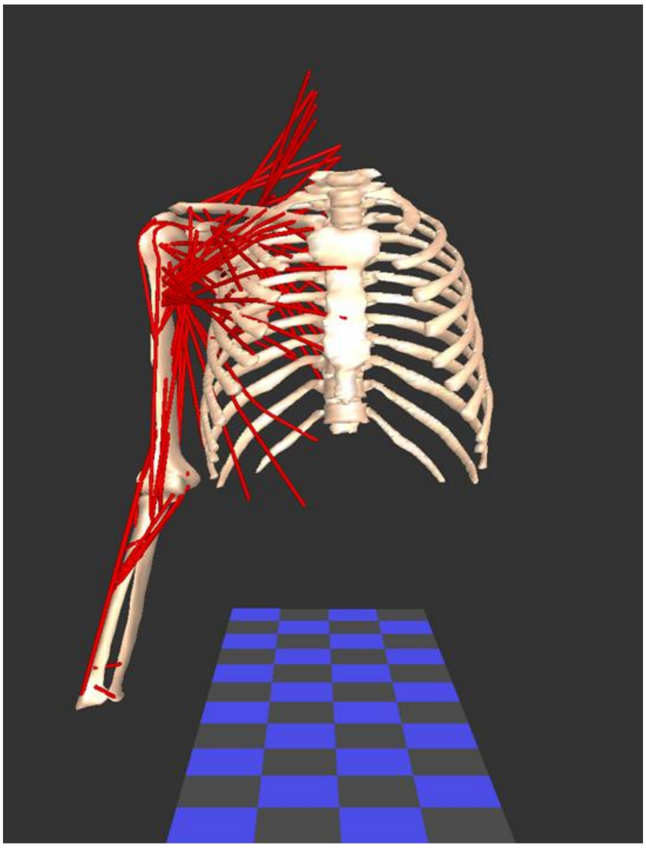

Figure 7.5: *Muscles and tendons of the shoulder represented by their lines action calculated from their origin points, insertion points and wrapping objects.*

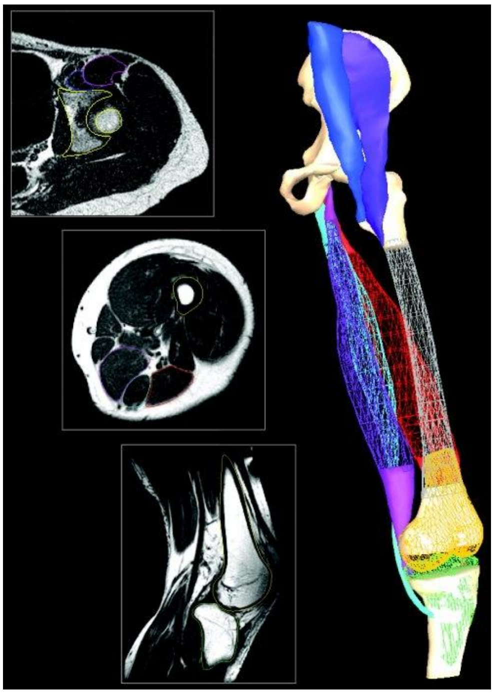

Figure 7.6: *Using MRI to build a subject specific anatomical model. Adapted from Blemker et al (2007).*

An et al (1979) studied ten cadavers to produce a dataset of all the muscles and tendons of the right hand. The data are presented for the hand in a neutral position, therefore rigid body transformations need to be carried out to calculate the moment arms at different degrees of flexion. These data have formed the basis of subsequent modelling analyses of the fingers (Vigouroux et al., 2006), and have been used in assessing more complex models including wrapping surfaces (Wu et al., 2010). The effect of including wrapping surfaces compared to via points has been examining in relation to the hand (Kociolek and Keir, 2011). This study, along with that of Wu et al (2010), highlighted the issues of using both wrapping and via point techniques. Particularly at the extreme ranges of motion, there can be large and unrealistic changes in moment arms. This was also noted in Chapter 3. This is a limitation to using such methods in application to the hand.

7.1.4 Direct load

Direct load methods use the principle of moment equilibrium across a joint to calculate the moment arm. Assuming a single degree of freedom and planar motion at a given joint, equation (2.3) can be simplified to:

$$M = Tr, \qquad \textbf{(7.2)}$$

where M is the magnitude of the resultant moment and r is the moment arm in the joint plane and T is the magnitude of the applied force. If the tension and moment can be measured then it is a simple case of calculating the moment arm from this equation. It is only possible however to measure these parameters on cadaveric specimens (Figure 7.7), as has been carried out for the fingers (Lee et al., 2008; Buford et al., 2005). In both these studies the finger tip was attached to a load cell whilst tension was applied to the flexor tendons via a set of weights. This technique has the advantage that it gives an instantaneous value for the moment arm without the need for multiple joint angles to be measured. Also no knowledge of the joint axes of rotation is needed, but it relies on several assumptions. The first, that there is no friction in the system that would affect the tension required. This is not strictly true for the finger flexors as there is known to be a varying degree of friction present as the tendon slides through the pulley mechanism (Schweizer et al., 2003). The second is that this method can only be conducted on cadaver specimens.

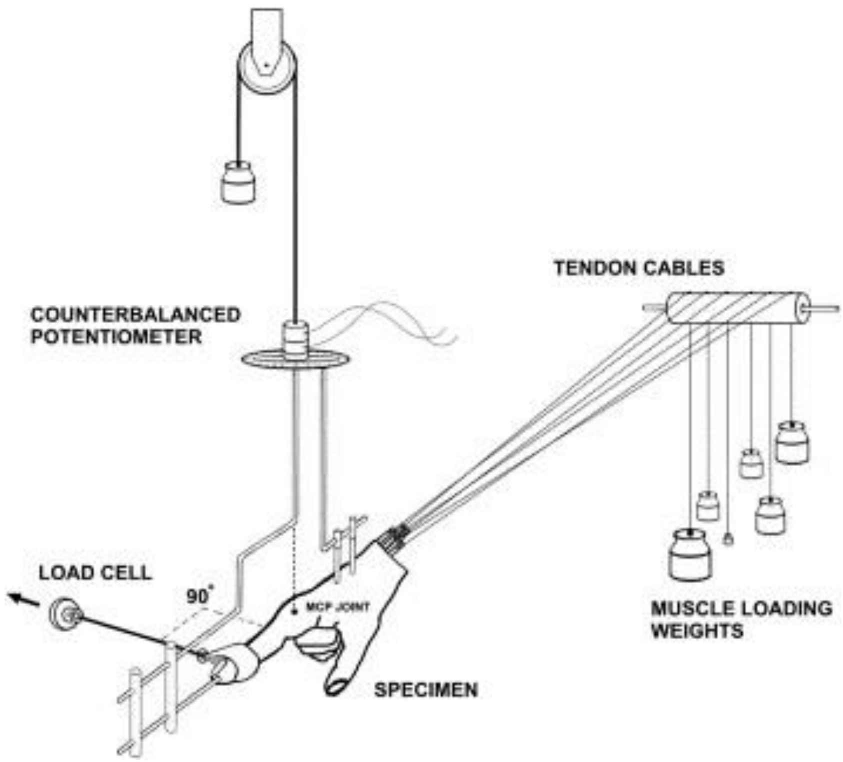

Figure 7.7: *Use of direct load to measure moment arms. The tendons are connected to known loads using wires and the force at the finger tip measured. Adapted from Buford et al (2005).*

7.2 Existing finger moment arms data comparison

As has been discussed in Chapter 3, the measurement of the anatomical parameters is of great importance in obtaining accurate predictions from a biomechanical model. For the grip type examined in Chapter 3, it was found that the most highly loaded tendon was the most sensitive to any changes in the measurement of the moment arm. In this case it was the FDP tendon. As described in the previous sections several papers have proposed methods or provided datasets for calculating the moment arm of this tendon. A scaling factor has to be defined to provide comparison between studies. It has been proposed to scale to either joint thickness (An et al., 1983) or middle phalanx length (Wu et al., 2010). For the purpose of this thesis the middle phalanx length has been used as the scaling factor. This is because it can be measured using the kinematic analysis techniques described in Chapter 5, unlike joint thickness which relies on a direct anatomical measurement. For this scaling to be possible the appropriate anthropometric measures must be available. For this reason only the papers by An et al (1979), An et al (1983), Fowler et al (2001), Wu et al (2010) and Kociolek and Keir (2011) could be compared. Kociolek and Keir (2011) proposed a method using both control points (CP) similar to An et al (1979) and a method incorporating joint wrapping (JW) surfaces. The moment arms for the FDP crossing the DIP, PIP and MCP joints is presented in Figure 7.8, Figure 7.9 and Figure 7.10. The moment arms acted about the axes of the anatomical coordinate systems (ACSs) described in Chapter 3 and shown in Figure 3.1. For the coordinate system chosen this means that flexion/extension is about the *z-axis* (flexion positive), adduction/abduction about the *x-axis* (adduction positive) and pronaton/supination about the *y-axis* (pronation positive). Thus for the finger tendons, a moment arm with a positive x component will produce a flexion moment, and with a positive z component it will produce an abduction moment. It was possible to calculate the moment arm about all three axes at all three joints using the data from An et al (1979) and Fowler et al (2001). The other studies presented only the moment arms about the flexion/extension axis (and the adduction/abduction axis at the MCP joint from An et al (1983)).

Considering the flexion moment arm of the FDP crossing all the joints, the largest difference was observed at the larger degrees of flexion. This is particularly evident at the PIP joint where beyond 90° of flexion the moment arms of An et al (1979), Fowler et al (2001) and Kociolek and Kier (2011) dropped off. Kociolek and Kier (2011) and

An et al (1979) both use CP methods. As highlighted previously this can lead to unrealistic moment arms at the extremes of flexion angle. This was due to the more distal of the two CPs from which the line of action and moment arm were calculated moving closer to the proximal one, until it became more proximal. This resulted in the flipping of the moment arm so it actually became an extension moment arm as observed at the PIP joint in Figure 3.12. In the case of Fowler et al (2001), the abnormal moment arms resulted from interpolation of the data from the static poses measured in their study.

An important point to consider is the large variation in moment arm as measured between studies. Even disregarding the anomalies encountered at high degrees of flexion there is still a range of 0.04, 0.19 and 0.26 x middle phalanx length in the flexion moment arm at the DIP, PIP and MCP joints respectively in a neutral pose. Considering the results found in Chapter 3 and shown in Figure 3.12 this can change the predicted internal loading by over 100%.

These results indicate that there is still much room for improvement in the measurement of the moment arms of the highly loading tendons of the fingers. The work done to address this is described in Chapter 8.

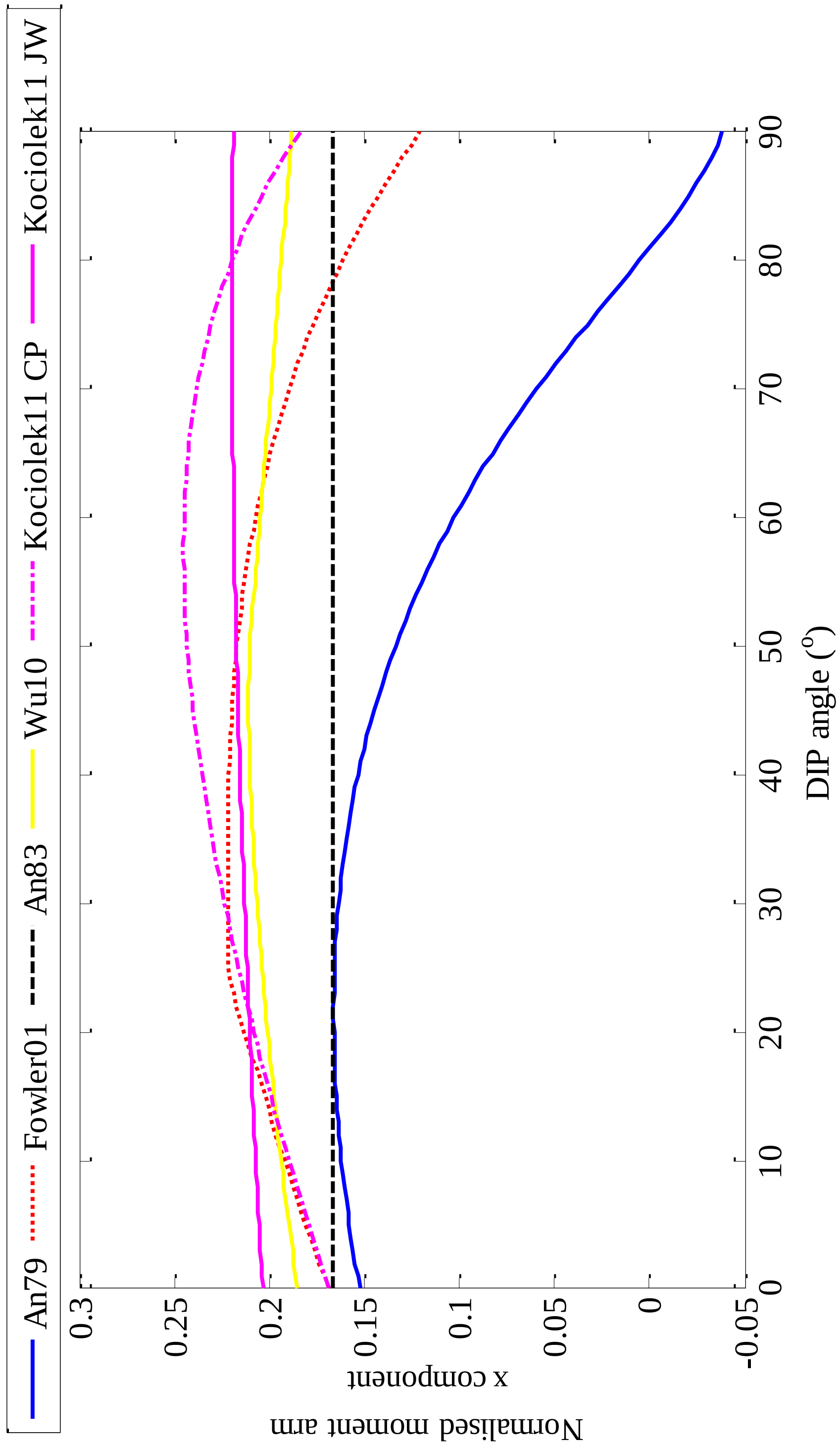

Figure 7.8: *Moment arms of the FDP tendon crossing the DIP joint expressed as a fraction of middle phalanx length. As measured and calculated by An et al (1979), Fowler et al (2001), An et al (1983), Wu et al (2010) and Kociolek and Keir (2011).*

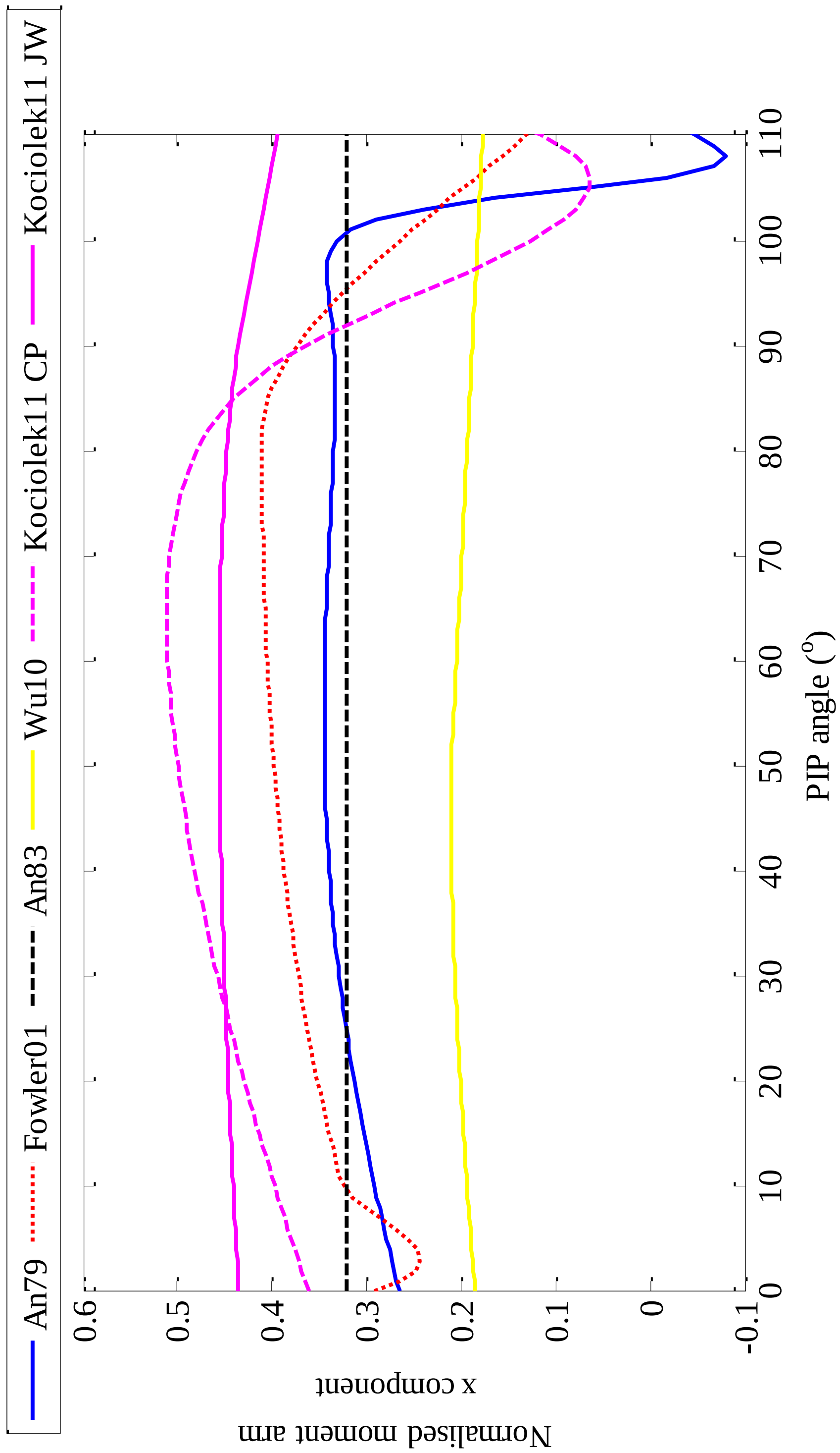

Figure 7.9: *Moment arms of the FDP tendon crossing the PIP joint expressed as a fraction of middle phalanx length.*

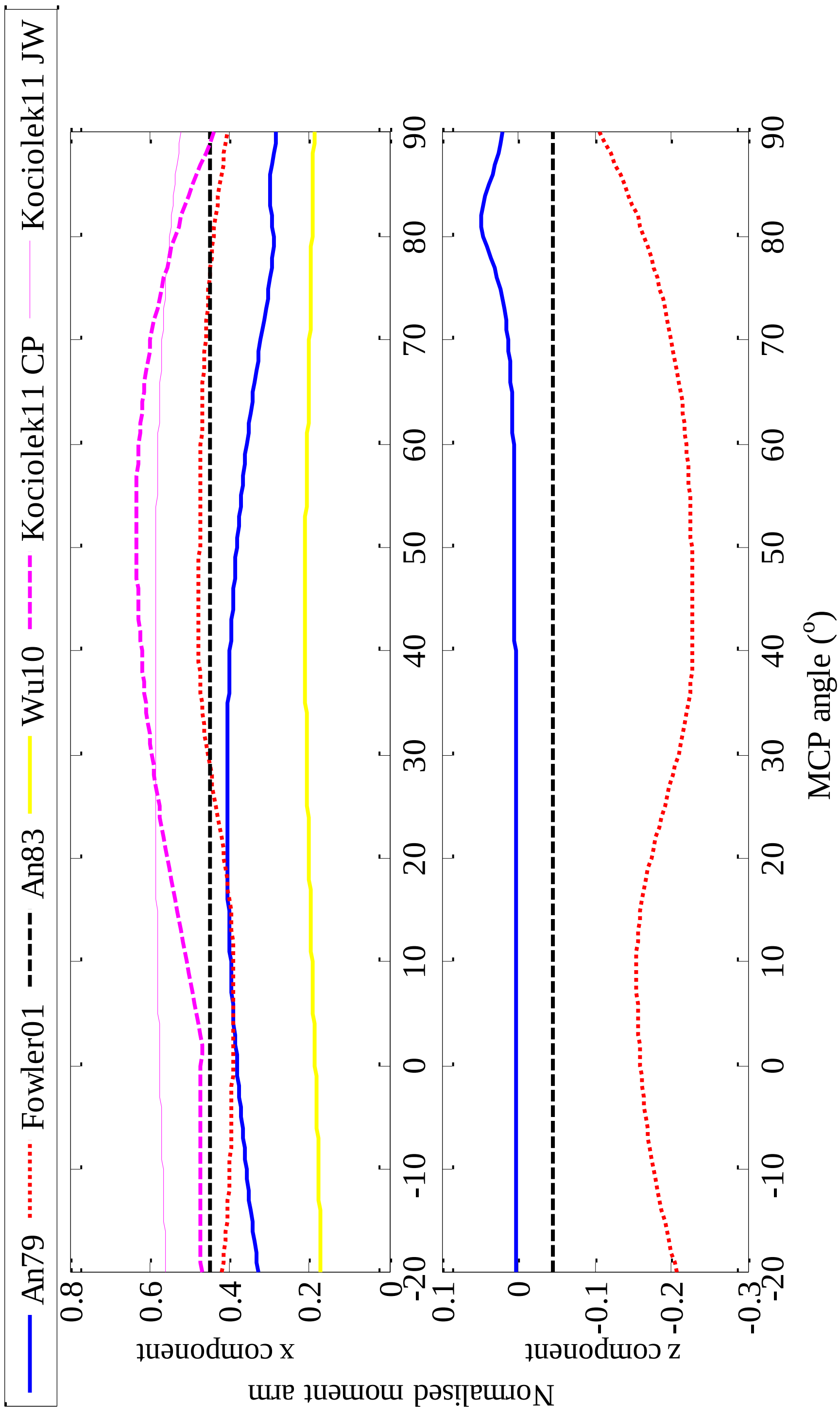

Figure 7.10: *Moment arms of the FDP tendon crossing the MCP joint expressed as a fraction of middle phalanx length.*

Chapter 8. Combined ultrasound and stereo-photogrammetry to measure tendon moment arms and lines of action

In Chapter 3 I showed that predicted internal loading from biomechanical models of the fingers was sensitive to changes in any of the measured inputs. The new method of motion capture presented in Chapter 5, both aimed to reduce errors in kinematic measurement and to give an estimate of the accuracy achieved. In this thesis a simple open grip type (requiring flexion of the fingers) has been studied. It has been shown that the biomechanical model was most sensitive to changes to the moment arm of the flexor digitorum profundus (FDP) tendon. The methods of measuring and calculating the properties of this tendon have predominantly used cadaver based datasets, be that through direct measurement (Franko et al., 2011; Buford et al., 2005; An et al., 1983; An et al., 1979) or through a modelling approach (Kociolek and Keir, 2011; Wu et al., 2010). Anthropometric scaling based on middle phalanx length can then be applied to represent subject specific measurements. In Chapter 7 it was observed that each of these methods would produce quite different moment arms using the same scaling factor. These different methods could in turn affect the predicted internal loading by over 100%. The only study that measured subject specific anatomy directly was that of Fowler et al (2001). This method based on measuring properties from magnetic resonance imaging (MRI) was not without compromise however, such as the expense involved and difficulty in identifying the muscles, tendons and axes of rotation.

Manal et al (2010) proposed a method to measure the subject specific properties of the Achilles tendon using ultrasound and stereophotogrammetry. As detailed in Section 7.1.1 there were several compromises specifically in calibration of the ultrasound image in the photogrammetric frame and the position of the axes of rotation. The method proposed in this chapter will quantify and reduce these errors to produce a valid method for application to the fingers.

The aim of this chapter is to describe and assess the procedure for measuring subject specific moment arms and lines of action of the FDP across the distal interphalangeal (DIP), proximal interphalangeal (PIP) and metacarpo-phalangeal (MCP) joints of the index finger. This method utilises a combination of stereo-photogrammetry and ultrasound. It uses the kinematic analysis techniques described in Chapter 5 to define the anatomical coordinate system (ACS) of each finger segment, and ultrasound to locate the tendons. Once measured these properties could be used with the model described in Chapter 3 and the effect of subject specific measurement quantified.

8.1 Three-dimensional ultrasound imaging from two-dimensional scans

The concept of using two dimensional (2D) ultrasound to build a three dimensional (3D) image or measurement of a subject has been around for some years. In general 3D reconstruction from 2D ultrasound scanning can be classed in two ways (Fenster et al., 2001).

The first is referred to as feature based reconstruction. This is where anatomical features are digitised in one or more 2D ultrasound images. Using known transformations between the ultrasound image scan plane and global reference, the locations of the anatomical features can be expressed in a common global frame.

The second is referred to as voxel based reconstruction. In this process a full 3D image is reconstructed which can be viewed in a similar way to an MR or computed tomography image. Again through knowledge of the transformations each pixel from a 2D image can be reconstructed in a 3D Cartesian grid. In this way a full 3D image can be re-sliced and viewed. This technique relies on a sufficient number of 2D images in the required proximity to work (Tong et al., 1996). Although voxel reconstruction enables the production of navigable 3D images, the precise measurement of lengths, sizes and volumes could be compromised because of the interpolation routines used to fill in blank space in the image.

Both feature and voxel based reconstructions require the position of the image scan plane in a global reference frame to be known (Fenster et al., 2001). Leaving aside issues relating to calibration of the image plane with the probe head (covered later in Section 8.2), this requires knowledge of the spatial and temporal location of the imaging probe head. The way of achieving this can be generalised into three techniques; Mechanical scanning, freehand scanning and 2D array scanning. Mechanical and freehand techniques require the movement of the probe head of a regular 2D scanner. The third technique, 2D array scanning, uses a fixed transducer and electronic scanning to collect multiple images (Fenster et al., 2001).

8.1.1 Mechanical scanning

Mechanical scanning techniques refer to the use of a device to move the probe head along a known trajectory or arc. Because this movement is precisely controlled, calculation of the relative spatial position of each image is straightforward. Tong et al (1996) used a mechanical arm to produce 3D images of the prostate using a voxel reconstruction technique.

8.1.2 Free-hand scanning

Free-hand techniques allow a more flexible movement of the probe head as it is held by whoever is carrying out the examination. This makes it more practical for measuring live subjects because the mechanical devices used to automatically manoeuvre the probe can be restrictive (Fenster et al., 2001). The challenge occurs in establishing the spatial and temporal relationships between each 2D image. It is most common to achieve this with some form of position sensing device fixed to the probe head (Fenster et al., 2001) and there are a number of methods available to achieve this.

An articulating arm has been used to track the position of the probe head (Geiser et al., 1982). Unlike the mechanical scanning which drives the position of the probe, this arm used potentiometers to passively measure the position. Although not as restrictive as mechanical scanning this method still limits how the probe can be manoeuvred.

To reduce the restriction on the free movement of the probe head a number of ways of tracking its position without direct measurement have been proposed. Acoustic positioning has been used to track the probe head for reconstructing images of heart valves (Levine et al., 1989). Limitations of acoustic positioning include the inability to measure orientation.

Electro-magnetic sensors have been used for tracking the probe head and applied to measuring the volume of kidneys and livers (Hughes et al., 1996). Electromagnetic sensors are able to measure both position and orientation (Raab et al., 1979), giving them an advantage over the acoustic techniques. Commercial products are available (Polhemus, Fastrak) which allow real-time tracking using these sensors.

More recently stereo-photogrammetry has been used to track the probe head position. It has been applied to the measurement of gastrocnemius length using feature based reconstruction (Fry et al., 2003). Subsequently the size and position of this muscle has also been measured using voxel reconstruction (Fry et al., 2004). The position of the hip joint centre has been measured (Peters et al., 2010) and the moment arm of the Achilles tendon (Manal et al., 2010), both using feature based reconstruction. Using a minimum of three non-collinear makers rigidly attached to the probe head, a reference frame can be fixed to it. Like the electro-magnetic sensors, this allows real-time tracking of the probe head. The principle advantage of this system in a biomechanics context is that it can be applied using equipment found in a standard gait analysis laboratory.

8.1.3 Array scanning

The third method uses 2D scanning arrays to reconstruct a 3D image. Using a stationary transducer the ultrasound beam is swept across the volume to be imaged. Although able to produce clear voxel based reconstructed images, its application is limited due to its cost (Fenster et al., 2001) and its inability to scan more than a limited volume.

8.2 Calibration of the ultrasound image coordinate system

All of the methods described above rely on the transformation between the scan plane and a global reference system being known. Figure 8.1 shows the relevant coordinate systems. Coordinate system $\{U\}$ is that fixed to the ultrasound scan plane. The origin of this coordinate system is located in the top left corner of the image. The *y-axis* aligns with the scan direction i.e. away from the probe casing. The *x-axis* is directed perpendicular to the scan direction. The *z-axis* is the out of plane axis. Positions in this coordinate system cannot be measured out of plane, they can only be expressed in terms of their *x* and *y* components. Therefore the components of any position ${}^{U}\boldsymbol{p}$ will be:

$$ {}^{U}\boldsymbol{p} = \begin{bmatrix} p_x \\ p_y \\ 0 \\ 1 \end{bmatrix}. \quad \textbf{(8.1)} $$

Coordinate system $\{P\}$ is fixed to whatever motion sensing device is attached to the probe casing. This could be an electromagnetic, inertial or marker based coordinate system. Coordinate system $\{G\}$ is the global coordinate system fixed in the laboratory. In some cases there may be an additional coordinate system $\{M\}$ fixed to the transmitter used for electromagnetic tracking. If this is case then the transformation between this and the global coordinate system must be known. Positions measured in the ultrasound frame can be expressed in the global frame by:

$$ {}^{G}\boldsymbol{p} = {}^{G}_{M}\boldsymbol{T}\,{}^{M}_{P}\boldsymbol{T}\,{}^{P}_{U}\boldsymbol{T}\,{}^{U}\boldsymbol{p}. \quad \textbf{(8.2)} $$

The calculation of the transformations ${}^{M}_{P}\boldsymbol{T}$ and ${}^{G}_{M}\boldsymbol{T}$ will depend on the tracking system used. In principle the methods are similar to those of stereo-photogrammetry with technical frames fixed to any relevant rigid object.

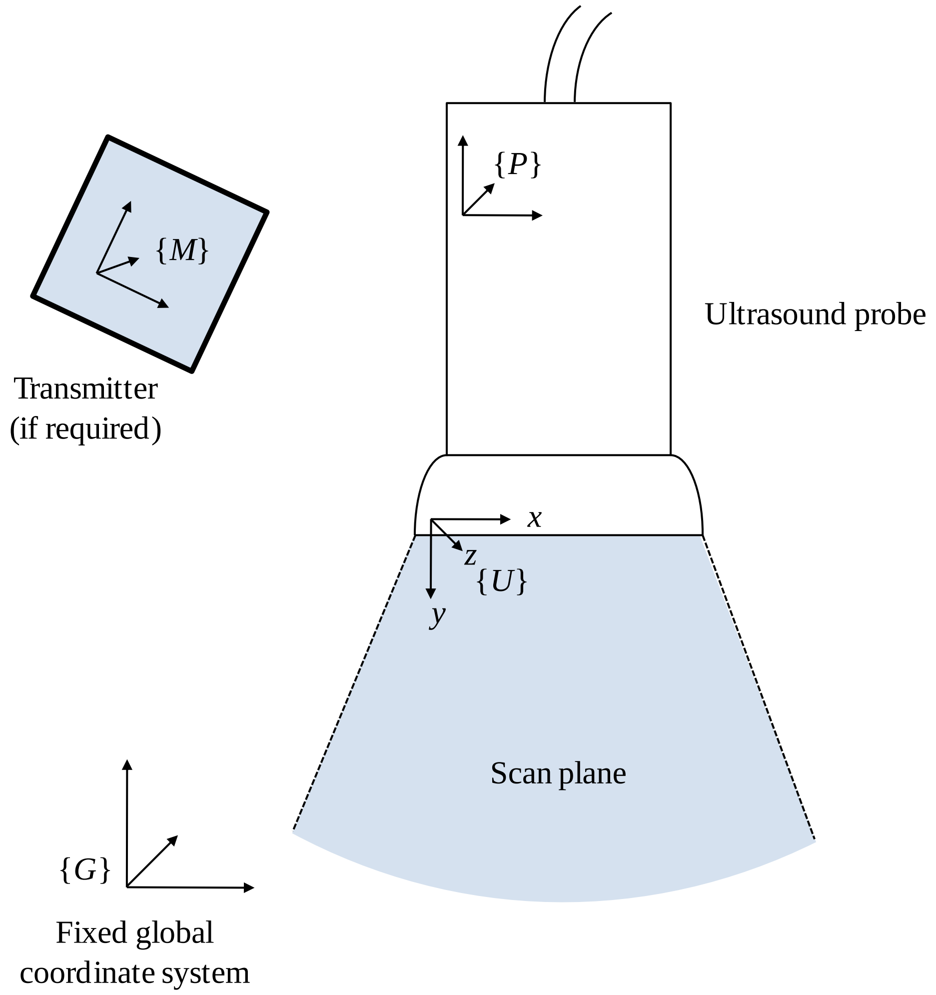

Figure 8.1: *Coordinate systems relevant for 3D ultrasound scanning. Coordinate system $\{U\}$ fixed to the ultrasound scan plane, system $\{P\}$ fixed to the probe casing, system $\{M\}$ fixed to the transmitter (if needed) and the fixed global system $\{G\}$.*

The definition of the transformation between $\{U\}$ and $\{P\}$ is not straightforward and can be calculated in different ways. In its simplest form, the transformation can be expressed in terms of three rotations and three translations. The three rotations, α, β and γ occur about the *x*, *y* and *z-axes* respectively. The rotation matrix ${}^{P}_{U}\boldsymbol{R}$ giving the rotation between coordinate systems $\{U\}$ and $\{P\}$ can be constructed using an ***xy'z''*** Cardan sequence (see Section 4.2.3). The translation between origins of the two coordinate systems is given by the 3D vector ${}^{P}\boldsymbol{o}$. The rotations and translations can then be combined into a single transformation matrix ${}^{P}_{U}\boldsymbol{T}$.

The rotations and translations can be found by making an assumption about how the scan plane aligns with the probe casing (Manal et al., 2010). Making this assumption is dangerous however, as the position and orientation of the scan plane do not necessarily relate to the probe casing geometry in any consistent way (Prager et al., 1998). An alternative is to use a specific calibration procedure (Peters et al., 2010; Fry et al., 2004; Fry et al., 2003).

Several studies have been made to review the available methods of calibration (Hsu et al., 2008; Rousseau et al., 2006; Prager et al., 1998). All methods described used a phantom object, which was scanned, usually in a water bath. These phantom objects were of known dimensions and their positions in the coordinate system $\{G\}$ known. Prager et al (1998) initially set out to assess the suitability of two different wire calibration procedures. They first used a cross wired calibration. Two intersecting wires were submerged in a water bath with the position of the apex of the two wires in a known fixed position. The wires were then scanned from a variety of directions with their apex being visible in the ultrasound image as shown in Figure 8.2 (a). This gave a set of point locations in the scan plane coordinate system $\{U\}$. These relate to a fixed point in the global coordinate system $\{G\}$ and the calibration parameters were subsequently calculated using an optimisation procedure. The second method assessed by Prager et al (1998) was referred to as a three-wire phantom. In this case the wires were again submerged in a water bath, however on this occasion the wires were mounted in three orthogonal directions. The probe was then moved along each of these wires, resulting in a cross being visible in the image (Figure 8.2 (b)). Although it was easier to align the probe to image the wires rather than a cross, it relied on very accurate positioning of the three orthogonal wires. It was noted that both of these methods required manual digitisation of the images because the signal from the wires was not clear enough for an automated routine to work effectively.

The authors then proposed a new method, where instead of a separate phantom object the sides of the water bath were used as reference points. By carrying out a prescribed set of motions and rotations the calibration parameters could be calculated by assuming the straight line reflections (Figure 8.2 (c)) lay on the plane formed by the *x* and *y-axes* of the global coordinate system. This system had the principle advantage that the strong reflections from the wall of the water bath could be automatically segmented.

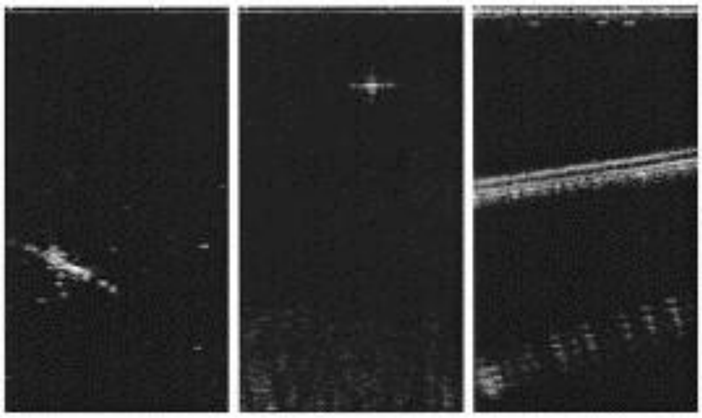

(a) (b) (c)

Figure 8.2: *Images obtained by Prager et al (1998) using two intersecting wires (a), three orthogonal wires (b) and the wall of the water bath (c).*

Rousseau et al (2006) further assessed methods of calibration both using the planar wall method favoured by Prager et al (1998) and a procedure known as the Medtronic calibration. The Medtronic calibration used a complex phantom made of a set of 39 nylon wires. Rousseau et al (2006) proposed improvements to the planar wall procedure in the post processing which meant that digitisation of the images was improved. It also negated the effects of beam width which was counteracted previously by use of the more complex Cambridge phantom (Prager et al., 1998). The Medtronic calibration produced accurate results but because of the time consuming nature of the procedure the authors proposed that the improved planar wall method was more practical and achieved similar accuracies.

The planar wall methods require a specific set of translations and rotations to be carried out to ensure the calibration parameters are properly constrained (Prager et al., 1998). For this reason Hsu et al (2008) carried out an assessment of point calibration techniques. Instead of using the crossed wires the authors investigated the use of stylus type phantoms. The principle of these was that the probe could be fixed in position and the phantom object moved within the scan plane whilst simultaneously being tracked using some form of motion capture. Each stylus type phantom had a geometric feature that could be identified in the scan image. It was found that point and spherical styluses were difficult to position correctly within the scan image compared to a cone type stylus. The cone type stylus was easier to locate due to the clear umbrella shaped reflections visible when the phantom was aligned correctly. Using the other types of stylus, the interpretation of the image was more ambiguous. The precision of measurement using the Cambridge stylus was found to be 0.6mm and the accuracy was estimated at 2.2mm.

All of the techniques described above used electro-magnetic sensors to track the location of the probe and phantoms. In the context of biomechanical applications it has been more common to use stereo-photogrammetry when calibrating the ultrasound image (Peters et al., 2010; Fry et al., 2004; Fry et al., 2003). Fry et al (2003 and 2004) used point location calibration methods first using a cross wire method (Fry et al., 2003) and then using a single reflective marker (Fry et al., 2004). Peters et al (2010) highlights the problems with using a scanned reflective marker because its position in a water bath can compromise the ability to locate it accurately. Peters et al (2010) used a variation of the Cambridge stylus proposed by Hsu et al (2008). They attempted to validate accuracy using a submerged reflective marker observing an accuracy of 4mm, worse than that previously shown by Hsu et al (2008). This was in some part attributed to the difficulty in locating the reflective markers as described above.

Another factor to consider is the scaling of pixels to millimetres in the ultrasound image. A position measured on any image will be in pixels so the location ${}^{U}\boldsymbol{p}$ is in fact expressed as:

$$ {}^{U}\boldsymbol{p} = \begin{bmatrix} \boldsymbol{s}_x u \\ \boldsymbol{s}_y v \\ 0 \\ 1 \end{bmatrix}, \qquad \textbf{(8.3)} $$

Were u and v are the x and y locations measured in terms of pixels and s_x and s_y are appropriate scaling factors (Peters et al., 2010). Although many ultrasound scanners provide the information required to make this transformation, they will make assumptions about the speed of sound in the scanning medium. This must be taken into account through accurate measurement of the temperature in the water bath (Hsu et al., 2008).

8.3 Measurement of moment arms and lines of action from ultrasound images

In my study the ultrasound probe head was tracked using a stereo-photogrammetric system (Vicon, U.K.) and the hand position determined using the phalanx transformation technique (PTT) with the marker set described in Chapter 5. The ultrasound machine used was an Esaote MyLab 70 XCG, using a linear array probe-head with a 40mm footprint (model LA435). This allowed both still images and video to be collected. The frequency range of the probe (6-18 MHz) allowed for optimal imaging of the flexor tendons at a shallow depth. A gel standoff pad was considered, however it was found that transmission gel was more suitable for scanning the flexor tendons, particularly when the fingers were flexed. The probe was held in two orientations, either longitudinal with the image aligned with the tendon line of action or in a transverse position imaging the cross section of the tendon.

To determine the moment arm of a tendon across a particular joint a minimum of two images was required. The first was the longitudinal image which was used to identify the line of action of the tendon. Figure 8.3(a) shows an example of this for the FDP crossing the MCP joint. The line of action of the tendon was manually digitised (location defined in an image) giving a normalised direction vector defined in the image coordinate system ${}^{U}\boldsymbol{e}$. For accurate determination of the line of action the probe had to be aligned exactly with the direction of the tendon. This was done by manoeuvring the probe until the striations on the tendon were clearly visible. This could be done with the finger flexed <20°, above this it becomes difficult to maintain the acoustic contact. The second probe position was a transverse scan with the cross section of the tendon visible (Figure 8.3(b)). This was used to define a point or series of points through which the tendon travels (${}^{U}\boldsymbol{t}$). In this instance it is important to align the probe so that the cross section is imaged as close to the joint centre as possible. These vectors and positions could be transformed into the global coordinate system giving ${}^{G}\boldsymbol{e}$ and ${}^{G}\boldsymbol{t}$.

Using the techniques described in Chapter 5 the anatomical coordinate system (ACS) for each body segment could be defined relative to the markers attached to the finger. Therefore any joint centre could also be located in the global coordinate system.

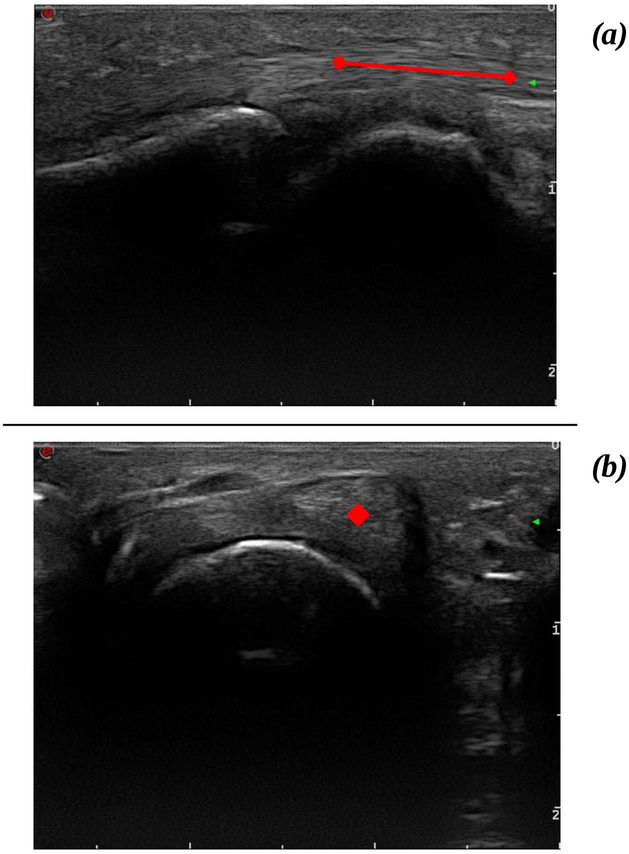

Figure 8.3: *Longitudinal view of the FDP crossing the MCP joint (a), the line of action of the tendon indicated by the line. Transverse view of the same tendon (b), with the centre of the tendon cross-section indicated by the dot.*

The procedure for calculating the moment arm was as follows. A line of infinite length with direction vector ${}^{G}\boldsymbol{e}$ was defined to pass through the point ${}^{G}\boldsymbol{t}$. The location lying on this line with a minimum perpendicular distance between it and the relevant joint centre was then found. The resulting vector between the joint centre and this point was the moment arm ${}^{G}\boldsymbol{r}$. This moment arm and line of action could then be transformed into the ACS relevant for the particular joint. For the DIP joint this would be the distal phalanx ACS $\{dp\}$, for the PIP joint the middle phalanx ACS $\{mp\}$ and for the MCP joint the proximal phalanx ACS $\{pp\}$. Once these transformations had been made it was straightforward to calculate the unit-force moment.

8.4 Calibration of ultrasound image using the Cambridge stylus

Calibration of the ultrasound image frame $\{U\}$ was carried out using the Cambridge stylus with both the probe head and phantom tracked using stereo-photogrammetry.

Local technical frames were fixed to both the probe head and phantom using clusters of retro reflective markers.

8.4.1 Probe head technical frame

A U-Shaped clip was manufactured from mild steel which could be clamped over the narrow part of the probe (Figure 8.4). The inside of the clip was covered with 6mm neoprene rubber, ensuring a firm grip of the probe casing. Additionally it meant the clip could be tightened without damaging the probe. The clip was fixed using a 5mm bolt tightened by hand using a wing nut. Rigidly mounted to the clip was a nylon cylinder with four rods of 30mm length mounted upon it. A 10mm marker was attached to each of these rods. Three markers (A, B and C in Figure 8.4) defined the probe technical frame $\{P\}$. The fourth marker D provided redundancy in case of occlusion of one of the other markers. It also made it possible to identify the orientation of the cluster when labelling the raw data. This system of using a U-clip meant the cluster could be easily fixed to and removed from the probe head. As long as the probe head was not subject to unreasonable force (such as being dropped) the cluster remained fixed relative to the probe casing. The cluster could be mounted onto probes of different dimensions by changing the size of the U-clip.

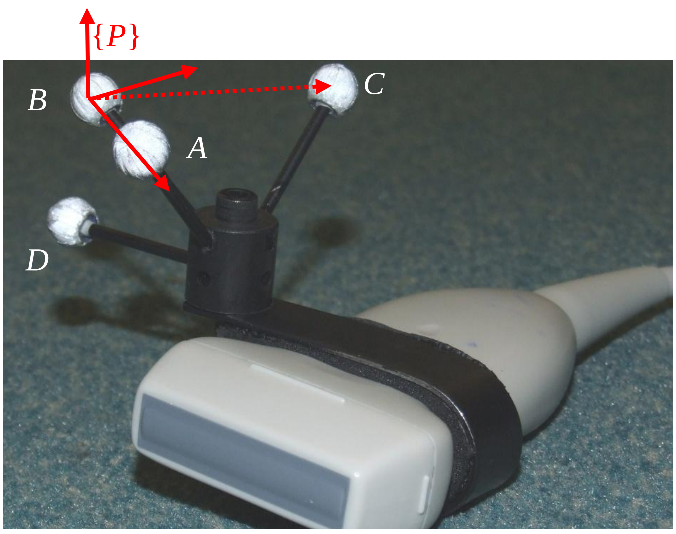

Figure 8.4: *Local technical frame $\{P\}$ fixed to the cluster of markers rigidly mounted to the probe head casing using a U-clip.*

.

8.4.2 Cambridge phantom

A variation of the Cambridge phantom (Hsu et al., 2008) was manufactured by our own workshop. Made from stainless steel the phantom consisted of a rod 250mm long and 13mm in diameter (Figure 8.5). One end was machined into a twin cone and a point. Post manufacture, the diameter of the apex of the two cones was measured to be 2.5mm at a distance of 19.2mm from the tip. The accurate measurement of these dimensions was crucial for the calibration of the ultrasound image. At the other end of the rod were mounted three markers (*A*, *B* and *C*) in a non-collinear arrangement to define a technical frame fixed to the phantom. A fourth marker *D*, lay on the centre line of the rod. Along with the tip at the other end this defined the long axis of the phantom. The tip position was calibrated by fixing it to a surface and rotating the rod above it. The tip position could then be found using the centre transformation technique described in Section 5.1.3.

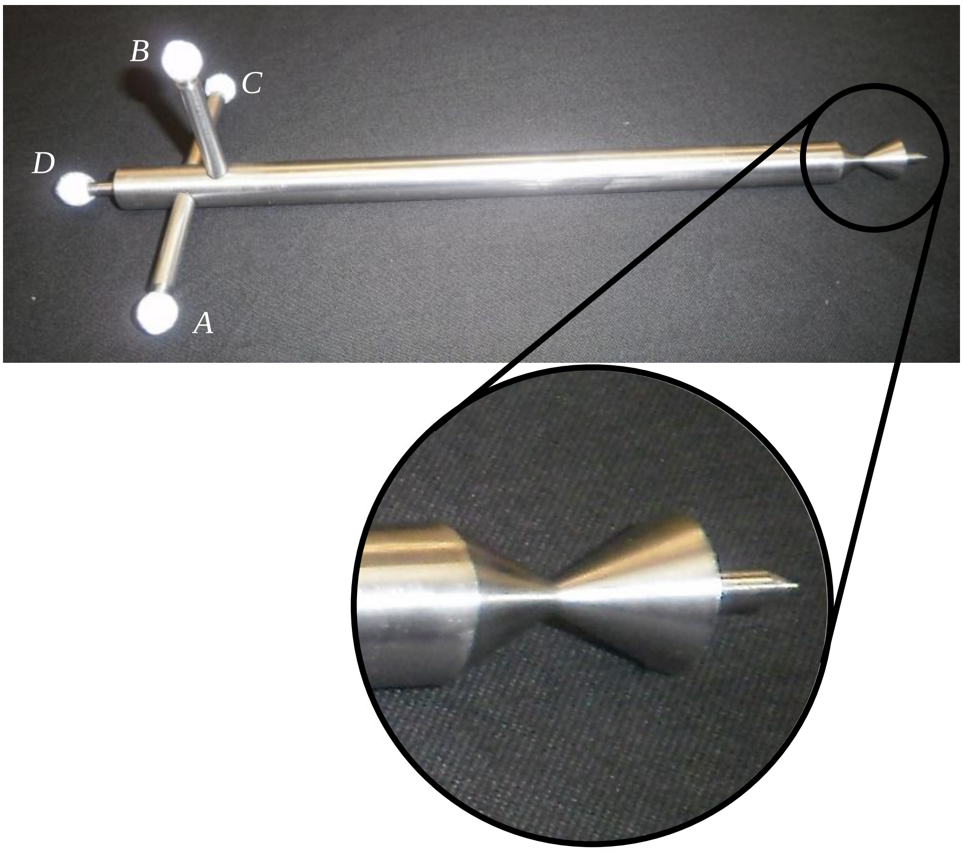

Figure 8.5: *Phantom used for calibration of the ultrasound image plane. Three markers (A-C) defined the local technical frame and the fourth marker D defined the centre line of the rod. One end was machined to a sharp point with a twin cone.*

8.4.3 Calibration procedure

With the clip attached, the ultrasound probe was fixed above a water bath with the probe slightly submerged in the water (Figure 8.6). The water was maintained at 40°C throughout the experiment. The tip of the phantom was then submerged in the water bath with the cluster of markers still above the surface. Its position was manipulated by hand until the apex of the twin cones aligned with the scan-plane. This was signified by the characteristic 'umbrella' image caused by the reflections from the curved surface of the phantom (Hsu et al., 2008). The circular cross section of the phantom was also visible at the centre of the umbrella as seen in Figure 8.7. By manual digitisation of the top of the circle the apex could be calculated by addition of the radius of the apex (in this case 1.25mm). A set of a minimum of nine positions were scanned, covering the area of the image relevant for tendon scanning (the top two thirds of the image). The capture of these positions was synchronised between the ultrasound scanner and the motion capture system using an infra-red light emitting diode (LED) attached to a pressure switch. This switch was located on the capture button of the ultrasound base unit. This LED could be located in the stereo-photogrammetric frame to provide the synchronisation.

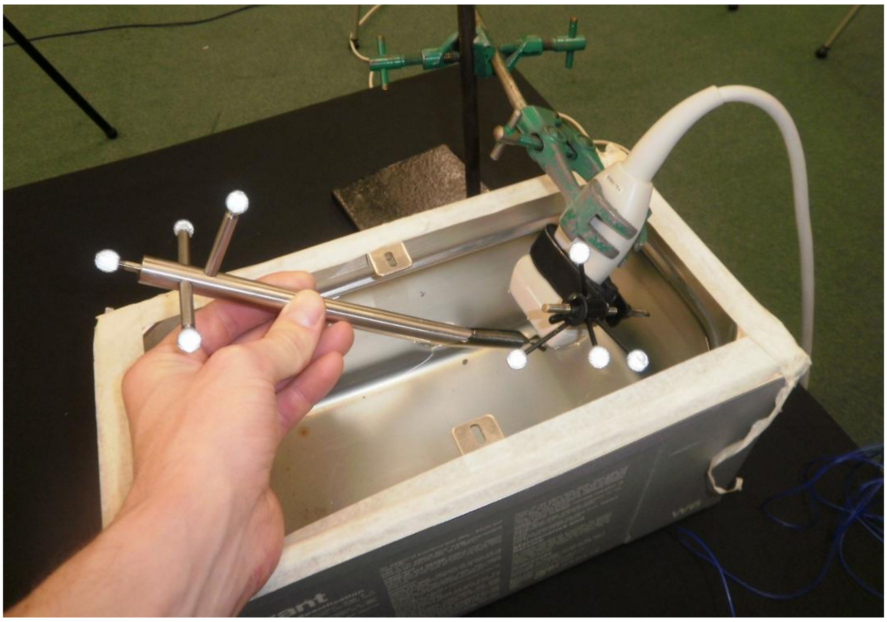

Figure 8.6: *Probe clamped so that it just touched the surface of the water. The phantom was manoeuvred so that the apex of the twin cones aligned with the scan plane.*

Figure 8.7: *Umbrella shape reflection occurring when the scan plane aligns with the apex of the twin cones. The circular cross section of the apex can be seen at the centre of the umbrella.*

The digitisation procedure enabled a set of locations $\boldsymbol{a}_i$ to be simultaneously located in both the ultrasound scan plane $\{U\}$and the probe technical frame $\{P\}$, *i* = *1-N* with *N* being the total number of positions scanned. If the two coordinate systems were assumed to align then the resulting plot would look something like that presented in Figure 8.8 (a). Because the location of $\{P\}$ was arbitrary relative to $\{U\}$ the two sets of points would not align. The set of rotations and translations must be found that give the appropriate transformation ${}^{P}_{U}\boldsymbol{T}$ that will satisfy the constraint:

$$ {}^{P}\boldsymbol{a}_i = {}^{P}_{U}\boldsymbol{T}\,{}^{U}\boldsymbol{a}_i \text{ for all } i. \quad \textbf{(8.4)} $$

Once the points have undergone this transformation they will align.

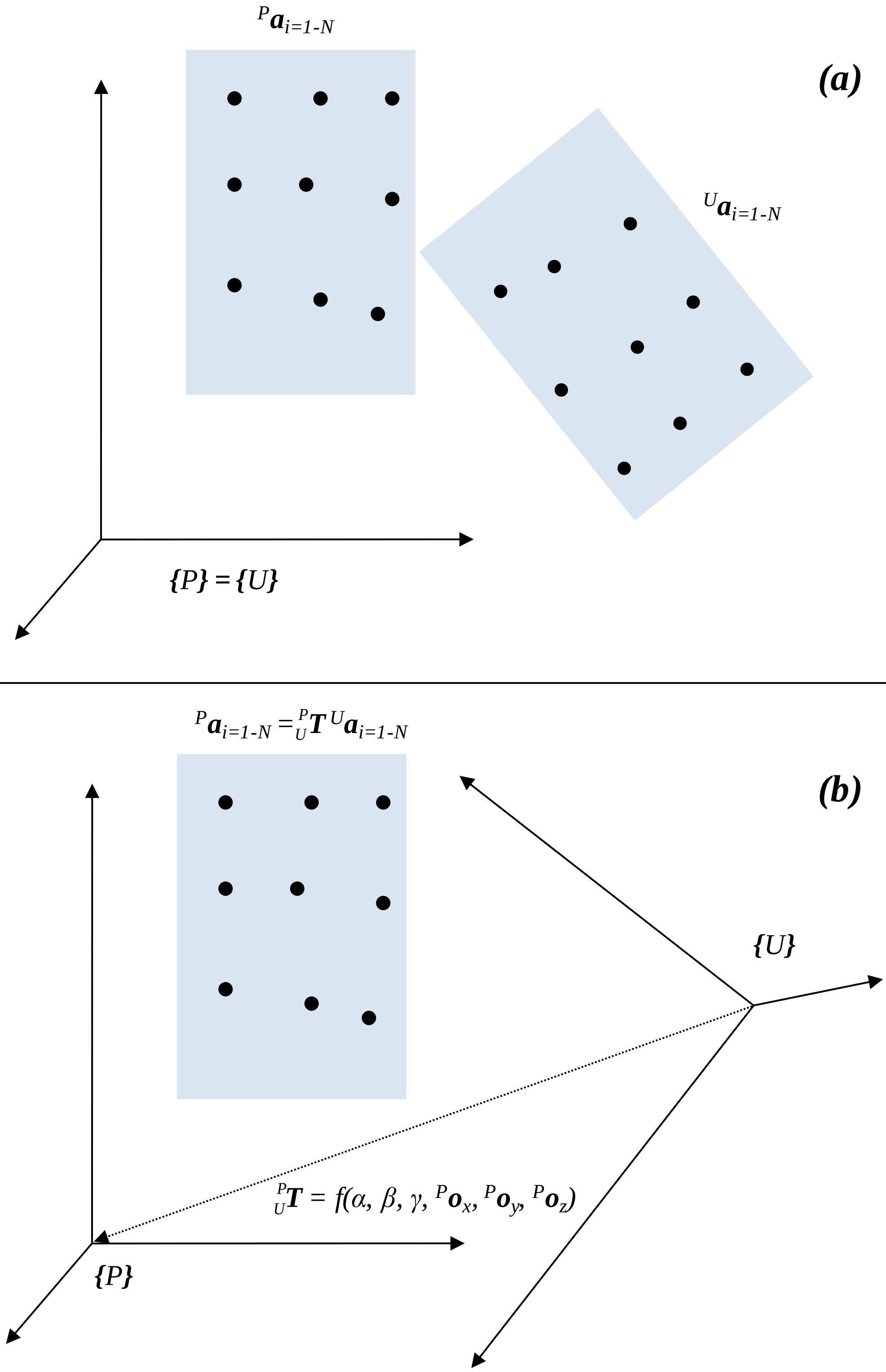

Figure 8.8: *If the coordinate systems {U} and {P} are assumed to align, the points defined in each* $^{P}\boldsymbol{a}_{i=1\text{-}N}$ *and* $^{U}\boldsymbol{a}_{i=1\text{-}N}$*) will not correspond (as shown in (a)). The transformation* ${}^{P}_{U}\boldsymbol{T}$ *was found to minimise any difference between the sets of points. Once this transformation has been carried out the points will align as shown in (b).*

Figure 8.8 (b) shows how this will occur once $\{U\}$ has been transformed appropriately. The transformation ${}^{P}_{U}\boldsymbol{T}$ is made up of the three unknown rotations (α, β and γ) and the unknown translation (${}^{P}\boldsymbol{o}$) between $\{U\}$ and $\{P\}$ Using an $\boldsymbol{xy'z''}$ rotation sequence, the transformation matrix is:

$$ {}^{P}_{U}\boldsymbol{T} = \begin{bmatrix} c\beta c\gamma & -c\beta s\gamma & s\beta & {}^{P}o_x \\ s\alpha s\beta c\gamma + c\alpha s\gamma & -s\alpha s\beta s\gamma + c\alpha c\gamma & -s\alpha c\beta & {}^{P}o_y \\ -c\alpha s\beta c\gamma + s\alpha s\gamma & c\alpha s\beta + s\alpha c\gamma & c\alpha c\beta & {}^{P}o_z \\ 0 & 0 & 0 & 1 \end{bmatrix}. \tag{8.5} $$

To simplify the matrix in this equation cosine terms are represented by a *c* and sine terms represented by an *s*. The six unknowns that make up this transformation were found by minimising the cost function:

$$ cost = \sum_{i=1}^{N} {}^{P}\boldsymbol{a}_i - {}^{P}_{U}\boldsymbol{T}\,{}^{U}\boldsymbol{a}_i \tag{8.6} $$

using an interior-point algorithm in the *optimisation toolbox* available in MATLAB (The MathWorks).

An initialisation of the matrix was made by manually pointing positions on the probe casing. This pointing gave an initial alignment and position of $\{U\}$ relative to $\{P\}$, ensuring a true optimal solution was found.

8.4.4 Accuracy, precision and repeatability of calibration

Hsu et al (2008) proposed an automated digitisation routine to define the phantom positions in each ultrasound image. For this study however, it was decided to use a manual digitisation process. It was therefore necessary to examine the effect of the observer on the digitisation. Five observers carried out digitisation of five different sets of images. Each set of images consisted of nine phantom positions. Each observer was asked to repeat the process five times.

Accuracy could not be determined specifically as no unique object could be measured that would not be susceptible to the same systematic errors. As discussed earlier the scanning of a separate reflective marker has its own compromises. The accuracy was assumed to be of a similar magnitude to that stated previously as 2.2mm (Hsu et al., 2008).

By applying the calibration calculated from one set of data to the other four it was possible to calculate the precision of the calibration. This was the mean discrepancy in position between points and found to be 0.6mm, similar to that found previously (Hsu et al., 2008).

Because manual digitisation was being carried out it was important to assess how repeatable calibrations were by examining the inter-subject variability. This was found to be on average 0.2mm. Because this was less than the precision of the measurements it was concluded that the manual digitisation was adequate.

8.5 Measurement of the flexor digitorum profundus moment arms and lines of action

8.5.1 Experimental procedure

A single subject was recruited to participate in the experiment (right handed male aged 26 years). An arrangement of 12 Vicon cameras (six T20 and six MX13+) was set up to provide a non-occluded view of the subject and probe (Figure 8.9). It was important to position some of the cameras in the low positions to ensure capture of the probe mounted cluster. Data were captured on a PC using Vicon Nexus software (Oxford, U.K.).

Figure 8.9: *Set up with six T20 cameras and six MX13+ cameras. Locations optimised for a subject sitting in the centre of the arena with cameras positioned low to capture the markers fixed to the ultrasound probe.*

The first step of the experimental procedure was to carry out calibration of the ultrasound image plane. Once this had been carried out care was taken not to disturb the position of the U-clip on the probe casing. 12x4mm hemispherical markers were attached to the dorsal surface of the right index finger in the arrangement described in Section 5.1.1. Through the PTT calibration procedure the ACS were defined relative to these markers.

Once these two calibration procedures had been carried out, taking approximately 20 minutes in total, the subject was ready to be scanned. A set of scans was taken in both the longitudinal position (Figure 8.10 (a)) and transverse position (Figure 8.10 (b)) across the MCP, PIP and DIP joints. Still images were recorded for the longitudinal images with the subject's hand in a neutral pose. Video recordings were made for the transverse images with the subject moving from a neutral pose to fully flexed and then back to neutral. This enabled the moment arm to be recorded for the non-flexed joint, the fully flexed joint and all positions between. This procedure was repeated twice for each joint to ensure the full range of angles was covered.

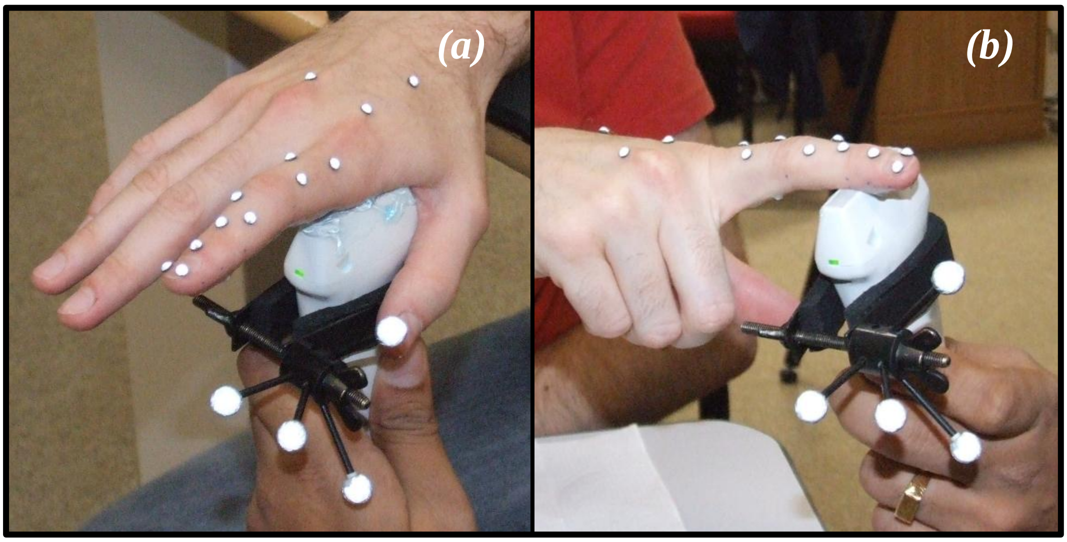

Figure 8.10: *Probe scanning the tendon longitudinally (a) and transversely (b). The 12 markers were attached to the right hand in an identical manner as in Section 5.1.1.*

8.5.2 Data processing

Data were synchronised between the ultrasound images and the Nexus programme using the LED signal described in Section 8.4.3. A suite of programmes was written in MATLAB (The MathWorks, U.S.A.) to calculate tendon properties. This allowed a visualisation of the tendon line of action relative to each body ACS as shown in Figure 8.11.

The subject measured in this study was the same used in the sensitivity analysis carried out in Chapter 3. Therefore the FDP moment arms measured could be applied to the data measured in this previous chapter, enabling the effect of subject specific measurement of the moment arms on internal loading to be quantified.

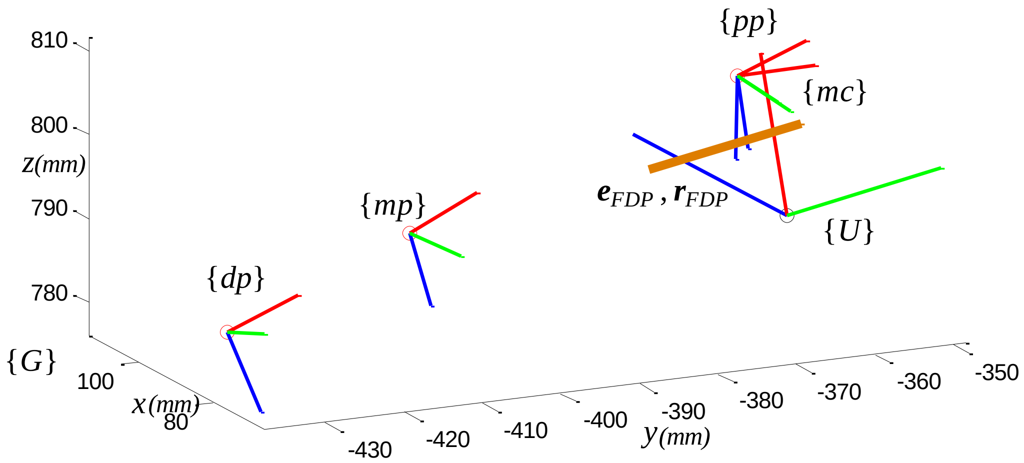

Figure 8.11: *Visualisation of each segment ACS, the ultrasound scan plane* $\{U\}$ *and the FDP in the global coordinate system* $\{G\}$*. ACS shown; distal phalanx* $\{dp\}$*, middle phalanx* $\{mp\}$*, proximal phalanx* $\{pp\}$ *and metacarpal* $\{mc\}$*. The tendon is represented by the orange line, with a line of action* $\boldsymbol{e}_{FDP}$ *and the moment arm* $\boldsymbol{r}_{FDP}$*.*

8.6 Results

Figure 8.12, Figure 8.13 and Figure 8.14 show the moment arms for the FDP using the combined method compared with those available in the literature as described in Section 7.2. All moment arms have been scaled to the middle phalanx length of the subject studied in Chapter 3 which was 25.4mm.

For all three joints the combined method produced moment arms within the range of those proposed previously. The one place where it deviated from this pattern was for high degrees of flexion at the DIP joint. Here the moment arms using the combined methods got progressively larger whereas using the previous methods they tended to plateau or decrease.

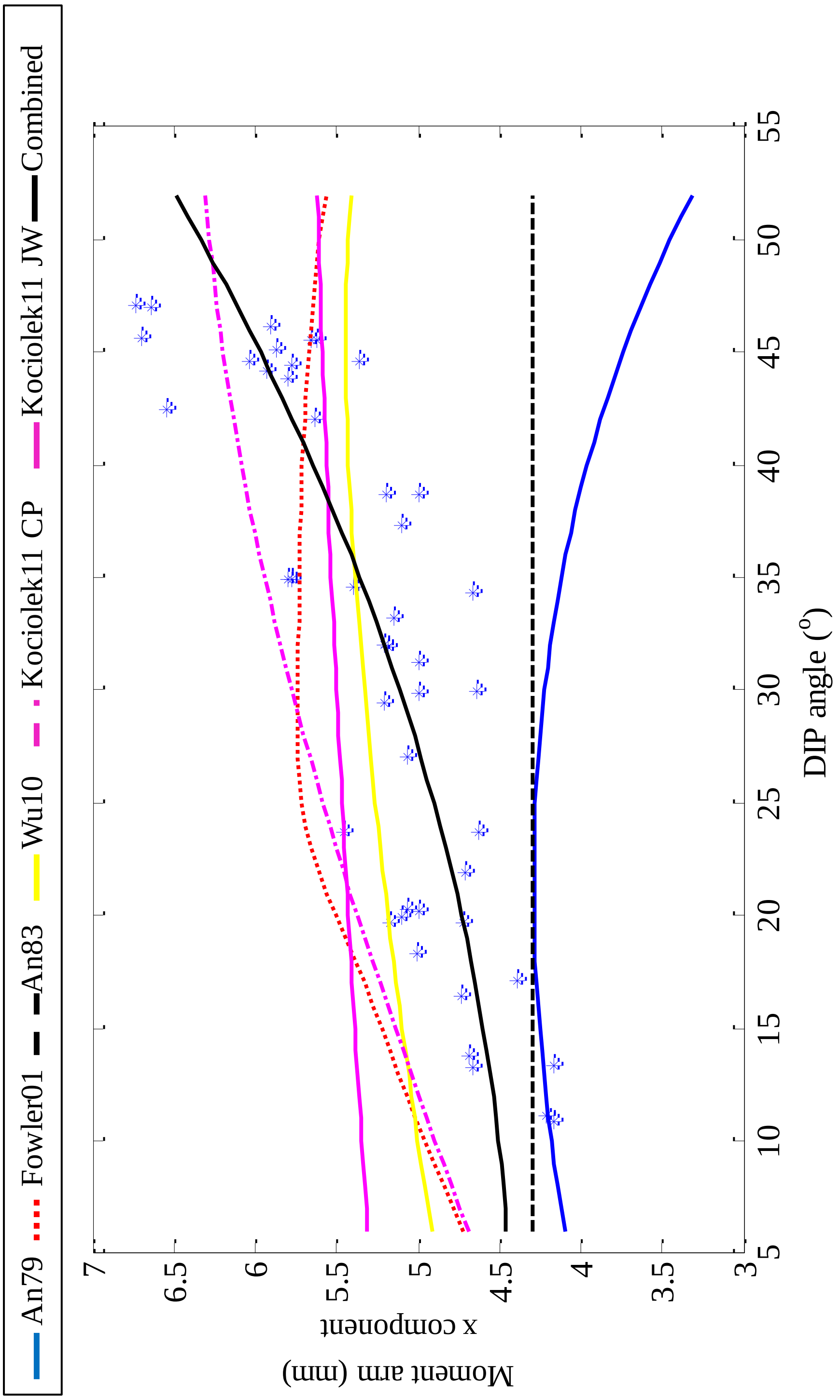

Figure 8.12: *Moment arm of the FDP crossing the DIP joint as a function of joint angle. The blue crosses represent the individually measured moment arms and the solid black line the fitted trend.*

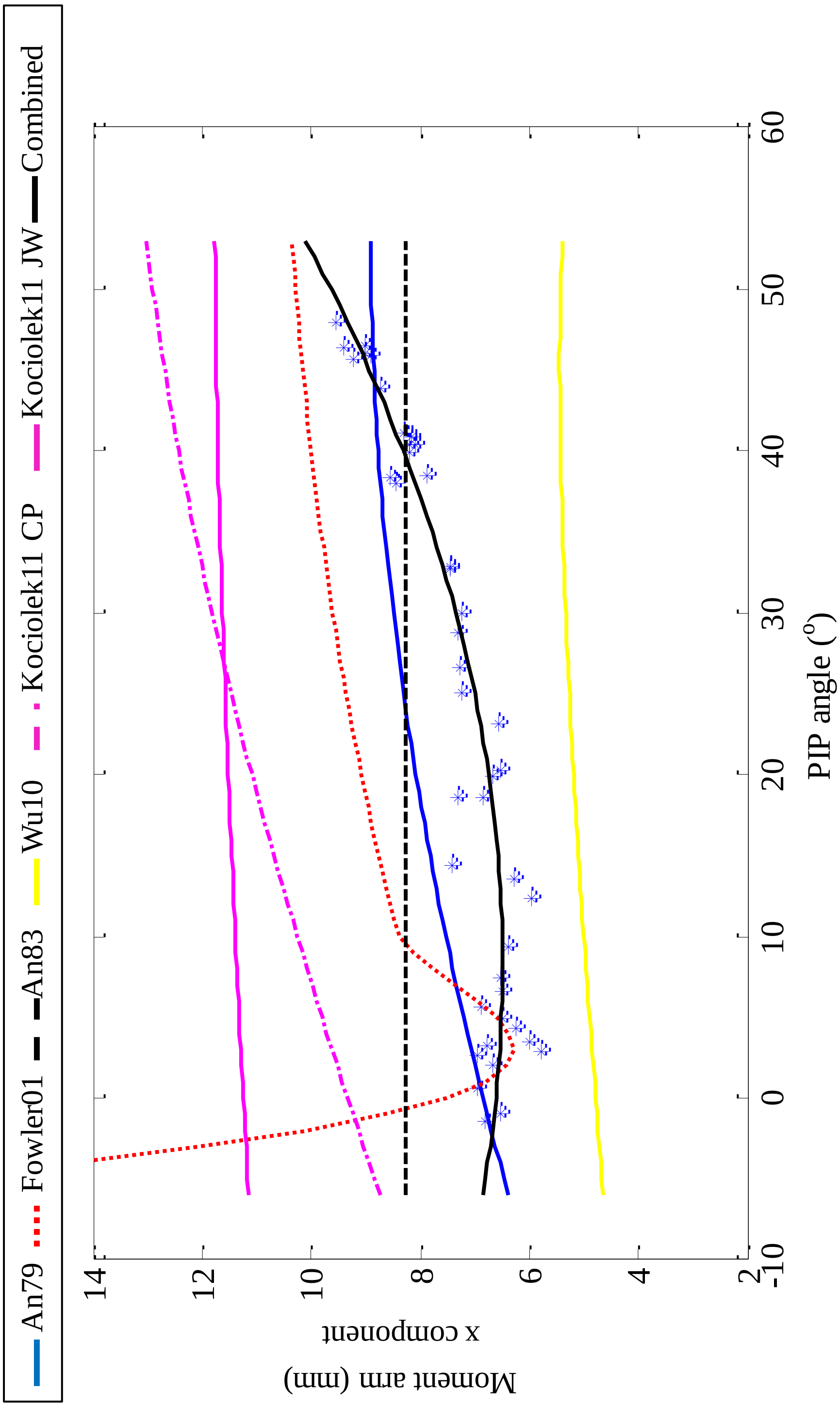

Figure 8.13: *Moment arm of the FDP crossing the PIP joint as a function of joint angle. The blue crosses represent the individually measured moment arms and the solid black line the fitted trend.*

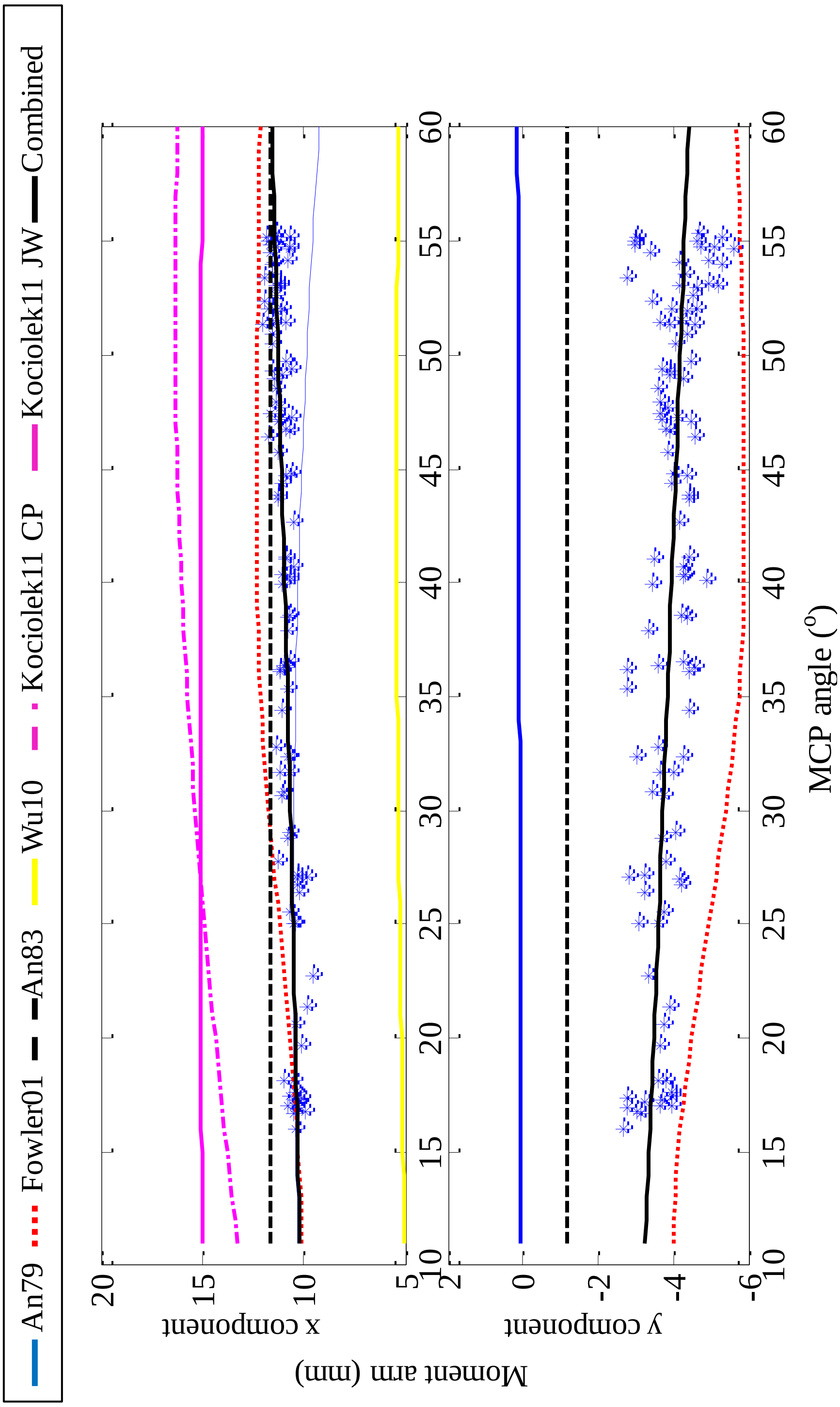

Figure 8.14: *Moment arm of the FDP crossing the MCP joint as a function of joint angle. The blue crosses represent the individually measured moment arms and the solid black line the fitted trend.*

For the combined method a 3rd order polynomial was fitted to the measured results to enable calculation of the moment arm at any degree of flexion within the range measured. This allowed the calculation of the subject specific moment arms for the subject tested using the open handed grip type in Chapter 3. The relevant flexion angles for this grip type are shown in Table 8.1.

Figure 8.15 and Figure 8.16 show the effect of applying these new subject specific moment arms to the model. Originally the moment arms of the FDP were scaled from cadavers. These are presented in comparison with the new moment arms measured using the combined method. To examine the effect of a subject specific measurement when applied to only one of the three joints, the results are presented as five groups. The first group used the original cadaveric scaled anatomy applied at each joint. The following three groups applied the subject specific anatomy to a joint whilst still using the cadaveric for the other two. This was applied to the, MCP, PIP and DIP joints in turn. The final group used the subject specific anatomy applied to all three joints.

Apart from when applied to the DIP joint, the subject specific moment arms increased the predicted tension in the FDP. In all instances however the normalised joint reaction force (nJRF) increased due to increases in tension in the flexor tendons. The mean nJRF increase was significant ($p < 0.05$) in every instance, although it is evident that the change in moment arm at the PIP joint had the greatest effect. Making the change to the moment arm at this joint in isolation increased the mean nJRF from 4.3 to 6.3. The increase in nJRF when the moment arm using the subject specific anatomy was applied at each joint simultaneously was 3.6, increasing to 7.9. Overall this was equivalent to an increase in nJRF of 84%.

Joint	Flexion angle (°)	Standard deviation (°)
DIP	46.6	2.9
PIP	25.3	2.9
MCP	11.7	2.9

Table 8.1: *Flexion angles for the hand in the open hand grip positions tested in Chapter 3.*

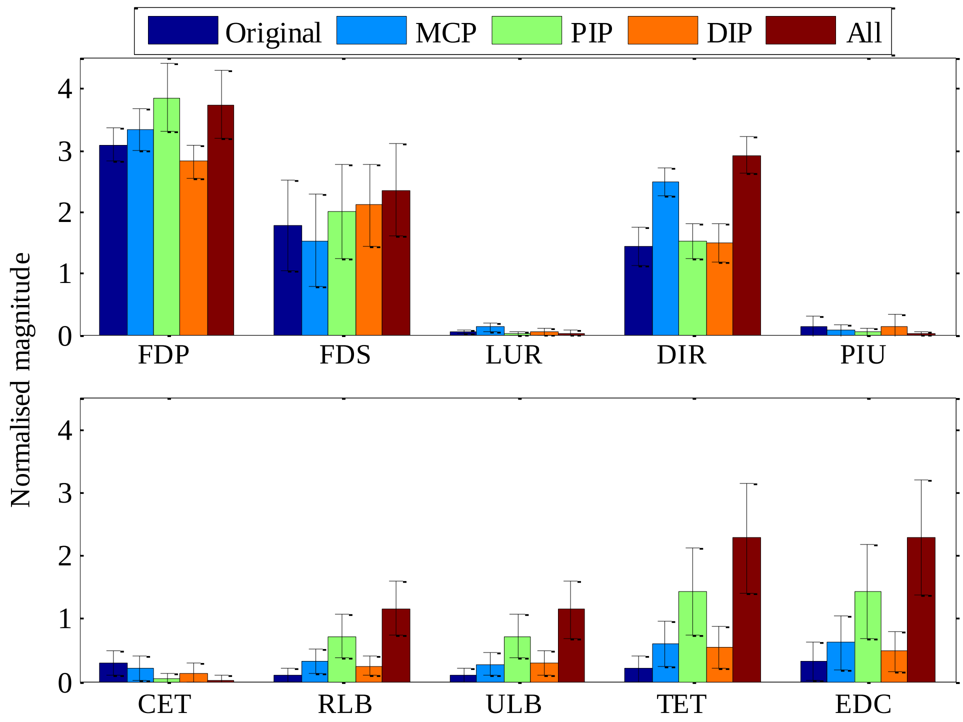

Figure 8.15: *Comparison between predicted actuator tensions from scaled anatomical data and subject specific measurements of the FDP moment arm. For clarity the joint actuators have been split into flexors in the top plot and extensors in the bottom plot. The five bars represent; the original scaled anatomy, subject specific anatomy applied individually to the DIP, PIP and MCP joints and finally with it applied to all joints simultaneously. Functional units: flexor digitorum profundus (FDP), flexor digitorum superficialis (FDS), lumbrical (LUR), dorsal interosseous (DIR), palmer interosseous (PIU), central band of the extensor tendon (CET), radial lateral band of the extensor tendon (RLB), ulnar lateral band of the extensor tendon (ULB), terminal extensor tendon (TET), extensor digitorum communis (EDC). Error bars represent ±1 Standard Deviation.*

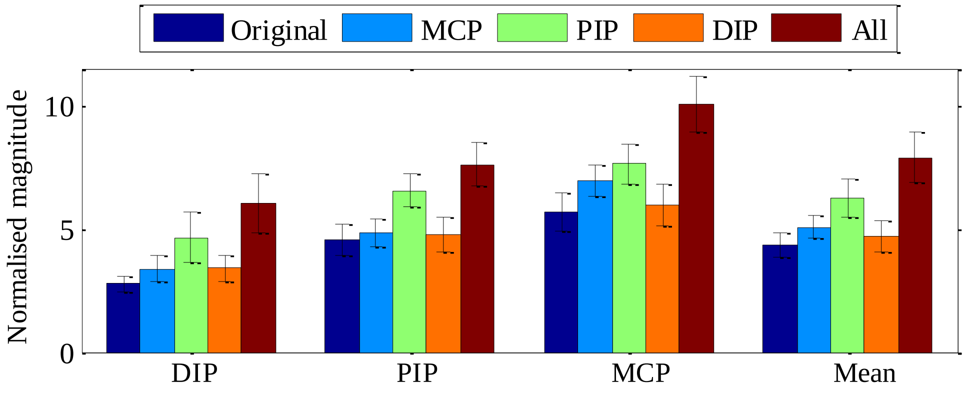

Figure 8.16: *Comparison between predicted nJRF from scaled anatomical data and subject specific measurements of the FDP moment arm. The four groups represent the joint reaction force at each individual joint and the mean. The five bars represent; the original scaled anatomy, subject specific anatomy applied individually to the DIP, PIP and MCP joints and finally with it applied to all joints simultaneously.*

8.7 Discussion

The aim of this study was to determine the suitability of the combined ultrasound and stereo-phorogrammetric technique for measuring the moment arms of the finger flexors.

Firstly it had to be determined if the ACSs of the finger could be accurately tracked in the same coordinate system as positions measured in an ultrasound image. The low profile of the markers used for kinematic analysis using the PTT make it suitable for use when the subject has to interact with other objects as it put little restriction on their movement.

Unlike the previous combined method (Manal et al., 2010) the joint axes were defined functionally. This meant no assumption needed to be made about how the joint axes lay relative to external landmarks. Although this hasn't been specifically investigated for the fingers, this assumption is known to be unsafe at other joints (Della Croce et al., 2005).

Tracking the ultrasound probe head was straightforward using a technical cluster rigidly fixed upon it. It was important to calibrate the ultrasound image plane relative to this cluster (Prager et al., 1998). From review of available methods it was decided to use the Cambridge stylus phantom (Hsu et al., 2008) to calibrate this image plane. The speed and ease of calibration made it practical in a clinical context whilst still achieving the same accuracy as the more time consuming methods. Although it was possible to use an automated digitisation routine, in this case it was done manually. It was shown that any manual repeatability inaccuracies were less than the overall precision. For wider applications automated digitisation could be used to save time, but for this small study the manual process was deemed adequate. This calibration procedure was an improvement on that previously used by Manal et al (2010), who are the only previous authors to measure moment arms in this way. The assumptions made by these authors in how the scan plane lies relative to the probe casing could have greatly affected their results.

As shown in Chapter 7, there is significant variation in the moment arm calculated or measured depending on the technique used. Additionally in Chapter 3, it was shown that these differences will have a significant effect on the predicted internal loading, hence the motivation to achieve a subject specific measurement. Figure 8.12, Figure 8.13 and Figure 8.14, show that the measurements made by this study lay in a similar region to the previous studies. There was a wide range in possible moment arms when using previously published data, resulting in up to a 6.6mm difference in some cases. The moment arms measured using the combined method are subject to an experimental error of up to 2.2mm and there is significant scatter observed. However, because of the wide range of moment arms possible when using previously published data, the subject specific measurement was considered an improvement.

As observed in Chapter 7 some of the previous methods give erroneous results at extreme angles of flexion. My combined technique attempted to address this by measuring the moment arms at as high degrees of flexion as possible. Because of limitations in maintaining an acoustic contact with the finger it was only possible to measure up to 50°-55°. This was less than was anticipated and less than the 110° of PIP flexion measured by Fowler et al (2001). This is a compromise using this technique reducing its applicability to situations where the joint is highly flexed. The results can still be extrapolated, although this would be subject to errors and should be used with care.

Figure 8.15 and Figure 8.16 show that application of these subject specific moment arms would have a significant effect on the predicted internal loading. The difference in moment arm of the FDP correlated with a change in the required tension in this tendon.

An increase in moment arm at the DIP resulted in reduced tension and the decreased moment arm at the other two joints resulted in a greater tension. Overall the mean nJRF always increased due to increases in the tension in the extensors. This was particularly evident when the subject specific moment arm was applied to the PIP joint. For this degree of flexion (25.3°) the moment arm was decreased to 7.0mm compared to 8.3mm when using the original moment arm scaled from An et al (1979). The resulting increase in mean nJRF was significant and when subject specific measurements were used at all joints resulted in an increase of over 80%. If this predicted internal loading is considered true (if we were to ignore my own experimental errors), the implications of using subject specific anatomy are large. The internal forces could be much greater than previously thought. This could have a significant effect on the design of joint replacements or planning rehabilitation for a patient.

Although the moment arms measured in my study fall within the range defined previously in the literature, the limitations must also be considered. As previously mentioned the errors in ultrasound measurement could be over 2mm, which would significantly change any result. What is of greatest concern however is the positioning of the probe head and identification of the tendon in the ultrasound image.

Identification of the correct tendons should also be considered. Sound knowledge of the anatomy is required to correctly identify the tendons crossing the joint. The use of video rather than still images made identification of the flexor tendons easier as they could be identified as the subject flexed their finger.

This method is not suitable for the extensors for two reasons. Firstly they lie much closer to the skin surface making identification difficult. Secondly and more importantly maintaining an ultrasound contact with the dorsal surface of the finger is impossible with the marker set used, this is a major drawback. The reason for the continued use of this marker set is highlighted by the results in Chapter 3. This showed that it was changes in the moment arm of the flexors that would have the most significant effect on the internal loading. Therefore if only the FDP can be measured on a subject specific basis there would still be an improved prediction of the internal loading.

8.8 Conclusions

The method described in this chapter extended the work of Manal et al (2010) to measure subject specific moment arms of the FDP in the finger using a geometric method. The issues associated with identifying the joint axes of rotation were addressed by using the PTT. The ultrasound scan plane was calibrated using the Cambridge stylus which has been shown to be the most accurate and useable of the methods currently available.

The subject specific moment arms measured were found to be within the range reported in previous literature. These previous methods relied on scaling from cadavers or some form of modelling to calculate the moment arms. When applied to the biomechanical model the subject specific measurements were found to significantly affect the results increasing the mean internal loading by 84%. If the subject had any injury or pathology that needed to be addressed this difference would no doubt affect the treatment plan.

My method was not without its drawbacks. It was only suitable for measurement of the flexor tendons due to the markers on the dorsal surface of the finger. It would be possible to scan the dorsal surface of the hand if it was submerged in a water bath, but this would make it impossible to track the hand using stereo-photogrammetry. The size of my study was limited to a single healthy subject. This was enough to show proof of concept of the method, but a larger study would be needed to validate it fully.

Subject specific measurement is of greatest use for abnormal subjects, e.g. those with a deformity, injury or pathology that makes their anatomy different. This can also include children, as most datasets used for anthropometric scaling are based on adult specimens. Suggested future work would involve at least one of these groups. Aims would be to both show its applicability and also the significance of using subject specific rather than scaled anatomy in predicting internal loading in these cases.

Chapter 9. Summary and directions of future work

The overall aims of this study were first to understand the most influential factors in the prediction of internal loading of the fingers using a biomechanical model and their effect on model error. Secondly it was to propose and assess new methods of kinematic analysis and subject specific anatomical measurement.

Through comparison of two different published models it was found that the most significant difference between them was the way in which the proximal interphalangeal (PIP) joint was modelled. A more complex model of this joint using more than a single degree of freedom required accurate measurement of the subject specific anatomy. In the absence of such accurate measurement, tendon tensions and joint reaction forces (JRFs) were predicted as being unrealistically large.

When using a model with simpler joint kinematics, the anatomical measurements were found to be a significant factor. Sensitivity analysis showed that for the open handed grip case the most highly loaded tendons (in this case the flexor tendons) were in absolute terms, the most sensitive to any change in their moment arms. The sensitivity analysis was also used to find coefficients to transform between errors in the position of the joint centres and errors in the predicated JRF. This was used subsequently in assessing the suitability of a new kinematic analysis technique.

For kinematic analysis of the fingers a new marker set was proposed using 4mm hemispherical markers. These markers had minimal protrusion from the surface of the hand and were of minimal weight so as to limit any restriction on the subjects' movement. Using this marker set combined with calibration movements it was possible to define the anatomical coordinate system of each finger segment, using functional axes. Two methods of functional calibration were assessed, the first referred to the phalanx fitting technique (PFT) and the second as the phalanx transformation technique (PTT). It was found that once the joint position errors had been transformed into those in predicted JRF, the errors using the PFT were 6.3% compared to 2.2% using the PTT. From this it could be concluded that in application to the fingers the PTT was more suitable.

Both the PTT and PFT relied on the subject having some mobility of their joints so they could carry out the calibration movements. This is not always possible for subjects who have a restriction due to an injury or pathology. It was found that reducing the calibration range of motion available, to that of a subject with a range of motion (RoM) typical of pathological mobility, increased the errors in predicted JRF when using the PTT to 4.4%. Although this gives an indication of the technique's applicability to subjects with reduced RoM, it is important to understand that this technique will not be suitable for all subjects. For those with severely restricted movement or fixed deformity it will not be possible to perform the analysis in this way.

The final part of this thesis was the development and assessment of a method of measuring the moment arms and lines of action of the flexor tendons using combined ultrasound and stereo-photogrammetry. It was shown that previous methods of measuring these properties could produce varying results, affecting the predicted JRF by more than 100%. The measurements made in this study produced moment arms within the range of those previously proposed. The use of these subject specific moment arms resulted in a significant change in the predicted JRF by up to 84%. Although potentially an improvement of previous methods of anthropometric scaling and expensive imaging methods such as magnetic resonance imaging (MRI), this combined technique was not without its drawbacks which are discussed in the recommendations for future work.

9.1 Direction of future work

For understanding the limitations of this study, a set of recommendations and possibilities for future investigation are proposed.

A more detailed comparison of existing finger models could be carried out including more model types and anatomical measurements. In this thesis it was chosen to examine only two contrasting models to give an indication of the variation possible from the same experimental measurements. A more comprehensive study could provide cross-validation between more of the models.

Both sensitivity analyses did not include interaction effects and the errors were applied linearly. This was because the aim of the study was not only to gain an understanding of the errors but also to identify factors that could improve the overall model accuracy. A more complex numerical simulation would include errors in all variables applied with realistic Gaussian distributions. This would give a more robust estimate of error in the final prediction of internal loading, but would require significantly greater computer run time and statistical analysis.

It would be of more clinical relevance if a full set of activities of daily living were assessed rather than a single open handed grip type. The effect of the different models and any inaccuracies of measurement could then be quantified in more ‘real world’ applications such as those measured by Fowler and Nicol (199b).

The marker set and method of defining the joint axes functionally has only been applied to a small number (13) of subjects. A more comprehensive study involving a wider variety of subjects would be useful to show the applicability of this technique. Additionally it was only used for assessment of the index finger (digit two). In theory it can be applied in a similar manner to digits three, four and five. The thumb (digit one) is more complex because the metacarpal has more freedom to rotate relative to the carpal bones. The kinematics of the thumb would need to be quantified in detail to define an appropriate method of defining the joint axes functionally.

This study utilised small 4mm hemispherical markers. This was to reduce any restriction on the subject. It does compromise the accuracy due to cluster deformation however, and this could affect the results of the more detailed multiple arc analysis carried out in Chapter 6. To enable greater accuracy, the cluster technical frames could be defined using triads of clusters. These rigid clusters avoid the issues such as cluster deformation and provide more visibility to the cameras as well as reducing skin movement artefact. A comparison could be made between this kind of technique and the surface mounted markers used in my study to quantify the compromise on accuracy due to using the hemispherical markers.

Both the PTT and PFT require some form of anatomical pointing to define hinge joints. The ability to define this kind of joint fully without the need for any observer input would be worthwhile.

It is important to note that only healthy subjects were used in this thesis, principally because it was concerned with method development rather than its application to a particular study. Use with other subjects with pathology such as osteo or rheumatoid arthritis might highlight deficiencies in the method not encountered with the healthy group. An attempt has been made to address this by examining the importance of the calibration range of motion. But this was only a simulation, as was discussed in previous chapters these subjects could also have severe deformity of the joint causing a change in the kinematics. A true validation can only be obtained by use with the subject group of interest.

The combined ultrasound and stereo-photogrammetric technique for finding the flexor digitorum profundus moment arm attempted to address some of the issues highlighted in Chapter 3 with regard to subject specific measurement. Although it did this to some extent there is still much work to be done.

The method of image calibration required manual digitisation of the phantom position. Although it was shown that this would not adversely affect the results it would be time consuming for a larger study. An automated technique was proposed by Hsu et al (2008). It would be of interest to apply a similar technique and compare it with the manual digitisation method.

It was not possible to measure the moment arms at as high degrees of flexion as was initially hoped. Because of the size of the probe head it could not be held with an acoustic contact as the finger was highly flexed. To address this, a system could be used with the hand submerged in a water bath. A new method of defining the joint axes would need to be used however as it is not possible to use retro-reflective markers submerged in water.

It was discussed in Chapter 7 that there are many compromises with static imaging such as MRI. The problems of static imaging and lack of clarity of muscle and tendon were noted. The advantages of such methods should not be discounted however, particularly as the field of medical imaging is constantly improving. The use of ultra-short echo time (UTE) sequencing and magic angle scanning can allow measurement of the required soft tissues. The ability to measure the subject without the application of markers would be desirable to the clinicians. A worthwhile avenue of future study would be to compare the moment arms measured using the proposed combined method and more traditional imaging. This would allow cross validation of methods and increase the number of options available for measurement as well as increase confidence in the results.

A potential application of this work would be to aid in the design of finger joint replacement. The success of these replacements is not as great as those achieved at the larger joints in the lower limb, mainly down to failure of the component itself. Through the techniques described in this thesis greater understanding of internal loading and joint kinematics at different stages of disease progression could be achieved. This in turn could guide designs of future prosthesis.

Many of the techniques described in this thesis although developed for the fingers could equally be applied to different joints of the body with little modification. This applies both to the sensitivity analyses, the assessment of the kinematic analysis and combined ultrasound and stereo-photogrammetry. It would be interesting to see how this work could be applied to larger joints more widely studied in the biomechanics community.

References

Addis, P. R. and Lawson, S. E. M. (2010) 'The role of tendon stiffness in development of equine locomotion with age', *Equine Veterinary Journal (Supplement)*, 42 (Suppl. 38), pp. 556-560.

An, K. N., Chao, E. Y., Cooney, W. P. and Linscheid, R. L. (1979) 'Normative model of human hand for biomechanical analysis', *Journal of Biomechanics*, 12, pp. 775-788.

An, K. N., Kwak, B. M., Chao, E. Y. and Morrey, B. F. (1984) 'Determination of muscle and joint forces: A new technique to solve the indeterminate problem', *Transactions of the ASME, Journal of Biomechanical Engineering*, 106, pp. 364-367.

An, K. N., Ueba, Y., Chao, E. Y., Cooney, W. P. and Linscheid, R. L. (1983) 'Tendon excursion and moment arms of index finger muscles', *Journal of Biomechanics*, 16, (6), pp. 419-425.

Andriacchi, T. P. and Alexander, E. J. (2000) 'Studies of human locomotion: past, present and future', *Journal of Biomechanics*, 33, (10), pp. 1217-1224.

Andriacchi, T. P., Alexander, E. J., Toney, M. K., Dyrby, C. and Sum, J. (1998) 'A point cluster method for in Vivo motion analysis: applied to a study of knee kinematics', *Journal of Biomedical Engineering*, 120, pp. 743-749.

Arnold, A. S., Salinas, S., Asakawa, D. J. and Delp, S. L. (2000) 'Accuracy of muscle moment arms estimated from MRI-based musculoskeletal models of the lower extremity', *Computer Aided Surgery*, 5, pp. 108-119.

Benjamin, M., Milz, S. and Bydder, G. M. (2008) 'Magnetic resonance imaging of entheses. Part 1', *Clinical Radiology*, 63, (6), pp. 691-703.

Biggs, J. and Horch, K. (1999) 'A three-dimensional kinematic model of the human long finger and the muscles that actuate it', *Medical Engineering & Physics,* 21, (9), pp. 625-639.

Bisi, M. C., Riva, F. and Stagni, R. (2011) 'A non invasive protocol to estimate muscle tendon lengths and moment arms through ultrasound images', *Gait & Posture,* 33, Supplement 1, (0), pp. S28-S29.

Blemker, S. S., Asakawa, D. S., Gold, G. E. and Delp, S. L. (2007) 'Image-based musculoskeletal modeling: Applications, advances, and future opportunities', *Journal of Magnetic Resonance Imaging,* 25, (2), pp. 441-451.

Brook, N., Mizrahi, J., Shoham, M. and Dayan, J. (1995) 'A biomechanical model of index finger dynamics', *Medical Engineering & Physics,* 17, (1), pp. 54-63.

Buczek, F. L., Sinsel, E. W., Gloekler, D. S., Wimer, B. M., Warren, C. M. and Wu, J. Z. (2011) 'Kinematic performance of a six degree-of-freedom hand model (6DHand) for use in occupational biomechanics', *Journal of Biomechanics,* 44, (9), pp. 1805-1809.

Buford, J. W. L., Koh, S., Andersen, C. R. and Viegas, S. F. (2005) 'Analysis of Intrinsic-Extrinsic Muscle Function Through Interactive 3-Dimensional Kinematic Simulation and Cadaver Studies', *The Journal of Hand Surgery,* 30, (6), pp. 1267-1275.

Cappozzo, A., Catani, F., Leardini, A., Benedetti, M. G. and Della Croce, U. (1996) 'Position and orientation in space of bones during movement: experimental artefacts', *Clinical Biomechanics,* 11, (2), pp. 90-100.

Cappozzo, A., Della Croce, U., Leardini, A. and Chiari, L. (2005) 'Human movement analysis using stereophotogrammetry: Part 1: theoretical background', *Gait & Posture,* 21, (2), pp. 186-196.

Carpinella, I., Mazzoleni, P., Rabuffetti, M., Thorsen, R. and Ferrarin, M. (2006) 'Experimental protocol for the kinematic analysis of the hand: Definition and repeatability', *Gait & Posture,* 23, (4), pp. 445-454.

Cerveri, P., Lopomo, N., Pedotti, A. and Ferrigno, G. (2005) 'Derivation of Centers and Axes of Rotation for Wrist and Fingers in a Hand Kinematic Model: Methods and Reliability Results', *Annals of Biomedical Engineering,* 33, (3), pp. 402-412.

Chao, E. Y. S., An, K. N., Cooney, W. P. and Linscheid, R. L. (1989) *Biomechanics of the hand, a basic research study.* World Scientific.

Chiu, H. Y., Su, F. C., Wang, S. T. and Hsu, H. Y. (1998) 'The motion analysis system and goniometry of the finger joints', *The Journal of Hand Surgery: Journal of the British Society for Surgery of the Hand,* 23, (6), pp. 788-791.

Chung, K. C., Kotsis, S. V. and Kim, H. M. (2004) 'A prospective outcomes study of Swanson Metacarpophalangeal Joint Arthroplasty for the rheumatoid hand', *The Journal of Hand Surgery,* 29, (4), pp. 646-653.

Chung, K. C., Kotsis, S. V., Wilgis, E. F. S., Fox, D. A., Regan, M., Kim, H. M. and Burke, F. D. (2009) 'Outcomes of Silicone Arthroplasty for Rheumatoid Metacarpophalangeal Joints Stratified by Fingers', *The Journal of Hand Surgery,* 34, (9), pp. 1647-1652.

Degeorges, R., Parasie, J., Mitton, D., Imbert, N., Goubier, J. N. and Lavaste, F. (2005) 'Three-dimensional rotations of human three-joint fingers: an optoelectronic measurement. Preliminary results', *Surgical and Radiologic Anatomy,* 27, (1), pp. 43-50.

Della Croce, U., Leardini, A., Chiari, L. and Cappozzo, A. (2005) 'Human movement analysis using stereophotogrammetry: Part 4: assessment of anatomical landmark misplacement and its effects on joint kinematics', *Gait & Posture,* 21, (2), pp. 226-237.

Ehrig, R. M., Heller, M. O., Kratzenstein, S., Duda, G. N., Trepczynski, A. and Taylor, W. R. (2011) 'The SCoRE residual: A quality index to assess the accuracy of joint estimations', *Journal of Biomechanics,* 44, (7), pp. 1400-1404.

Ehrig, R. M., Taylor, W. R., Duda, G. N. and Heller, M. O. (2006) 'A survey of formal methods for determining the centre of rotation of ball joints', *Journal of Biomechanics,* 39, (15), pp. 2798-2809.

Ehrig, R. M., Taylor, W. R., Duda, G. N. and Heller, M. O. (2007) 'A survey of formal methods for determining functional joint axes', *Journal of Biomechanics,* 40, (10), pp. 2150-2157.

Erdemir, A., McLean, S., Herzog, W. and van den Bogert, A. J. (2007) 'Model-based estimation of muscle forces exerted during movements', *Clinical Biomechanics,* 22, (2), pp. 131-154.

Esteki, A. and Mansour, J. (1997) 'A dynamic model of the hand with application in functional neuromuscular stimulation', *Annals of Biomedical Engineering,* 25, (3), pp. 440-451.

Fath, F., Blazevich, A. J., Waugh, C. M., Miller, S. C. and Korff, T. (2010) 'Direct comparison of in vivo Achilles tendon moment arms obtained from ultrasound and MR scans', *Journal of Applied Physiology,* 109, (6), pp. 1644-1652.

Fenster, A., Downey, D. B. and Cardinal, H. N. (2001) 'Three-dimensional ultrasound imaging', *Physics in Medicine and Biology,* 46, pp. 67-99.

Finni, T., Komi, P. V. and Lukkariniemi, J. (1998) 'Achilles tendon loading during walking: application of a novel optic fiber technique', *European Journal of Applied Physiology and Occupational Physiology,* 77, (3), pp. 289-291.

Fowler, N. K. and Nicol, A. C. (1999a) 'A force transducer to measure individual finger loads during activities of daily living', *Journal of Biomechanics,* 32, (7), pp. 721-725.

Fowler, N. K. and Nicol, A. C. (1999b) 'Measurement of external three-dimensional interphalangeal loads applied during activities of daily living', *Clinical Biomechanics,* 14, (9), pp. 646-652.

Fowler, N. K. and Nicol, A. C. (2000) 'Interphalangeal joint and tendon forces: normal model and biomechanical consequences of surgical reconstruction', *Journal of Biomechanics*, 33, (9), pp. 1055-1062.

Fowler, N. K., Nicol, A. C., Condon, B. and Hadley, D. (2001) 'Method of determination of three dimensional index finger moment arms and tendon lines of action using high resolution MRI scans', *Journal of Biomechanics,* 34, (6), pp. 791-797.

Franko, O. I., Winters, T. M., Tirrell, T. F., Hentzen, E. R. and Lieber, R. L. (2011) 'Moment arms of the human digital flexors', *Journal of Biomechanics,* 44, (10), pp. 1987-1990.

Fry, N. R., Childs, C. R., Eve, L. C., Gough, M., Robinson, R. O. and Shortland, A. P. (2003) 'Accurate measurement of muscle belly length in the motion analysis laboratory: potential for the assessment of contracture', *Gait & Posture,* 17, (2), pp. 119-124.

Fry, N. R., Gough, M. and Shortland, A. P. (2004) 'Three-dimensional realisation of muscle morphology and architecture using ultrasound', *Gait & Posture,* 20, (2), pp. 177-182.

Gamage, S. S. H. U. and Lasenby, J. (2002) 'New least squares solutions for estimating the average centre of rotation and the axis of rotation', *Journal of Biomechanics,* 35, (1), pp. 87-93.

Gatehouse, P. D. and Bydder, G. M. (2003) 'Magnetic resonance imaging of short T2 components in tissue', *Clinical Radiology,* 58, (1), pp. 1-19.

Geiser, E. A., Christie, L. G., Conetta, D. A., Conti, C. R. and Gossman, G. S. (1982) 'A mechanical arm for spatial registration of two-dimensional echocardiographic sections', *Catheterization and Cardiovascular Diagnosis,* 8, (1), pp. 89-101.

Gislason, M. K., Nash, D. H., Nicol, A., Kanellopoulos, A., Bransby-Zachary, M., Hems, T., Condon, B. and Stansfield, B. (2009) 'A three-dimensional finite element model of maximal grip loading in the human wrist', *Proceedings of the Institution of Mechanical Engineers, Part H: Journal of Engineering in Medicine,* 223, (7), pp. 849-861.

Gold, G. E., Thedens, D. R., Pauly, J. M., Fechner, K. P., Bergman, G., Beaulieu, C. F. and Macovski, A. (1998) 'MR imaging of articular cartilage of the knee: new methods using ultrashort TEs', *Am. J. Roentgenol.*, 170, (5), pp. 1223-1226.

Gold, G. E., Wren, T. A. L., Nayak, K., Nishimura, D. G. and Beaupre, G. (2001) 'In vivo short echo time imaging of achilles tendon', *Proc Intl Soc Mag Reson Med*, 9, pp. 244.

Goldfarb, C. A. and Stern, P. J. (2003) 'Metacarpophalangeal Joint Arthroplasty in Rheumatoid Arthritis: A Long-Term Assessment', *J Bone Joint Surg Am,* 85, (10), pp. 1869-1878.

Goodson, A., McGregor, A. H., Douglas, J. and Taylor, P. (2007) 'Direct, quantitative clinical assessment of hand function: Usefulness and reproducibility', *Manual Therapy,* 12, (2), pp. 144-152.

Halvorsen, K. (2003) 'Bias compensated least squares estimate of the center of rotation', *Journal of Biomechanics,* 36, (7), pp. 999-1008.

Halvorsen, K., Lesser, M. and Lundberg, A. (1999) 'A new method for estimating the axis of rotation and the center of rotation', *Journal of Biomechanics,* 32, (11), pp. 1221-1227.

Harrington, M. E., Zavatsky, A. B., Lawson, S. E. M., Yuan, Z. and Theologis, T. N. (2007) 'Prediction of the hip joint centre in adults, children, and patients with cerebral palsy based on magnetic resonance imaging', *Journal of Biomechanics,* 40, (3), pp. 595-602.

Henkelman, R. M., Stanisz, G. J. and Graham, G. J. (2001) 'Magnetization transfer in MRI: a review', *NMR in Biomedicine,* 14, pp. 57-64.

Holcomb, G. R., Irving, T. E. and Smith, D. (1958) 'Coronal deviation and tilt in the proximal interphalangeal joints of man', *Journal of Anthropology,* 16, pp. 429-440.

Hsu, P.-W., Treece, G. M., Prager, R. W., Houghton, N. E. and Gee, A. H. (2008) 'Comparison of Freehand 3-D Ultrasound Calibration Techniques Using a Stylus', *Ultrasound in Medicine & Biology,* 34, (10), pp. 1610-1621.

Hughes, S. W., D'Arcy, T. J., Maxwell, D. J., Chiu, W., Milner, A., Saunders, J. E. and Sheppard, R. J. (1996) 'Volume estimation from multiplanar 2D ultrasound images using a remote electromagnetic position and orientation sensor', *Ultrasound in Medicine & Biology,* 22, (5), pp. 561-572.

Ito, M., Akima, H. and Fukunaga, T. (2000) 'In vivo moment arm determination using B-mode ultrasonography', *Journal of Biomechanics,* 33, (2), pp. 215-218.

Jennings, C. D. and Livingstone, D. P. (2008) 'Surface Replacement Arthroplasty of the Proximal Interphalangeal Joint Using the PIP-SRA Implant: Results, Complications, and Revisions', *The Journal of Hand Surgery,* 33, (9), pp. 1565.e1-1565.e11.

Kavanagh, J. J. and Menz, H. B. (2008) 'Accelerometry: A technique for quantifying movement patterns during walking', *Gait & Posture,* 28, (1), pp. 1-15.

Keir, P. J. and Wells, R. P. (1999) 'Changes in geometry of the finger flexor tendons in the carpal tunnel with wrist posture and tendon load: an MRI study on normal wrists', *Clinical Biomechanics,* 14, (9), pp. 635-645.

Kociolek, A. M. and Keir, P. J. (2011) 'Modelling tendon excursions and moment arms of the finger flexors: Anatomic fidelity versus function', *Journal of Biomechanics,* 44, (10), pp. 1967-1973.

Komi, P. V., Salonen, M., Jarvinen, M. and Kokko, O. (1987) 'In vivo registration of achilles tendon forces in man I. methodological development', *International Journal of Sports Medicine (suppl),* 8, pp. 3-8.

Korstanje, J.-W. H., Schreuders, T. R., van der Sijde, J., Hovius, S. E. R., Bosch, J. G. and Selles, R. W. (2010a) 'Ultrasonographic Assessment of Long Finger Tendon Excursion in Zone V During Passive and Active Tendon Gliding Exercises', *The Journal of Hand Surgery,* 35, (4), pp. 559-565.

Korstanje, J.-W. H., Selles, R. W., Stam, H. J., Hovius, S. E. R. and Bosch, J. G. (2010b) 'Development and validation of ultrasound speckle tracking to quantify tendon displacement', *Journal of Biomechanics,* 43, (7), pp. 1373-1379.

Landsmeer, J. M. (1961) 'Studies in the anatomy of articulation. I. The equilibrium of the 'Intercalated' bone', *Acta Morphol Neerl Scand,* 3, pp. 287-303.

Leardini, A., Cappozzo, A., Catani, F., Toksvig-Larsen, S., Petitto, A., Sforza, V., Cassanelli, G. and Giannini, S. (1999) 'Validation of a functional method for the estimation of hip joint centre location', *Journal of Biomechanics,* 32, (1), pp. 99-103.

Lee, S. W., Chen, H., Towles, J. D. and Kamper, D. G. (2008) 'Estimation of the effective static moment arms of the tendons in the index finger extensor mechanism', *Journal of Biomechanics,* 41, (7), pp. 1567-1573.

Levine, R. A., Handschumacher, M. D., Sanfilippo, A. J., Hagege, A. A., Harrigan, P., Marshall, J. E. and Weyman, A. E. (1989) 'Three-dimensional echocardiographic reconstruction of the mitral valve, with implications for the diagnosis of mitral valve prolapse', *Circulation,* 80, (3), pp. 589-598.

Lluch, A. (2006) 'Examination of the rheumatoid hand and wrist', *International Congress Series*, 1295, pp. 9-26.

Maganaris, C. N. (2004) 'Imaging-based estimates of moment arm length in intact human muscle-tendons ', *European Journal of Applied Physiology,* 91, pp. 130-139.

Maganaris, C. N., Baltzopoulos, V. and Sargeant, A. J. (1998) 'Changes in achilles tendon moment arm from rest to maximum isometric plantarflexion: in vivo observations in man', *The Journal of Physiology,* 510, (3), pp. 977-985.

Maganaris, C. N., Baltzopoulos, V. and Sargeant, A. J. (2000) 'In vivo measurement-based estimations of the human Achilles tendon moment arm', *European Journal of Applied Physiology,* 83, (4), pp. 363-369.

Manal, K., Cowder, J. D. and Buchanan, T. S. (2010) 'A hybrid method for computing achilles tendon moment arm using ultrasound and motion analysis', *Journal of Applied Biomechanics,* 26, (2), pp. 224-228.

Marin, F. d. r., Mannel, H., Claes, L. and DÃ¼rselen, L. (2003) 'Accurate Determination of a Joint Rotation Center Based on the Minimal Amplitude Point Method', *Computer Aided Surgery,* 8, (1), pp. 30-34.

Marsden, S. P. and Swailes, D. C. (2008) 'A novel approach to the prediction of musculotendon paths', *Proceedings of the Institution of Mechanical Engineers, Part H: Journal of Engineering in Medicine,* 222, (1), pp. 51-61.

Masjedi, M. (2009) *Preclinical testing and patient specific implantation/design of shoulder prosthesis.* thesis. Newcastle University.

Metcalf, C. D., Notley, S. V., Chappell, P. H., Burridge, J. H. and Yule, V. T. (2008) 'Validation and Application of a Computational Model for Wrist and Hand Movements Using Surface Markers', *Biomedical Engineering, IEEE Transactions on,* 55, (3), pp. 1199-1210.

Miyata, N., Kouchi, M., Kurihara, T. and Mochimaru, M. (2004) *Intelligent Robots and Systems, 2004. (IROS 2004). Proceedings. 2004 IEEE/RSJ International Conference on.*

Mundermann, L., Corazza, S. and Andriacchi, T. (2006) 'The evolution of methods for the capture of human movement leading to markerless motion capture for biomechanical applications', *Journal of NeuroEngineering and Rehabilitation,* 3, (1), pp. 6.

Pagowski, S. and Piekarski, K. (1977) 'Biomechanics of the metacarpophalangeal joint', *Journal of Biomechanics,* 10, pp. 205-209.

Peters, A., Baker, R. and Sangeux, M. (2010) 'Validation of 3-D freehand ultrasound for the determination of the hip joint centre', *Gait & Posture,* 31, (4), pp. 530-532.

Peters, A., Galna, B., Sangeux, M., Morris, M. and Baker, R. 'Quantification of soft tissue artifact in lower limb human motion analysis: A systematic review', *Gait & Posture,* 31, (1), pp. 1-8.

Piazza, S. J., Okita, N. and Cavanagh, P. R. (2001) 'Accuracy of the functional method of hip joint center location: effects of limited motion and varied implementation', *Journal of Biomechanics,* 34, (7), pp. 967-973.

Prager, R. W., Rohling, R. N., Gee, A. H. and Berman, L. (1998) 'Rapid calibration for 3-D freehand ultrasound', *Ultrasound in Medicine & Biology,* 24, (6), pp. 855-869.

Qin, J., Lee, D., Li, Z., Chen, H. and Dennerlein, J. T. (2010) 'Estimating in vivo passive forces of the index finger muscles: Exploring model parameters', *Journal of Biomechanics,* 43, (7), pp. 1358-1363.

Raab, F. H., Blood, E. B., Steiner, T. O. and Jones, H. R. (1979) 'Magnetic Position and Orientation Tracking System', *Aerospace and Electronic Systems, IEEE Transactions on,* AES-15, (5), pp. 709-718.

Rash, G. S., Belliappa, P. P., Wachowiak, M. P., Somia, N. N. and Gupta, A. (1999) 'A demonstration of the validity of a 3-D video motion analysis method for measuring finger flexion and extension', *Journal of Biomechanics,* 32, (12), pp. 1337-1341.

Reuleaux, F. (1876) *Kinematics of Machinery.* London: Macmillan.

Robson, M. D., Benjamin, M., Gishen, P. and Bydder, G. M. (2004) 'Magnetic resonance imaging of the Achilles tendon using ultrashort TE (UTE) pulse sequences', *Clinical Radiology,* 59, (8), pp. 727-735.

Robson, M. D. and Bydder, G. M. (2006) 'Clinical ultrashort echo time imaging of bone and other connective tissues', *NMR in Biomedicine,* 19, (7), pp. 765-780.

Rousseau, F., Hellier, P., Letteboer, M. M. J., Niessen, W. J. and Barillot, C. (2006) 'Quantitative Evaluation of Three Calibration Methods for 3-D Freehand Ultrasound', *Medical Imaging, IEEE Transactions on,* 25, (11), pp. 1492-1501.

Rugg, S. G., Gregor, R. J., Mandelbaum, B. R. and Chiu, L. (1990) 'In vivo moment arm calculations at the ankle using magnetic resonance imaging (MRI)', *Journal of Biomechanics,* 23, (5), pp. 495-501.

Sancho-Bru, J. L., Pérez-González, A., Vergara-Monedero, M. and Giurintano, D. (2001) 'A 3-D dynamic model of human finger for studying free movements', *Journal of Biomechanics,* 34, (11), pp. 1491-1500.

Sancho-Bru Joaquin, L., Perez-Gonzalez, A., Vergara, M. and Giurintano, D. J. (2003) 'A 3D Biomechanical Model of the Hand for Power Grip', *Journal of Biomechanical Engineering,* 125, (1), pp. 78-83.

Scheys, L., Spaepen, A., Suetens, P. and Jonkers, I. (2008) 'Calculated moment-arm and muscle-tendon lengths during gait differ substantially using MR based versus rescaled generic lower-limb musculoskeletal models', *Gait & Posture,* 28, (4), pp. 640-648.

Schöffl, I., Oppelt, K., Jüngert, J., Schweizer, A., Neuhuber, W. and Schöffl, V. (2009) 'The influence of the crimp and slope grip position on the finger pulley system', *Journal of Biomechanics,* 42, (13), pp. 2183-2187.

Schuind, F., Garcia-Elias, M., Cooney Iii, W. P. and An, K.-N. (1992) 'Flexor tendon forces: In vivo measurements', *The Journal of Hand Surgery,* 17, (2), pp. 291-298.

Schwartz, M. H. and Rozumalski, A. (2005) 'A new method for estimating joint parameters from motion data', *Journal of Biomechanics,* 38, (1), pp. 107-116.

Schweizer, A. (2001) 'Biomechanical properties of the crimp grip position in rock climbers', *Journal of Biomechanics,* 34, (2), pp. 217-223.

Schweizer, A., Frank, O., Ochsner, P. E. and Jacob, H. A. C. (2003) 'Friction between human finger flexor tendons and pulleys at high loads', *Journal of Biomechanics,* 36, (1), pp. 63-71.

Shakarji, C. M. (1998) 'Least-squares fitting algorithms of the NIST algorithm testing system', *Journal of Research of the National Institute of Standards and Technology,* 103, (6), pp. 633-641.

Shea, K. M., Lenhoff, M. W., Otis, J. C. and Backus, S. I. (1997) 'Validation of a method for location of the Hip Joint Center', *Gait & Posture,* 5, (2), pp. 157-158.

Simon, S. R. (2004) 'Quantification of human motion: gait analysis--benefits and limitations to its application to clinical problems', *Journal of Biomechanics,* 37, (12), pp. 1869-1880.

Stokes, I. A. F. (1981) *Mechanical factors and the skeleton.* London: John Libbey.

Su, F. C., Chou, Y. L., Yang, C. S., Lin, G. T. and An, K. N. (2005) 'Movement of finger joints induced by synergistic wrist motion', *Clinical Biomechanics,* 20, (5), pp. 491-497.

Taylor, W. R., Kornaropoulos, E. I., Duda, G. N., Kratzenstein, S., Ehrig, R. M., Arampatzis, A. and Heller, M. O. (2010) 'Repeatability and reproducibility of OSSCA, a functional approach for assessing the kinematics of the lower limb', *Gait & Posture,* 32, (2), pp. 231-236.

Taylor, W. R., Rainald, M. E., Georg, N. D., Hanna, S., Petra, S. and Markus, O. H. (2005) 'On the influence of soft tissue coverage in the determination of bone kinematics using skin markers', *Journal of Orthopaedic Research,* 23, (4), pp. 726-734.

Tong, S., Downey, D. B., Cardinal, H. N. and Fenster, A. (1996) 'A three-dimensional ultrasound prostate imaging system', *Ultrasound in Medicine & Biology,* 22, (6), pp. 735-746.

Tsaopoulos, D. E., Baltzopoulos, V. and Maganaris, C. N. (2006) 'Human patellar tendon moment arm length: Measurement considerations and clinical implications for joint loading assessment', *Clinical Biomechanics,* 21, (7), pp. 657-667.

Tyler, D. J., Robson, M. D., Henkelman, M., Young, I. R. and Bydder, G. M. (2007) 'Magnetic resonance imaging with ultrashort TE (UTE) PULSE sequences: technical considerations', *Journal of Magnetic Resonance Imaging,* 25, pp. 279-289.

Valero-Cuevas, F. J., Zajac, F. E. and Burgar, C. G. (1998) 'Large index-fingertip forces are produced by subject-independent patterns of muscle excitation', *Journal of Biomechanics,* 31, (8), pp. 693-703.

Veltink, P. H., Slycke, P., Hemssems, J., Buschman, R., Bultstra, G. and Hermens, H. (2003) 'Three dimensional inertial sensing of foot movements for automatic tuning of a two-channel implantable drop-foot stimulator', *Medical Engineering & Physics,* 25, (1), pp. 21-28.

Vergara, M., Sancho-Bru, J. L. and Perez-Gonzalez, A. (2003) 'Description and validation of a non-invasive technique to measure the posture of all hand segments', *Journal of Biomechanical Engineering,* 125, (6), pp. 917-922.

Vigouroux, L., Quaine, F., Labarre-Vila, A., Amarantini, D. and Moutet, F. (2007) 'Using EMG data to constrain optimization procedure improves finger tendon tension estimations during static fingertip force production', *Journal of Biomechanics,* 40, (13), pp. 2846-2856.

Vigouroux, L., Quaine, F., Labarre-Vila, A. and Moutet, F. (2006) 'Estimation of finger muscle tendon tensions and pulley forces during specific sport-climbing grip techniques', *Journal of Biomechanics,* 39, (14), pp. 2583-2592.

Vigouroux, L., Quaine, F., Paclet, F., Colloud, F. and Moutet, F. (2008) 'Middle and ring fingers are more exposed to pulley rupture than index and little during sport-climbing: A biomechanical explanation', *Clinical Biomechanics,* 23, (5), pp. 562-570.

Warlow, O. M. E. and Johnson, G. R. (2012) 'Sensitivity of a biomechanical model of the finger to errors in experimental input', *Proceedings of the Institution of Mechanical Engineers, Part H: Journal of Engineering in Medicine,* Accepted.

Warlow, O.M.E. and Lawson, S.E.M. (2012) ‘A technique of motion capture of the finger using functional joint centres and the effect of calibration range of motion on its accuracy’, *Proceedings of the Institution of Mechanical Engineers, Part H: Journal of Engineering in Medicine*, 226, (5), pp. 360-367.

Westerhoff, P., Graichen, F., Bender, A., Rohlmann, A. and Bergmann, G. (2009) 'An instrumented implant for in vivo measurement of contact forces and contact moments in the shoulder joint', *Medical Engineering & Physics,* 31, (2), pp. 207-213.

Wilson, D. L., Zhu, Q., Duerk, J. L., Mansour, J. M., Kilgore, K. and Crago, P. E. (1999) 'Estimation of tendon moment arms from three-dimensional magnetic resonance images', *Annals of Biomedical Engineering,* 27, (2), pp. 247-256.

Woltring, H. J. (1991) 'Representation and calculation of 3-D joint movement', *Human Movement Science,* 10, (5), pp. 603-616.

Woltring, H. J., Huiskes, R., de Lange, A. and Veldpaus, F. E. (1985) 'Finite centroid and helical axis estimation from noisy landmark measurements in the study of human joint kinematics', *Journal of Biomechanics,* 18, (5), pp. 379-389.

Wu, G., Siegler, S., Allard, P., Kirtley, C., Leardini, A., Rosenbaum, D., Whittle, M., D'Lima, D. D., Cristofolini, L., Witte, H., Schmid, O. and Stokes, I. (2002) 'ISB recommendation on definitions of joint coordinate system of various joints for the reporting of human joint motion--part I: ankle, hip, and spine', *Journal of Biomechanics,* 35, (4), pp. 543-548.

Wu, G., van der Helm, F. C. T., Veeger, H. E. J., Makhsous, M., Van Roy, P., Anglin, C., Nagels, J., Karduna, A. R., McQuade, K., Wang, X., Werner, F. W. and Buchholz, B. (2005) 'ISB recommendation on definitions of joint coordinate systems of various joints for the reporting of human joint motion--Part II: shoulder, elbow, wrist and hand', *Journal of Biomechanics,* 38, (5), pp. 981-992.

Wu, J. Z., An, K.-N., Cutlip, R. G., Krajnak, K., Welcome, D. and Dong, R. G. (2008) 'Analysis of musculoskeletal loading in an index finger during tapping', *Journal of Biomechanics,* 41, (3), pp. 668-676.

Wu, J. Z., An, K. N., Cutlip, R. G. and Dong, R. G. (2010) 'A practical biomechanical model of the index finger simulating the kinematics of the muscle/tendon excursions', *Bio-Medical Materials and Engineering,* 20, (2), pp. 89-97.

Zhang, X., Lee, S.-W. and Braido, P. (2003) 'Determining finger segmental centers of rotation in flexion-extension based on surface marker measurement', *Journal of Biomechanics*, 36, (8), pp. 1097-1102.

Appendix A. Finding the axis of rotation using singular value decomposition

As detailed in Chapter 5 Section 5.13 singular value decomposition (SVD) was used to find the axis of rotation (AoR). This is identical to the technique described by Ehrig et al (2007).

Assuming a common AoR $\boldsymbol{a}$ between two adjacent segments (Figure A.1). Rigid body transformations between cluster technical frames (CTF) attached to segments distal and proximal to the joint of interest can be defined as rotations $\boldsymbol{R}_i$ and translations $\boldsymbol{t}_i$. Using these, a constraint function f_{ATT} was defined as:

$$f_{ATT}(\boldsymbol{c}, \tilde{\boldsymbol{c}}) = \sum_{i=1}^{N} \|\boldsymbol{R}_i \tilde{\boldsymbol{c}} + \boldsymbol{t}_i - \boldsymbol{c}\|^2, \tag{A.1}$$

where N was the total number of capture frames. Positions on the AoR in either CTF proximal or distal to the joint of interest were defined as $\tilde{\boldsymbol{c}}$ and $\boldsymbol{c}$ respectively. The valid solutions of $\tilde{\boldsymbol{c}}$ and $\boldsymbol{c}$ were non-unique as they could be positioned anywhere along these infinite axes.

To find the single unique solution the equation was posed as a least squares problem in the matrix notation:

$$\begin{pmatrix} \boldsymbol{R}_1 & -\boldsymbol{I} \\ \vdots & \vdots \\ \boldsymbol{R}_N & -\boldsymbol{I} \end{pmatrix} \begin{pmatrix} \tilde{\boldsymbol{c}} \\ \boldsymbol{c} \end{pmatrix} = -\begin{pmatrix} \boldsymbol{t}_1 \\ \vdots \\ \boldsymbol{t}_N \end{pmatrix}. \tag{A.2}$$

This is equivalent to the equation:

$$\boldsymbol{Ax} = \boldsymbol{b}. \tag{A.3}$$

Matrices $\boldsymbol{U}$, $\boldsymbol{\Sigma}$, and $\boldsymbol{V}$ were calculated using the SVD of the matrix $\boldsymbol{A}$:

$$\boldsymbol{A} = \boldsymbol{U\Sigma V}^t. \tag{A.4}$$

The direction vectors of the AoR in each CTF ($\tilde{\boldsymbol{a}}$ and $\boldsymbol{a}$) were the first and last three components respectively of the last column of $\boldsymbol{V}$. The minimal norm was then given by:

$$\boldsymbol{x}^* = \sum_{i=5}^{5} \frac{\boldsymbol{u}_i^T b \boldsymbol{v}_i}{\sigma_i}. \tag{A.5}$$

The first three and last three components of $\boldsymbol{x}^*$ give the points $\tilde{\boldsymbol{c}}$ and $\boldsymbol{c}$ defining the unique solution in each segment's CTF. The sets of vectors $\boldsymbol{u}_i$ and $\boldsymbol{v}_i$, $i = 1,...,6$ were the columns of matrices $\boldsymbol{U}$ and $\boldsymbol{V}$ respectively. The entries of the main diagonal of the matrix $\boldsymbol{\Sigma}$, gave the singular values σ_i, $i = 1,...,6$.

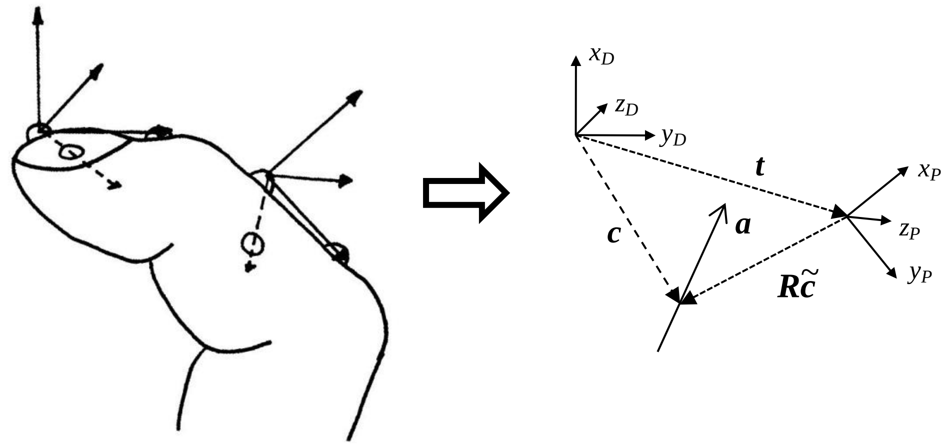

Figure A.1. *The phalanx transformation technique. CTFs were defined on each phalanx and the transformation between them defined as rotations* $\boldsymbol{R}$ *and translations* $\boldsymbol{t}$*. Any position* $\boldsymbol{c}$ *laying on the common AoR* $\boldsymbol{a}$ *can be expressed in the other CTF by the relationship* $\boldsymbol{c} = \boldsymbol{R}\tilde{\boldsymbol{c}} + \boldsymbol{t}$.

Appendix B. Multiple arc analysis

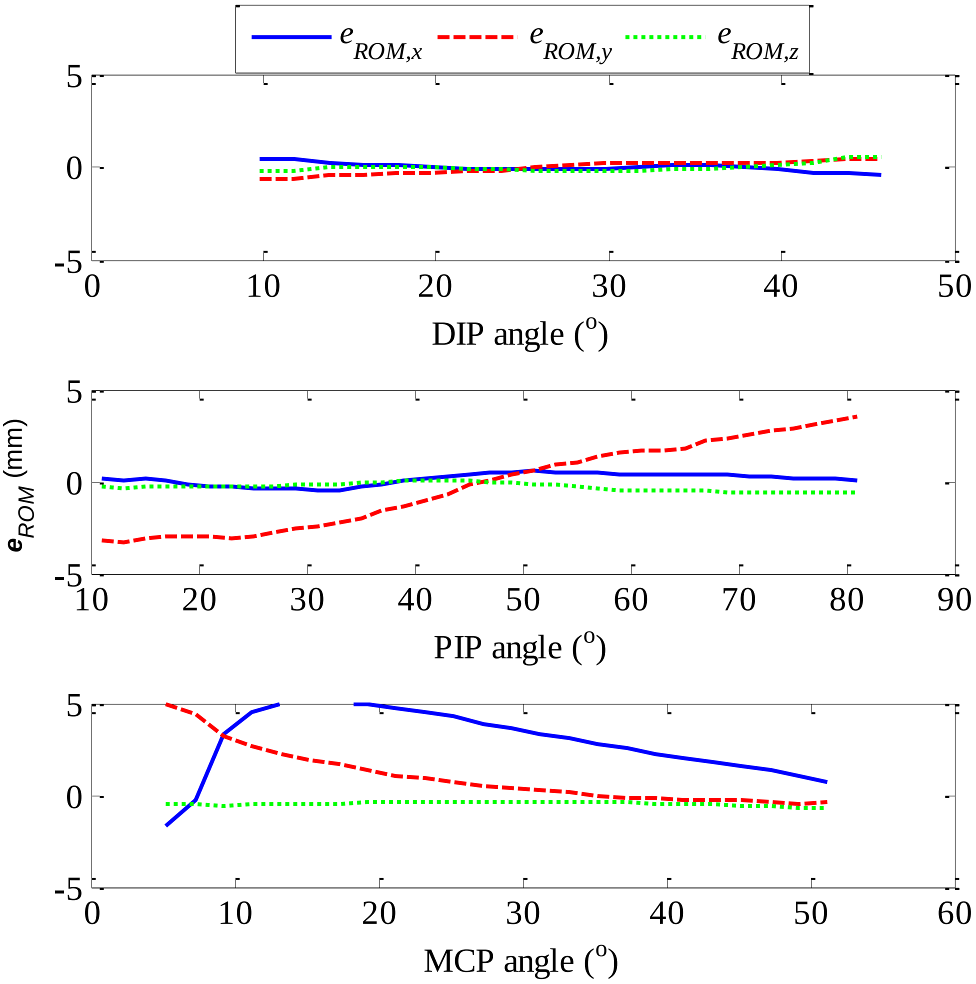

Figure B.1: $\boldsymbol{e}_{ROM}$ *from multiple arc analysis for Subject 1 at all joints with a magnitude* $|\varphi| = 30°$.

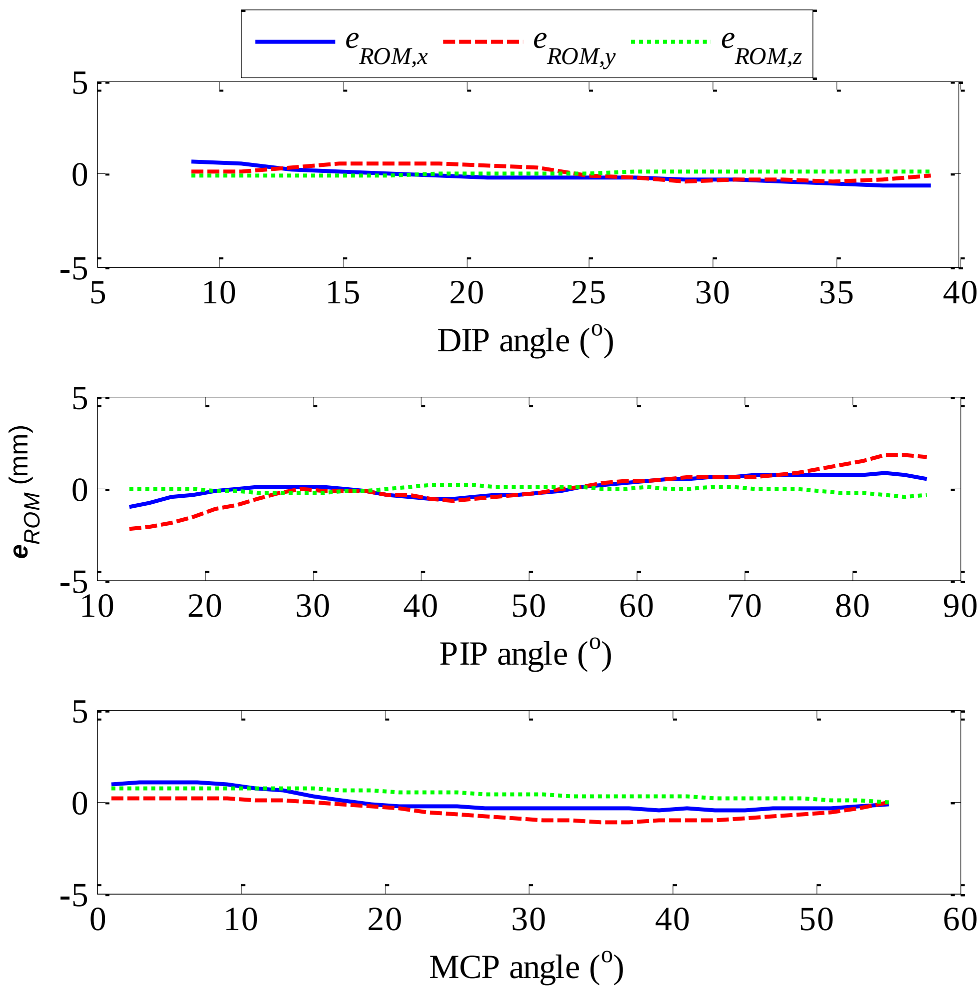

Figure B.2: ***e****ROM* *from multiple arc analysis for Subject 2 at all joints with a magnitude* $|\varphi| = 30°$.

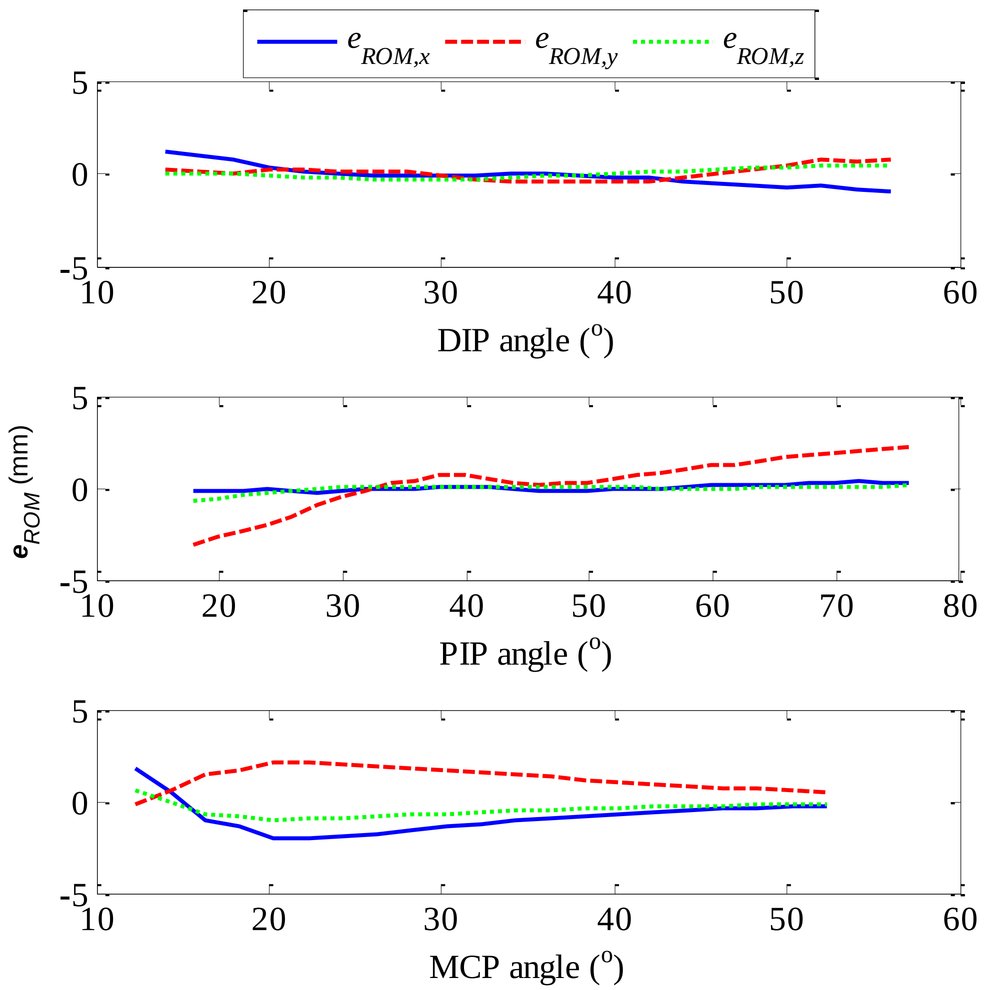

Figure B.3: ***e****ROM* *from multiple arc analysis for Subject 3 at all joints with a magnitude* $|\varphi| = 30°$.

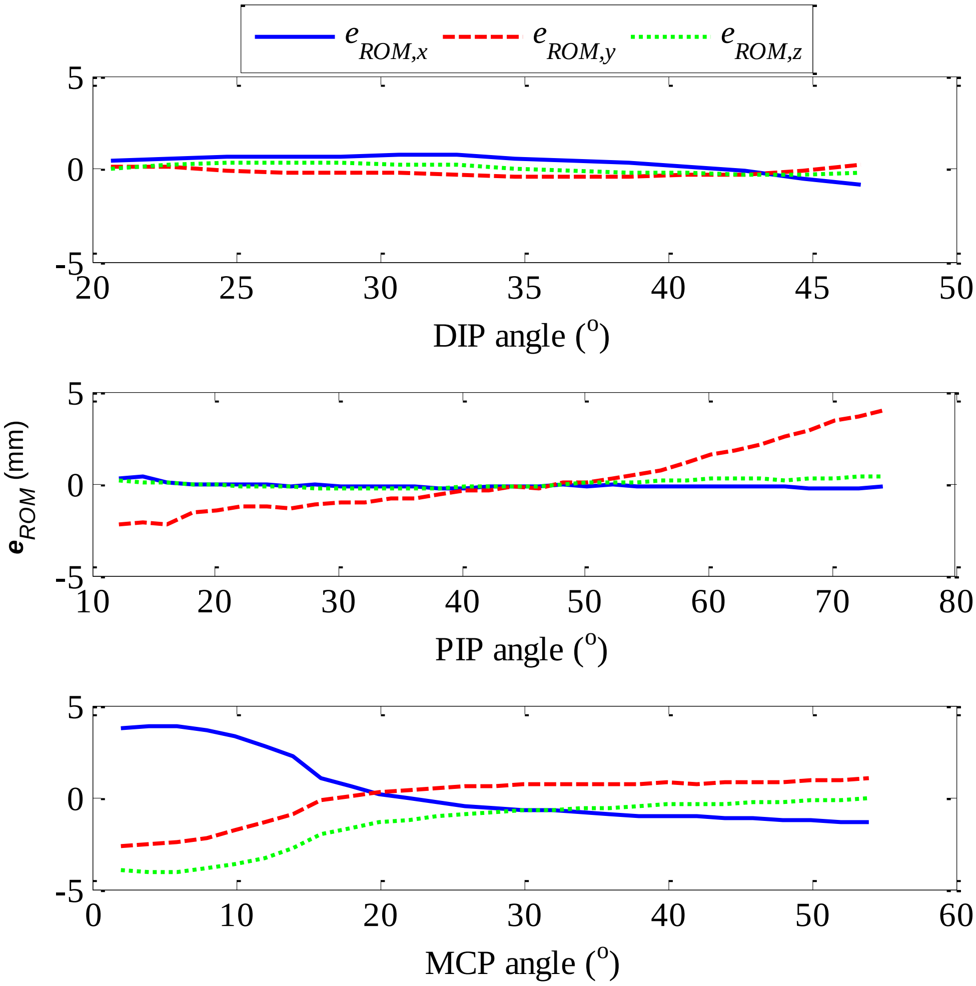

Figure B.4: ***e****ROM from multiple arc analysis for Subject 4 at all joints with a magnitude |φ| = 30°.*

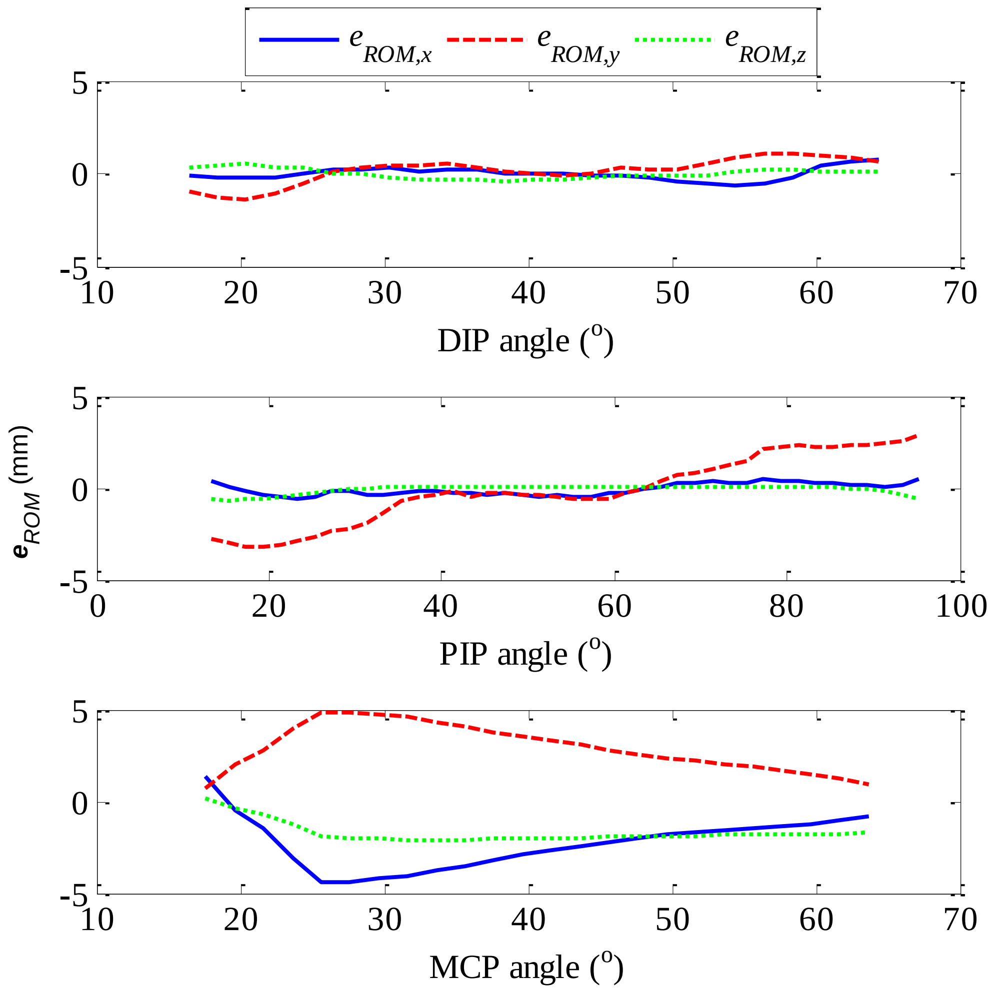

Figure B.5: ***e****ROM from multiple arc analysis for Subject 5 at all joints with a magnitude $|\varphi| = 30°$.*

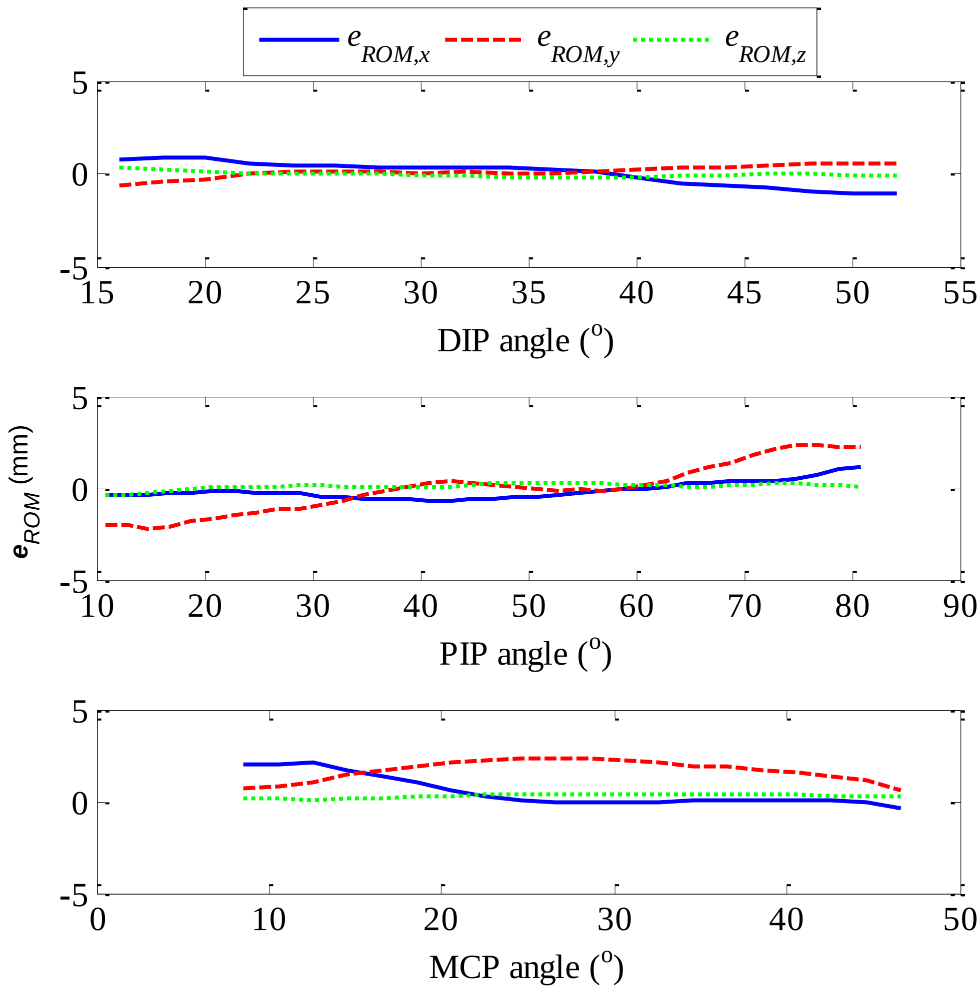

Figure B.6: ***e**$_{ROM}$ from multiple arc analysis for Subject 6 at all joints with a magnitude $|\varphi| = 30°$.*

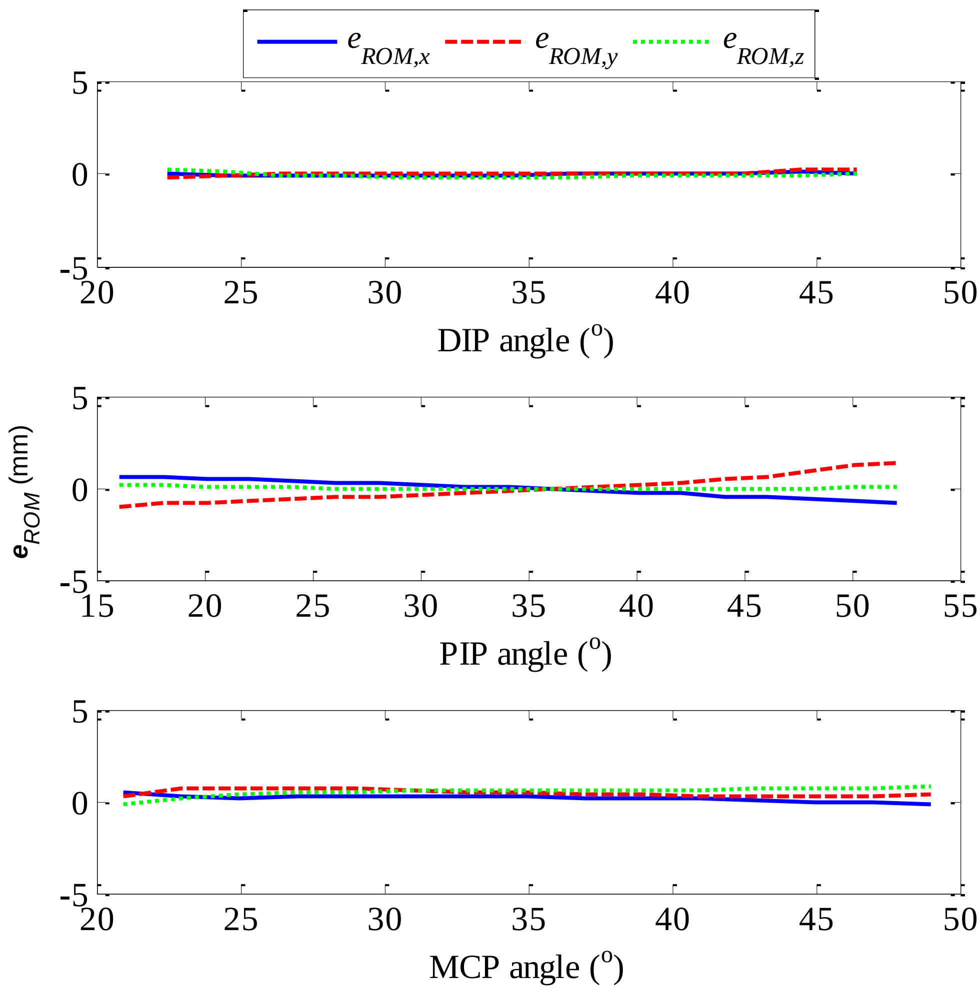

Figure B.7: $\boldsymbol{e}_{ROM}$ *from multiple arc analysis for Subject 7 at all joints with a magnitude* $|\varphi| = 30°$.

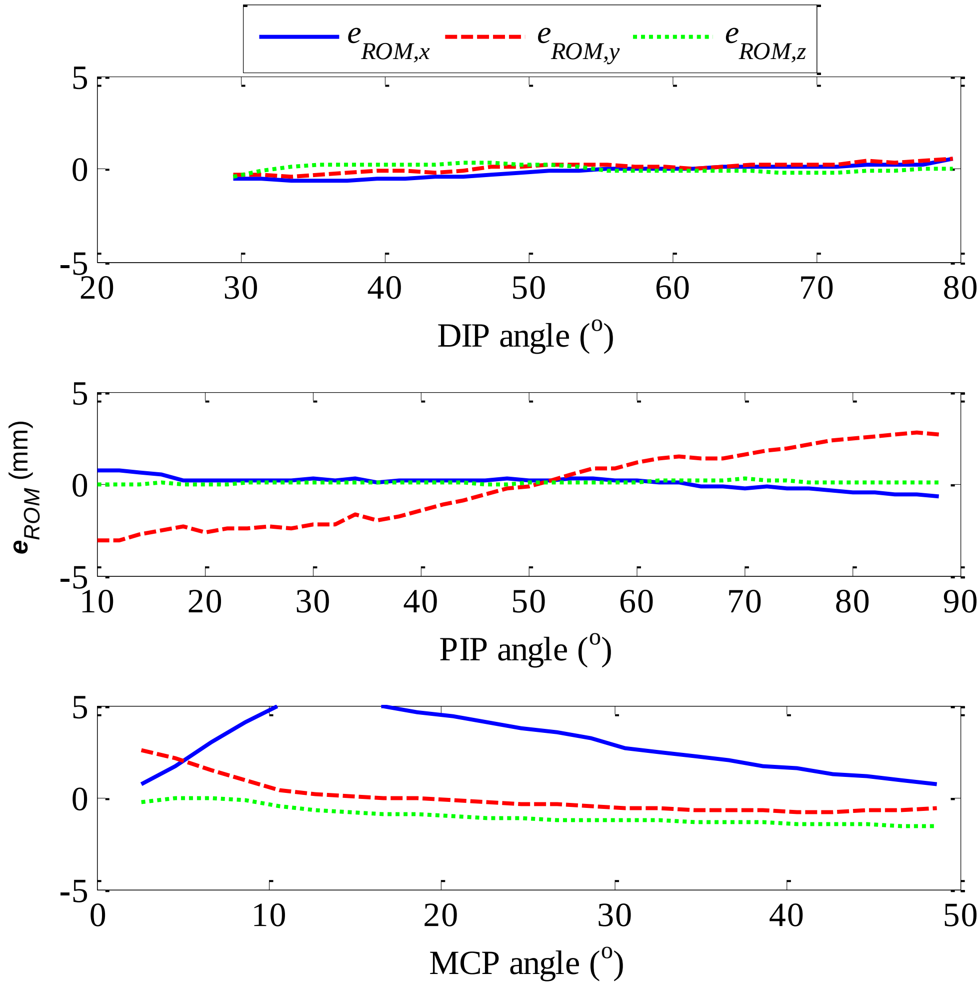

Figure B.8: ***e***$_{ROM}$ *from multiple arc analysis for Subject 8 at all joints with a magnitude* $|\varphi| = 30°$.

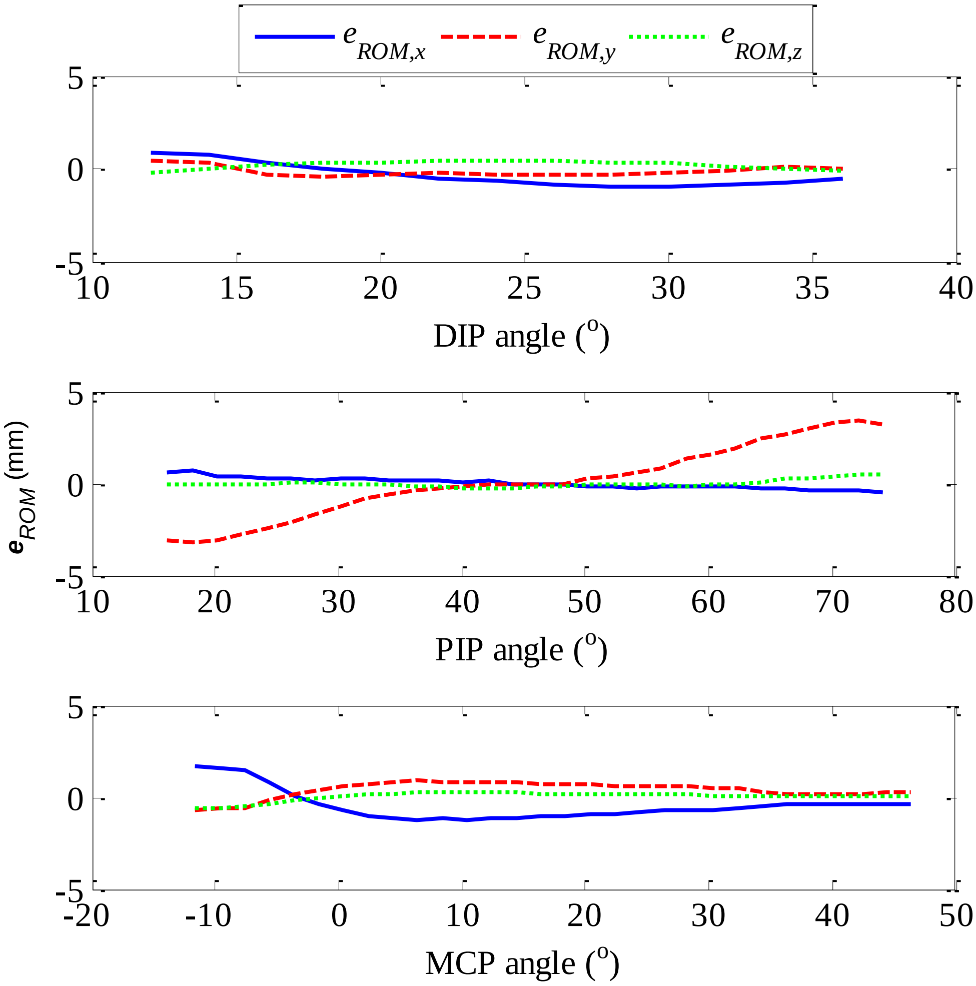

Figure B.9: $\boldsymbol{e}_{ROM}$ *from multiple arc analysis for Subject 9 at all joints with a magnitude* $|\varphi| = 30°$.

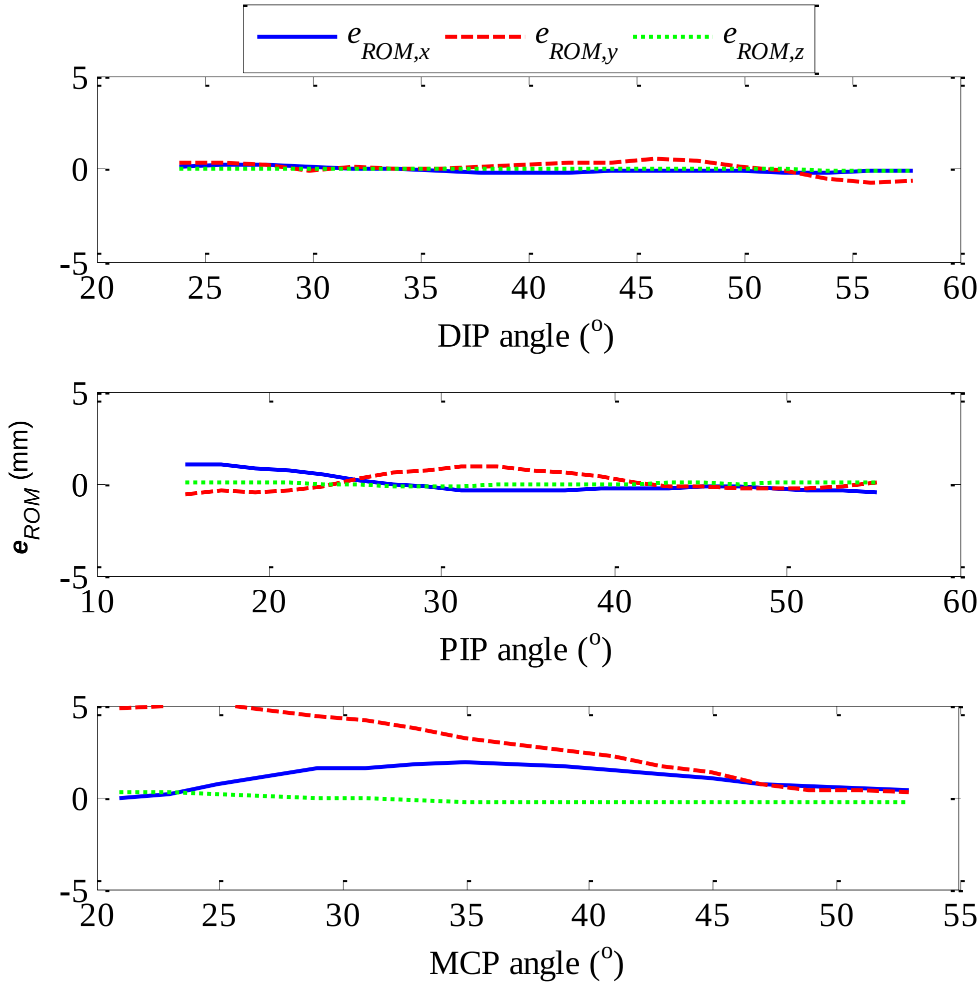

Figure B.10: ***e***$_{ROM}$ *from multiple arc analysis for Subject 10 at all joints with a magnitude* $|\varphi| = 30°$.

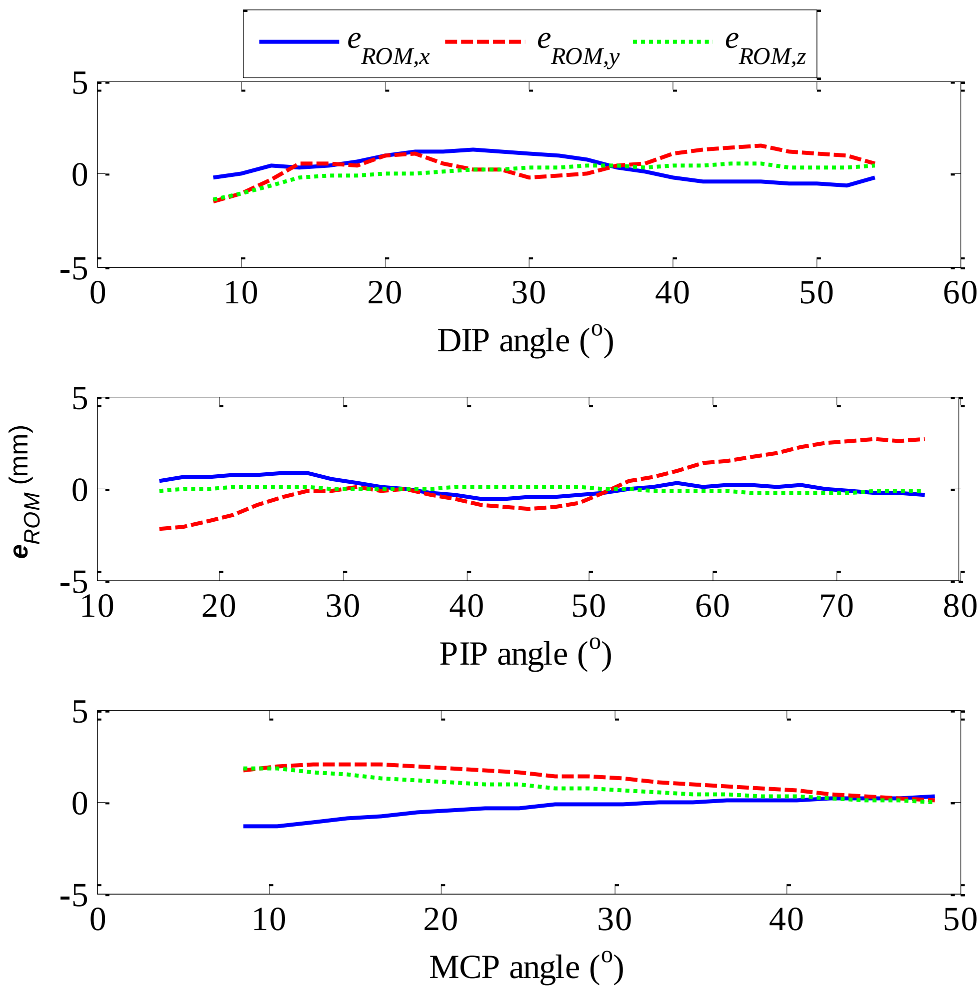

Figure B.11: ***e***$_{ROM}$ *from multiple arc analysis for Subject 11 at all joints with a magnitude* $|\varphi| = 30°$.

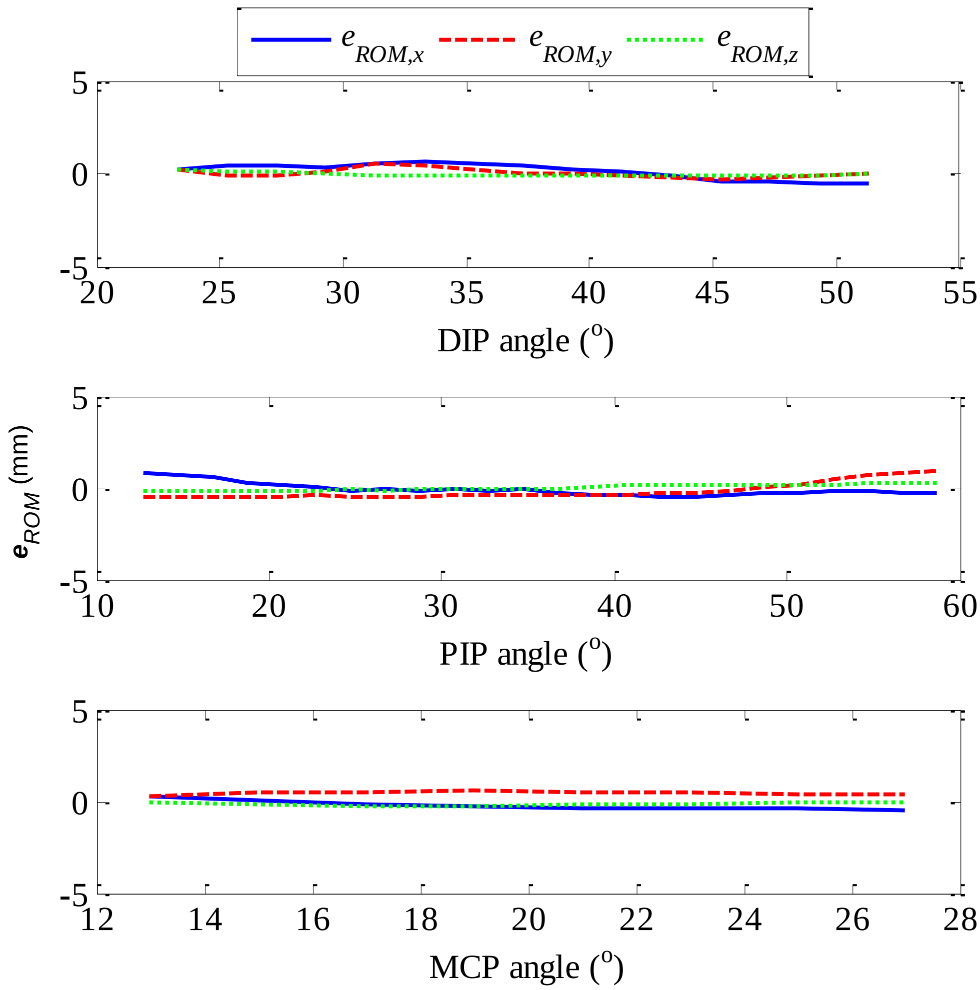

Figure B.12: $\boldsymbol{e}_{ROM}$ *from multiple arc analysis for Subject 12 at all joints with a magnitude* $|\varphi| = 30°$.

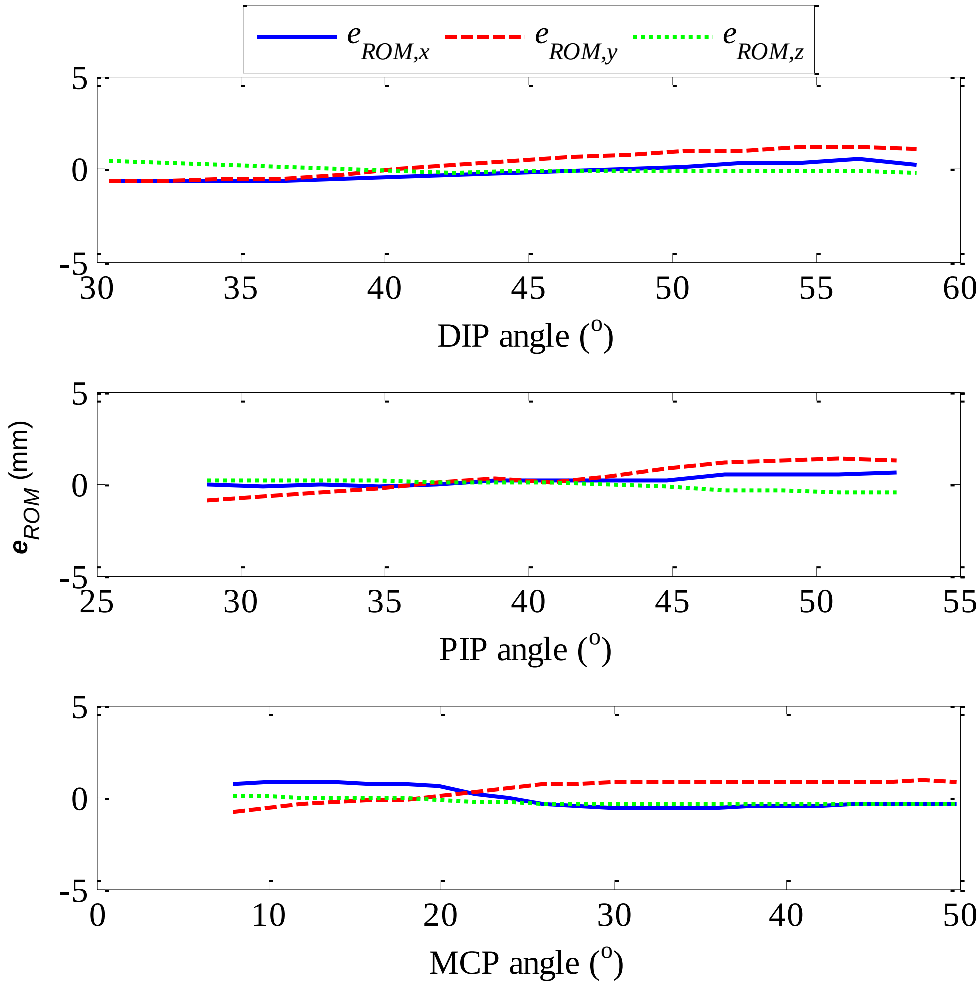

Figure B.13: $\boldsymbol{e}_{ROM}$ *from multiple arc analysis for Subject 13 at all joints with a magnitude* $|\varphi| = 30°$.